THERMODYNAMIC MODELING OF HCCI COMBUSTION WITH RECOMPRESSION AND DIRECT INJECTION

by

Prasad Sunand Shingne

A dissertation submitted in partial fulfillment
of the requirements for the degree of
Doctor of Philosophy
(Mechanical Engineering)
in the University of Michigan
2015

Doctoral Committee:

Professor Dionissios N. Assanis, Co-Chair
Associate Professor Claus Borgnakke, Co-Chair
Assistant Research Scientist Jason B. Martz, Co-Chair
Professor Andre L. Boehman
Assistant Research Scientist Stanislav V. Bohac
Professor James F. Driscoll

To my Parents.

ACKNOWLEDGMENTS

I am very grateful for the opportunity to work with many brilliant and meticulous individuals during the course of this degree. I would like to begin by thanking Professor Dennis Assanis for giving me the opportunity to join his group in the Automotive Laboratory. He has been a truly inspirational teacher. I would not have pursued a PhD had I not taken ME438 and ME538, the two engines classes taught by him. I have learned a great deal from our interactions over the years.

I am extremely fortunate to have worked closely with Dr. Jason Martz over the course of the last four and a half years. I have truly learned a great deal about engine combustion modeling as well as conducting independent research from him. His strong work ethic, constant guidance and support have been instrumental in my progress. I can truly say that none of this work would have been possible without his guidance. I am thankful for his critical inputs and high standards with regards to this thesis.

I would like to thank Prof. Claus Borgnakke for serving as one of the co-chairs on my committee. I greatly appreciate the interest he has taken in my work especially over the last year and a half. His suggestions and inputs have played an important part in shaping and improving the quality of this thesis. Above all, I am grateful for his willingness and availability to discuss my work, or any facet of thermal sciences in general.

I acknowledge Professor James Driscoll, Professor Andre Boehman and Dr. Stani Bohac for serving on my committee and taking time out of their busy schedules to devote to my thesis.

I thank Robert Bosch LLC for providing the funding for this work. I am grateful to the entire Bosch Advanced System Engineering team consisting of Alan Mond (former employee), Dr. Li Jiang, Oliver Miersch-Wiemers, Hakan Yilmaz and especially Jeff Sterniak for their support. I thank Jeff for collecting the majority of the engine data used in this work and for his patient replies to my several inquiries regarding the experimental setup and procedure. I was fortunate to work more closely with the entire team as part of two internships I undertook at Bosch at the beginning of my Ph.D. It was a great learning experience in a supportive environment.

I am thankful to Dr. Janardhan Kodavasal, Dr. Elliot Ortiz-Soto and especially Dr. Robert Middleton for their assistance with programming throughout my PhD. The CFD work in my thesis would have taken a significantly longer time to perform without the help of Dr. Middleton. I also thank him for several useful discussions and reviewing sections of this thesis. I acknowledge Dr. Laura Olesky for providing experimental data used as validation for the CFD simulations in this work. I'm grateful to my friends from the Autolab, especially from the Bosch ACCESS project, particularly Vasilis, Adam and Pat who have always kept my spirits high even when the circumstances appeared to be negative. I would also like to acknowledge my friends Philipp, Sakthish, Satyajeet, Fabrice, Avani, Mallory, Harish, Vickey, Siddhesh, Suyash and others. Also my friends from back home, Parikshit, Akshay S., Akshay D., Rahul, Mikhil, Harshawardhan and Vivek. Your support has contributed to my well-being on several occasions and I am thankful for that.

I thank my extended family and especially my cousins Shruti and Radha who have been more like my sisters, for always being there for me. Finally, I thank my parents Nutan S. and Sunand D. Shingne for all their love and support.

TABLE OF CONTENTS

DEDICATION ..... **ii**
ACKNOWLEDGMENTS ..... **iii**
LIST OF FIGURES ..... **x**
LIST OF TABLES ..... **xxiv**
ABSTRACT ..... **xxvi**
CHAPTER 1 INTRODUCTION **1**

1.1 Homogeneous charge compression ignition 2
1.2 Characteristics of HCCI combustion 2
1.3 Crucial HCCI actuators and their effects on combustion 3
1.3.1 Variable valve actuation 4
1.3.2 Boosting 5
1.3.3 Direct injection and reactions during NVO 7
1.4 Necessity of fast 0D models for HCCI studies 8
1.5 Prior model and breakdown compared to experiment 9
1.6 Motivation, Objectives and document organization 10
1.6.1 Motivation for current study 10
1.6.2 Research objectives 11
1.7 References 16
CHAPTER 2 TOOLS USED AND ANALYSIS METHOD **23**

2.1 Overview of CFD software 24
2.2 Chemical kinetic modeling 24
2.3 Fully coupled CFD and multi-zone model 25
2.4 Experimental engine setups 27

2.4.1 Fully flexible valve actuation engine (FFVA) 27
2.4.2 Four cylinder boosted engine (FCB)..... 28
2.5 CFD model setup..... 29
2.5.1 Multi-cycle simulation procedure..... 30
2.5.2 Baseline NVO-DI case..... 32
2.5.3 Thermal and compositional stratification metrics..... 32
2.6 Analysis method for CFD data..... 33
2.6.1 Reaction space analysis..... 34
2.6.2 Decoupling thermal and compositional stratification effects on reactivity…… 35
2.6.3 Isolation of the thermal stratification effect on burn duration using Quasi-Dimensional model 35
2.7 Cycle simulation software for systems-level simulations 37
2.7.1 Three pressure analysis (TPA) of experimental data..... 37
2.7.2 Modelling combustion and heat transfer in GT-Power..... 38
2.8 References 52
CHAPTER 3 EFFECT OF OPERATING CONDITIONS ON NVO-DI HCCI COMBUSTION: SPEED, LOAD (ϕ') AND BOOST..... 57
3.1 Background 57
3.2 Effect of Varying Engine Speed on NVO-DI HCCI..... 59
3.2.1 Stratification evolution from IVC to TDC..... 60
3.2.2 Analysis of reaction space at 12.5°CA 62
3.2.3 Decoupling the effect of compositional stratification on reactivity.... 62
3.2.4 Removing the effect of differing residence time on reactivity 63
3.2.5 Isolating the effect of stratification on reactivity..... 63
3.3 Effect of Varying Load [Total Dilution (ϕ')] on NVO-DI HCCI..... 64
3.3.1 Analysis of reaction space at 12.5^{o} CA bTDC..... 65

3.3.2 Decoupling the effect of compositional stratification on reactivity.... 65
3.3.3 Decoupling thermodynamic effects from chemical kinetic effects 66
3.4 Effect of Varying Boost on NVO-DI HCCI..... 67
3.4.1 Analysis of reaction space at 12.5°CA bTDC 68
3.4.2 Decoupling the effect of compositional stratification on reactivity.... 69
3.4.3 Decoupling the effect of pressure on burn duration..... 69
3.4.4 Isolating the effect of thermal stratification on burn duration 70
3.5 Summary and conclusions..... 71
3.6 References 93
CHAPTER 4 EFFECT OF INPUT ACTUATORS ON NVO-DI HCCI COMBUSTION: INJECTION TIMING, NEGATIVE VALVE OVERLAP AND INTAKE TEMPERATURE..... 95
4.1 Effect of Varying Start of Injection (SOI) on NVO-DI HCCI..... 95
4.1.1 Analysis of reaction space at 12.5°CA bTDC 97
4.2 Effect of Varying Negative Valve Overlap (NVO) on NVO-DI HCCI..... 97
4.2.1 Analysis of reaction space at 12.5°CA bTDC 98
4.3 Effect of Varying Intake Temperature on NVO-DI HCCI..... 99
4.3.1 Analysis of reaction space at 11.5°CA before θ10..... 99
4.3.2 Decoupling the combustion timing effect on burn duration 100
4.4 Summary and conclusions..... 101
4.5 References 116
CHAPTER 5 ADIABATIC CORE IGNITION MODEL 117
5.1 Background 117
5.2 Interrogation of HCCI ignition process using CFD 119
5.3 Adiabatic core ignition model performance..... 120
5.4 Validation for RPM sweep..... 124
5.5 Validation for ϕ' sweep..... 125

5.6 Validation for boost sweep 125
5.7 Validation for SOI sweep 126
5.8 Validation for NVO sweep 127
5.9 Validation for intake temperature sweep 127
5.10 Summary 128
5.11 References 142
CHAPTER 6 EMPIRICAL BURN PROFILE AND VALIDATION OF COMBUSTION MODEL 147
6.1 Background 147
6.2 Burn profile model 149
6.3 Model validation 153
6.3.1 Ignition model calibration 154
6.3.2 Transient response to changing engine speed 155
6.3.3 Transient response to changing EVC timing 157
6.3.4 Transient response to change in SOI 158
6.3.5 Transient response to change in fueling 159
6.4 Summary 159
6.5 References 174
CHAPTER 7 HCCI RECOMPRESSION HEAT RELEASE AND CYCLIC COUPLING 177
7.1 Multi-cycle simulation of HCCI with late combustion phasing 179
7.1.1 Validity of reduced gasoline reaction mechanism for lean NVO conditions 180
7.2 Impact of NVO heat release on cylinder temperature and subsequent cycle 181
7.3 Effect of residual fuel on the next cycle without NVO heat release 182
7.4 Effect of combustion efficiency on the subsequent cycle 182

7.5 Effect of injection timing on NVO heat release 183
7.5.1 Validity of reduced reaction mechanism for rich NVO conditions .. 184
7.6 State of reacting charge during NVO 184
7.6.1 Late injection 185
7.6.2 Early injection 185
7.7 Effect of varying mass diffusion on NVO heat release for early injection 186
7.8 0D model for NVO heat release 186
7.9 Summary 188
7.10 References 207
CHAPTER 8 SUMMARY, CONCLUSIONS AND RECOMMENDATIONS 210
8.1 Summary and conclusions 210
8.1.1 Effect of operating conditions on reactivity stratification and HCCI combustion 210
8.1.2 Adiabatic core ignition model 213
8.1.3 New burn correlation and improved 0D model performance 214
8.1.4 Recompression heat release 215
8.2 Scientific Contributions 216
8.3 Recommendations for future work 218
8.4 References 219

LIST OF FIGURES

Figure 1.1 – Example SI and HCCI cam profiles. 14

Figure 1.2 – Continuous modeling process with different fidelity models [44]. 14

Figure 1.3– Old model predictions and experimental measurements for a transient speed change: (a) speed change (b) fuel-to-air equivalence ratio (ϕ), (c) combustion phasing ($\theta 50$), (d) burn duration ($\theta 10-90$), (e) peak pressure rise rates (PPRR), and (c) peak pressure (P_{MAX}) 15

Figure 2.1 – Schematic of the four cylinder boosted (FCB) engine showing the main components; with the BorgWarner KP31 turbocharger. 44

Figure 2.2 – Recompression NVO valve lifts at two phasings. Solid lines show zero NVO position. 44

Figure 2.3 – Computation mesh used in this work, containing 156,000 cells, based on the FFVA engine [15]. Exhaust ports on the left, intake ports on the right. 45

Figure 2.4 – Example valve lifts from FFVA engine for HCCI operation with negative valve overlap. 45

Figure 2.5 – Schematic of multi-cycle simulation procedure. (a) Simulation is initialized prior to EVO of Cycle 0 and run through the gas exchange and fuel injection using a small chemical mechanism (fuel, O_2, N_2, CO_2, H_2O) with no reactions. The mechanism is changed to the reduced gasoline surrogate mechanism [7] and chemistry is started at Restart 1. (b) Threshold and mechanism swap [23] is similarly performed at Restart 2 – 5 to speed up simulations by reducing species and turning off the chemistry during the breathing events while capturing the effect of NVO reactions on subsequent cycle. 46

Figure 2.6 - (a) Pressure traces and (b) mass fraction burned curves for experiments versus CFD: 9.4 mg/cycle injected, NVO =157°CA, T_{in} = 106°C, RGF (experiment) = 48%, RGF (CFD) = 43%, Φ (experiment) = 0.6, Φ (CFD) = 0.58, Φ'(experiment) = 0.32, Φ'(CFD) = 0.32. 47

Figure 2.7 – Evolution of stratification from IVC (130° CA bTDC) to TDC for the NVO-DI case visualized in terms of (a) $2\sigma T$, (b) $2\sigma\phi FO$ and (c) $2\sigma\chi O2$. 48

Figure 2.8 – Reaction space at -12.5° CA aTDC from CFD simulations visualized in terms of bins denoted by temperature, (a) ϕFO (b) $\chi O2$ and colored by the mass fraction. 48

Figure 2.9 – Reaction space at -12.5° CA aTDC from CFD simulations visualized in terms of bins denoted by temperature, ϕFO and colored by ignition delay of the bin. 49

Figure 2.10 – Reaction space (at 12.5° CA bTDC) visualized in terms of cumulative charge mass below a certain ignition delay with the cell and mean composition. ... 49

Figure 2.11 – Mass fraction burned predictions from the quasi-dimensional model for NVO-DI and NVO-DI with mean composition. The results indicate that neglecting the compositional stratification does not significantly impact the overall burn duration. 50

Figure 2.12 – Intake runner – to – exhaust runner model in GT-Power with appropriate inputs to isolate Cylinder 1 from rest of the engine system for three pressure heat release analysis. 50

Figure 2.13 – Cycle to cycle variation in pressure data at steady state for an operating point, a) cylinder pressure traces for all cycles b) Frequency of occurrence based on cyclic peak pressure. Cycle closest to the mean peak pressure, cycle with the median peak pressure and ten most frequently operating peak pressure cycles have also been marked. 51

Figure 2.14 – Sample result from heat release analysis (for cycle closest to the mean peak pressure cycle) including (a) the experimental/simulated pressure, estimated mean charge temperature and (b) mass fraction burned curve for HCCI operation at 1500RPM, 5.6 bar net IMEP, 1.4 bar/1.5 bar absolute intake/exhaust pressure, 93^{o} CA NVO, ϕ=0.67, RGF = 34% and ϕ'=0.44. 51

Figure 3.1 – Comparison of MFB curves from CFD for the speed sweep in Table 3.1. Plotted against crank angle; the burn duration increases with engine speed. 75

Figure 3.2 – Evolution of (a) thermal and (b) compositional stratification from IVC to TDC. The thermal stratification falls after IVC due to mixing until ~60^{o} CA bTDC but rises from there to TDC as it is subsequently dominated by wall heat losses. The higher speed cases have a higher initial compositional stratification which falls from IVC to TDC due to mixing. 75

Figure 3.3 – Spatial distribution of CO2 (gm/cc) as a marker of residuals in a clip plane from CFD at intake valve closing for (a) 1000 RPM and (b) 3000 RPM..... 76

Figure 3.4 – Spatial distribution of temperature in a clip plane from CFD at intake valve closing for (a) 1000 RPM and (b) 3000 RPM..... 76

Figure 3.5 – Spatial distribution of ϕFO in a clip plane from CFD at intake valve closing for (a) 1000 RPM and (b) 3000 RPM. 77

Figure 3.6 – Evolution of (a) thermal and (b) compositional stratification from IVC to TDC plotted versus number of eddy turnovers. 77

Figure 3.7 – Evolution of compositional stratification in terms of $2\sigma\phi FO$ for the speed sweep plotted versus time. 78

Figure 3.8 – Mass distribution over (a) temperature and (b) ϕFO from non-reacting CFD simulations plotted at 12.5^{o} CA bTDC. The thermal stratification increases slightly with speed and ϕFO stratification increases nearly linearly with speed. 78

Figure 3.9 – Reaction space at 12.5^{o} CA bTDC visualized in terms of cumulative charge mass below a certain ignition delay, for the speed sweep computed from non-

reacting CFD simulations with cell temperature and composition. The higher speed cases appear more reactive..... 79

Figure 3.10 – Quasi-D model results for the speed sweep with zone temperatures and compositions obtained from non-reacting CFD, initialized at 12.5^{o} CA bTDC. 79

Figure 3.11 – Reaction space at 12.5^{o} CA bTDC visualized in terms of the cumulative charge mass below a certain ignition delay, for the speed sweep computed from non-reacting CFD simulation with the cell level and mean composition at (a) 1000 RPM, (b) 2000 RPM, (c) 3000 RPM. The reactivity of the high speed case shows more sensitivity to compositional stratification. 80

Figure 3.12 – Quasi-D model results for speed sweep with stratification initialized at 12.5^{o} CA bTDC. All cases are simulated at 2000 RPM to remove the effect of different residence times (*). 81

Figure 3.13 – Reaction space at 12.5^{o} CA bTDC visualized in terms of cumulative charge mass below a certain ignition delay, for the speed sweep computed from non-reacting CFD simulations. Cell temperatures have been shifted for 1000 RPM and 3000 RPM case (♦) so that the hottest temperature for all cases is matched. The additional mean cmp. case corresponds to the 3000 RPM case simulated with the mean composition. 81

Figure 3.14 – Quasi-dimensional model results for the speed sweep with stratification initialized at 12.5^{o} CA bTDC. All cases are simulated at 2000 RPM to remove the effect of different residence times. Additionally the temperatures for 1000 RPM and 3000 RPM case (♦) are shifted so that hottest temperature for all cases is matched. The additional mean cmp. case corresponds to the 3000 RPM case simulated with the mean composition. 82

Figure 3.15 – Comparison of MFB curves from CFD for the ϕ' sweep in Table 3.2, with $\theta 10$ matched. The burn durations are shorter for richer ϕ' values. 82

Figure 3.16 – Mass distribution over (a) temperature and (b) ϕFO from non-reacting CFD simulations plotted at -12.5 ^{o}CA aTDC. The thermal and compositional stratification remains roughly the same. 83

Figure 3.17 – Reaction space (at 12.5^{o} CA bTDC) visualized in terms of cumulative charge mass below a certain ignition delay, for ϕ' computed from non-reacting CFD cell temperature and composition. The higher ϕ' cases are more reactive. 83

Figure 3.18– Reactivity distribution plotted as cumulative charge mass below a certain ignition delay using the cell level and mean composition, for (a) ϕ'= 0.24, (b) ϕ'= 0.29, (c) ϕ'= 0.32 and (d) ϕ'= 0.37. Compositional stratification has minimal affect on reactivity under the conditions studied. 84

Figure 3.19 – Distribution of γ (at 12.5^{o} CA bTDC) from non-reacting CFD simulation for the ϕ' sweep. 85

Figure 3.20 – Quasi-dimensional model results for the ϕ' sweep; (a) Mass fraction burned curves, (b) variation of γ with progress of combustion. 85

Figure 3.21 – Quasi-D results for the ϕ' sweep with initial γ matched; (a) Mass fraction burned curves, (b) variation of γ with reaction progress. 86

Figure 3.22 – Variation of c_p with reaction progress (Quasi-D) for the ϕ' sweep with the initial c_p (a) unmatched and (b) matched to the baseline case. 86

Figure 3.23 - Comparison of MFB curves from the CFD intake boost sweep in Table 3.3, with $\theta 10$ matched. The burn durations are shorter for greater boost. 87

Figure 3.24 - Evolution of thermal stratification from IVC to TDC (a) $2\sigma T$ plotted versus crank angle, the thermal stratification falls after IVC due to mixing until ~60^{o} CA bTDC but rises from there to TDC due to dominant wall heat losses. The higher boost cases have a lower mean cylinder temperature due to which the wall heat loss driven thermal stratification is lower. This is explicitly clear when (b) $2\sigma T$ is plotted versus mean cylinder temperature normalized to the maximum mean temperature. 87

Figure 3.25 – Mass distribution over (a) temperature and (b) ϕFO from non-reacting CFD simulations plotted at -12.5^{o} CA aTDC. The thermal stratification decreases with boost and the compositional stratification remains roughly the same. 88

Figure 3.26 - Reaction space (at 12.5^{o}CA bTDC) visualized in terms of the cumulative charge mass below a certain ignition delay, for the boost sweep computed from non-reacting CFD simulations with cell temperature and composition. Reactivity increases with boost pressure. 88

Figure 3.27 - Quasi-D model results for the boost pressure sweep with default stratification initialized at 12.5^{o} CA bTDC. 89

Figure 3.28 – Reaction space (at 12.5^{o} CA bTDC) visualized in terms of the cumulative charge mass below a certain ignition delay computed with the cell level and mean composition for (a) $PIN - EX$= 1 bar, (b) $PIN - EX$= 1.5 bar and (c) $PIN - EX$= 2 bar. 90

Figure 3.29 – Reaction space at 12.5^{o} CA bTDC visualized in terms of the cumulative charge mass below a certain ignition delay, for the boost pressure sweep computed from non-reacting CFD simulations with cell temperature and composition and baseline pressure. Removing the pressure effect (*) makes the ignition delays for the original higher pressure cases longer. 91

Figure 3.30 – Quasi-D model results for the boost pressure sweep initialized at 12.5^{o} CA bTDC initialize with the baseline pressure to decouple the effect of pressure on combustion characteristics. Removing the pressure effect pushes the phasing later for the original higher pressure (*) cases. 91

Figure 3.31 – Reaction space (at 12.5^{o} CA bTDC) visualized in terms of the cumulative charge mass below a certain ignition delay, for the boost pressure sweep computed from non-reacting CFD simulations to isolate the effect of stratification. Ignition delays are computed with the baseline pressure, cell composition and leading edge

of the temperature distribution matched to the baseline case. The original high pressure (♦) cases have a lower thermal stratification and higher reactivity. 92
Figure 3.32 – Quasi-D model results for the boost pressure sweep initialized at 12.5° CA bTDC to isolate the effect of stratification on combustion. Cases initialized with baseline pressure and the hottest temperatures are matched to hottest temperature of baseline case. Original high pressure (♦) cases with lower thermal stratification burn faster. 92
Figure 4.1 – Mean cylinder temperature from CFD during NVO for the SOI sweep in Table 4.1. Temperatures are different for different injection events but match during the intake due to temperature compensation to match $\theta 10$. 105
Figure 4.2 – Comparison of MFB curves from CFD for the SOI sweep in Table 4.1. Burn duration remains nearly the same. 105
Figure 4.3 – Mass distribution over (a) temperature and (b)ϕFO from non-reacting CFD simulations plotted at -12.5°CA aTDC. The thermal stratification remains the same whereas compositional stratification increases with later injection timing. 106
Figure 4.4 – Reaction space (at 12.5°CA bTDC) visualized in terms of cumulative charge mass below a certain ignition delay, for the ϕ' sweep computed from non-reacting CFD simulation 106
Figure 4.5– Reaction space (at 12.5°CA bTDC) visualized in terms of cumulative charge mass below a certain ignition delay for the SOI sweep, computed from non-reacting CFD with cell level and mean composition (a) SOI= 310°CA aTDC, (b) SOI= 390°CA aTDC, and (c) SOI= 430°CA aTDC. 107
Figure 4.6 – Comparison of MFB curves from CFD NVO sweep in Table 4.2. $\theta 10$ being matched the burn durations are nearly the same. 108
Figure 4.7 – Mass distribution over (a) temperature and (b)ϕFO from non-reacting CFD simulations plotted at -12.5°CA aTDC. The thermal stratification remains the same whereas compositional stratification increases with larger NVOs. 108

Figure 4.8 – Reaction space (at 12.5°CA bTDC) visualized in terms of (a) cumulative charge mass below a certain ignition delay and (b) mass at a certain ignition delay, for the NVO sweep computed from non-reacting CFD simulations. 109

Figure 4.9 – Reaction space (at 12.5°CA bTDC) visualized in terms of cumulative charge mass below a certain ignition delay computed with the cell level and mean composition for (a) NVO = 197°CA, (b) NVO = 177°CA, (c) NVO = 157°CA, (d) NVO = 137°CA and (e) NVO = 117°CA. 110

Figure 4.10 – Comparison of MFB curves from CFD for intake temperature sweep in Table 4.3. 111

Figure 4.11 – Mass distribution over (a) temperature and (b)$\phi FO$from non-reacting CFD simulations plotted at 11.5°CA aTDC before $\theta 10$. The thermal and ϕFO stratification remains roughly the same for the intake temperature sweep..... 111

Figure 4.12 – Reaction space (at 11.5°CA before $\theta 10$) visualized in terms of cumulative charge mass below a certain ignition delay, for the intake temperature sweep computed from non-reacting CFD simulations with cell temperature and composition..... 112

Figure 4.13 – Reaction space (at 12.5^{o} CA bTDC) visualized in terms of cumulative charge mass below a certain ignition delay computed with the cell level and mean composition for (a) TIN= 66^{o}C, (b) TIN= 106^{o}C and (c) TIN= 146^{o}C 113

Figure 4.14 – Quasi-D model results for the intake temperature sweep initialized at 11.5^{o}CA before $\theta 10$show trends similar to CFD..... 114

Figure 4.15 – Quasi-D model results for the intake temperature sweep initialized at 12.5^{o}CA bTDC (θign of the baseline case). These MFB curves match the cumulative reactivity distribution seen in Figure 4.12..... 114

Figure 4.16 –Reaction space (at 11.5^{o}CA before $\theta 10$) visualized in terms of cumulative charge mass below a certain ignition delay, for the intake temperature sweep computed from non-reacting CFD simulations with cell temperature and

composition while using pressure for baseline case. Removing the $\theta 10$timing effect the cumulative reactivity distributions collapse. 115

Figure 4.17 – Quasi-D model results for boost pressure sweep initialized at 12.5^{o} CA bTDC to isolate the effect to thermal and compositional stratification on combustion. Cases initialized at the same crank angle have the $\theta 10$matched and nearly the same burn profiles. 115

Figure 5.1 – Variation of overall reaction progress denoted by mass fraction burned (MFB) with crank angle for the PVO and NVO case respectively from Table 5.1 131

Figure 5.2 – Reaction space from CFD simulation visualized in terms of Φ, Temperature and Reaction Progress (c) for PVO and NVO. 132

Figure 5.3 – Comparison of mean temperature (T_m), temperature of the hottest 1% of the charge mass ($T_{1\%}$) and the adiabatic core temperature (T_{ad}) for two operating conditions (a) PVO and (b) NVO from IVC to TDC of a motoring CFD simulation 133

Figure 5.4 – Comparison of fuel-to-oxygen equivalence ratio in the global vs. the hottest 1% of the charge through the compression stroke, for (a) PVO and (b) NVO..... 133

Figure 5.5 – Comparison of molar percentage of oxygen in the global vs. the hottest 1% of charge through the compression stroke, for (a) PVO and (b) NVO 134

Figure 5.6 –Reaction space (at 12.5^{o} CA bTDC) visualized in terms of the cumulative charge mass below a certain ignition delay, for (a) PVO (~0^{o} NVO) and (b) NVO (157^{o} NVO) computed from non-reacting CFD simulations 134

Figure 5.7 – Ignition delay vs. crank angle for the temperature and composition of hottest 1% of the charge ($T1\% - C1\%$ denoted by the dark solid line), the global mean charge temperature and composition ($Tmean - Cmean$ denoted by the light solid line) and the adiabatic core temperature and composition ($Tad - Cmean$ denoted by the dashed line) for the (a) PVO and (b) NVO cases..... 135

Figure 5.8 – Ignition delay vs. crank angle for the temperature and composition of hottest 1% of the charge ($T1\% - C1\%$ denoted by the dark solid line), the global mean charge temperature and composition ($Tmean - Cmean$and denoted by the light solid line) and the adiabatic core temperature and composition ($Tad - Cmean$and denoted by the dashed line) for the (a) 1000 RPM, (b) 2000 RPM and (c) 3000 RPM cases 136

Figure 5.9 – Ignition delay vs. crank angle for the temperature and composition of hottest 1% of the charge ($T1\% - C1\%$ denoted by the dark solid line), the global mean charge temperature and composition ($Tmean - Cmean$and denoted by the light solid line) and the adiabatic core temperature and composition ($Tad - Cmean$and denoted by the dashed line) for the ϕ'sweep (a) ϕ'=0.24, (b) ϕ'=0.29, (c) ϕ'=0.32 and (d) ϕ'=0.37 137

Figure 5.10 – Ignition delay vs. crank angle for the temperature and composition of hottest 1% of the charge ($T1\% - C1\%$ denoted by the dark solid line), the global mean charge temperature and composition ($Tmean - Cmean$and denoted by the light solid line) and the adiabatic core temperature and composition ($Tad - Cmean$and denoted by the dashed line) for the boost sweep (a) $PIN - EX$=1bar, (b) $PIN - EX$=1.5bar and (c) $PIN - EX$=2bar..... 138

Figure 5.11 – Ignition delay vs. crank angle for the temperature and composition of hottest 1% of the charge ($T1\% - C1\%$ denoted by the dark solid line), the global mean charge temperature and composition ($Tmean - Cmean$and denoted by the light solid line) and the adiabatic core temperature and composition ($Tad - Cmean$and denoted by the dashed line) for the SOI sweep (a) SOI = 310^o CA aTDC (b) SOI = 390^o CA aTDC and (c) SOI = 430^o CA aTDC cases 139

Figure 5.12 – Ignition delay vs. crank angle for the temperature and composition of hottest 1% of the charge ($T1\% - C1\%$ denoted by the dark solid line), the global mean charge temperature and composition ($Tmean - Cmean$and denoted by the

light solid line) and the adiabatic core temperature and composition ($Tad - Cmean$and denoted by the dashed line) for the NVO sweep (a) NVO = 197^o CA, (b) NVO = 177^o CA, (c) NVO = 157^o CA, (d) NVO = 137^o CA and (e) NVO = 117^o CA cases 140

Figure 5.13 – Ignition delay vs. crank angle for the temperature and composition of hottest 1% of the charge ($T1\% - C1\%$ denoted by the dark solid line), the global mean charge temperature and composition ($Tmean - Cmean$and denoted by the light solid line) and the adiabatic core temperature and composition ($Tad - Cmean$and denoted by the dashed line) for the intake temperature sweep (a) TIN=66^o C, (b) TIN=106^o C and (c) TIN=146^o C 141

Figure 6.1 – (a) Example MFB curve for measured HCCI case, (b) Schematic description of the three-step HCCI combustion process. 163

Figure 6.2 – Comparison of correlation predictions to the experimental values of (a) location of 25% fuel burned (θ_{25}), (b) location of 50% fuel burned (θ_{50}) and (c) location of 75% fuel burned (θ_{75}) 163

Figure 6.3 – Combustion efficiency variation with peak temperature from closed cycle reacting CFD simulations [3]. The two intersecting lines provide a basis for the hyperbolic fit used in the model..... 164

Figure 6.4 - Comparison of correlation predictions to the experimental values of combustion efficiency..... 164

Figure 6.5 – Comparison between experiment and simulation (a) pressure trace, (b) mass fraction burned and (c) rate of heat release at 1500 RPM, 17.5 mg fuel, 95 deg NVO and 1.4 bar boost. The grey lines represent all cycles, the black line represents the cycle with the peak pressure closest to the mean PP and the dashed black line represents the simulation result..... 165

Figure 6.6 – Location of 50% MFB ($\theta 50$) for the mean PP cycle as a function of the mean experimental location of $\theta 50$ with the Goldsborough correlation activation

energy (a) un-tuned, (b) divided by a constant δEAC=1.04 and (c) divided by the calibration factor δEac 165

Figure 6.7 – Model predictions and experimental measurements for a transient speed change: (a) speed input (b) ϕ, (c) ϕ', (d) θIGN, (e) $PTDC$, (f) $\theta 50$, (g) $\theta 10-90$, (h) PPRR, (i) $PMAX$ and (j) MEP's..... 166

Figure 6.8 – Effect of individual variables on the burn profile for speed transient; (a) $\theta 50$, (b) $\theta 10-90$ 167

Figure 6.9 – Model predictions compared to experiment for a transient exhaust valve timing change: (a) EVC input, (b) ϕ, (c) ϕ', (d) θIGN, (e) $PTDC$, (f) $\theta 50$, (g) $\theta 10-90$, (h) PPRR, (i) $PMAX$ and (j) MEP's..... 168

Figure 6.10 – Effect of individual variables on the burn profile for EVC transient; (a) $\theta 50$, (b) $\theta 10-90$ 169

Figure 6.11 – Model predictions compared to experiment for a transient start of injection timing change: (a) injection timing, (b) ϕ, (c) ϕ', (d) θIGN, (e) $PTDC$, (f) $\theta 50$, (g) $\theta 10-90$, (h) PPRR, (i) $PMAX$ and (j) MEP's..... 170

Figure 6.12 – Effect of individual variables on the burn profile for SOI transient; (a) $\theta 50$, (b) $\theta 10-90$ 171

Figure 6.13 – Model predictions compared to experiment for a transient in fuel mass injected: (a) $mfuel$ per cycle per cylinder, (b) ϕ, (c) ϕ', (d) θIGN, (e) $PTDC$, (f) $\theta 50$, (g) $\theta 10-90$, (h) PPRR, (i) $PMAX$ and (j) MEP's. 172

Figure 6.14 – Effect of individual variables on the burn profile for fuel mass transient; (a) $\theta 50$, (b) $\theta 10-90$ 173

Figure 7.1 – Pressure traces for high variability cycles showing consecutive early and late phasing cycles. 195

Figure 7.2 – Average images of chemiluminescence from 10 separate HCCI cycles at respective crank angles. OH radicals are seen during NVO in addition to near TDC main..... 195

Figure 7.3 – (a) Pressure traces and (b) mass fraction burned for experiments versus CFD: 9.4 mg/cycle injected, NVO =157°CA, T_{in} = 66°C, RGF (experiment) = 48%, RGF (CFD) = 43%, Φ (experiment) = 0.6, Φ (CFD) = 0.58. 196
Figure 7.4 – Pressure traces from the experiment, Cycle 1 and Cycle 2 (from CFD) (a) during NVO and (b) during main compression. 196
Figure 7.5 – (a) Cumulative heat release for NVO and main compression and (b) Mean temperature during NVO with and without heat release. 197
Figure 7.6 – Evolution of species mass fractions through NVO (a) fuel, (b) intermediates and (c) oxygen and products of complete combustion. 197
Figure 7.7 – Comparison of ignition delays computed by the detailed [17] and reduced [17] gasoline surrogate mechanisms for selected KIVA cells at 380°CA bTDC for the baseline case. 198
Figure 7.8 – CFD result for second cycle simulation with carried over species and simple composition with the same $TIVC$ 198
Figure 7.9 – CFD result for second cycle simulation with and without NVO heat release while carrying over species from previous cycle. 199
Figure 7.10 – (a) Pressure traces and (b) MFB from CFD intake temperature sweep for Cycle 1. 199
Figure 7.11 – Pressure traces of Cycle 1 and Cycle 2 for the intake temperature sweep. (a) TIN = 81°C, (b) TIN = 66°C and (c) TIN = 51°C. 199
Figure 7.12 – (a) Cumulative heat release and (b) mean cylinder temperature during NVO for the intake temperature sweep. 200
Figure 7.13 – (a) Pressure traces and (b) MFB from CFD for Cycle 2 of the SOI sweep. Combustion advances with advancing SOI as there is more heat release during NVO. 200
Figure 7.14 – Cumulative (a) NVO HR and (b) Main HR from CFD for Cycle 2 of the SOI sweep. 201

Figure 7.15 – Mean temperature through NVO from CFD for the SOI sweep. 201
Figure 7.16 –Global Φ and temperature of each cell at end of injection (-375°CA)..... 201
Figure 7.17 – Comparison of the detailed and reduced gasoline surrogate mechanism ignition delays over a range of temperatures for selected cells with (a) 1 < Φ < and (b) 8.5 < Φ < 20. The solid lines denote the detailed mechanism and the dashed line denote the reduced mechanism. 202
Figure 7.18 – Reaction progress plotted against local temperature and global equivalence ratio from -381^{o}CA aTDC to -355^{o}CA aTDC for TIN=51^{o}C case..... 203
Figure 7.19 – Reaction progress plotted against local temperature and global equivalence ratio from -391^{o}CA aTDC to -275^{o}CA aTDC for SOI=390^{o}CA bTDC case. 204
Figure 7.20 – Cumulative (a) NVO HR and (b) NVO mean temperature from CFD for a Schmidt Number sweep. 205
Figure 7.21 – Homogeneous constant volume ignition delays calculated for all KIVA cells at 20^{o}bTDC NVO for the baseline case (red dots) compared to air dilute (blue circles) and EGR dilute (black squares) charge at the global ϕ'=0.32 and the same temperature as the CFD domain. 205
Figure 7.22 – Three consecutive cycles simulated in GT-Power cycle simulation with NVO-HR (dark likes) and without NVO-HR (light lines)..... 206

LIST OF TABLES

Table 2.1 – Gasoline surrogate composition by Mehl et al. [7]..... 40
Table 2.2 – FFVA engine specifications..... 40
Table 2.3 – FCB engine specifications 41
Table 2.4 – Operating conditions for data collected on the UM Boosted HCCI Engine.. 41
Table 2.5 – Mesh Thermal Boundary Conditions..... 42
Table 2.6 – CFD simulation conditions for the baseline NVO-DI case 42
Table 2.7 – Variable temperature bins to initialize Quasi-D model 43
Table 3.1 – Operating conditions for engine speed sweep 73
Table 3.2 – Operating conditions for load (ϕ') sweep..... 73
Table 3.3 – Operating conditions for boost sweep 74
Table 4.1 – Operating conditions for SOI sweep..... 103
Table 4.2 – Operating conditions for NVO sweep 103
Table 4.3 – Operating conditions for intake temperature sweep 104
Table 5.1 – CFD simulation conditions for the PVO, NVO study 130
Table 6.1 – Experimental operating conditions for speed transient..... 161
Table 6.2 – Experimental operating conditions for exhaust valve timing transient 161
Table 6.3 – Experimental operating conditions for injection timing transient 161
Table 6.4 – Experimental operating conditions for mass of fuelling transient..... 162
Table 7.1 – CFD simulation conditions for late phasing NVO-DI case. 190
Table 7.2 – Mass percent of species at IVC of cycle 2 after recompression heat release. 191

Table 7.3 – Mass percent of species at IVC of cycle 2 without recompression heat release. 192
Table 7.4 – CFD simulation conditions for intake temperature sweep. Other parameters such as fueling rate = 9.3 mg/cyc, NVO = 157°CA, Speed = 2000 RPM, ϕFO=0.44, $\chi O2$=15%, SOI = 330°CA bTDC and RGF = 43% are held constant..... 193
Table 7.5 – CFD simulation conditions for injection timing sweep. Other parameters such as fueling rate = 9.3 mg/cyc, NVO = 157°CA, Speed = 2000 RPM, ϕFO=0.44, $\chi O2$=15%, TIN= 66°C and RGF = 43% are held constant. 193
Table 7.6 – Simulation conditions for NVO heat release demonstration in GT-Power. 194

ABSTRACT

Homogeneous Charge Compression Ignition (HCCI) engines have the potential to reduce pollutant emissions while achieving diesel-like thermal efficiencies. The absence of direct control over the start and rate of auto-ignition and a narrow load range makes implementation of HCCI engines into production vehicles a challenging affair. Effective HCCI combustion control can be achieved by manipulating the amount of residual gases trapped from the previous cycle by means of variable valve actuation. In turn, the temperature at intake valve closing and hence auto-ignition phasing can be controlled. Intake charge boosting can be used to increase HCCI fueling rates and loads, while other technologies such as direct injection provide means for achieving cycle to cycle phasing control.

Thermodynamic zero-dimensional (0D) models are a computationally inexpensive tool for defining systems and strategies suitable for the implementation of new HCCI engine technologies. These models need to account for the thermal and compositional stratification in HCCI that control combustion rates. However these models are confined to a narrow range of engine operation given that the fundamental factors governing the combustion process are currently not well understood. CFD has therefore been used to understand the effect of operating conditions and input variables on pre-ignition charge stratification and combustion, allowing the development and use of a more accurate ignition model, which is proposed and validated here.

A new empirical burn profile model is fit with mass fraction burned profiles from a large HCCI engine data set. The combined ignition model and burn correlation are then exercised and are shown capable of capturing the trends of a diverse range of transient

HCCI experiments. However, the small cycle to cycle variations in combustion phasing are not captured by the model, possibly due to recompression heat release effects associated with variable valve actuation. Multi-cycle CFD simulations are therefore performed to gain physical insight into recompression heat release phenomena and the effect of these phenomena on the next cycle. Based on the understanding derived from this CFD work, a simple model of recompression heat release has been implemented in the 0D HCCI modeling framework.

CHAPTER 1

INTRODUCTION

With increasingly strict emissions norms and concerns over diminishing fossil fuel reserves there is an urgent need for more efficient transportation. As a result, the two well established technologies (namely spark ignited (SI) engines and diesel engines) have undergone a great transformation over the last ten to fifteen years. The adjusted fuel economy for new gasoline and diesel vehicles has increased by 25% from 2004 to 2013 with a corresponding decrease in emissions [1]. However, these changes have been at systems and hardware level, with downsizing and boosting, gasoline direct injection, operating strategies to meet diesel emissions standards and several others. Little change has taken place in the nature of combustion within the engine. One of the ways to comply with future emissions and fuel economy regulations is by a fundamental change in the way fuel is burned in the internal combustion engine. In parallel, new technologies such as hybrid powertrains, electric powertrains, fuel cells, renewable fuels and hydrogen fuel are also developing and experiencing renewed interest as potential options/paths to improved vehicle efficiency. However, if there are no significant transportation-sector changes, gasoline and diesel fuel will continue to provide greater than 90% of the energy used for transportation [2]. Advanced combustion technologies utilizing gasoline and diesel, such as low temperature combustion (LTC), will continue to be an important topic of research in the automotive sector.

1.1 Homogeneous charge compression ignition

Homogeneous Charge Compression Ignition (HCCI) was first observed in the late 1970's in a 2-stroke spark ignited gasoline engine and also an opposed piston engine. Some benefits in fuel consumption, NOx and HC emissions were noted in these early studies [3, 4]. Later, experiments on 4-stroke engines were performed and effects of equivalence ratio (φ), intake temperature and residual gases on HCCI combustion were studied. Experiments and cycle simulations showed that HCCI combustion is driven and limited by chemical kinetics [5, 6]. More recently, HCCI has been a topic of widespread research due to its potential of reducing in cylinder NOx and particulate emissions while achieving high thermal efficiency. HCCI combustion falls in the broad category of Low Temperature Combustion (LTC).

1.2 Characteristics of HCCI combustion

HCCI Combustion is achieved when a lean, homogeneous mixture of fuel and air at the right temperature is compressed and combusts at near constant volume just after TDC. HCCI engines are operated with geometric compression ratios higher than typical SI engines for ease of auto-ignition. Since the mixture is lean there is no need to throttle the engine, reducing pumping losses relative to a traditional SI engine. The lean mixtures and lack of throttling improve the efficiency of these engines. Auto-ignition also leads to rapid, near constant volume, combustion compared to SI where the flame takes longer to propagate and consume the mixture, adding further to the gain in efficiency. HCCI operates with a nearly uniform mixture and no rich zones which reduces the possibility of soot formation. Additionally, HCCI utilizes large amounts of dilution which reduce the peak cylinder temperatures compared to SI engines and NOx formation is greatly reduced.

HCCI does not have a direct ignition trigger and is controlled by chemical kinetics [7] unlike SI or diesel combustion. The temperature and mixture quality should be at such levels at intake valve closing (IVC) so that the charge auto-ignites shortly after top dead center (TDC) [8]. Furthermore, HCCI burn rates are a strong function of the ignition delay time for the different parts of the cylinder charge, where small changes to conditions at intake valve closing (IVC) can lead to large changes in combustion phasing. As HCCI combustion is determined by autoignition, the charge cannot be completely homogeneous and uniform as it would all burn at the same time leading to very high pressure rise rates. In order to comply with engine operating constraints for peak pressure rise rates, the combustion period must be stretched out in time and its phasing must be retarded. However, as combustion phasing is retarded the combustion becomes unstable and operation becomes impossible. Therefore, HCCI is constrained at high loads by the pressure rise rate limits. At low loads the opposite is true, even though a large amount of residual gas fraction (RGF) from the previous cycle is trapped the resulting temperatures at IVC are not high enough for the charge to auto-ignite around TDC [9]. These constraints limit HCCI to a relatively narrow load range and make controlling HCCI difficult, both of which have made it challenging to implement in production engines.

1.3 Crucial HCCI actuators and their effects on combustion

Successful HCCI operation relies on having a thermochemical environment near TDC which favors auto-ignition producing burn rates that are within the operational limits of the engine hardware. Concurrently, the mixture must be dilute enough to keep the peak temperatures below the threshold where significant NOx production occurs yet not so dilute that the combustion limit is approached. Some of the more widely adopted technologies to enable HCCI operation are discussed below.

1.3.1 Variable valve actuation

As mentioned above the mixture composition and temperature near TDC have to be appropriate for auto-ignition in the absence of spark discharge or fuel injection to directly initiate combustion. HCCI needs higher charge temperatures than SI or diesel and hence requires some form of charge heating. This is commonly accomplished either by intake preheating [10] or by retaining/re-inducting hot residual gases from the previous cycle [11]. Intake heating is typically slow therefore residual gases are preferred for controlling the charge temperature in automotive applications which mostly operate under transient conditions. Over the last thirty years an increasing number of production SI automobiles have been equipped with variable valve actuation (VVA) systems. They have been primarily used to optimize the amount of charge trapped and the effective compression ratio by changing the valve timing [12]. VVA systems capable of modifying lift and duration in addition to phasing have also become common [13] to improve the torque performance of the vehicle over a range of engine speeds.

Such VVA systems can typically be used, along with full lift/duration (SI) cams and low lift/duration (HCCI) cams to operate the engine in SI and HCCI mode respectively. Figure 1.1 shows an example of SI and HCCI cams and lift profiles. The HCCI valve strategy employed here is called the negative valve overlap (NVO) type strategy in which hot exhaust gases are trapped by closing the exhaust valves early and opening the intake valves late. This leads to the "recompression" of a portion of the charge from the previous cycle. Mixing of the hot residuals with the fresh charge leads to an increase in the initial charge temperature needed to achieve auto ignition. Zhao et al. [14] have demonstrated the operation of NVO actuated HCCI over 1000 RPM to 3500 RPM from 0.5 bar to 4 bar BMEP. They observed a significant reduction in brake specific fuel consumption (BSFC), carbon monoxide (CO) and nitrogen oxide (NO_x) emissions throughout. Other researchers [15, 16, 17] have also demonstrated NVO

operated HCCI with similar findings. Another strategy of internally heating the charge is by a small secondary exhaust rebreathing event while the intake valves are open. This results in hot gases from the exhaust flow back into the cylinder along with the fresh charge [18]. Borgqvist et al. provide a detailed experimental comparison of various residual handling methods for HCCI [19]. However this thesis focuses on NVO operated HCCI alone.

It has been shown that NVO introduces more stratification due to the mixing of the hot residuals with fresh charge [20]. Kodavasal et al. have explained the effect of NVO compared to positive valve overlap (PVO) on HCCI combustion [21]. Beyond this, Lawler has investigated the effect of PVO compared to rebreathing valve actuation on HCCI combustion [22]. However, the effect of changing NVO on stratification and HCCI combustion while holding the start of combustion and overall dilution constant is not understood. This thesis numerically illustrates with CFD analysis the phenomenon of changing stratification with NVO and the associated impact on HCCI combustion.

1.3.2 Boosting

Intake charge boosting has proven to be an effective method of extending the high load limit of HCCI engines. Researchers such as Christensen et al. [37], Olsson & Johansson et al. [24], Kalghatgi et al. [25] and Yang & Dec [26] have demonstrated the use of boosting to achieve loads greater than 14 bar IMEP in HCCI mode. These studies were “pure HCCI” where the engine was operated with full SI valve lifts (no NVO), external boosting (shop air) and intake charge preheating. Other studies by Johansson et al. [27] and Kulzer et al. [28] applied boosting to engines operating in HCCI mode with production capable compression ratios and cams. They reported the potential of achieving 6 bar – 8 bar IMEP for engine speeds of 1000 rpm – 2500 rpm. Boosting provides additional means to dilute the charge, lowering pressure rise rates at higher fueling rates.

Higher pressures lead to shorter ignition delays and reduce the temperature required to achieve ignition at similar combustion timing. Boosting therefore reduces the need to preheat the charge and allows operation with shorter NVO duration.

The low exhaust enthalpies associated with HCCI pose systems level challenges with its boosted operation. Simulation studies by Mamalis et al. [29, 30] and Shingne et al. [31] discuss at length the high pumping losses incurred by turbochargers while boosting HCCI to high intake pressures. Gharabaghi et al. [32] suggested the use of small superchargers with moderate boost for HCCI operation to offset the fuel penalty typically associated with supercharging. Shingne et al. [33] performed a simulation study comparing a turbocharged and supercharged HCCI system. They found that at high load HCCI operation the supercharger friction losses were comparable to the pumping losses of the turbocharged HCCI system. Pending optimization of a feasible system, boosting is a promising method to make HCCI commercially viable.

The above mentioned studies demonstrate the benefits and system requirements for boosted HCCI. In his single cylinder experimental study, Klinkert [34] has attempted to isolate the effect of boost on HCCI burn rate. He maintained the location of 50% mass burned constant (θ_{50}) while the total dilution decreased slightly with increasing boost. It was found that increasing boost resulted in a small shortening of burn duration. He suggested that this effect could be due to pressure induced shortening of ignition delays, changing thermal stratification at TDC or due to changing stratification due to changing internal residuals between cases. To date, the dominant mechanism affecting burn durations with changing boost has not been identified. This thesis uses CFD to isolate and explain the effect of boost on HCCI burn rates. The global composition can be ensured to be constant with simulations which is exceedingly difficult in experimental studies.

1.3.3 Direct injection and reactions during NVO

In addition to higher initial temperatures HCCI also relies on higher compression ratios (CR's) to achieve TDC temperatures appropriate for auto-ignition. Any future engine employing HCCI will have to be capable of running SI combustion at high loads to cover the entire operating regime required for a production vehicle, loads higher than the high load limit of HCCI. This puts an upper limit on the CR since SI is prone to knock at low speed and high loads. Direct injection (DI) of fuel provides a means of charge cooling due to fuel vaporization which makes SI more tolerant to higher CR. Researchers have also demonstrated the use of DI during NVO (pilot and main) to extend the low load limit of HCCI combustion [35, 36]. Although there are concerns over increased NOx emissions due to DI into NVO [37], the method has been demonstrated to be a powerful control actuator [38] and a means to extend the low load limit of HCCI. DI introduces stratification in contrast to PFI [37] but it is unclear how the stratification changes when the injection timing is changed. CFD is employed in this thesis to explain the effect of varying injection timing on HCCI stratification and combustion while combustion timing and total dilution are held constant.

Additionally, re-heating of the charge during the NVO period provides a means to alter the state of the charge in both temperature and composition due to the possibility of reactions; as temperatures are fairly high. Berntsson et al. [39] have shown evidence of high temperature reactions during NVO by means of OH chemiluminescence. Hellstrom et al. [40] have attributed heat release during NVO to the reactions in trapped residual, even before fuel injection. Song et al. [41] have attributed recompression reactions to the direct injection event. They observed endothermic reactions for rich mixtures and more exothermic behavior as the mixture was leaned out. Others have performed experimental and simple 0D chemical kinetic simulations of recompression heat release [42, 43]. Past experimental work has generated several hypotheses regarding the recompression heat

release mechanisms and their effect on the next cycle. Several 0D chemical kinetic simulations have been performed to better understand this process but these models are unable to capture the stratification associated with typical NVO operated engines. This thesis uses CFD to resolve high levels of stratification expected during recompression, especially for direct injection into the residual gas. Multi-cycle CFD simulations have been performed using detailed gasoline kinetics to investigate the effect of HCCI recompression behavior on the next cycle.

1.4 Necessity of fast 0D models for HCCI studies

It is established that HCCI is a challenging engine technology to control. The previous section summarizes the several actuators that can be varied to achieve desired HCCI operation. Extensive experiments are typically required to define systems suitable for new engine technologies. Models are being used to a greater extent for systems level analysis and control studies in advanced propulsion systems as a cheap alternative to experiments. 3D CFD simulations with detailed kinetics capture the physics governing HCCI combustion but are too expensive for batch simulations. Mean value models run faster than real time but provide little or no insight into the processes within each cycle. Albrecht et al. have presented a continuous modeling approach for engine systems and control design shown in Figure 1.2 [44]. The process starts with fully coupled 3D CFD / chemical kinetics models. By progressive systematic reduction of the more complicated models they finally end up with simple look-up table type models. It is of utmost importance to select the models pertinent to the studies to be performed. For systems level analysis it is desired to have a model that can capture the key HCCI combustion characteristics while being computationally efficient. The model should be able to capture experimental trends over a wide range of engine operating conditions with minimal tuning while executing within a few seconds (10,000 to 100,000 times faster

than the detailed CFD models). This thesis aims to understand the key physical processes governing HCCI using high fidelity models and experiments. This understanding is then applied in the development of a simple 0D thermodynamic model for cycle simulations.

1.5 Prior model and breakdown compared to experiment

The prior HCCI combustion model consists of an ignition model and burn rate correlation. The model is briefly described here. Details are provided by Babajimopoulos et al. [9] and more discussion regarding this model in the context of this research is provided in Chapter 5 (improved 0D ignition model) and Chapter 6 (improved burn profile model) of the thesis. The ignition is modeled by an auto-ignition integral using the mean composition and a temperature that has been offset from the mean by a fixed multiplication factor (ΔT). The ΔT factor accounts for the difference between the mean temperature and the temperature of the first gas parcel to auto-ignite as well as for fuel effects. Post ignition burn is described by a correlation developed from closed cycle CFD simulations. The CFD simulations were performed over the following range of operating conditions: $0.2 < \Phi < 0.6$, $750 <$ RPM < 4000 and $0 <$ RGF $< 40\%$, $P_{IN\text{-}EX} = 1$bar.

Figure 1.3 shows the performance of the old model compared to a speed transient experiment. The experiment was performed on a four cylinder boosted engine which is described in detail in Chapter 2. All the actuators except speed were held constant during the experiment. The old model has been tuned by changing ΔT to match the initial $\theta_{50}$of the experiment as seen in Figure 1.3(c). It is noted in Figure 1.3(d) the initial burn duration predicted by the old model is significantly smaller than experimental values and consequently the peak pressure rise rate (PPRR) is much greater than in the experiment (Figure 1.3(e)). The initial peak pressure shown in Figure 1.3(f) is also over predicted by the model. Closed cycle CFD simulations cannot capture the stratification accurately, which strongly affects the burn rates, resulting in the disagreement. As the speed changes

from 2500 rpm to 1500 rpm, the ϕ reduces. The model initially tracks the experimental value of ϕ as shown in Figure 1.3(b). The model ϕ value is slightly smaller than the experiment because the measured value is the average for the engine and the simulated value is the in-cylinder value for Cylinder 1 alone. The model predicts later θ_{50} than the experiment with falling speed and continues to do so until misfire occurs, as shown in Figure 1.3(c). Thus the ΔT calibration for the ignition model is not sufficient when the operating conditions are changed. This thesis work aims to develop some improvements to the ignition and burn rate models to capture HCCI transient experiments over a wide range of engine operation.

1.6 Motivation, Objectives and document organization

1.6.1 Motivation for current study

The current state of the art systems level model [9] cannot capture experimental engine trends without extensive calibration. Other models published recently present improvements to the main burn prediction [45] but do not consider heat release during NVO. There are some control oriented models [38, 40 and 46] that have shown model effectiveness over certain engine speeds and loads while modeling NVO HR as well. However there isn't extensive validation; and the calibrations applied to the models may not be physics based.

As mentioned in Section 1.3 several input actuators have to work in unison to achieve the desired HCCI combustion phasing and rate. It was also mentioned that there is limited understanding of the effect of operating conditions/input actuators on HCCI combustion. This thesis aims to understand the stratification mechanisms governing HCCI ignition and combustion rates under different operating conditions. The findings from this study may then be used to improve 0D HCCI ignition and burn rate models.

Although several researchers have observed NVO heat release [47, 48], there are gaps in the core understanding of HCCI recompression heat release behavior. This effect should not be ignored for 0D modeling considering the large amount of NVO (up to 200°CA) and high recompression temperatures (> 1000 K) achieved during HCCI. It is desired to understand the mechanisms governing recompression reactions and their effect on the consequent cycle. A 0D model for NVO heat release may then be proposed based on what is learned from this study.

1.6.2 Research objectives

The objectives of the current study are to explain the effects of changing operating conditions/input actuators on HCCI stratification and burn rates. CFD is used to resolve the large scale flow structures which give rise to the charge stratification that dictates the sequential auto-ignition of the mixture. This understanding is used to develop an improved burn correlation for HCCI.

Next, the HCCI ignition process will be interrogated with CFD to understand the state of the initial auto-igniting charge. The adiabatic core concept will be introduced and its validity assessed under stratified conditions over a wide range of operating conditions. It is desired to show that the ignition prediction improves by using the adiabatic core temperature compared to the mean temperature. The improved performance of the full model, comprised of the improved ignition and burn rate models, will be demonstrated for engine transient experiments.

The final objective of this work is to investigate HCCI recompression heat release. Reactive CFD simulations are to be performed for consecutive cycles to understand the heat release mechanisms during NVO and its effect on the subsequent

cycle. It is desired to understand if the heat release is primarily from the residuals of the previous cycles or due to the fuel injected during NVO. The understanding from this study is to be used to propose a 0D model for HCCI recompression heat release.

The document is organized as follows. Chapter 2 describes the simulation tools used to interrogate the HCCI combustion process, to analyze the experimental data and implement the 0D model. These include the CFD code (KIVA-3V) and the commercial engine cycle simulation software GT-Power©. The chapter also describes the reaction space analysis method used to understand the changing thermal and compositional stratification. An ignition delay expression used as a metric for reactivity stratification is introduced. A quasi dimensional code is also described which is used in conjunction with KIVA-3V as a sequential multi-zone to isolate effects of variables on combustion.

Chapter 3 describes computational investigations into the effect of operating conditions on HCCI combustion. The effect of changing engine speed, total dilution and boost are analyzed while keeping the combustion phasing (location of 10% mass fraction burned) constant. Similarly, Chapter 4 describes investigations into the effect of varying actuators typically used to control HCCI combustion timing. The changing thermal and compositional stratifications are presented. It is shown that thermal stratification continues to dominate combustion.

Chapter 5 interrogates the ignition process in HCCI. It is demonstrated that there is no low temperature heat release and auto-ignition is isolated to the hottest portion of charge. An adiabatic core ignition model is introduced and is shown to be effective under different operating conditions.

In Chapter 6 a new empirical burn model is parameterized based on experimental data. The burn rate model is combined with the adiabatic core ignition model and compared to experimental transient sweeps. The post ignition model is used to isolate the effects of individual variables on the burn profile.

Chapter 7 investigates the NVO heat release observed in HCCI. It is demonstrated that the deterministic cyclic coupling is captured by means of multi-cycle CFD simulations. Insights are drawn into the in-cylinder process during the NVO period for late and early injection. Recommendations are provided for modeling this phenomenon in fast cycle simulations.

Chapter 8 summarizes the studies performed in this thesis and provides conclusions and insights drawn from this work. Recommendations for further studies are also provided.

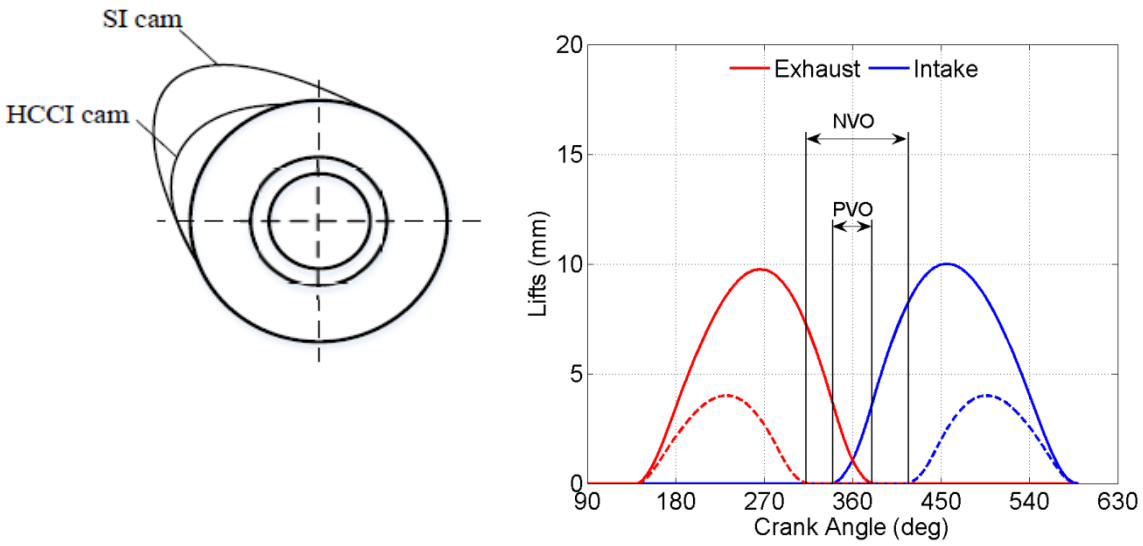

(a) (b)

Figure 1.1 – Example SI and HCCI cam profiles.

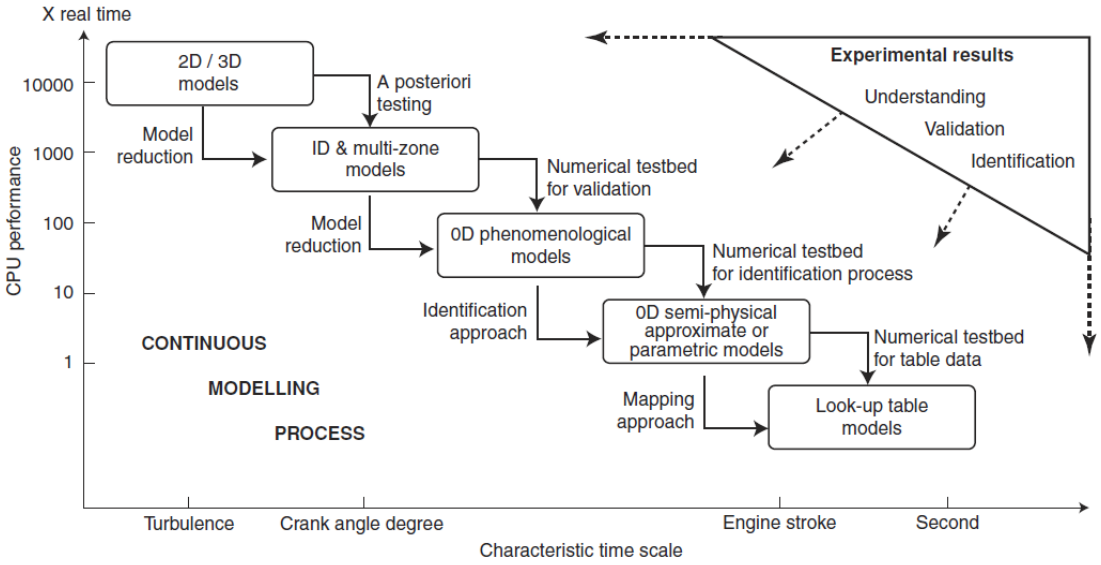

Figure 1.2 – Continuous modeling process with different fidelity models [44].

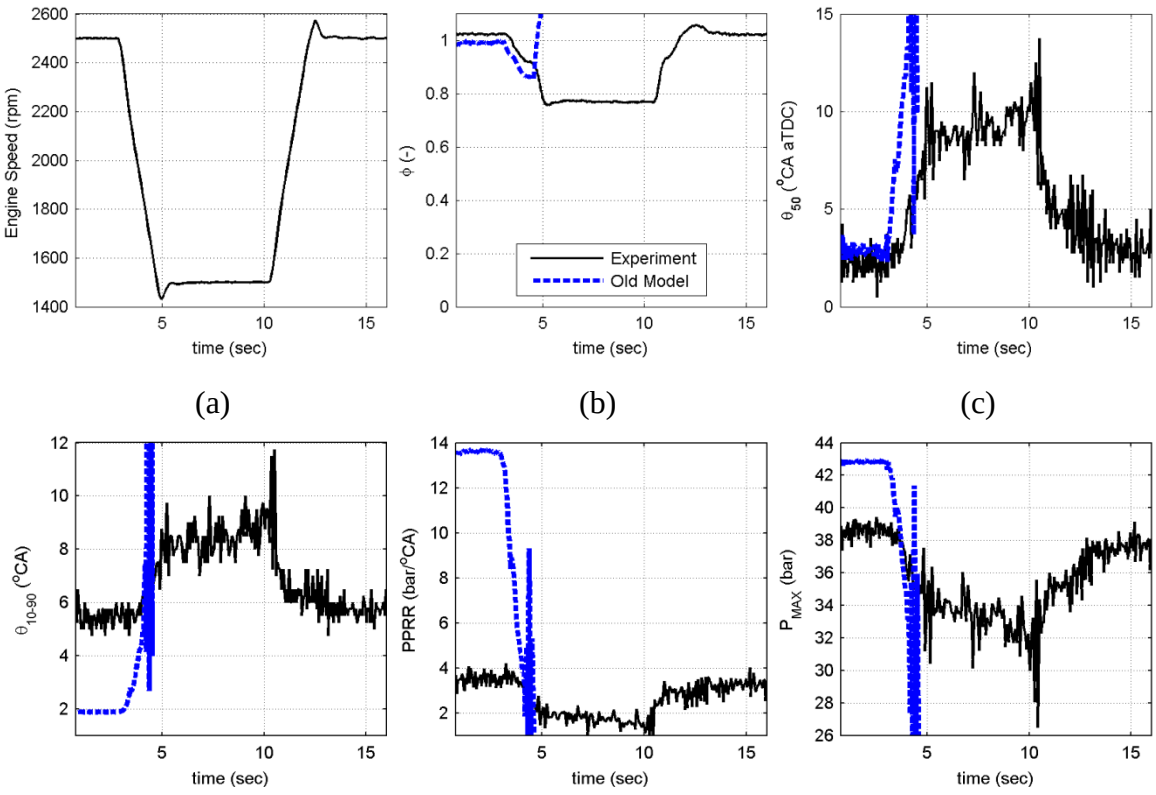

Figure 1.3– Old model predictions and experimental measurements for a transient speed change: (a) speed change (b) fuel-to-air equivalence ratio (ϕ), (c) combustion phasing (θ_{50}), (d) burn duration (θ_{10-90}), (e) peak pressure rise rates (PPRR), and (c) peak pressure (P_{MAX})

1.7 References

1. Alson, J., Hula, A., and Bunker, A., "Light-Duty Automotive Technology, Carbon Dioxide Emissions, and Fuel Economy Trends: 1975 Through 2013," U. S. E. P. Agency, ed., Office of Transportation and Air Quality, 2013.

2. Melaina, M.W., Heath, G., Sandor, D., Steward, D., Vimmerstedt, L., Warner, E., Webster, K.W., "Alternative Fuel Infrastructure Expansion: Costs, Resources, Production Capacity, and Retail Availability for Low-Carbon Scenarios. Transportation Energy Futures Series." Prepared for the U.S. Department of Energy by National Renewable Energy Laboratory, Golden, CO. DOE/GO-102013-3710. 101 pp, April 2013.

3. Onishi, S., Jo, S.H., Shoda, K., Jo, P.D. and Kato,S., "Active Thermo-Atmosphere Combustion (ATAC) – A New Combustion Process for Internal Combustion Engines", SAE Paper No. 790501, 1979.

4. Noguchi, M., Tanaka, Y., Tanako, T. and Takeuchi, Y., "A Study on Gasoline Engine Combustion by Observation of Intermediate Reactive Products During Combustion", SAE Paper No. 790840, 1979.

5. Najt, P. and Foster, D.E., "Compression-Ignited Homogeneous Charge Combustion", SAE Paper No. 830264, 1983.

6. Thring, R.H.: "Homogeneous-Charge Compression Ignition (HCCI) Engines", SAE Paper No. 892068, 1989.

7. Epping, K., Aceves, S., Bechtold, R., and Dec, J., "The Potential of HCCI Combustion for High Efficiency and Low Emissions," SAE Paper 2002-01-1923, 2002.

8. Caton, P.A, Song, H.H., Kaahaaina, N.B. and Edwards, C.F., "Residual-effected homogeneous charge compression ignition with delayed intake-valve closing at elevated compression ratio," Int. J. Engine Res Vol.6, No.4, p.399-219, 2005.

9. Babajimopoulos, A., Challa, V.S.S.P., Lavoie, G.A. and Assanis, D.N., "Model-Based Assessment of Two Variable Cam Timing Strategies for HCCI Engines: Recompression vs. Rebreathing," ICES2009-76103, Proceedings of the ASME Internal Combustion Engine Division, Milwaukee, WI, 2009.

10. Shibata, G., and Urushihara, T., "Dual Phase High Temperature Heat Release Combustion," SAE Paper No. 2008-01-0007, 2008.

11. Kuo T.-W., "Valve and Fueling Strategy for Operating a Controlled Auto-Ignition Combustion Engine", SAE 2006 HCCI Symposium, September 25-26, 2006, San Ramon, CA, 2006.

12. Gray, C., "A review of variable engine valve timing", SAE Technical Paper 880386, 1988.

13. Horie, K., Nishizawa, K., Ogawa, T., Akazaki, S., and Miura, K., "The development of a high fuel economy and high performance four-valve lean burn engine" SAE Technical Paper. 920455, 1992.

14. Zhao, Hua, Jian Li, Tom Ma, and Nicos Ladommatos., "Performance and analysis of a 4-stroke multi-cylinder gasoline engine with CAI combustion" SAE Technical paper, 2002.

15. Koopmans, L., and Denbratt, I., "A Four Stroke Camless Engine, Operated in Homogeneous Charge Compression Ignition Mode with Commercial Gasoline," SAE Paper 2001-01-3610, 2001.

16. Hiraya, K., Hasegawa, K., Urushihara, T., Iiyama, A., and Itoh, T., "A Study on Gasoline Fueled Compression Ignition Engine ~ A Trial of Operation Region Expansion," SAE Paper 2002-01-0416, 2002.

17. Milovanovic N., Chen R., and Turner J., "Influence of the Variable Valve Timing Strategy on the Control of a Homogeneous Charge Compression Ignition Engine", SAE Paper 2004-01-1899, 2004.

18. Chang, J., Guralp, O., Filipi, Z., Assanis, D., Kuo, T.-W., Najt, P., and Rask, R., "New Heat Transfer Correlation for an HCCI Engine Derived from Measurements of Instantaneous Surface Heat Flux," SAE Paper 2004-01-2996, 2004.

19. Borgqvist, Patrick, Per Tunestal, and Bengt Johansson., "Investigation and comparison of residual gas enhanced HCCI using trapping (NVO HCCI) or rebreathing of residual gases" SAE Technical Paper 2011-01-1772, 2011.

20. D. A. Rothamer, J. A. Snyder, R. K. Hanson, R. R. Steeper, and R. P. Fitzgerald. "Simultaneous imaging of exhaust gas residuals and temperature during HCCI combustion," Proceedings of the Combustion Institute, 32(2):2869–2876, 2009.

21. Kodavasal, J., Lavoie, G. A., Assanis, D. N., & Martz, J. B., "The effects of thermal and compositional stratification on the ignition and duration of homogeneous charge compression ignition combustion," Combustion and Flame, 162(2), 451-461, 2015.

22. Lawler, B. J., "A methodology for assessing thermal stratification in an HCCI engine and understanding the impact of engine design and operating conditions," PhD Thesis, The University of Michigan, Ann Arbor, MI, 2013.

23. Christensen M., Johansson B., Amneus P., and Mauss F., "Supercharged Homogeneous Charge Compression Ignition", SAE Paper 980787, 1998.

24. Olsson J., Tunestal P., Haraldsson G., and Johansson B., "A Turbo Charged Dual Fuel HCCI Engine", SAE Paper 2001-01-1896, 2001.

25. Kalghatgi, G. T., Risberg, P. and Angstrom, H. E., "Partially Pre-Mixed Auto-Ignition of Gasoline to Attain Low Smoke and Low NOx at High Load in a Compression Ignition Engine and Comparison with a Diesel Fuel", SAE Paper 2007-01-0006, 2007.

26. Dec, J. E., and Yi, Y.: "Boosted HCCI for High Power without Engine Knock and Ultra-Low NOx Emissions – using Conventional Gasoline", SAE Paper 2010-01-0186, 2010.

27. Johansson, T., Johansson, B., and Tunestal P., "HCCI Operating Range in a Turbo-charged Multi Cylinder Engine with VVT and Spray-Guided DI", SAE Paper 2009-01-0494, 2009.

28. Kulzer, A., Lejsek, D., and Nier, T., "A Thermodynamic Study on Turbocharged HCCI: Motivation, Analysis and Potential", SAE Paper 2010-01-0422, 2010.

29. Mamalis, S., Nair, V., Andruskiewicz, P., Assanis, D., Babajimopoulos, A., Wermuth, N., and Najt, P., "Comparison of Different Boosting Strategies for Homogeneous Charging Compression Ignition Engine – A Modeling Study", SAE Paper 2010-01-0571, 2010.

30. Mamalis, S., and Babajimopoulos, A., "Model Based Estimation of Turbocharger Requirements for Boosting and HCCI Engine", Proceedings of the ASME Internal Combustion Engine Division 2010 Fall Technical Conference, ICEF2010-35122, 2010.

31. Shingne, P., Assanis, D., Babajimopoulos, A., Keller, P., Roth, D., and Becker, M., "Turbocharger Matching for a 4-Cylinder Gasoline HCCI Engine Using a 1D Engine Simulation", SAE Paper 2010-01-2143, 2010.

32. Gharahbaghi, S., Wilson, T. S., Xu, H., Cyran, S., Richardson, S., Wyszynski, M. L., and Misztal, J., "Modelling and Experimental Investigations of Supercharged HCCI Engines", SAE Paper 2006-01-0634, 2006.

33. Shingne, P., Assanis, D., Babajimopoulos, A., Mond, A., and Yilmaz, H., "Application of a Supercharger in a Two-Stage Boosting System for a Gasoline HCCI Engine: A Simulation Study", ICEF2011-60220, Proceedings of the ASME Internal Combustion Engine Division 2011 Fall Technical Conference, 2011.

34. Klinkert, S., "An Experimental Investigation of the Maximum Load Limit of Boosted HCCI Combustion in a Gasoline Engine with Negative Valve Overlap," PhD Thesis, The University of Michigan, Ann Arbor, MI, 2014.

35. Urushihara, T., Hiraya, K., Yoshizawa, K., and Itoh, T., "Expansion of HCCI operation Region by the Combination of Direct Fuel Injection, Negative Valve Overlap and Internal Fuel Reformation," SAE Paper 2003-01-0749, 2003.

36. Kulzer, A., Hathout, J.-P., Sauer, C., Kerrelmeyer, R., Fisher, W., and Christ, A., "Multi-mode combustion strategies with CAI for a GDI engine", SAE Paper 2007-01-0214, 2007.

37. Kodavasal, J., "Effect of charge preparation strategy on HCCI combustion," PhD Thesis, The University of Michigan, Ann Arbor, MI, 2013.

38. Ravi N., Liao, H., JungKunz, A., and Gerdes,. C., "Modeling and control of exhaust recompression HCCI using split injection", 972-1-4244-7427-1/10, 2010 American Control Conference, 2010.

39. Berntsson, A. W. and Denbratt, I., "Optical Study of HCCI Combustion Using NVO and an SI Stratified Charge," SAE Paper 2007-24-0012, 2007.

40. Hellström, E., Stefanopoulou, A., Vavra, J., Babajimopoulos, A. et al., "Understanding the Dynamic Evolution of Cyclic Variability at the Operating Limits of HCCI Engines with Negative Valve Overlap," SAE Int. J. Engines, 5(3), 2012.

41. Song, H. H. and Edwards, C. F. "Understanding chemical effects in low-load-limit extension of HCCI engines via recompression reaction," Int. J. Engine Res., 2009, 10(4), 231–250. DOI: 10.1243/14680874JER03409.

42. Fitzgerald, R. P. and Steeper, R. R., "Thermal and Chemical Effects of NVO Fuel Injection on HCCI Combustion," SAE Int. J. Engines 3(1):46-64, 2010, doi: 10.4271/2010-01-0164.

43. Hunicz, J., Kordos, P., and Ignaciuk, P., "Experimental Investigation into Thermal and Chemical Effects of Negative Valve Overlap Injection in a Gasoline HCCI Engine," SAE Technical Paper 2014-01-2660, 2014, doi:10.4271/2014-01-2660.

44. Albrecht, A., Grondin, O., Le Berr, F., and Le Solliec, G., “Towards a Stronger Simulation Support for Engine Control Design: a Methodological Point of View”, Oil & Gas Science and Technology – Rev. IFP, Vol. 62 (2007), No. 4, pp. 437-456.

45. E. Ortiz-Soto, “Combustion Modeling of Spark Assisted Compression Ignition for Experimental Analysis and Engine System Simulations,” PhD Thesis, The University of Michigan, 2013.

46. S. Jade, E. Hellstrom, A. Stefanopoulou, and L. Jiang, “On the ¨ influence of composition on the thermally-dominant recompression HCCI combustion dynamics,” in Dynamic Systems and Control Conference, 2011.

47. E. Hellstrom, A. G. Stefanopoulou, J. Vavra, A. Babajimopoulos, D. Assanis, L. Jiang, and H. Yilmaz, “Understanding the dynamic evolution of cyclic variability at the operating limits of HCCI engines with negative valve overlap,” SAE International Journal of Engines, 5 (3) (2012), pp. 995–1008.

48. Vaughan, A., “Adaptive Machine Learning for Modeling and Control of Non-Stationary, Near Chaotic Combustion in Real-Time,” PhD Thesis, The University of Michigan, Ann Arbor, MI 2015.

CHAPTER 2

TOOLS USED AND ANALYSIS METHOD

This chapter describes the tools used as a part of the thesis work. First, an overview of the CFD software used in this work is provided. The chemical kinetics scheme is then introduced. A brief description of the fully-coupled CFD/kinetics approach is provided. The method of CFD simulations initialization is explained for the first cycle as well as multi cycles. The baseline NVO-DI case used in this work is introduced and the CFD predictions are evaluated against engine experiments. An approach to analyze the reaction space and a sequential multi-zone developed by Kodavasal [1] is introduced along with the metrics used to present pre-ignition thermal and compositional stratification. The reaction space analysis and sequential multi-zone are used in the subsequent chapters to isolate and explain the effect of pre-ignition stratification on charge reactivity and combustion.

Additionally, the GT-Power engine cycle simulation used to extract the heat release data from experiments has been introduced. The three pressure analysis module from GT-Power is used to extract the heat release data. This is preferred over other analysis methods [2] as it provides a better estimate of residual gases trapped per cycle which is critical in determining the IVC mixture quality and mean cylinder temperature. GT-Power user subroutines to model the in-cylinder combustion and heat transfer are also discussed briefly.

2.1 Overview of CFD software

The CFD software used in this work is KIVA-3V [3], which uses a Reynolds Averaged Navier Stokes (RANS) solver for fluid dynamic calculations. This is a free open-source FORTRAN code for two and three dimensional (2D, 3D) engine simulations developed by Los Alamos National Laboratory (LANL). It enables the modeling of ports and moving valves making open cycle simulations possible. The software solves the governing equations for continuity, momentum and energy for the fluid phase as described in the KIVA-II manual [4]. The software package provides models for turbulence such as the standard $k-\epsilon$ (SKE) and renormalization group (RNG) theory variant of the $k-\epsilon$ developed by Han and Reitz [5] which includes the effect of compressibility using a rapid distortion analysis. KIVA-3V also includes other sub-models for injection, spray breakup, droplet evaporation and wall film evaporation. Details regarding the sub models and the Arbitrary Lagrangian Eulerian (ALE) numerical scheme are provided in the KIVA-II manual [1, 6].

2.2 Chemical kinetic modeling

This work uses a 4-component surrogate for gasoline fuel developed by Mehl et al. [7] at the Lawrence Livermore National Laboratory (LLNL). It is comprised of isooctane, n-heptane, toluene and 2-pentene in a relative proportion based on mass fraction as given in Table 2.1. The designed surrogate has been shown to replicate the major hydrocarbon components, reactivity, molecular weight (100-110 g/mol) and (RON+MON)/2 of gasoline where RON is the Research Octane Number and MON is the Motor Octane Number.

The simulations use a 312-species, 1488-reaction reduced mechanism [7] based on a detailed gasoline mechanism [8] which consists of roughly 1400 species and 5000 reactions. The detailed mechanism has been validated over a wide range of temperatures

and pressures as encountered in internal combustion engines, with experimental data from rapid compression machines, shock tubes and jet stirred reactors. It is however prohibitively expensive to implement the detailed mechanism with the 3-D CFD simulation. Mehl et al. [7] have compared the ignition delays from the reduced and detailed mechanisms over a range of conditions relevant to HCCI operation, and showed excellent agreement not only under high temperature conditions but also within low temperature and NTC regimes. The reduced mechanism was also validated against HCCI engine experiments [9] over a range of intake pressures and load conditions and was found to capture features such as intermediate temperature heat release (Dec et al. [10]). Comparison of ignition delays computed by the reduced mechanism and detailed mechanism for NVO conditions is provided in Chapter 7. The favorable comparison results give confidence in the reduced mechanism under NVO conditions.

2.3 Fully coupled CFD and multi-zone model

The reacting CFD simulations in this thesis are performed using the fully coupled Multi-Zone approach of Babajimopoulos [11]. In this approach tens of thousands of KIVA computational cells in an engine are grouped together to form a relatively small number of chemistry zones with similar thermodynamic states. Doing this reduces the computational cost of detailed chemistry by an order of magnitude or more relative to calculating a chemical kinetic update in every cell with minimal loss of fidelity. Each chemistry zone is treated as a constant volume homogeneous reactor initialized with the state information from the KIVA cells composing the zone. After the kinetic calculations are performed for each zone over the simulation time step, updated species composition and thermodynamic state information is passed back to the original KIVA cell using a remapping process described below.

The multi-zone model creates the zones based on temperature and progress equivalence ratio φ, defined as:

$$\varphi = \frac{2C^{\#}_{-CO_2} + H^{\#}_{-H_2O}}{O^{\#}_{-CO_2-H_2O}} \qquad \text{Equation 2.1}$$

where $C^{\#}$, $H^{\#}$and $O^{\#}$represent the number of carbon, hydrogen and oxygen atoms (respectively) present with a CFD cell. The subscripts $-CO_2$and $-H_2O$ indicate that the C, H and O atoms present in products of complete combustion (CO_2 and H_2O) within the CFD cell are excluded from the computation of φ. For unreacted mixtures the definition of φ is identical to the fuel/O_2 equivalence ratio for a lean mixture φ<1.0 and a stoichiometric mixture φ=1.0. Rich mixtures have φ in the range of 1.0 to ∞, when the mixture contains only fuel. To handle this wide range of potential conditions that may occur during a direct injection event a new progress equivalence ratio is adopted in this work:

$$\varphi^* = \begin{cases} \varphi & : \varphi \leq 1.0 \\ 2 - 1/\varphi & : \varphi > 1.0 \end{cases} \qquad \text{Equation 2.2}$$

where the range of φ^* is 0.0 to 2.0 from pure air to pure fuel [6]. This scaling prevents the model from creating an excessively large number of chemistry zones for rich cells with high levels of reaction progress, which can have very large differences in φ for very similar compositions. The resolution for the thermo-chemical zones is ΔT within zones limited to 5 K and $\Delta\varphi$ within a zone limited to 0.03. The average temperature, pressure and composition of the computational cells in each chemistry zone are used to perform chemical kinetic calculations over the time step with CHEMKIN [13]. After the chemistry call, the new composition is remapped from the zone to the individual cells through a variable *ch*, which represents the number of C and H atoms in non-product species:

$$ch = 2C^{\#}_{-CO_2} + \frac{H^{\#}_{-H_2O}}{2}$$ Equation 2.3

For species except CO_2, H_2O, O_2 and N_2 the new mass of species *m* is calculated by:

$$m_m = \frac{ch_{cell}}{ch_{zone}} m_{m,zone}$$ Equation 2.4

The new masses of CO_2, H_2O, O_2 and N_2 are calculated through atom balances in the cell to enforce the overall cell mass remains invariant over the chemistry calculation as well as ensuring atom conservation. Additional information about the coupled CFD multi-zone model is provided by Martz [14], Kodavasal [1] and Middleton [6].

2.4 Experimental engine setups

The experimental data included in this thesis are from a single cylinder fully flexible valve actuation research engine (FFVA) and from a four cylinder boosted engine (FCB) modified for HCCI operation, both present at the University of Michigan. The single cylinder engine data is used to validate the CFD model whereas the data from the four cylinder engine is used for tuning and validation of the 0D model developed as part of this work. The CFD grid of the FCB engine was unavailable while that engine was operated over a wider range of operating conditions than the FFVA engine. It is noted here that the two engines have similar combustion chamber geometries. Thus the insights drawn from the CFD simulations for the FFVA engine can be leveraged for the FCB engine.

2.4.1 Fully flexible valve actuation engine (FFVA)

This engine is a single-cylinder gasoline direct-injected engine with a Ricardo Hydra crankcase. The fully flexible valve actuation is from Sturman Industries and provides independent control to set timing, lift and duration. The engine specifications

are provided in Table 2.2. The valves were operated in a symmetric negative overlap manner to retain hot exhaust gases for initial thermal inertia needed in HCCI combustion in the 12.4:1 compression ratio engine. The fuel in the experiments was 87 octane research grade gasoline injected during NVO at 330^{o}CA bTDC. A side mounted direct fuel injector is located between the two intake valves and aimed into the piston bowl. A centrally mounted spark plug is present in the cylinder head. High speed cylinder pressure data were collected at 0.1^{o} CA resolution for 200 consecutive cycles for each condition. Instantaneous manifold pressures were also collected at the same resolution for the intake and exhaust. Detailed description of the experimental facility is provided in several publications [15, 16, 17 and 18].

2.4.2 Four cylinder boosted engine (FCB)

The engine providing data for the development of the new burn profile model and validation of the thermodynamic 0D model is described here. It is part of the Advanced Combustion Controls Enabling Systems and Solutions (ACCESS) project; a joint research project partially funded by the Department of Energy and Robert Bosch LLC [19]. The hardware is similar to the engine described by Polovina et al. [20]. It is a modified General Motors 2.0 L in-line four-cylinder Ecotec turbocharged engine equipped with direct injection; specifications provided in Table 2.3. Figure 2.1 shows the schematic of engine setup. The engine has been modified by increasing the geometric compression ratio from 9.25:1 to 11.0:1. A recompression-type negative valve overlap (NVO) strategy is used to enable HCCI operation with hydraulic operated VVT cams. The peak lift is 3.5 mm and duration is 153°CA as shown in Figure 2.2. An EPA Tier II Gasoline fuel (RON = 97.0 and MON = 88.1) by Haltermann is used. The flow is regulated to each cylinder by specifying the injection pulse width in the Bosch ECU. In turn, the fuel flow rate to each cylinder is correlated to the fuel direct injector pulse from

injector bench experiments. The total fuel flow into the engine is measured by a Pierburg PLU 103A positive displacement flow meter. Fuel-air equivalence ratio (ϕ) is reported based on the exhaust wideband BOSCH LSU 4.9 oxygen sensor, mounted post turbine. An MKS FTIR MultiGas Analyzer 2031 is used to measure the CO, CO_2, and H_2O in the exhaust, while a heated Horiba FIA-236 FID is used to measure the THC emissions. All the emissions sampling is also done post turbine. A redundant equivalence ratio determination is made based on the measured exhaust constituents [21]. The stock BorgWarner K04 turbocharger is replaced with a smaller BorgWarner KP31 turbocharger which is necessary to achieve boost in the HCCI combustion mode due to the low enthalpy of the exhaust gas [22]. The compressor outlet is fed to a water cooled intercooler and the boosting system is capable of producing intake manifold pressures of 2.25 bar absolute from 1500 RPM to 3500 RPM. In-cylinder pressure is measured for all cylinders with Kistler piezoelectric pressure transducers at 0.1°CA resolution for 300 consecutive cycles at steady state. Intake and exhaust runner pressures are also measured at the same resolution for Cylinder 1 alone. The experimental HCCI data were obtained from a large set of experiments which were performed to map the maximum operating region of the engine. Hence the intake actuators were all varying simultaneously (without single actuator sweeps). The range of operating conditions is summarized in Table 2.4.

2.5 CFD model setup

The CFD simulations are performed with a three-dimensional (3D) mesh matching the FFVA engine shown in Figure 2.3. The exhaust ports are on the left while the intake ports are on the right. The mesh contains approximately 100,000/22,000 computational cells at BDC/TDC and describes the open intake and exhaust ports, pent roof cylinder head, asymmetrical bowl-in piston, and moving valves. Crevices are not modeled in this mesh. The turbulence model used is the standard KIVA-3V SKE model.

Standard KIVA-3V wall functions and the log-law of the wall approach are used to model heat losses to the cylinder liner, head, piston and valves. The spray breakup model used for fuel spray is the in-built Taylor Analogy Breakup (TAB) model. The valve motion is imposed from experimental recorded data. Due to the FFVA's hydraulic valve actuation the lifts do not follow a traditional cam profile, but have a fast nearly linear motion during opening and closing while holding a constant lift for the duration. Figure 2.4 shows an example set of lift profiles for HCCI with 160^{o} NVO. Although the timings of the valve events may change the shape of the lifts remain the same.

The thermal boundary conditions on the solid surfaces of the mesh are the same as used by Kodavasal et al. [1] and specified in Table 2.5. The intake and exhaust temperatures were set based on experimentally reported measurements on a case by case basis. The composition in the intake was pure air and the exhaust was initialized by assuming complete combustion products. To remove modeling complexity and remain consistent with the KIVA simulations introduced in Chapter 3 and Chapter 4, average pressures are used in the intake and exhaust manifolds. The manifold pressures had to be changed by up to ± 0.1 bars in order to match the predicted and measured pressures at TDC of NVO and 20^{o}CA bTDC of firing.

2.5.1 Multi-cycle simulation procedure

Open cycle KIVA-3V simulations are conducted for HCCI combustion including reactions during NVO. Figure 2.5 shows the schematic of the simulation procedure. Simulation is initialized at 80^{o}CA aTDC of firing of Cycle 0. The pressure is initialized based on experimental data and composition is assumed to be products of complete combustion. The temperature is estimated based on GT-Power three pressure heat release analysis. Until IVC the simulation is run with a non-reacting 8 species mechanism (4 component gasoline surrogates, O_2, N_2, CO_2 and H_2O). Liquid gasoline fuel is injected at

390^{o} CA aTDC during expansion of NVO. Shortly after IVC a restart file (Restart 1) is written and the simulations are re-initialized for detailed chemistry with the 312 species reduced gasoline mechanism [7]. All the simulations discussed in this work except those in Chapter 7 end at 800^{o} CA after the simulation of Cycle 1.

Chapter 7 contains simulations to study the reactions during NVO and its effect on the subsequent cycle. CFD simulations performed with the full mechanism and chemistry "on" after 800^{o} CA through breathing and NVO onto the next cycle IVC are prohibitively expensive. Most of the cost is associated with the breathing process since the fluids calculations need to be performed at a shorter time step in order to resolve the high velocities during the open valve period. Additionally it is computationally intensive to do the transport of a large number of species through breathing. A significant speed up while losing little fidelity can be achieved by following the threshold and chemical mechanism swap method proposed by Middleton and Martz [23]. This is done by searching through all the computational cells and keeping all the species that have mole fractions greater than 10^{-4} in any cell, in addition to the fuel and the major species at 800^{o} CA. The remapping of species is done based on the *ch*, and atom balance in a manner similar to Babajimopoulos et al. [11]. A Restart 2 file is written and simulations are re-initialized with the new smaller mechanism and no reactions until EVC. Here another file Restart 3 is written and simulations are re-initialized for detailed chemistry with the reduced gasoline mechanism similar to the previous IVC. Similar process is followed at EVO after the reactive NVO event that includes liquid fuel injection. A speed up from ~400 hours to ~12 hours is observed for the open cycle part by following this method. Results using the thresholding method replicated the results from simulations with chemistry active everywhere within 1°CA of combustion phasing (θ_{50}) [23].

2.5.2 Baseline NVO-DI case

This thesis focuses on NVO operated HCCI with gasoline DI during NVO. A baseline NVO-DI case has been selected from the work of Kodavasal [1]. The operating conditions are summarized in Table 2.6. This case is simulated in KIVA-3V based on the above simulation procedure. Figure 2.6(a) compares the CFD predictions to the 200 experimental pressure traces and Figure 2.6(b) compares the CFD to experimental mass fraction burned curves collected at steady state at the same operating condition. The predicted pressure and mass fraction burned trace has a shape similar to the experimental data and lies well within the total range. The ignition timing (θ_{IGN}) is -12.5^{o} CA aTDC, defined in this work as the crank angle where the mass fraction burned equals 0.1%. The 10-90% mass fraction burned (θ_{10-90}) is 6.1^{o} CA for this case.

2.5.3 Thermal and compositional stratification metrics

The first part of this thesis aims to explain the combustion behavior of NVO-DI HCCI under different operating conditions based on pre-ignition thermal and compositional stratification in a manner similar to Kodavasal et al. [24]. The charge thermal stratification is computed based on two standard deviations (2σ) in charge temperature from non-reacting CFD simulations. The standard deviation is computed on a mole-weighted basis as follows:

$$\sigma T = \sqrt{\frac{\sum_{i=1}^{N} n_i (T_i - \bar{T})^2}{\left(\frac{N-1}{N}\right)\sum_{i=1}^{N} n_i}} \qquad \text{Equation 2.5}$$

where “i” is the subscript denoting a CFD cell, “n” represents number or moles, “N” represents the total number of CFD cells, and $\bar{T}$ is the mole-weighted average temperature within CFD domain. The charge compositional stratification is computed

based on two standard deviations (2σ) in fuel-to-oxygen equivalence ratio (ϕ_{FO}) and oxygen mole percentage (χ_{O_2}) in a manner similar to Equation 2.5.

Figure 2.7(a) shows the evolution of the charge thermal stratification from IVC (-130^{o}CA aTDC) to TDC for non-reacting simulations. There is significant initial thermal stratification ($2\sigma T(IVC)$ = 43.5 K) which reduces until 80^{o}CA bTDC ($2\sigma T(-80^o)$ = 34.38 K) and increases after this point until the end of compression ($2\sigma T(TDC)$ = 91.7 K). The initial high thermal stratification is in part due to the hot residuals not mixed with the fresh charge. The mixing accounts for the reduction of the thermal stratification until 80^o CA bTDC, however the wall driven heat losses are dominant and the thermal stratification increases as the mean mixture temperatures and wall heat losses increase proportionally. Figure 2.7(b) and Figure 2.7(c) show the evolution of the charge compositional stratification from IVC to TDC visualized as $2\sigma\phi_{FO}$and $2\sigma\chi_{O_2}$. There is high initial compositional stratification ($2\sigma\phi_{FO}(IVC)$ = 0.48 and $2\sigma\chi_{O_2}(IVC)$ = 2.24%) and it reduces throughout compression due to mixing ($2\sigma\phi_{FO}(TDC)$ = 0.19 and $2\sigma\chi_{O_2}(TDC)$ = 0.6%). Thus the charge becomes more uniform in term of composition but the heat loss dominant thermal stratification increase with compression. More discussion regarding stratification evolution from IVC to TDC is provided in Chapter 3 in the context of changing engine speed.

2.6 Analysis method for CFD data

Two analysis methods used to isolate effect of thermal and compositional stratification on combustion that are used repeatedly in Chapter 3 and Chapter 4 are described here. More details are provided by Kodavasal in other publications [1, 24].

2.6.1 Reaction space analysis

This method is used to quantify the stratification in mixture reactivity. The iso-octane ignition delay expression by Goldsborough [25] is used as the metric for reactivity where shorter ignition delays indicate a more reactive charge. The ignition delays evaluated at local (per cell) thermodynamic states in the cylinder provide a measure of the reactivity stratification. The Goldsborough correlation is given in Equation 2.6.

$$\tau = A\phi_{FO}^{\alpha} P^{\beta} \chi_{O_2}^{\gamma} \times \exp(\lambda) \qquad \text{Equation 2.6}$$

where τ represents the ignition delay in milliseconds, P represents pressure in bar, ϕ_{FO} represents the fuel-oxygen equivalence ratio, χ_{O_2} represents the oxygen mole percentage and function of activation energy, temperature and the universal gas constant (R). α, β and γ are functions of temperature while the activation energy in λ is a function of pressure and temperature. This expression has been used as a surrogate for gasoline ignition delays as commonly accepted. Kodavasal et al. [24] have shown that iso-octane ignition delays match those predicted by the reduced gasoline mechanism [7] for temperatures greater than 1000 K, providing justification to use iso-octane ignition delays. The dimensions used to represent the reaction space are temperature, $\phi_{FO}$and χ_{O_2}which directly contribute to the ignition delay metric as show in Equation 2.6.

The pre-ignition reaction space is visualized for the baseline case in Figure 2.8 by grouping individual CFD cells into bins based on temperature and ϕ_{FO}or χ_{O_2}that are colored by mass fraction corresponding to the bin. Kodavasal et al. [1] has shown that NVO operated HCCI with DI during recompression has greater pre-ignition thermal and compositional stratification than either PVO-PFI or PVO-DI operated HCCI. As seen in Figure 2.8(a), the thermal stratification, $2\sigma T$ = 78.6 K and the ϕ_{FO} stratification $2\sigma\phi_{FO}$ = 0.2. As seen in Figure 2.8(b), the stratification in $\chi_{O_2}$is $2\sigma\chi_{O_2}$= 0.62% for the NVO case. Kodavasal et al. also show that even though the compositional stratification is relatively

high the thermal stratification is nearly four times as important as the stratification in ϕ_{FO} and ten times as important as the stratification in χ_{O_2} with respect to its effect on the ignition delay. It is noted that the ϕ_{FO} stratification under NVO-DI conditions may have significant relative importance on the reactivity with respect to temperature but the stratification in χ_{O_2} will be ignored here onward. Figure 2.9 shows the reaction space visualized in terms of temperature and ϕ_{FO} bins colored by the reactivity i.e. the ignition delay for each bin. The figure depicts the sequential auto-ignition of HCCI charge in the reaction space with the hottest and richest charge starting the auto-ignition. The ignition delays grow longer as charge gets colder and leaner.

2.6.2 Decoupling thermal and compositional stratification effects on reactivity

To understand the importance of thermal and compositional stratification on the reactivity, the cumulative distribution of reactivity in terms of the ignition delay computed in every CFD cell using the individual temperature, ϕ_{FO} and χ_{O_2} is visualized at ignition (12.5°CAbTDC) in Figure 2.10. To remove the impact of the compositional stratification on the overall reactivity stratification, the ignition delay is again computed in every CFD cell with the cell temperature and mean ϕ_{FO} and χ_{O_2} of the cylinder instead of the local cell values. This case is called the "Mean Composition" and effectively neglects the effects of compositional stratification while maintaining the thermal stratification. There are small differences between the two lines using the cell composition and the mean composition confirming that the thermal stratification dominates the reactivity stratification for the NVO-DI operation.

2.6.3 Isolation of the thermal stratification effect on burn duration using Quasi-Dimensional model

A quasi-dimensional (Quasi-D) multi-zone model developed by Kodavasal et al. [26] is employed to decouple the effect of thermal stratification from the compositional

stratification. It has been subsequently used to isolate the effect of operating conditions on HCCI combustion. This model uses hundreds of Lagrangian zones to represent the cylinder domain. Each closed adiabatic zone has its own temperature and composition and multiple zones are used to replicate the effect of stratification. While there is no heat or mass transfer between zones or to the surroundings, the zones interact through boundary work, expanding or contracting to satisfy the constraint of uniform pressure throughout the cylinder, with the sum of the individual zones volumes equal to the cylinder volume at the given crank angle.

This model is initialized at -12.5^{o} CA aTDC based on a non-reacting CFD simulations run up to that location. The CFD domain is zoned in terms of temperature and ϕ_{FO}. The temperature zones are variable as shown in Table 2.7 while $\Delta\phi_{FO}$<0.1. The finer resolution for higher temperatures was necessary in order for the successful execution of the model; this is due to the strong non-linear variation of the chemical reaction rates with temperature. This resolution led to the creation of 255 zones. These zones are used to initialize the quasi-dimensional model which then calculates reaction progress. A shift of 7 K is applied to the initial temperature profile to match the θ_{10} combustion location of the MZ baseline case and the CFD baseline case. Two simulations are performed here; first with the initialization as described above and second "NVO-mean-comp." is conducted where the compositional stratification is eliminated while the thermal stratification is maintained. This is achieved by mapping the mean composition within the CFD domain onto all zones within the quasi-dimensional model. Figure 2.11 shows the burn profiles for the two cases from the quasi-dimensional model. The NVO case replicates the CFD behavior and it is seen that the elimination of compositional stratification in the NVO-mean-comp. case does not significantly affect the overall burn performance. This reinforces the notion that thermal stratification is much more important than the compositional stratification under NVO-DI conditions.

2.7 Cycle simulation software for systems-level simulations

Systems-level engine cycle simulations have become indispensable with the increasing complexity of automotive engines and advances in computational capabilities. These employ simplified thermodynamic zero-dimensional combustion models which significantly reduce the computational cost and provide an ideal platform to define new systems and for control development and testing. Several engine cycle simulation frameworks have been presented over the years [27- 29]. Concurrently, Morel et al. [30-32] presented a comprehensive engine simulation program using similar combustion models and also included finite element method (FEM) solvers for heat transfer in the combustion chamber and 1-D gas dynamics for flow through pipes, valves and connectors amongst other improvements. These provided basis for commercial engine cycle simulation codes such as Ricardo WAVE, AVL Boost and GTI GT-Suite/GT-Power [33-35]. The current work uses GTI GT-Power software for experimental data analysis as well as implementation of the combustion and heat transfer models [36].

2.7.1 Three pressure analysis (TPA) of experimental data

GT-Power provides capability to calculate the burn rate based on measured instantaneous cylinder, intake/exhaust manifold pressure, intake temperature, speed and fueling rate. The advantage of this method is that estimation of the residual gas fraction, which is a large portion of the charge for HCCI, is better performed by this analysis compared to using other residual estimation methods [37]. This approach requires an engine model including the valves and port geometry. Figure 2.12 shows the intake runner to exhaust runner model for Cylinder 1 of the FCB engine as it appears in GT-Power. It is part of the full engine model which has been matched to the FCB engine under different operating conditions and combustion modes [38]. A modified Woschni [41] heat transfer correlation has been used for TPA as well as model implementation.

GT-Power TPA also reduces the effect of thermal shock that might affect the estimate of residuals since cylinder pressure close to valve openings is simulated and not imposed based on experimental pressure trace. In order to match the simulated in-cylinder pressure to the measured pressure at 20CA bTDC the intake manifold pressure is shifted by $\pm$0.05 bars. On the other hand, to match the simulated ϕ to the measured value the exhaust valve closing timing is shifted by $\pm$ 2.5°CA. This adjustment of EVC timing is within the error in timings introduced due to dynamic operation [39] for the wide range of operating conditions provided in Table 2.4.

Figure 2.13 displays the cyclic variability in terms of the cylinder pressure data and frequency of occurrence based on peak pressure for a case at 1500 RPM, 5.6 bar net IMEP and 1.4 bar intake boost. Cycles with peak pressure closest to the mean peak pressure, median peak pressure cycle and the cycle representative of the mode are tightly distributed which has been similarly presented by Middleton [6] for stable HCCI operation. Hence the cycle with peak pressure closest to the mean peak pressure has been used for heat release analysis and burn correlation development (Chapter 6). Figure 2.14 shows the output of the TPA for the mean peak pressure cycle at the operating point mentioned above. Figure 2.14(a) top shows the TPA predicted pressure compared to the measured pressure; they are well matched during the recompression portion as well. Figure 2.14(a) bottom and Figure 2.14(b) shows the estimated in-cylinder mean temperature and the cumulative mass fraction burned curve.

2.7.2 Modelling combustion and heat transfer in GT-Power

GT-Power provides the ability to incorporate user defined code in order to modify several aspects of the cycle simulation. Arbitrary user code can be programmed in any language and can be called from the FORTRAN [40] interface routine. GT-Power provides several built-in subroutines for calculation of mixture properties while external

libraries such as CHEMKIN routines can also be implemented. The code is compiled into a DLL which is called by GT-Power at each computational time step for the closed portion of the cycle. This work modifies the subroutines for combustion and heat transfer in order to model HCCI combustion. The mass continuity and energy equation computations are performed by GT-Power. The ignition and burn rate models discussed in Chapter 5 to Chapter 6 are implemented into the subroutines. They provide the location of start of combustion and the subsequent mass fraction of fuel burned at each time step. Additionally the cylinder averaged heat transfer coefficient is also provided at each computational time step based on a modified Woschni correlation (Section 1.7.1).

Table 2.1 – Gasoline surrogate composition by Mehl et al. [7]

Surrogate	**Mass Fraction**
Isooctane	0.5413
n-heptane	0.1488
toluene	0.2738
2-pentene	0.0361

Table 2.2 – FFVA engine specifications

Geometric Compression Ratio	12.4 : 1
Bore	86 mm
Stroke	94.6 mm
Connecting Rod	156.5 mm
Displacement	0.55 L
Injection	DI, side mounted

Table 2.3 – FCB engine specifications

Geometric Compression Ratio	11.0 : 1
Bore	86 mm
Stroke	86 mm
Connecting Rod	145.5 mm
Wrist Pin Offset	0.8 mm
Displacement	0.499 L
Head Design	Pent-roof
Max. Valve Lift/Duration	3.5mm/153^{o} CA
Valve Phasing	Dual VVT
Injector Type	Multi-Hole Solenoid
Maximum Injection Pressure	100 bar
Direct Injector Location	Side Mounted Wall Guided

Table 2.4 – Operating conditions for data collected on the UM Boosted HCCI Engine

Number of experiments	290
Engine speed (RPM)	1500 – 3500
Fuel – air equivalence ratio (-)	0.44 – 0.97
Residual gas fraction (%)	30 – 70
Exhaust valve closing (^{o}CA aTDC)	290 – 345
Intake valve opening (^{o}CA aTDC)	398 – 435
Intake manifold pressure (bar)	0.99 – 2.26
Start of Injection (^{o}CA aTDC)	345 – 450

Table 2.5 – Mesh Thermal Boundary Conditions

Cylinder Head	450 K
Piston Top	480 K
Cylinder Liner	450 K
Exhaust Valves	490 K
Intake Valves	480 K

Table 2.6 – CFD simulation conditions for the baseline NVO-DI case

Parameter	NVO-DI
Speed	2000 RPM
Load	3 bar net IMEP
Fueling	DI; SOI@330° bTDC
NVO	157° CA
$\boldsymbol{\phi_{FO}}$ (mean)	0.44
$\boldsymbol{\chi_{O2}}$ (mean)	15%
T_{in}	106°C
Internal Residual	43%
External Residual	0%
Total RGF	43%

Table 2.7 – Variable temperature bins to initialize Quasi-D model

Temperature range (K)	ΔT (K)
850 – 950	10
950 – 1040	5
1040 – 1060	4
1060 – 1075	3
1075 – 1100	2

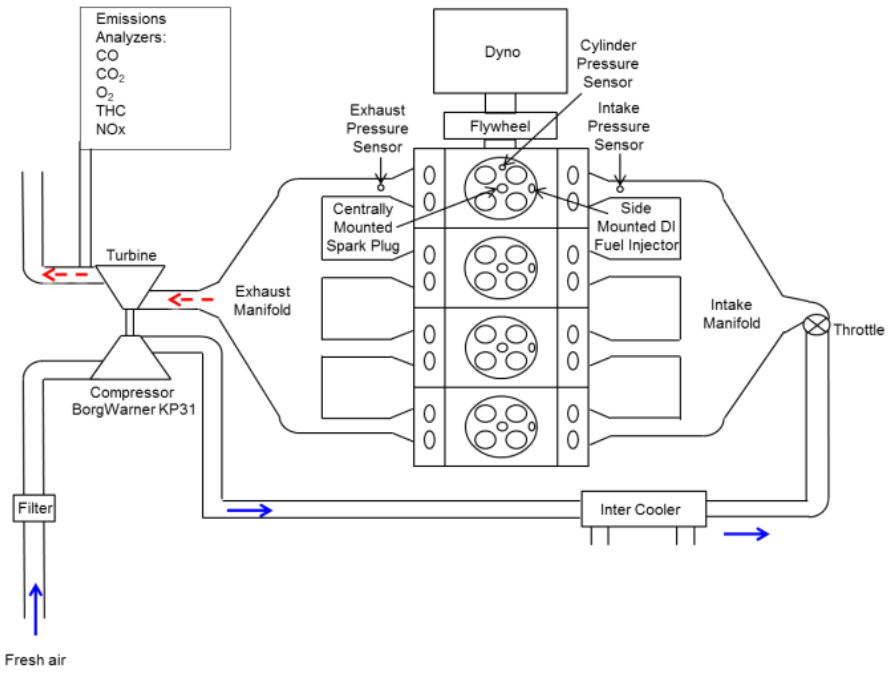

Figure 2.1 – Schematic of the four cylinder boosted (FCB) engine showing the main components; with the BorgWarner KP31 turbocharger.

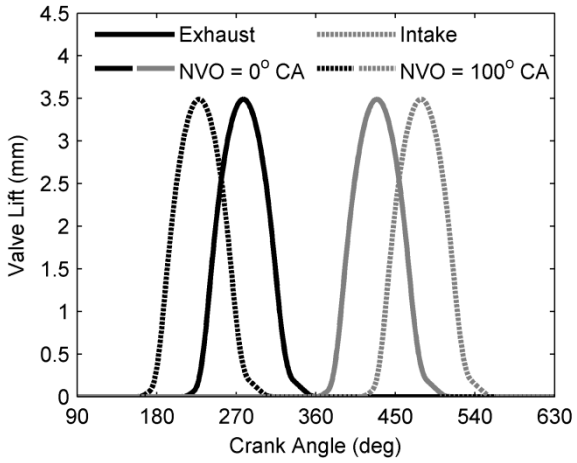

Figure 2.2 – Recompression NVO valve lifts at two phasings. Solid lines show zero NVO position.

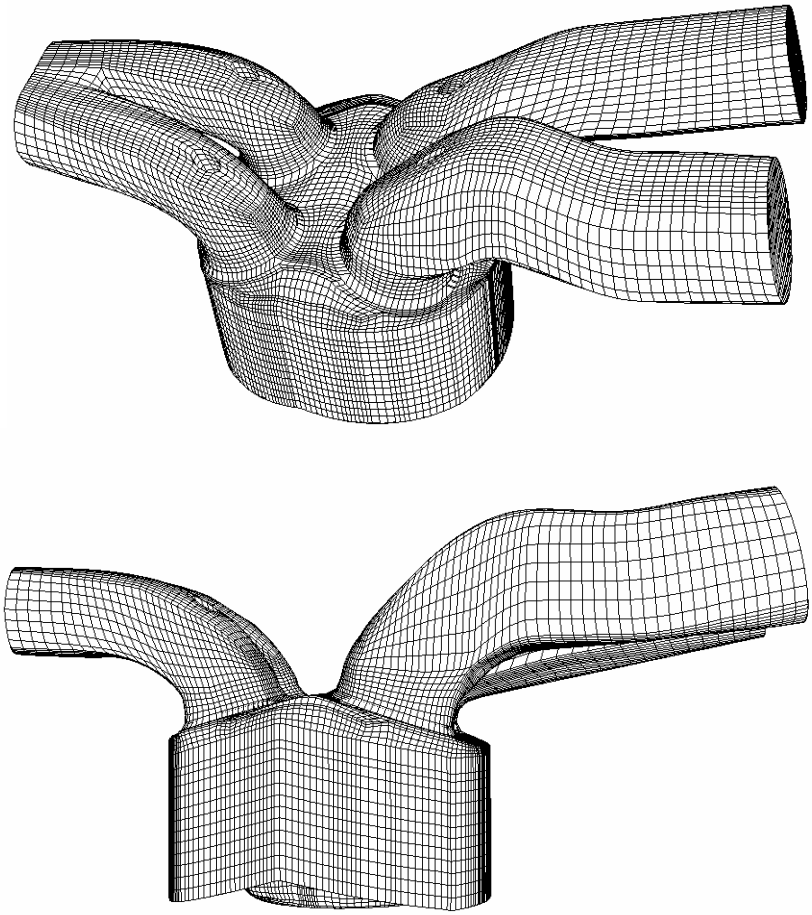

Figure 2.3 – Computation mesh used in this work, containing 156,000 cells, based on the FFVA engine [15]. Exhaust ports on the left, intake ports on the right**.**

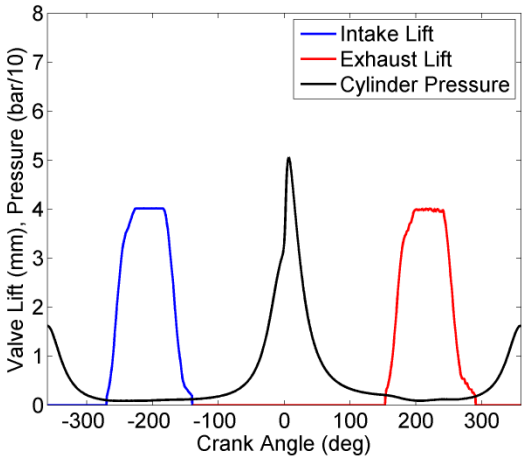

Figure 2.4 – Example valve lifts from FFVA engine for HCCI operation with negative valve overlap.

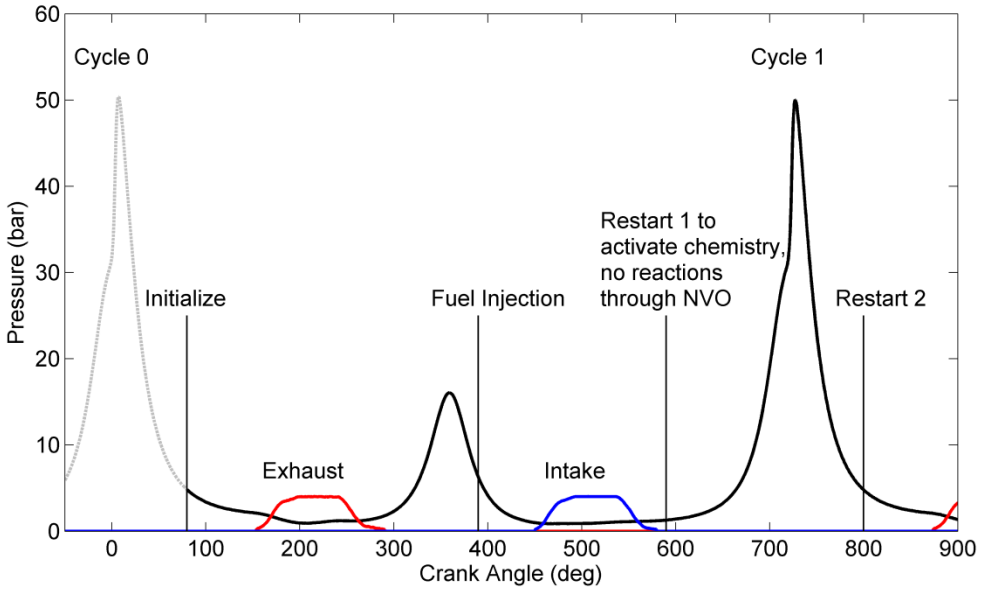

(a)

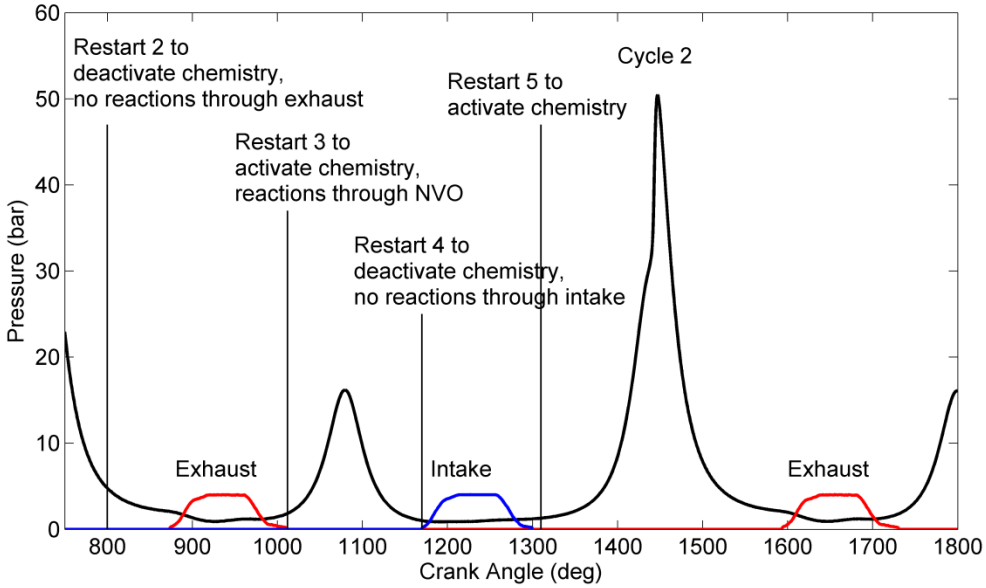

(b)

Figure 2.5 – Schematic of multi-cycle simulation procedure. (a) Simulation is initialized prior to EVO of Cycle 0 and run through the gas exchange and fuel injection using a small chemical mechanism (fuel, O_2, N_2, CO_2, H_2O) with no reactions. The mechanism is changed to the reduced gasoline surrogate mechanism [7] and chemistry is started at Restart 1. (b) Threshold and mechanism swap [23] is similarly performed at Restart 2 – 5 to speed up simulations by reducing species and turning off the chemistry during the breathing events while capturing the effect of NVO reactions on subsequent cycle.

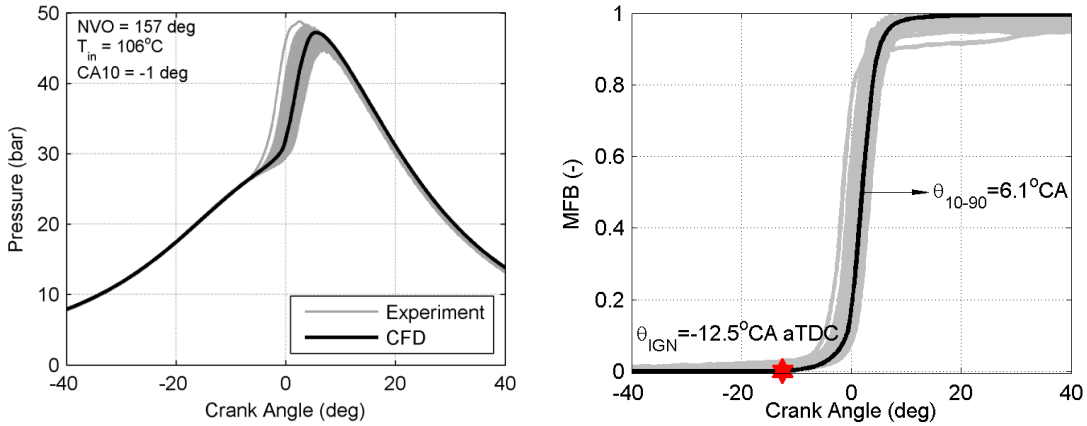

Figure 2.6 - (a) Pressure traces and (b) mass fraction burned curves for experiments versus CFD: 9.4 mg/cycle injected, NVO =157°CA, T_{in} = 106°C, RGF (experiment) = 48%, RGF (CFD) = 43%, Φ (experiment) = 0.6, Φ (CFD) = 0.58, Φ'(experiment) = 0.32, Φ'(CFD) = 0.32.

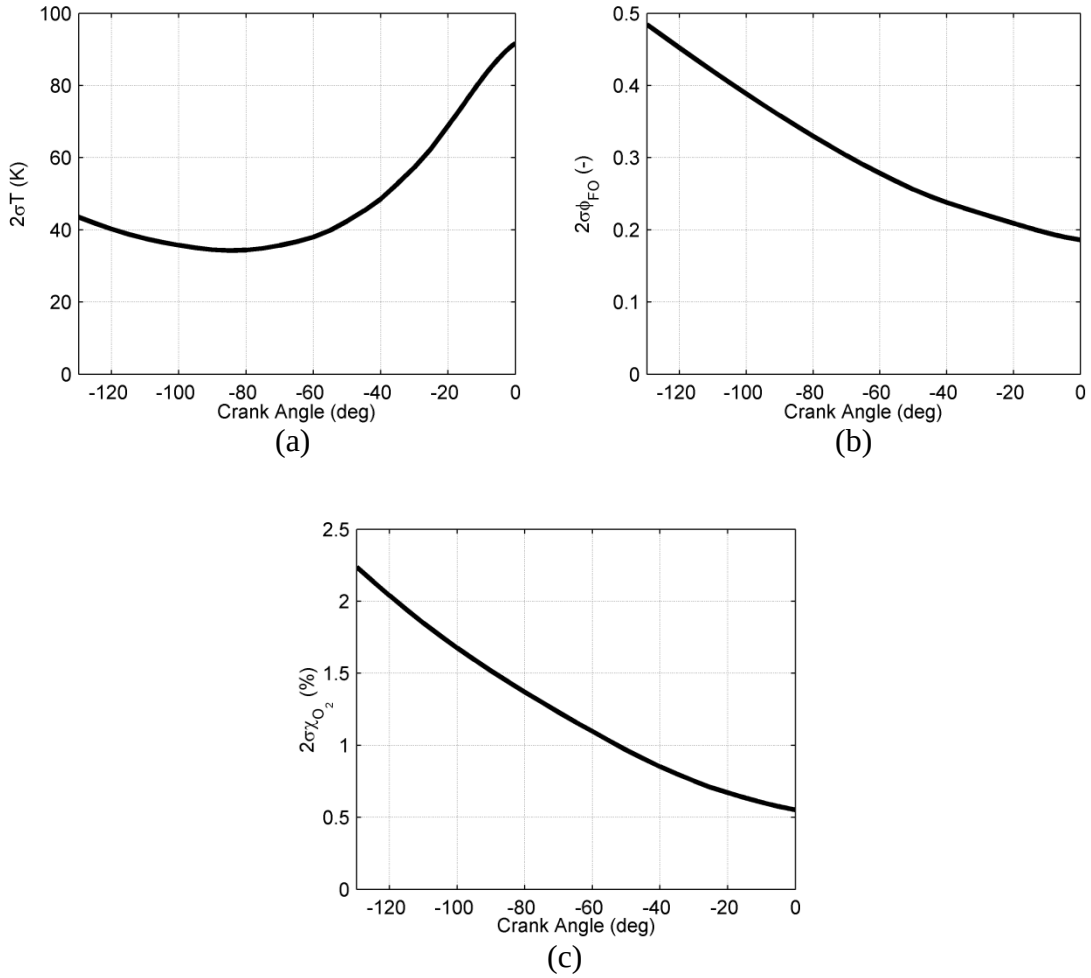

Figure 2.7 – Evolution of stratification from IVC (130° CA bTDC) to TDC for the NVO-DI case visualized in terms of (a) $2\sigma T$, (b) $2\sigma\phi_{FO}$ and (c) $2\sigma\chi_{O_2}$.

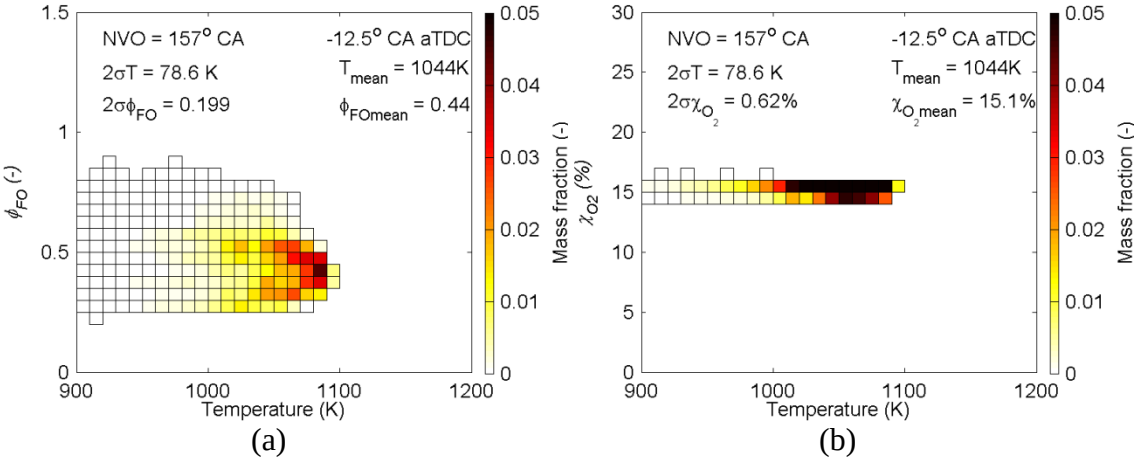

Figure 2.8 – Reaction space at -12.5° CA aTDC from CFD simulations visualized in terms of bins denoted by temperature, (a) ϕ_{FO} (b) χ_{O_2} and colored by the mass fraction.

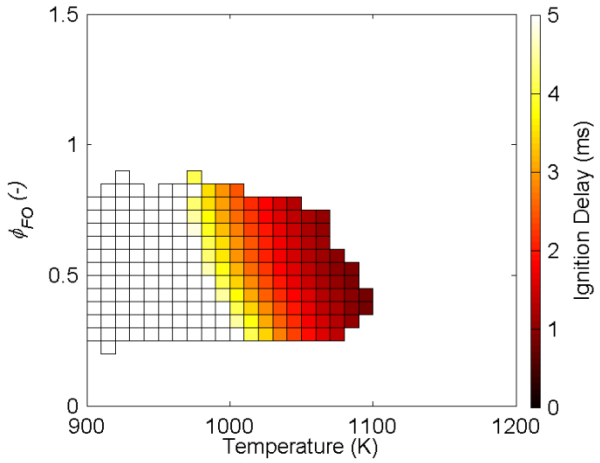

Figure 2.9 – Reaction space at -12.5° CA aTDC from CFD simulations visualized in terms of bins denoted by temperature, ϕ_{FO} and colored by ignition delay of the bin.

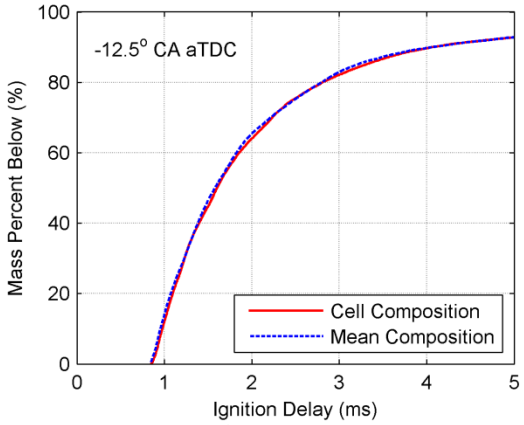

Figure 2.10 – Reaction space (at 12.5° CA bTDC) visualized in terms of cumulative charge mass below a certain ignition delay with the cell and mean composition.

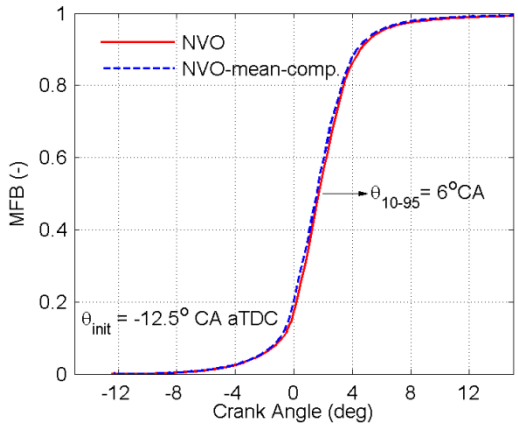

Figure 2.11 – Mass fraction burned predictions from the quasi-dimensional model for NVO-DI and NVO-DI with mean composition. The results indicate that neglecting the compositional stratification does not significantly impact the overall burn duration.

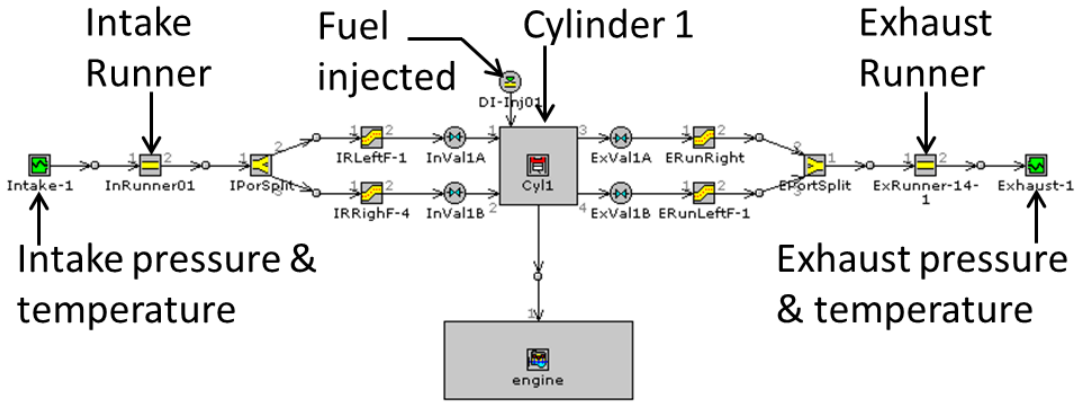

Figure 2.12 – Intake runner – to – exhaust runner model in GT-Power with appropriate inputs to isolate Cylinder 1 from rest of the engine system for three pressure heat release analysis.

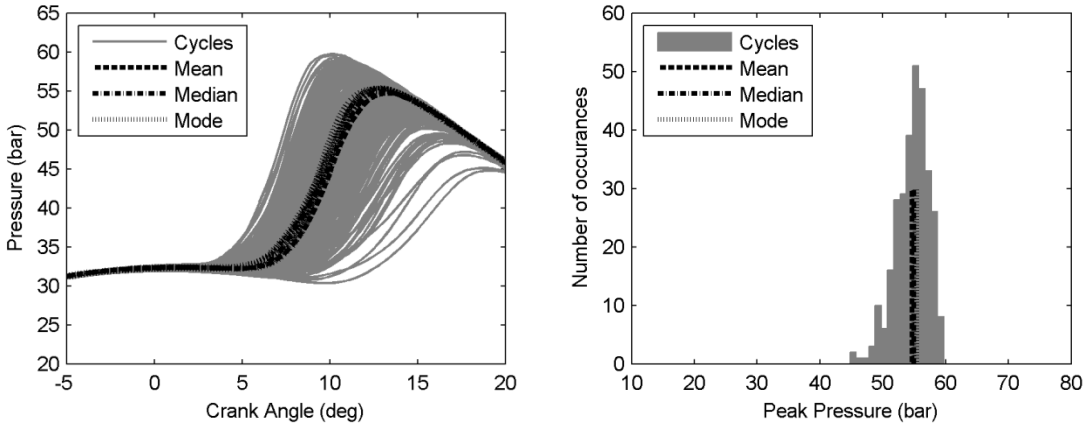

(a) (b)

Figure 2.13 – Cycle to cycle variation in pressure data at steady state for an operating point, a) cylinder pressure traces for all cycles b) Frequency of occurrence based on cyclic peak pressure. Cycle closest to the mean peak pressure, cycle with the median peak pressure and ten most frequently operating peak pressure cycles have also been marked.

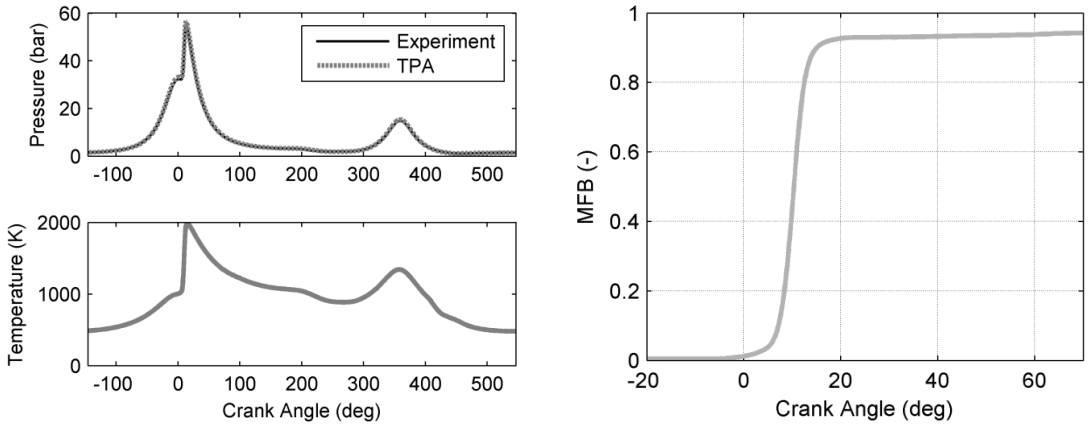

Figure 2.14 – Sample result from heat release analysis (for cycle closest to the mean peak pressure cycle) including (a) the experimental/simulated pressure, estimated mean charge temperature and (b) mass fraction burned curve for HCCI operation at 1500RPM, 5.6 bar net IMEP, 1.4 bar/1.5 bar absolute intake/exhaust pressure, 93^{o} CA NVO, ϕ=0.67, RGF = 34% and ϕ'=0.44.

2.8 References

1. Kodavasal, J., **"**Effect of charge preparation strategy on HCCI combustion," PhD Thesis, The University of Michigan, Ann Arbor, MI, 2013.
2. Ortiz-Soto, E. A., Lavoie, G. A., Martz, J. B., Wooldridge, M. S., and Assanis, D. N., "Enhanced Heat Release Analysis for Advanced Multi-Mode Combustion Engine Experiments," Applied Energy, Vol. 136, pp. 465-479, 2014.
3. Amsden, A.A., "KIVA-3V: A Block Structured KIVA Program for Engines with Vertical or Canted Valves," Los Alamos National Laboratory Report LA-13313-MS, 1997. Honeywell International, Inc., http://www.turbobygarrett.com
4. Amsden, A. A., O'Rourke, P. J., and Butler, T. D., "KIVA-II: A Computer Program for Chemically Reactive Flows and Sprays," Los Alamos National Laboratory Report LA-11560-MS, 1989.
5. Han, Z. and Reitz, R.D., "Turbulence Modeling of Internal Combustion Engines Using RNG k-ε Models," Combustion Science and Technology, Vol. 106, Issues 4-6, pp. 267-294, 1995.
6. Middleton, R. J., "Simulation of spark assisted compression ignition combustion under EGR dilute engine operating conditions," PhD Thesis, The University of Michigan, Ann Arbor, MI, 2014.
7. Mehl, M., Chen, J.Y., Pitz, W.J., Sarathy, S.M., and Westbrook, C. K., "An Approach for Formulating Surrogates for Gasoline with Application toward a Reduced Surrogate Mechanism for CFD Engine Modeling," Energy & Fuels, Vol. 25, Issue 11, pp. 5215-5223, 2011.
8. Mehl, M., Pitz, W.J., Westbrook, C.K., and Curran, H.J., "Kinetic Modeling of Gasoline Surrogate Components and Mixture Under Engine Like Conditions", Proceedings of the Combustion Institute, 33:193-200, 2011.

9. Mehl, M., Pitz, W.J., Sarathy, M., Yang, Y., and Dec, J.E., "Detailed Kinetic Modeling of Conventional Gasoline at Highly Boosted Conditions and the Associated Intermediate Temperature Heat Release," SAE Paper 2012-01-1109, 2013
10. Dec, J.E., and Yang, Y. "Boosted HCCI for High Power without Engine Knock and Ultra-Low NOx Emissions – using Conventional Gasoline," SAE Int. J. Engines 3(3):750-767, 2010
11. Babajimoppulos., A., "Development of Sequential and Fully Integrated CFD/Multi-Zone Models with Detailed Chemical Kinetics for the Simulation of HCCI Engines," PhD Thesis, The University of Michigan, Ann Arbor, MI, 2005.
12. Babajimopoulos, A., Assanis, D.N., Flowers, D.L., Aceves, S.M., and Hessel, R.P., "A fully coupled computational fluid dynamics and multi-zone model with detailed chemical kinetics for the simulation of premixed charge compression ignition engines," International Journal of Engine Research, Vol. 6, Issue 5, pp. 497-512, 2005.
13. Kee, R. J., Rupley, F. M., and Miller, J. A., "Chemkin-ii: A Fortran chemical kinetics package for the analysis of gas-phase chemical kinetics," Technical report, Sandia National Labs., Livermore, CA (USA), 1989.
14. Martz, J. B., "Simulation and model development for auto-ignition and reaction front propagation in low-temperature high-pressure lean-burn engines," PhD Thesis, The University of Michigan, Ann Arbor, MI, 2010.
15. Manofsky, L., Vavra, J., Assanis, D., and Babjimopoulos, A., "Bridging the Gap between HCCI and SI: Spark Assisted Compression Ignition," SAE Paper 2011-01-1179, 2011.
16. Olesky, L. M., Martz, J. B., Lavoie, G. A., Vavra, J., Assanis, D. N., & Babajimopoulos, A., "The effects of spark timing, unburned gas temperature, and negative valve overlap on the rates of stoichiometric spark assisted compression ignition combustion," Applied Energy, 105, 407-417, 2013.

17. Olesky, L. M., Lavoie, G. A., Assanis, D. N., Wooldridge, M. S., and Martz, J. B. "The effects of diluent composition on the rates of HCCI and spark assisted compression ignition combustion," Applied Energy, 124, 186-198, 2014
18. Olesky, L. M., "An Experimental Investigation of the Burn Rates of Naturally Aspirated Spark Assisted Compression Ignition Combustion in a Single Cylinder Engine with Negative Valve Overlap," PhD Thesis, The University of Michigan, Ann Arbor, MI, 2013.
19. H. Yilmaz, O. Miersch-Wiemers, and L. Jiang. "Advanced Combustion Concepts - Enabling Systems and Solutions (ACCESS)". DOE Vehicle Technologies Office Annual Merit Review. URL: http ://energy. gov/sites/prod/files/2014/03/f13/ace066_yilmaz_2013_o.pdf.2013, 2013.
20. Polovina, D., McKenna, D., Wheeler, J., Sterniak, J., Miersch-Wiemers, O., Mond, A., & Yilmaz, H., "Steady-state combustion development of a downsized multi-cylinder engine with range extended HCCI/SACI capability," SAE Int. J. Engines 6(1):2013, doi: 10.4271/2013-01-1655, 2013.
21. Stivender, D. L., "Development of a Fuel-based mass emission measurement procedure," SAE 710604, 1971.
22. Shingne, P. S., Assanis, D., Babajimopoulos, A., Keller, P., Roth, D., and Becker, M. "Turbocharger Matching for a 4-Cylinder Gasoline HCCI Engine Using a 1D Engine Simulation," SAE Paper 2010-01-2143, 2010.
23. Middleton, R. J. and Martz, J. B., , "An efficient model of gas exchange for multi-cycle CFD simulations with detailed chemistry," Publication in preparation.
24. Kodavasal, J., Lavoie, G. A., Assanis, D. N., & Martz, J. B., "The effects of thermal and compositional stratification on the ignition and duration of homogeneous charge compression ignition combustion," Combustion and Flame, 162(2), 451-461, 2015.

25. Goldsborough, S. S., “A chemical kinetically based ignition delay correlation for iso-octane covering a wide range of conditions including the NTC region,” Combustion and Flame, 156(6), 1248-1262, 2009.
26. Kodavasal, J., McNenly, M. J., Babajimopoulos, A., Aceves, S. M., Assanis, D., Havstad, M. A., & Flowers, D. L., “An accelerated multi-zone model for engine cycle simulation of homogeneous charge compression ignition combustion,” International Journal of Engine Research, vol. 14, no. 5, 416-433, 2013.
27. Heywood, J., Higgins, J., Watts, P., and Tabaczynski, R., “Development and Use of a Cycle Simulation to Predict SI Engine Efficiency and NOx Emissions,” SAE Technical Paper 790291, doi:10.4271/790291, 1979.
28. Blumberg, Paul N., George A. Lavoie, and Rodney J. Tabaczynski., “Phenomenological models for reciprocating internal combustion engines,” Progress in Energy and Combustion Science 5, no. 2, 123-167, 1979.
29. Karvounis, E. and Assanis, D., "FIND: Framework for Intelligent Design," SAE Technical Paper 931180, doi:10.4271/931180, 1993.
30. Morel, T., and Keribar R., “A Model for Predicting Spatially and Time Resolved Convective Heat Transfer Bowl-in-Piston Combustion Chambers,” SAE 850204, 1985.
31. Morel, T., Rackmil, C. I., Keribar, R., and Jennings, M. J., “Model for Heat Transfer and Combustion in Spark Ignited Engines and its Comparison with Experiments,” *SAE 880198*, 1988.
32. Morel, T., Keribar, R., and Blumberg, P. N., “A New Approach to Integrating Engine Performance and Component Design Analysis Through Simulation,” SAE 880131, 1988.
33. Morel, T., Keribar, R., Silvestri, J., and Wahiduzzaman, S., “Integrated Engine/Vehicle Simulation and Control,” SAE 1999-01-0907, 1999.

34. Ciesla, C., Keribar, R., and Morel, T., "Engine/Powertrain/Vehicle Modeling Tool Applicable to All Stages of the Design Process," SAE 2000-01-0934, 2000.
35. Morel, T., Keribar, R., and Leonard, A., "Virtual Engine/Powertrain/Vehicle Simulation Tool Solves Complex Interacting System Issues," SAE 2003-01-0372, 2002.
36. "Gamma Technologies - Engine and Vehicle simulation," *gtisoft.com*. [Online]. Available: http://gtisoft.com/. [Accessed: 04-Mar-2013].
37. Ortiz-Soto, E. A., Vávra, J., and Babajimopoulos, A.. Assessment of residual mass estimation methods for cylinder pressure heat release analysis of HCCI engines with negative valve overlap. In *Proc. ASME Internal Combust. Engine Div. Fall Tech. Conf.*, 2011.
38. Shingne, P. S., Gerow, M. S., Triantopoulos, V., Bohac, S. V., & Martz, J. B., "A Comparison of Valving Strategies Appropriate for Multi-Mode Combustion Within a Downsized Boosted Automotive Engine: Part A—High Load Operation Within the SI Combustion Regime," In ASME 2013 Internal Combustion Engine Division Fall Technical Conference (pp. V001T03A030-V001T03A030), 2013.
39. Sterniak, J. (Robert Bosch LLC), electronic communication, February, 4, 2014.
40. Chapman, S. J., "Fortran 95/2003 for Scientists and Engineers," 3rd ed. McGraw-Hill, Inc., 2010.
41. Woschni G., "A universally applicable equation for the instantaneous heat transfer coefficient in the internal combustion engine," SAE 670931, 1967.

CHAPTER 3

EFFECT OF OPERATING CONDITIONS ON NVO-DI HCCI COMBUSTION:

SPEED, LOAD (ϕ') AND BOOST

3.1 Background

Researchers have demonstrated the potential of achieving high efficiency HCCI operation while reaching very high loads (~16 bar gross IMEP) and ultra-low NOx with port fuel injected (PFI) gasoline fuel, intake boost, full lift cams and intake heating [1, 2]. However this system is not appropriate for the highly transient nature of automotive applications and differs from previous boosted HCCI engine studies [3, 4]. To allow the rapid control of intake valve closing (IVC) temperature required for the transient nature of automotive operation, negative valve overlap (NVO) type valve events are favored in automotive systems, compared to the relatively slow intake charge heating. Direct injection (DI) during the recompression phase of NVO is also used and favored over late DI injection during intake or PFI for stable, highly dilute engine operation [5]. DI into NVO is also used to control combustion phasing [6].

Rothamer et al. [7] have indicated that there is increased thermal and compositional stratification within the charge when going from PVO to NVO valve events. Kodavasal et al. [8] have demonstrated the effect of the varying stratification associated with the PVO to NVO valve events on HCCI combustion profiles. The results from this CFD study showed a significant increase in thermal stratification with NVO relative to PVO due to retention of high levels residual gases from previous cycle which

translates to a significant increase in the 10-90% burn duration. With a Quasi-D model they also decoupled the effect of thermal versus compositional stratification on the burn duration and found that burn duration is a strong function of thermal stratification with minimal dependence on compositional stratification. Kodavasal [9] has also investigated the effect of fueling strategy, namely DI vs. PFI in conjunction with PVO and NVO. He found that NVO-DI tends to increase the compositional stratification and slightly reduce the thermal stratification due to DI into hot residuals compared to NVO-PFI whereas DI under PVO conditions does not affect HCCI combustion.

These studies have demonstrated the effect of different charge preparation strategies on HCCI combustion. However it remains to be seen if there is a noticeable effect of changing operating conditions on the stratification and combustion with the same charge preparation method, namely NVO-DI operation. Lawler et al. [11] have performed metal engine experiments to study the effects of varying engine operating conditions on the unburned temperature distribution prior to ignition with their Thermal Stratification Analysis (TSA) technique. They found that pre-ignition thermal stratification and hence burn rates were insensitive to fueling strategy. Additionally they observed significant increase in pre-ignition thermal stratification when a rebreathing strategy was used versus PVO. They also observed an increase in thermal stratification due to an increase in intake temperature and a decrease in the thermal stratification with increasing fuel-to-charge equivalence ratio. Although the experimental setup used by Lawler et al. was equipped with a production like combustion chamber and DI as well as PFI operation, they were limited to either PVO or re-breathing type valves. Furthermore, the TSA methodology is limited by its assumptions to predicting only the effect of thermal stratification; it assumes that the charge is compositionally uniform. Finally, unlike a model, the experiments cannot completely isolate the effect of a particular variable on HCCI combustion.

In Part I (Chapter 3 and Chapter 4) of this dissertation, 3D CFD is used to analyze the effect of changing inputs on HCCI combustion. The objective is to isolate the effect of different inputs on the pre-ignition reactivity distributions and hence HCCI combustion rates. CFD simulations are performed where an input variable is swept while changing the intake manifold temperature to match the location of 10% mass fraction burned (θ_{10}) (except for intake temperature sweep) while also changing the injected fuel mass to match the total mixture dilution (except for the load sweep). In this chapter speed, load (ϕ') and boost are chosen as the variables to sweep since they determine the operating condition of the engine. The reactivity stratification analysis and quasi-dimensional model introduced in Chapter 2 are used to isolate the effect of thermal and compositional stratification (from other thermodynamic variables) on HCCI combustion. The reactivity stratification for all the sweeps has been presented at 12.5°CA bTDC which is the ignition location for the baseline NVO case described in Chapter 2. The insights from this study are also used to inform a burn rate model (Chapter 6) for systems level simulations and controls testing.

3.2 Effect of Varying Engine Speed on NVO-DI HCCI

This section analyses the effect of speed on the thermal and compositional stratifications which in turn affect the charge reactivity and burn rate. Full cycle CFD simulations are performed at 1000 RPM and 3000 RPM with the FFVA mesh which form a speed sweep with the baseline case described in Chapter 2. The fueling rate and intake manifold temperature are varied in order to hold the total dilution (ϕ') and location of 10% mass fraction burned (θ_{10}) constant at baseline value. Table 3.1 summarizes the operating conditions for the speed sweep. Note that the global mixture composition is the same but the intake temperature is changed to compensate for the changing residence time to hold θ_{10} constant. Figure 3.1 shows the MFB data versus crank angle from CFD

for the three cases. The curves are roughly aligned until θ_{10}, while being significantly different later. At 1000 RPM, the burn duration (θ_{10-90} = 5.0°CA) is shorter compared to the 2000 RPM baseline case (θ_{10-90} = 6.1°CA) and at 3000 RPM the burn duration (θ_{10-90} = 7.4°CA) is longer than the baseline case. This trend is explained subsequently by the reaction space analysis.

3.2.1 Stratification evolution from IVC to TDC

Figure 3.2(a) and (b) respectively show the evolution of the thermal ($2\sigma T$) and compositional ($2\sigma\phi_{FO}$) stratification, from IVC to TDC, for the speed sweep. Non-reactive CFD simulations are used to compute the stratification values. Figure 3.2(a) shows that the higher speeds have a higher initial thermal stratification. Thermal stratification in all cases drops until ~60^{o}CA bTDC due to mixing after which it rises until TDC due to increasing wall heat losses. Towards end of compression the thermal stratification ($2\sigma T$) is nearly same for the three cases with the 3000 RPM case having a slightly higher value and 1000 RPM case having a slightly lower value compared to the 2000 RPM case. Figure 3.2(b) shows that the ϕ_{FO} stratification is high initially and reduces with mixing during compression. The higher speeds have higher ϕ_{FO} stratification throughout compression. Simulations were performed (not shown) where the end of injection was aligned between cases instead of the start of injection and this trend in ϕ_{FO} persisted indicating that this effect is independent of the injection event.

Figure 3.3 shows the spatial distribution of CO2 density in a clip plane from CFD at intake valve closing for (a) 1000 RPM and (b) 3000 RPM. Regions with high CO2 densities have elevated levels of residual fraction. There is significantly higher stratification in CO2 for the 3000 RPM case compared to the 1000 RPM case. Figure 3.4 shows the spatial distribution of temperature in a clip plane from CFD at intake valve closing for (a) 1000 RPM and (b) 3000 RPM. The 3000 RPM case is thermally more

stratified compared to the 1000 RPM case, and the temperature distribution is collocated with the distribution of CO2 density. Figure 3.5 shows the spatial distribution of ϕ_{FO} in a clip plane from CFD at intake valve closing for (a) 1000 RPM and (b) 3000 RPM. Similarly, the 3000 RPM case is more stratified in ϕ_{FO} compared to the 1000 RPM case with the ϕ_{FO} stratification trend being correlated with the temperature and CO2 density stratification. Hence the initial charge thermal stratification is a direct consequence of the residual stratification and it depends on the available time for mixing that will reduce the stratification.

Figure 3.6 shows the (a) thermal and (b) compositional stratification plotted versus non-dimensional turbulence time or Eddy turnovers. The non-dimensional turbulence time is computed by normalizing the turbulent time scale (L/u') with time. In Figure 3.6 (a) the thermal stratification decreases at a higher rate for higher speeds but later increases due to increasing wall heat losses. There are approximately 15- 17 eddy turnovers before the timescale peaks and reverses. This is due to the length scale becoming disproportionally small compared to u' near TDC. Similarly in Figure 3.6 (b) the compositional stratification decreases at a higher rate for high speeds. Since the initial compositional stratification is initially much greater for the higher speeds, the charge does not reach the lower levels of compositional stratification predicted for the lower speeds towards the end of compression. Figure 3.7 displays the compositional stratification ($2\sigma\phi_{FO}$) plotted versus time. It is apparent that for the high speed cases the $2\sigma\phi_{FO}$ falls at a faster rate compared to the low speed cases. However there is insufficient time for the high speed cases to "catch up" with the low speed ones in terms of $2\sigma\phi_{FO}$ before reaching their respective TDC. It is demonstrated that if the simulation is performed for a longer duration including the expansion stroke that the $2\sigma\phi_{FO}$ for the three cases will approximately converge and trend toward zero.

3.2.2 Analysis of reaction space at 12.5°CA

Mass distributions ϕ_{FO} and temperature are presented in Figure 3.8 at 12.5°CA bTDC. This crank angle is chosen to match the ignition location of the baseline NVO case shown in Chapter 2. The distributions are generated by grouping the CFD cells into bins of ΔT=5K and $\Delta\phi_{FO}$=0.05. The temperature distributions in Figure 3.8(a) show that at lower speeds the mass is distributed over a slightly smaller temperature range compared to higher speeds, with mean temperatures decreasing with speed to maintain the same θ_{10}. Figure 3.8 (b) shows the charge is more stratified in ϕ_{FO} at higher engine speeds compared to lower speeds although the mean ϕ_{FO} remains the same across the sweep. The cumulative distribution of reactivity is visualized in Figure 3.9 and shows the reduction in reactivity with speed necessary to match ignition in time. Figure 3.10 shows the mass fraction burned output from the Quasi-D model for the cases with the default stratification from CFD initialized at 12.5°CA bTDC; these predictions are similar to the reacting CFD predictions in Figure 3.1.

3.2.3 Decoupling the effect of compositional stratification on reactivity

In order to assess the relative importance of compositional stratification to the results, the cumulative distribution of reactivity is plotted twice at 12.5°CA bTDC as shown Figure 3.11. The solid line is calculated with the cell composition and temperature while the dashed line is calculated with the cell temperature and mean cylinder composition. At each speed, the cumulative reactivity distributions are nearly identical, except at 3000 RPM, where there is a noticeable difference in reactivity at the lower temperatures. While reactivities are largely unaffected by compositional stratification at lower speeds, some affect is noticeable for the relatively high compositional stratification ($2\sigma\phi_{FO}$=0.3) at high speed.

3.2.4 Removing the effect of differing residence time on reactivity

To remove the effect of different residence times on combustion, the Quasi-D model is initialized at 12.5°CA bTDC with the default stratification from CFD but now operated at 2000 RPM for all cases. Figure 3.12 shows the Quasi-D model results for the speed sweep. The asterisks within the legend for 1000 RPM and 3000 RPM cases denotes that these cases have been simulated at 2000 RPM from 12.5°CA bTDC onward. The 1000 RPM* case is phased late since it has shorter time to react whereas the 3000 RPM* case is phased early since it now has a longer time to react. The mass fraction burned curves now match the behaviors reflected within the cumulative reactivity distributions of Figure 3.9. Considering that heat loss rates increase with mean gas temperature, but cumulative heat loss per cycle decreases with speed [10], it remains to be seen if the variations in reactivity result from the necessary shifting in peak distribution temperatures to match ignition, or if wholesale differences in the thermal stratification drive the reactivity and associated combustion behavior.

3.2.5 Isolating the effect of stratification on reactivity

In order to isolate the effect of stratification on combustion, the leading edge of the reactivity distribution of the cases should be matched. The differences in the less reactive charge will reveal the effect of differing thermal and compositional stratification. This is achieved by shifting the temperature distribution for the 1000 RPM and 3000 RPM cases such that their hottest temperatures match the hottest temperature of the 2000 RPM case. The resulting cumulative reactivity distribution is displayed in Figure 3.13. The diamond symbol after the legend for the 1000 RPM and 3000 RPM cases denotes that the temperature shift has been performed. The reactivity is well matched for 1000 RPM♦ and 2000 RPM throughout. The 3000 RPM♦ matches the 2000 RPM reactivity initially but deviates beyond 60% cumulative mass with a relatively lower reactivity,

similar to the behavior in Figure 3.11. The cumulative reactivity distribution of the 3000 RPM♦ case computed with the mean composition (3000 RPM♦-mean cmp.) is also displayed on the Figure 3.13. 3000 RPM♦-mean cmp. curve nearly collapses on top of the 1000 RPM♦ and 2000 RPM curves. Figure 3.14 shows the mass fraction burned profiles from the corresponding Quasi-D model results, with the burn profile results reflecting the trends within the reactivity distribution. The 3000 RPM♦ case burns slower for MFB > 0.6 corresponding to the low reactivity in the distribution. Figure 3.14 also shows that the mass fraction burned result from the Quasi-D model for the 3000 RPM♦-mean cmp. case nearly matches the 1000 RPM♦ and 2000 RPM cases. Hence the compositional stratification at 3000 RPM is high enough to affect the combustion. Removing this effect at high speeds there is almost no difference between the burn profiles as the thermal stratification does not significantly vary between the cases.

3.3 Effect of Varying Load [Total Dilution (ϕ')] on NVO-DI HCCI

The fueling rate is varied in this study to vary load and total dilution, with the operating conditions shown in Table 3.2. The intake temperature is concurrently adjusted to hold the θ_{10} constant at the baseline NVO value. The fueling is changed from 6.85 mg/cycle to 10.7 mg/cycle and correspondingly the fuel-to-air equivalence ratio (ϕ) changes from 0.55 to 0.62. The metric ϕ' (phi prime) which is the total dilution is adopted to account for dilution due to large amounts of residual gasses in addition to excess air, is defined in Equation 7:

$$\phi' = \frac{m_{fuel}/\left(m_{total} - m_{fuel}\right)}{\left(m_{fuel}/m_{air}\right)_{st}} \sim \phi(1 - RGF) \qquad \text{Equation 7}$$

where RGF is the residual gas fraction in the cylinder. Figure 3.15 shows the MFB data versus crank angle from CFD for the ϕ'sweep. Burn durations (θ_{10-90}) decrease with

increases in ϕ' (θ_{10-90}=4.4^{o} CA for ϕ'=0.37, θ_{10-90}=6.1^{o} CA for ϕ'=0.32, θ_{10-90}=7.9^{o} CA for ϕ'=0.28 and θ_{10-90}=12.6^{o} CA for ϕ'=0.23).

3.3.1 Analysis of reaction space at 12.5^{o} CA bTDC

The mass distribution over temperature in Figure 3.16(a) remains approximately constant for different ϕ's while the mean temperature (T_m) varies slightly over the sweep ($\Delta T_m =$ 16K). T_m is increased with decreasing ϕ_{FO} in order to maintain the θ_{10} combustion phasing over the sweep. The ϕ_{FO} stratification shown in Figure 3.16(b) remains roughly the same over the sweep although the mean value increases with increasing ϕ'.

The cumulative distribution of reactivity is visualized at 12.5°CA bTDC in Figure 3.17 in order to relate the temperature and ϕ_{FO} variations to burn rates. The leading edge of the distributions is nearly matched since the θ_{10} across the sweep is matched. Although the thermal and compositional stratification doesn't vary in this sweep, the tail ends of the reactivity distributions are different, with leaner charge being less reactive and richer charge being more reactive.

3.3.2 Decoupling the effect of compositional stratification on reactivity

Figure 3.18 shows the cumulative distribution of reactivity at 12.5°CA bTDC computed from non-reactive CFD simulations with the cell temperature and composition overlaid with the distributions computed using cell temperature and the mean cylinder composition for the ϕ'sweep. There are minor differences between the two curves across the sweep indicating that the compositional stratification has an approximately negligible effect on charge reactivity compared to thermal stratification for the varying ϕ'values.

3.3.3 Decoupling thermodynamic effects from chemical kinetic effects

It is unclear if the relatively small differences in reactivity justify the large variation in θ_{10-90} burn duration; from θ_{10-90} = 4.4°CA for ϕ'= 0.37 to θ_{10-90} = 12.6° CA for ϕ'= 0.23. For example, Kodavasal et al. [12] found that significant combustion rate variations can result from thermodynamic property differences, which may be present in the current sweep. It is possible that the large differences are compounded due to differences in both the thermodynamic properties and chemistry. Figure 3.19 displays the distribution of the ratio of specific heats (γ) for the entire CFD domain (at 12.5°CA bTDC) over reactivity for the extremes of the ϕ'sweep (middle cases omitted for figure clarity). Although there is significant stratification in γ, the difference in the mean value is clear. Typically, decreasing γ lowers the rate of compression induced heating of the unburned charge by expansion of the burning regions, leading to slower sequential auto-ignition. In this scenario however, the cases with higher ϕ's have lower γ values and vice versa. It is hypothesized that if all cases have the same initial γ as the baseline case, i.e. if the lower ϕ'cases would have lower γ and that the higher ϕ'cases would have higher γ, the variation in θ_{10-90} compared to the baseline case would be even more exaggerated.

In order to test the validity of this hypothesis and to ensure that the effect is chemical and not related to the γ effect alone, the Quasi-dimensional (Quasi-D for short) approach from Chapter 2 is used. The cells from the non-reacting CFD simulations (-12.5^{o}CA aTDC) corresponding to the reacting CFD simulations from the ϕ'sweep are used to initialize the model. Figure 3.20(a) shows the mass fraction burned curves from the Quasi-D model. The ϕ'sweep has similar characteristics as the fully-coupled CFD/kinetics results in terms of the 10-90 burn duration, with the burn durations being inversely proportional to ϕ'. Figure 3.20(b) shows the corresponding γ variation with crank angle. The initial γ is different across the sweep in a manner similar to Figure 3.19, γ is inversely proportional to ϕ'. To remove the effect of varying γ, the Quasi-D model is

rerun for all the cases by either replacing CO_2 and H_2O with N_2 or by replacing N_2 with CO_2 and H_2O in every zone, in order to match the initial γ and heat capacity (C_p) of the baseline NVO case.

Figure 3.21 shows the results from the quasi dimensional model after the initial γ is matched. Figure 3.21(a) shows that there is no qualitative difference between the combustion characteristics with and without matchingγ. Figure 3.21(b) clearly shows that the initial γ values are matched. On closer examination it is apparent that the case with ϕ'=0.37 has an even shorter duration than when its initial gamma value wasn't matched to the baseline, whereas the cases with ϕ'=0.29 and ϕ'=0.24 have an even longer duration than when their initial gamma value wasn't matched to the baseline.

Figure 3.22 shows the variation in specific heat C_p with combustion when initial γ values are (a) unmatched and (b) matched. In Figure 3.22(a) there is small variation in initial C_p, when the initial γ values are not matched ($C_p(-5^0)$=1256 J/kg-K for ϕ'=0.24 and $C_p(-5^0)$=1262 J/kg-K for ϕ'=0.37). From Figure 3.22(b) when the initial γ values are matched the initial variation in C_p is even smaller ($C_p(-5^0)$=1258 J/kg-K for ϕ'=0.24 and $C_p(-5^0)$=1260 J/kg-K for ϕ'=0.37). When the initial C_p values (thermal sink effect) of the mixtures are nearly matched the change in combustion characteristics in terms of θ_{10-90} persists. Hence thermodynamic properties like C_p and γ do not significantly affect the combustion process.

3.4 Effect of Varying Boost on NVO-DI HCCI

The intake and exhaust manifold pressures are varied in this study, as shown in Table 3.3. The first case is the naturally aspirated baseline NVO case discussed in the previous chapter whereas the other two are P_{IN-EX} = 1.5 bar and P_{IN-EX} = 2 bar. The total dilution (ϕ') is held constant at the baseline value by changing the fueling at each boost pressure. The pressure induced enhancement of auto-ignition is compensated for by

lowering the intake temperature to hold θ_{10} constant. The global mixture quality is approximately matched in terms of ϕ_{FO}, χ_{O_2} and RGF. Figure 3.23 shows the MFB data versus crank angle from CFD for the three cases. The curves are nearly matched until 10% mass burned, however the θ_{10-90} duration reduces with increasing boost from θ_{10-90} = 6.1°CA for the naturally aspirated baseline case to θ_{10-90} = 4.9°CA for the case with P_{IN-EX} = 2 bar.

3.4.1 Analysis of reaction space at 12.5°CA bTDC

Figure 3.24(a) shows the evolution of $2\sigma T$ thermal stratification from IVC to TDC. The stratification initially falls until ~60°CA bTDC and then rises as the wall heat losses dominate thermal stratification closer to TDC, similar to previously seen for the speed sweep. The mean cylinder temperatures for higher boost cases are notably smaller than the naturally aspirated cases, resulting in lower heat losses close to TDC. This results in smaller thermal stratification for higher boost cases. Figure 3.24(b) shows the $2\sigma T$ thermal stratification plotted against the mean cylinder temperature normalized by the maximum mean temperature from IVC to TDC. Notice that the thermal stratification increases nearly linearly with temperature and the cases with higher absolute mean temperature have a higher thermal stratification.

Figure 3.25 visualizes the mass distribution over temperature and ϕ_{FO} for the boost sweep from the CFD domain at 12.5°CA bTDC; which corresponds to the ignition location of the baseline NVO case (Chapter 2). Figure 3.25(a) shows the thermal stratification ($2\sigma T$) decreasing from 79 K for the naturally aspirated baseline case to 72 K for the P_{IN-EX} =1.5 bar case, and to 66 K for the P_{IN-EX}= 2 bar case. The mean temperatures are reduced with increasing boost to maintain θ_{10}. Figure 3.25(b) shows the mass distribution over ϕ_{FO} is roughly the same for the boost sweep. Figure 3.26 shows the cumulative distribution of reactivity at 12.5°CA bTDC for the boost sweep. The

naturally aspirated baseline case has slightly shorter ignition delays initially compared to higher boost pressures for the most reactive portion of charge. However the trends in ignition delays are reversed for τ > 1.5 milliseconds with the naturally aspirated case having longer ignition delays and higher boost cases having progressively shorter ignition delays. Although the higher boost cases appear to start auto-ignition after the naturally aspirated case they burn much faster after ignition as seen from the burn profile trend observed from the CFD data. Figure 3.27 shows the mass fraction burned (MFB) results for the three cases from the Quasi-D model initialized at 12.5°CA bTDC. The burn profile trends are similar to CFD data.

3.4.2 Decoupling the effect of compositional stratification on reactivity

Figure 3.28 displays the cumulative charge reactivity for the boost sweep with and without compositional stratification by using the actual cell composition and the mean composition from the CFD domain to assess the importance of compositional stratification in determining charge reactivity. The curves calculated with cell and mean compositions lie nearly on top of each other throughout the sweep, indicating that for the conditions studied, thermal stratification is much more important to reactivity stratification compared to compositional stratification.

3.4.3 Decoupling the effect of pressure on burn duration

At 12.5°CA bTDC where reactivity stratification of cases is compared, the cylinder pressure (P_{cyl}) for the naturally aspirated case is 22.7 bar, 32 bar for the P_{IN-EX} = 1.5 bar case and 43.5 bar for the P_{IN-EX} = 2 bar case. Figure 3.29 displays the cumulative reactivity distribution for the three cases with ignition delays computed by using the pressure of the naturally aspirated case (denoted by an asterisks) while maintaining the cell level thermal and compositional stratification. The P_{IN-EX} = 1.5 bar*

and P_{IN-EX} = 2 bar* cases exhibit ignition delays shorter than the baseline cases. As the effect of pressure on reactivity is removed the lower temperatures of the original boosted cases reflect the lower reactivity, with ignition delays becoming progressively longer with pressure. Figure 3.30 shows the burn profile computed from the Quasi-D model initialized at 12.5°CA bTDC with the pressure of the baseline naturally aspirated case, while maintaining the thermal and compositional stratification of each case. Combustion rates for the P_{IN-EX}=1.5 bar* and P_{IN-EX}=2 bar* cases are now very slow compared to the baseline case due to lower temperatures.

3.4.4 Isolating the effect of thermal stratification on burn duration

The temperature of the P_{IN-EX}=1.5 bar* and P_{IN-EX}=2 bar* cases is shifted so that the hottest temperatures of all cases are aligned and the ignition delays recomputed with the baseline pressure. The resulting cumulative reactivity distribution is displayed in Figure 3.31. The higher boost cases have smaller thermal stratification and shorter ignition delays corresponding to the less reactive charge when the highest reactivity is matched. As a result, combustion rates increase as thermal stratification decreases. Similar behavior is exhibited from the predictions of the Quasi-D model in Figure 3.32.

The relative importance of temperature and pressure on reactivity can be compared by taking partial derivatives of τ_{ign} [13] to *T* and *P* individually for nominal conditions at 12.5°CA bTDC of T = 1045 K and *P* = 22.53 bar. Increasing manifold pressure to 1.5 bar and 2 bar increases the cylinder pressure to 31.8 bar and 43.0 bar at 12.5°CA bTDC respectively. This corresponds to increasing the temperature by 30 K and 60 K respectively. However in this sweep the hottest temperatures of the boosted cases (1.5 bar and 2 bar) are lower than the baseline case by 24 K and 48 K respectively. Additionally the high boost cases also have smaller thermal stratification. Therefore a combination of the pressure effect dominating the lowered temperatures and high boost

cases having smaller thermal stratification leads to shorter burn durations for high boost cases.

3.5 Summary and conclusions

In this chapter the effect of changing speed, load and boost on HCCI combustion profile are explained by means of the pre-ignition reactivity stratification. The thermal and compositional stratification available from the CFD domain is related to the reactivity by means of ignition delay calculations. There is significant variation in the pre-ignition ϕ_{FO} stratification with engine speed, while ϕ_{FO} stratification remains approximately constant with varying ϕ' and boost. Assessing the cumulative reactivity distributions computed based on cell composition and mean composition from CFD, it can be concluded that the compositional stratification has a much smaller effect on charge reactivity for these cases.

The thermal stratification of the charge pre-ignition increases slightly with speed, while the mean temperature increases to hold θ_{10} constant, compensating for the smaller residence time. Isolating the effect of thermal stratification on combustion demonstrates little variation in the burn profiles. The high compositional stratification at 3000 RPM affects the charge reactivity.

The thermal and compositional stratification remains roughly the same for the ϕ'sweep. The higher mean temperatures for the lower ϕ'cases compensate for the leaner charge when holding θ_{10} constant. For this sweep the higher reactivity and shorter burn durations are attributed to lower dilution, i.e., higher ϕ'values.

Finally, to hold θ_{10} constant for the boost sweep, the mean temperatures are reduced for the higher boost cases to compensate the increased reactivity associated with higher pressures. The burn duration shortens with increasing boost even though the cylinder temperatures are lower. Based on the He et al. [13] correlation for ignition delay,

the relative importance of temperature and pressure in isolation were determined for the baseline HCCI operating point. Removing the pressure effect and matching the hottest temperature of the charge demonstrates that the high boost cases burn faster due to smaller thermal stratification.

Table 3.1 – Operating conditions for engine speed sweep

Speed (RPM)	**1000**	**2000**	**3000**
NVO (^{o} CA)	157	157	157
SOI (^{o}CA aTDC)	390	390	390
Intake Temperature (^{o}C)	83	106	110
Fueling Rate (mg/cyc)	9.7	9.25	8.75
$\boldsymbol{\phi_{FO}}$	0.43	0.44	0.44
ϕ	0.57	0.58	0.59
ϕ'	0.32	0.32	0.32
RGF (%)	41.6	43.4	44.8
$\boldsymbol{\chi_{O2}}$ (%)	15.4	15.1	15.0
P_{IN-EX}(bar)	1	1	1

Table 3.2 – Operating conditions for load (ϕ') sweep

Speed (RPM)	2000	2000	2000	2000
NVO (^{o} CA)	157	157	157	157
SOI (^{o}CA aTDC)	390	390	390	390
Intake Temperature (^{o}C)	168	146	106	95
Fueling Rate (mg/cyc)	**6.85**	**8.3**	**9.25**	**10.7**
$\boldsymbol{\phi_{FO}}$	0.36	0.42	0.44	0.51
ϕ	0.55	0.58	0.58	0.62
$\boldsymbol{\phi'}$	**0.24**	**0.29**	**0.32**	**0.37**
RGF (%)	51.2	48.4	43.4	41.3
$\boldsymbol{\chi_{O2}}$ (%)	14.2	14.5	15.1	15.4
P_{IN-EX}(bar)	1	1	1	1

Table 3.3 – Operating conditions for boost sweep

Speed (RPM)	2000	2000	2000
NVO (^{o}CA)	157	157	157
SOI (^{o}CA aTDC)	390	390	390
Intake Temperature (^{o}C)	106	75	50
Fueling Rate (mg/cyc)	9.25	13.6	18.3
$\boldsymbol{\phi_{FO}}$	0.44	0.44	0.44
ϕ	0.58	0.58	0.58
ϕ'	0.32	0.32	0.32
RGF (%)	43.4	44.4	44.8
$\boldsymbol{\chi_{O2}}$ (%)	15.1	15.4	15.3
P_{IN-EX}(bar)	**1**	**1.5**	**2**

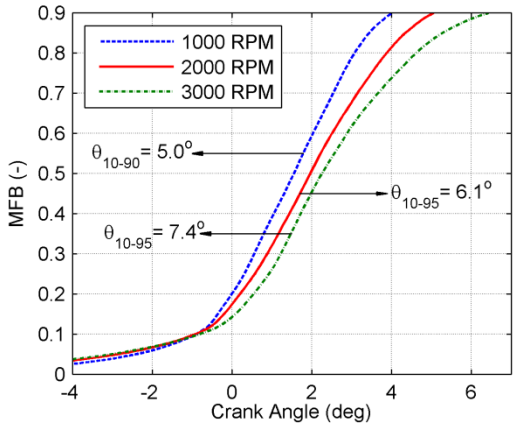

Figure 3.1 – Comparison of MFB curves from CFD for the speed sweep in Table 3.1. Plotted against crank angle; the burn duration increases with engine speed.

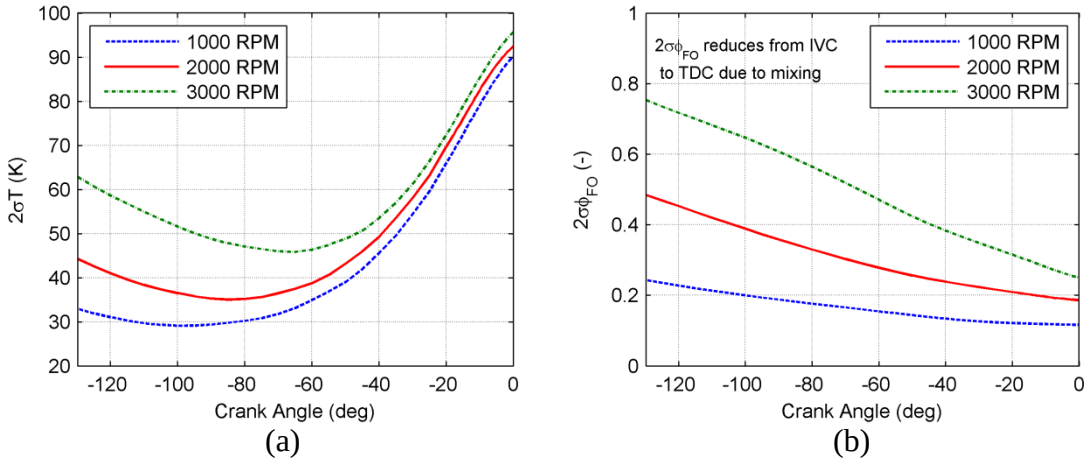

Figure 3.2 – Evolution of (a) thermal and (b) compositional stratification from IVC to TDC. The thermal stratification falls after IVC due to mixing until ~60^{o} CA bTDC but rises from there to TDC as it is subsequently dominated by wall heat losses. The higher speed cases have a higher initial compositional stratification which falls from IVC to TDC due to mixing.

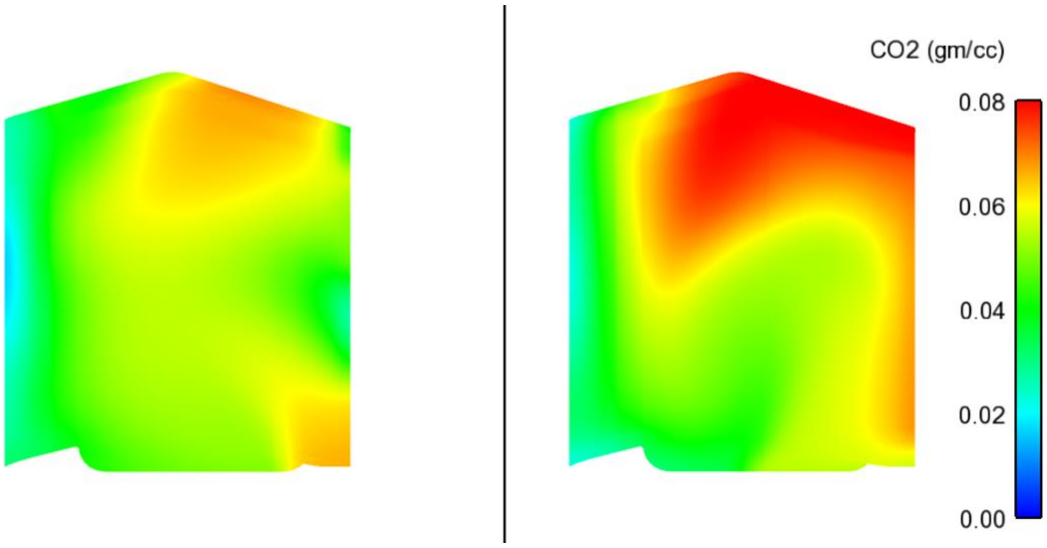

(a) (b)

Figure 3.3 – Spatial distribution of CO2 (gm/cc) as a marker of residuals in a clip plane from CFD at intake valve closing for (a) 1000 RPM and (b) 3000 RPM.

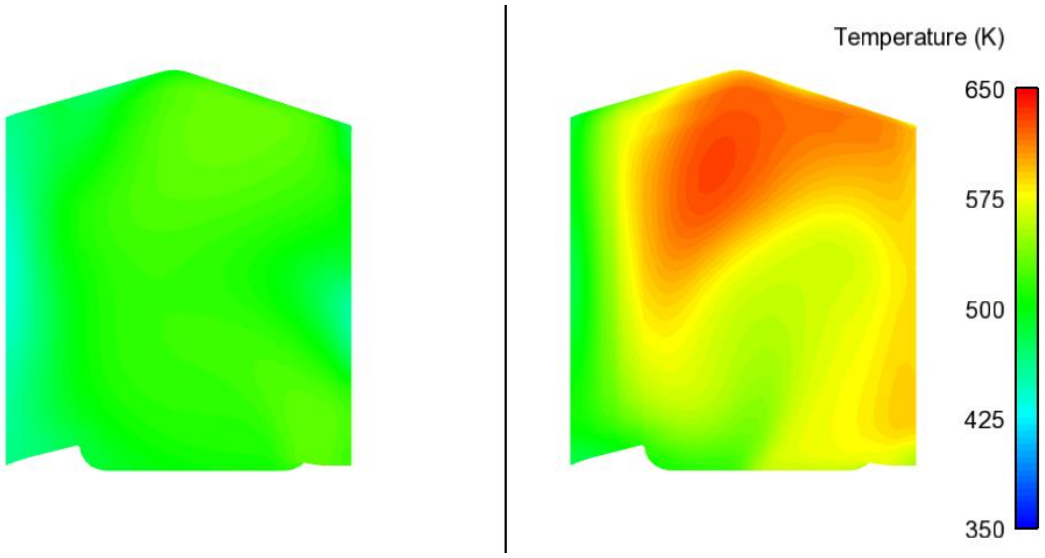

(a) (b)

Figure 3.4 – Spatial distribution of temperature in a clip plane from CFD at intake valve closing for (a) 1000 RPM and (b) 3000 RPM.

.

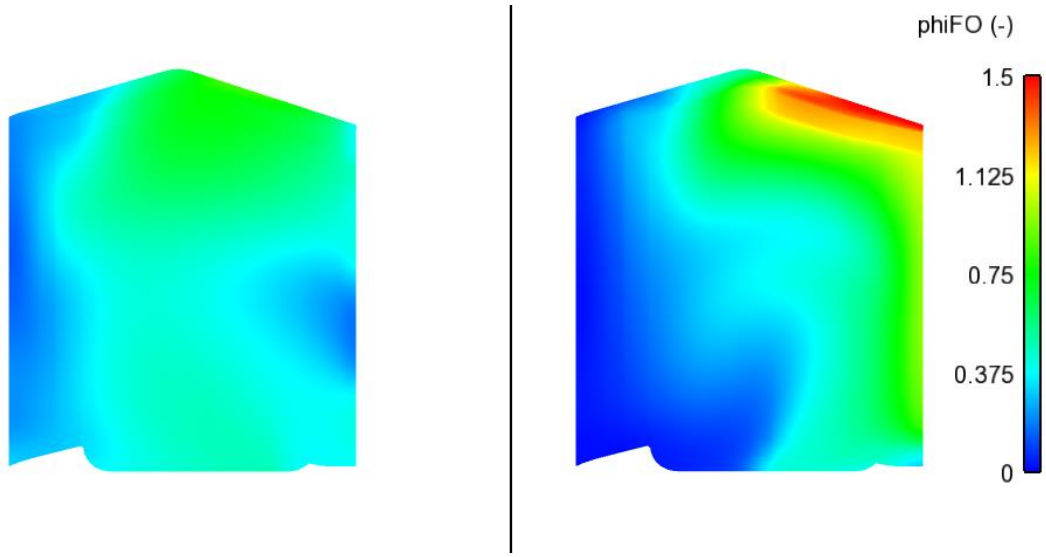

(a) (b)

Figure 3.5 – Spatial distribution of ϕ_{FO} in a clip plane from CFD at intake valve closing for (a) 1000 RPM and (b) 3000 RPM.

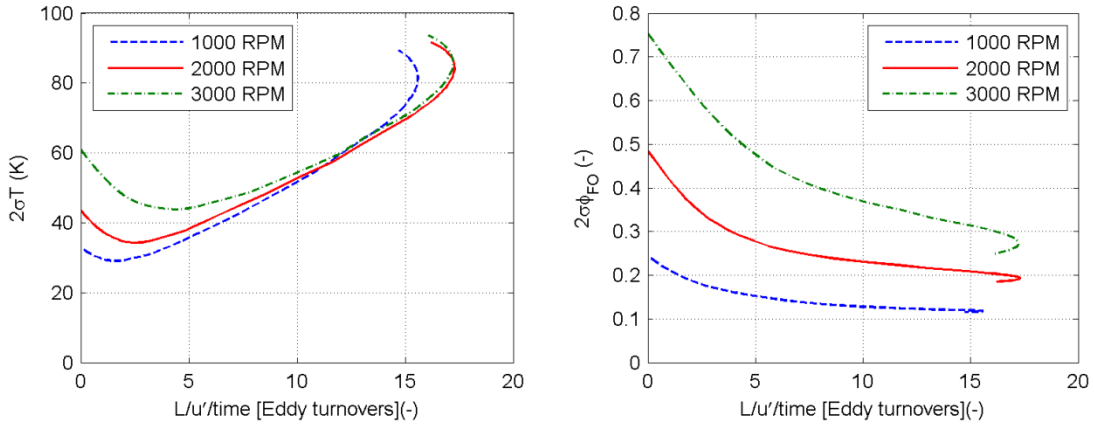

(a) (b)

Figure 3.6 – Evolution of (a) thermal and (b) compositional stratification from IVC to TDC plotted versus number of eddy turnovers.

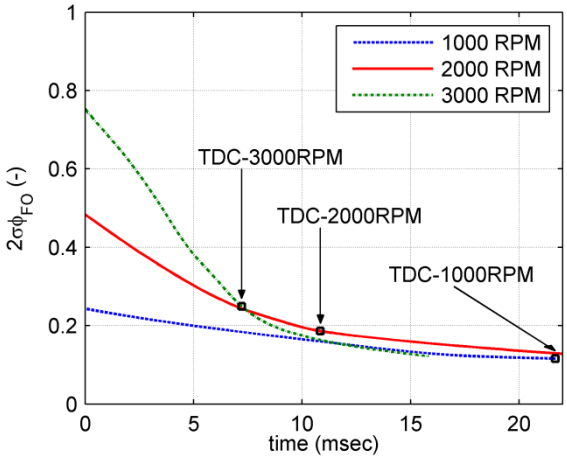

Figure 3.7 – Evolution of compositional stratification in terms of $2\sigma\phi_{FO}$ for the speed sweep plotted versus time.

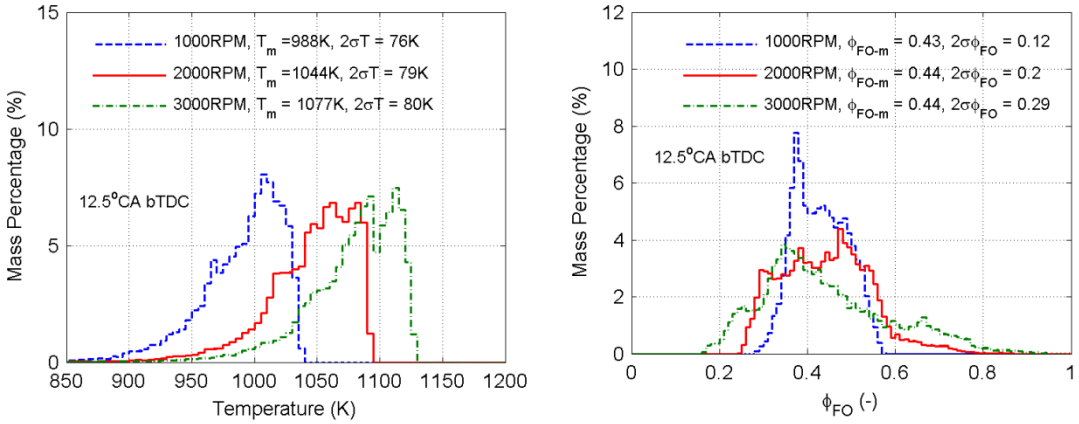

(a) (b)

Figure 3.8 – Mass distribution over (a) temperature and (b) ϕ_{FO} from non-reacting CFD simulations plotted at 12.5° CA bTDC. The thermal stratification increases slightly with speed and ϕ_{FO} stratification increases nearly linearly with speed.

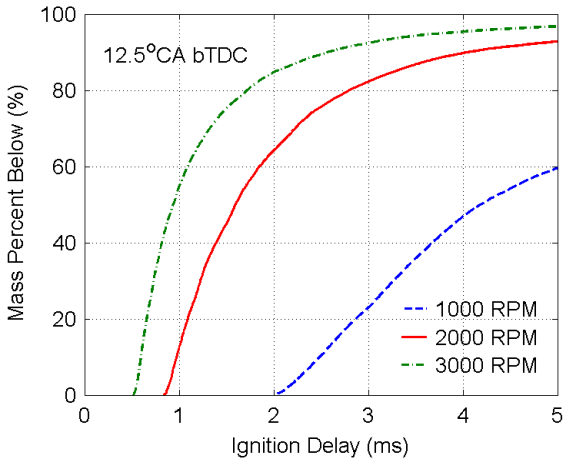

Figure 3.9 – Reaction space at 12.5° CA bTDC visualized in terms of cumulative charge mass below a certain ignition delay, for the speed sweep computed from non-reacting CFD simulations with cell temperature and composition. The higher speed cases appear more reactive.

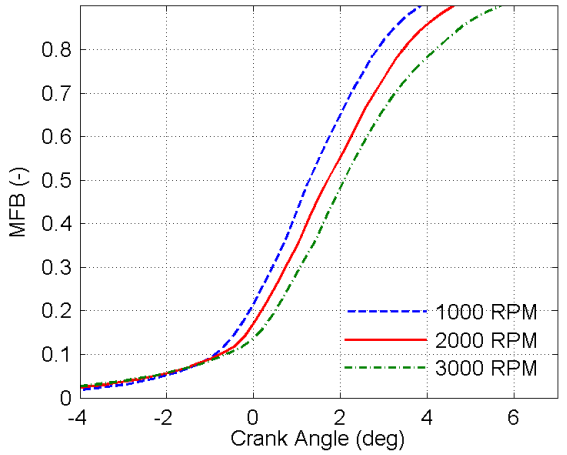

Figure 3.10 – Quasi-D model results for the speed sweep with zone temperatures and compositions obtained from non-reacting CFD, initialized at 12.5° CA bTDC.

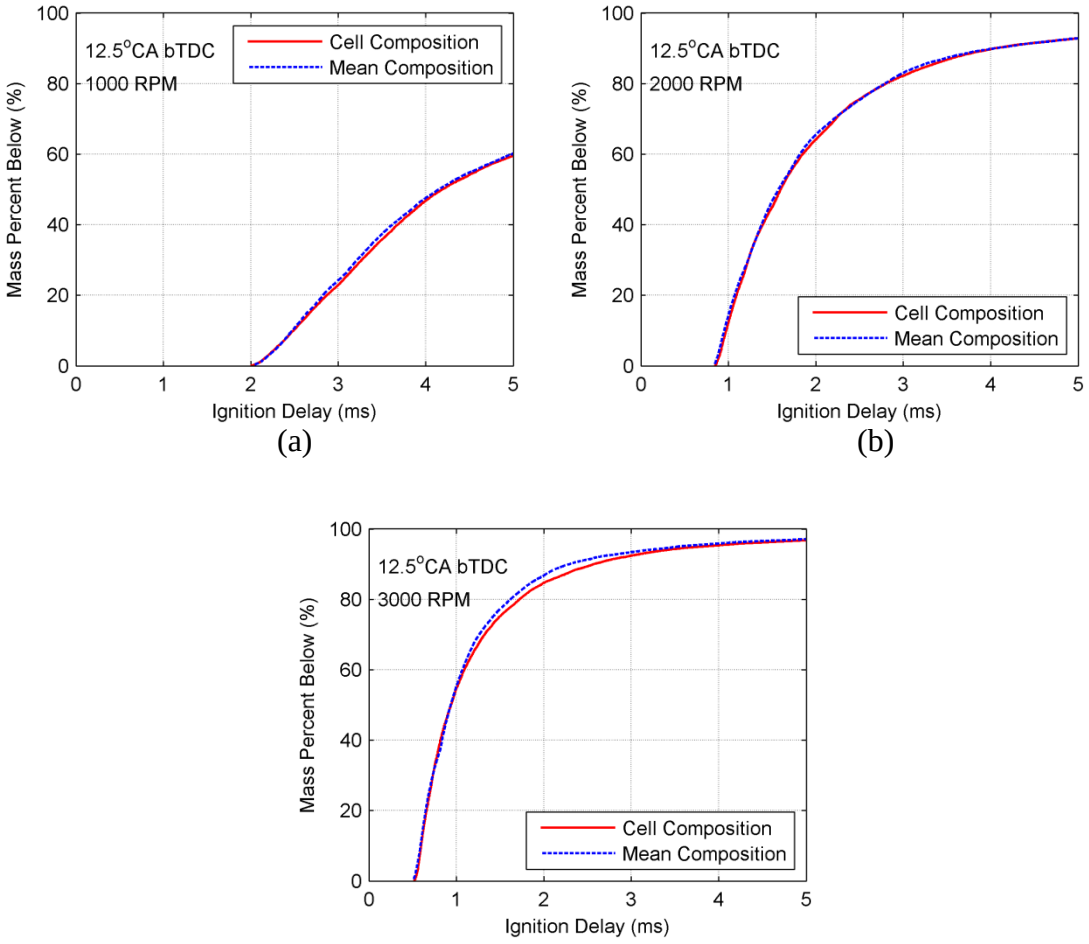

Figure 3.11 – Reaction space at 12.5° CA bTDC visualized in terms of the cumulative charge mass below a certain ignition delay, for the speed sweep computed from non-reacting CFD simulation with the cell level and mean composition at (a) 1000 RPM, (b) 2000 RPM, (c) 3000 RPM. The reactivity of the high speed case shows more sensitivity to compositional stratification.

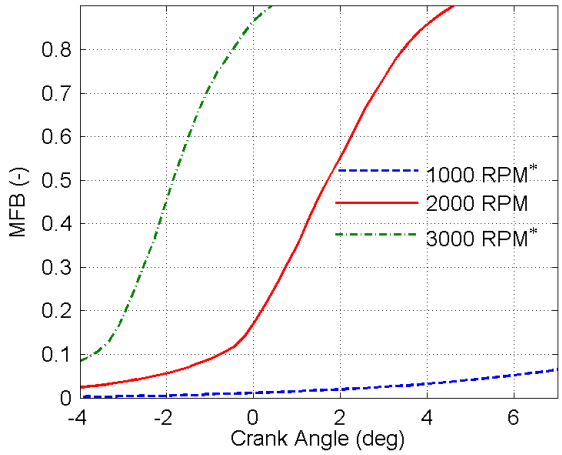

Figure 3.12 – Quasi-D model results for speed sweep with stratification initialized at 12.5° CA bTDC. All cases are simulated at 2000 RPM to remove the effect of different residence times (*).

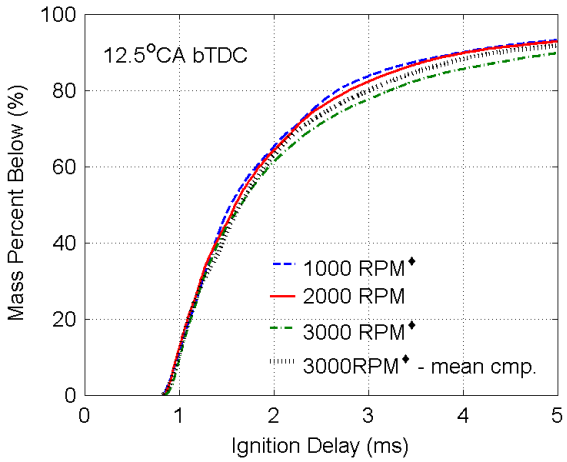

Figure 3.13 – Reaction space at 12.5° CA bTDC visualized in terms of cumulative charge mass below a certain ignition delay, for the speed sweep computed from non-reacting CFD simulations. Cell temperatures have been shifted for 1000 RPM and 3000 RPM case (♦) so that the hottest temperature for all cases is matched. The additional mean cmp. case corresponds to the 3000 RPM case simulated with the mean composition.

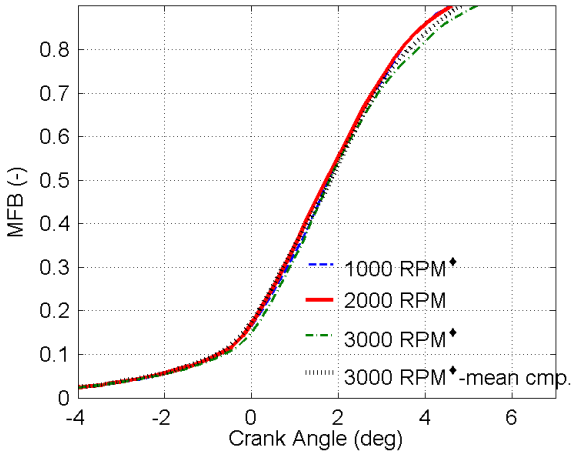

Figure 3.14 – Quasi-dimensional model results for the speed sweep with stratification initialized at 12.5° CA bTDC. All cases are simulated at 2000 RPM to remove the effect of different residence times. Additionally the temperatures for 1000 RPM and 3000 RPM case (♦) are shifted so that hottest temperature for all cases is matched. The additional mean cmp. case corresponds to the 3000 RPM case simulated with the mean composition.

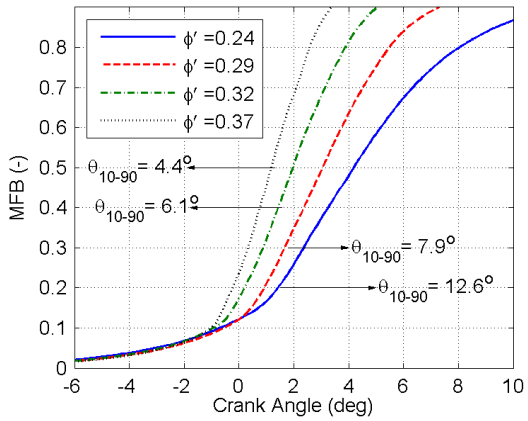

Figure 3.15 – Comparison of MFB curves from CFD for the ϕ' sweep in Table 3.2, with θ_{10} matched. The burn durations are shorter for richer ϕ' values.

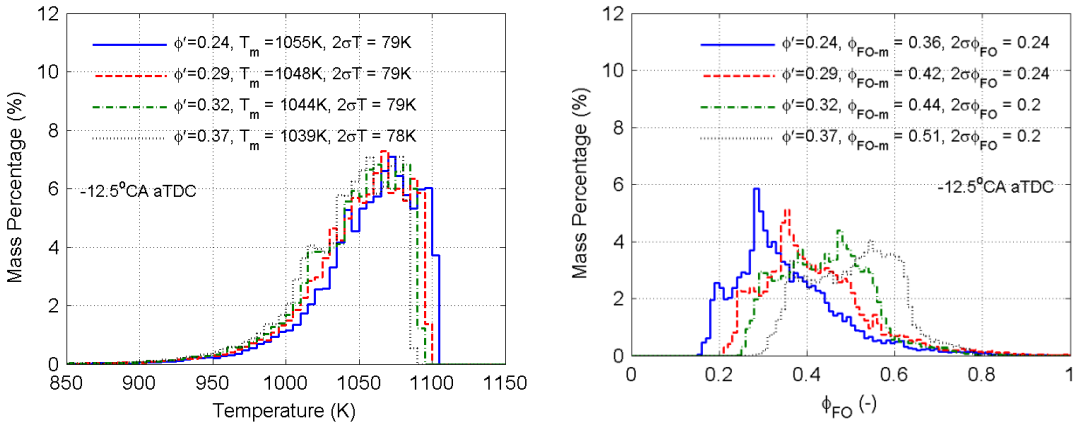

(b) (b)

Figure 3.16 – Mass distribution over (a) temperature and (b) ϕ_{FO} from non-reacting CFD simulations plotted at -12.5 ^{o}CA aTDC. The thermal and compositional stratification remains roughly the same.

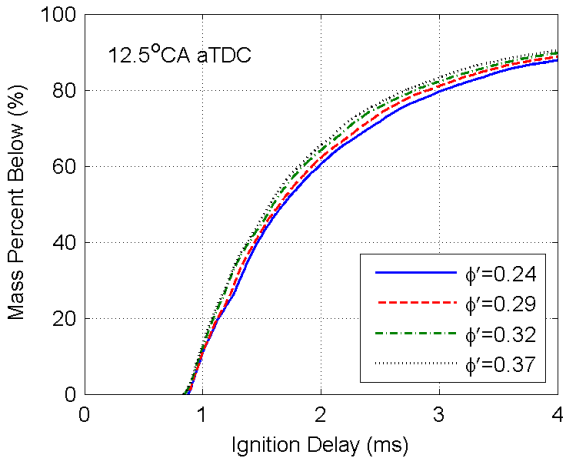

Figure 3.17 – Reaction space (at 12.5^{o} CA bTDC) visualized in terms of cumulative charge mass below a certain ignition delay, for ϕ' computed from non-reacting CFD cell temperature and composition. The higher ϕ' cases are more reactive.

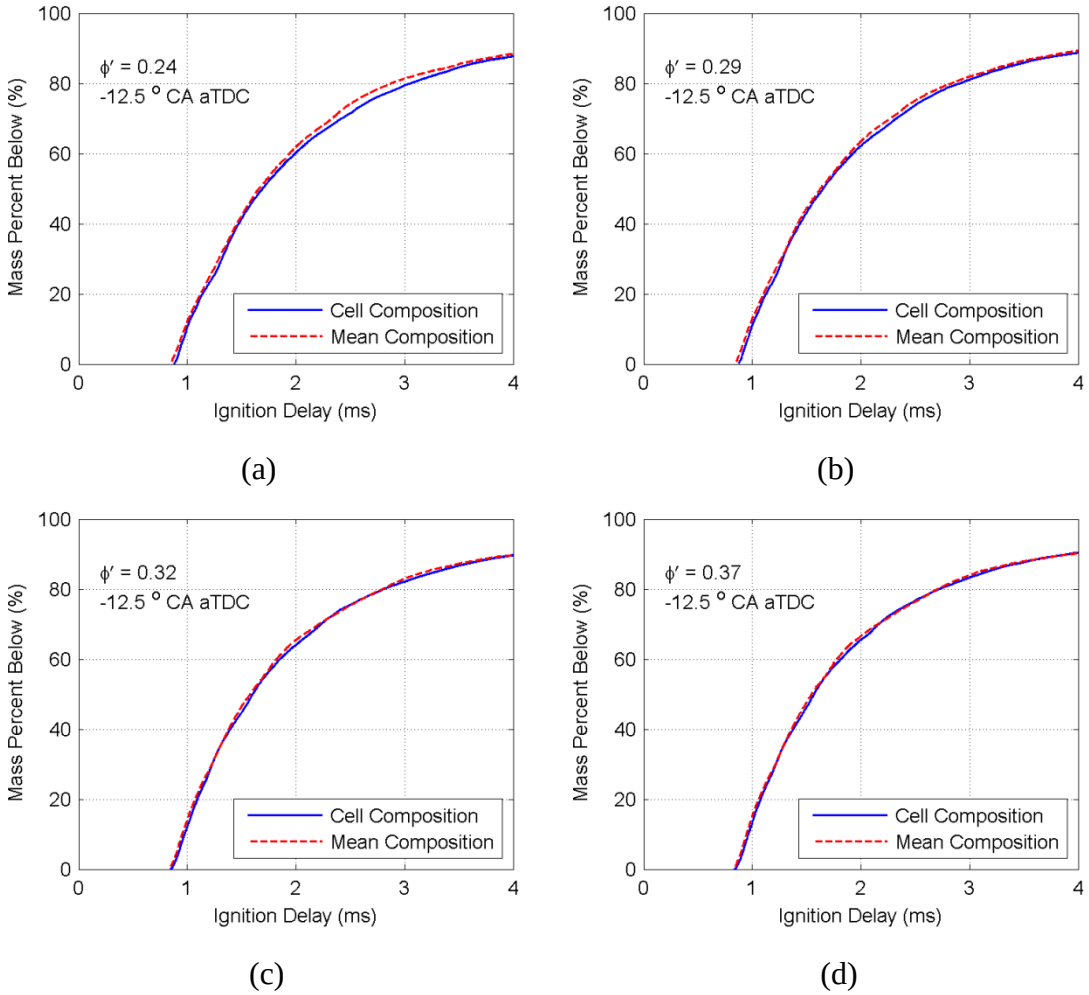

Figure 3.18– Reactivity distribution plotted as cumulative charge mass below a certain ignition delay using the cell level and mean composition, for (a) ϕ'= 0.24, (b) ϕ'= 0.29, (c) ϕ'= 0.32 and (d) ϕ'= 0.37. Compositional stratification has minimal affect on reactivity under the conditions studied.

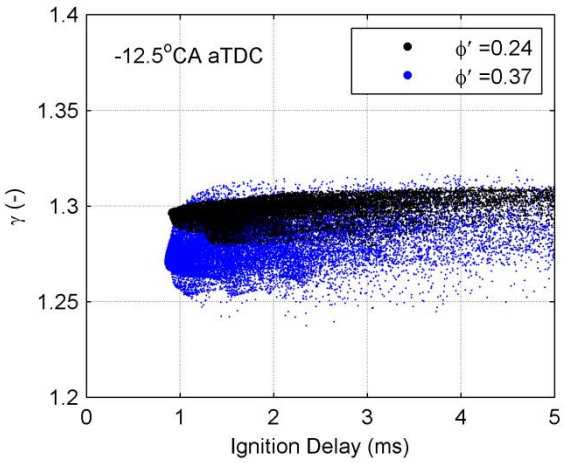

Figure 3.19 – Distribution of γ(at 12.5° CA bTDC) from non-reacting CFD simulation for the ϕ'sweep.

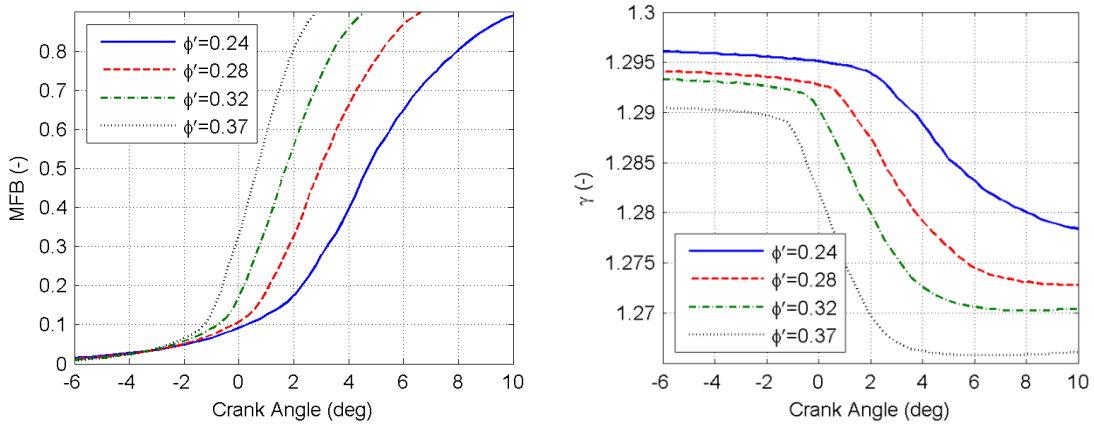

(c) (b)

Figure 3.20 – Quasi-dimensional model results for the ϕ' sweep; (a) Mass fraction burned curves, (b) variation of γ with progress of combustion.

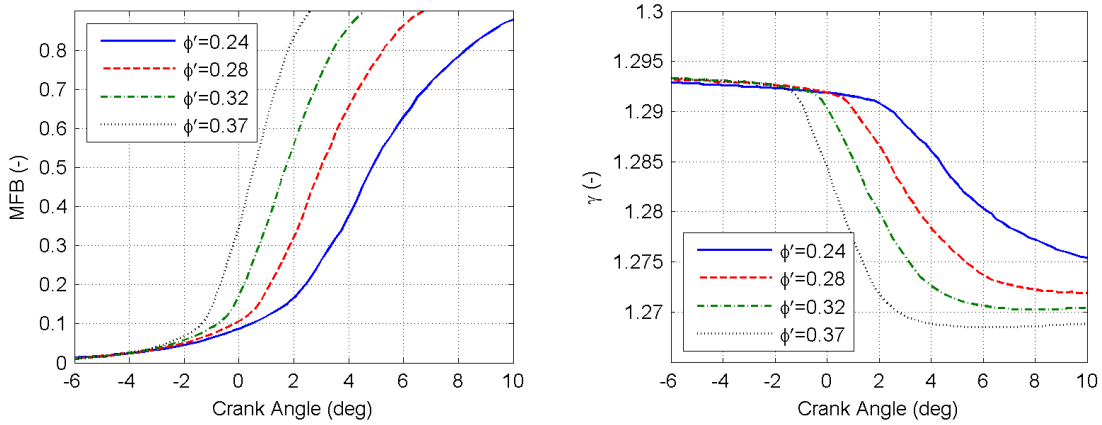

(a) (b)

Figure 3.21 – Quasi-D results for the ϕ'sweep with initial γ matched; (a) Mass fraction burned curves, (b) variation of γ with reaction progress.

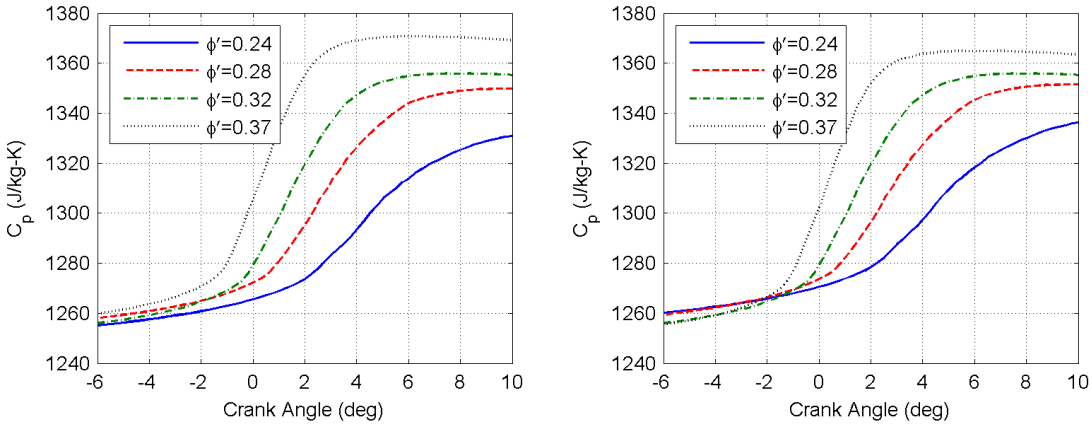

(a) (b)

Figure 3.22 – Variation of c_p with reaction progress (Quasi-D) for the ϕ'sweep with the initial c_p (a) unmatched and (b) matched to the baseline case.

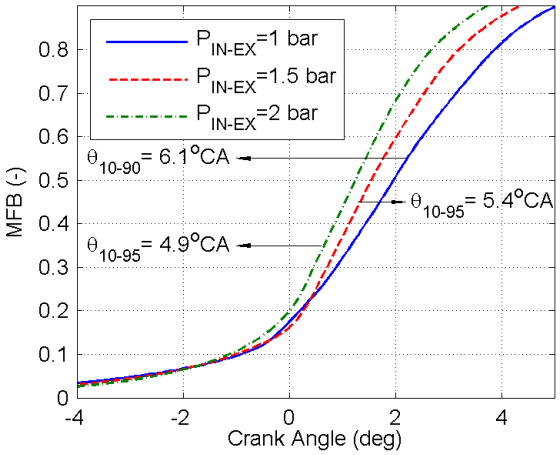

Figure 3.23 - Comparison of MFB curves from the CFD intake boost sweep in Table 3.3, with θ_{10} matched. The burn durations are shorter for greater boost.

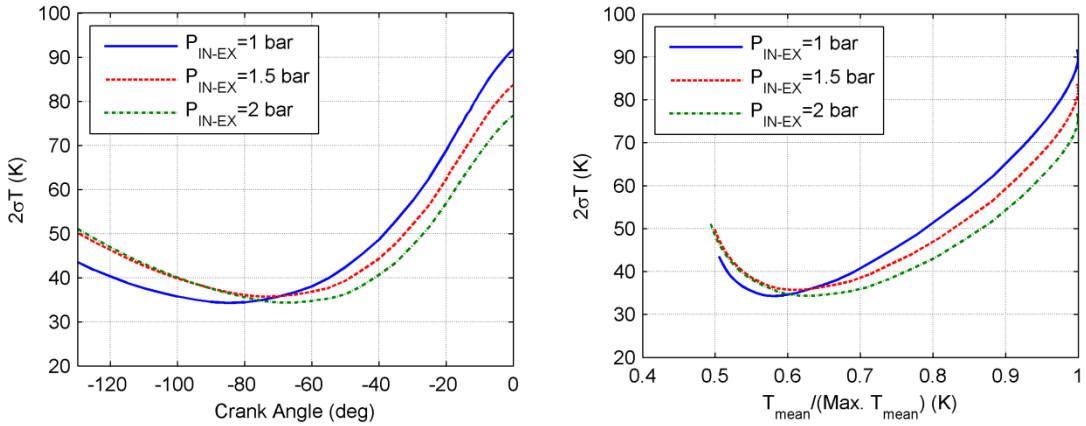

(a) (b)

Figure 3.24 - Evolution of thermal stratification from IVC to TDC (a) $2\sigma T$ plotted versus crank angle, the thermal stratification falls after IVC due to mixing until ~60° CA bTDC but rises from there to TDC due to dominant wall heat losses. The higher boost cases have a lower mean cylinder temperature due to which the wall heat loss driven thermal stratification is lower. This is explicitly clear when (b) $2\sigma T$ is plotted versus mean cylinder temperature normalized to the maximum mean temperature.

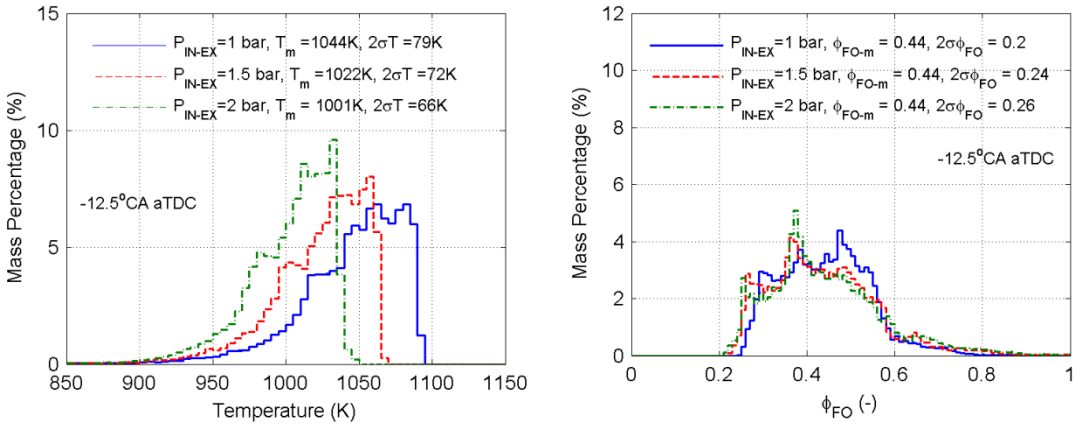

(a) (b)

Figure 3.25 – Mass distribution over (a) temperature and (b) ϕ_{FO} from non-reacting CFD simulations plotted at -12.5° CA aTDC. The thermal stratification decreases with boost and the compositional stratification remains roughly the same.

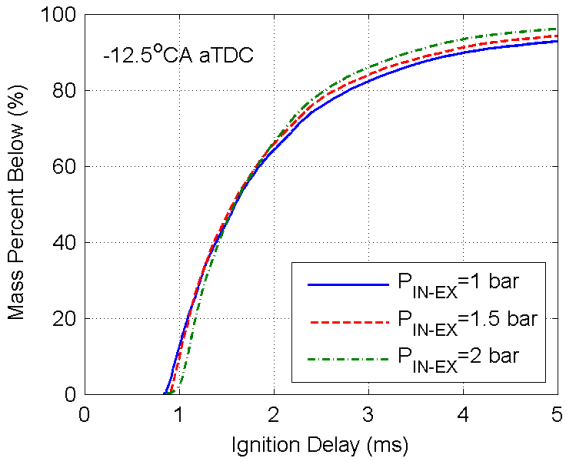

Figure 3.26 - Reaction space (at 12.5°CA bTDC) visualized in terms of the cumulative charge mass below a certain ignition delay, for the boost sweep computed from non-reacting CFD simulations with cell temperature and composition. Reactivity increases with boost pressure.

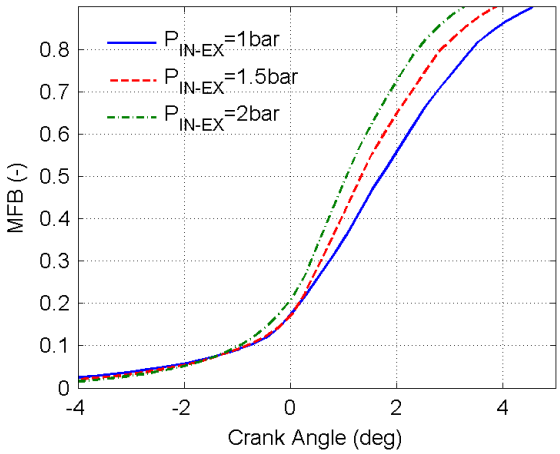

Figure 3.27 - Quasi-D model results for the boost pressure sweep with default stratification initialized at 12.5^{o} CA bTDC.

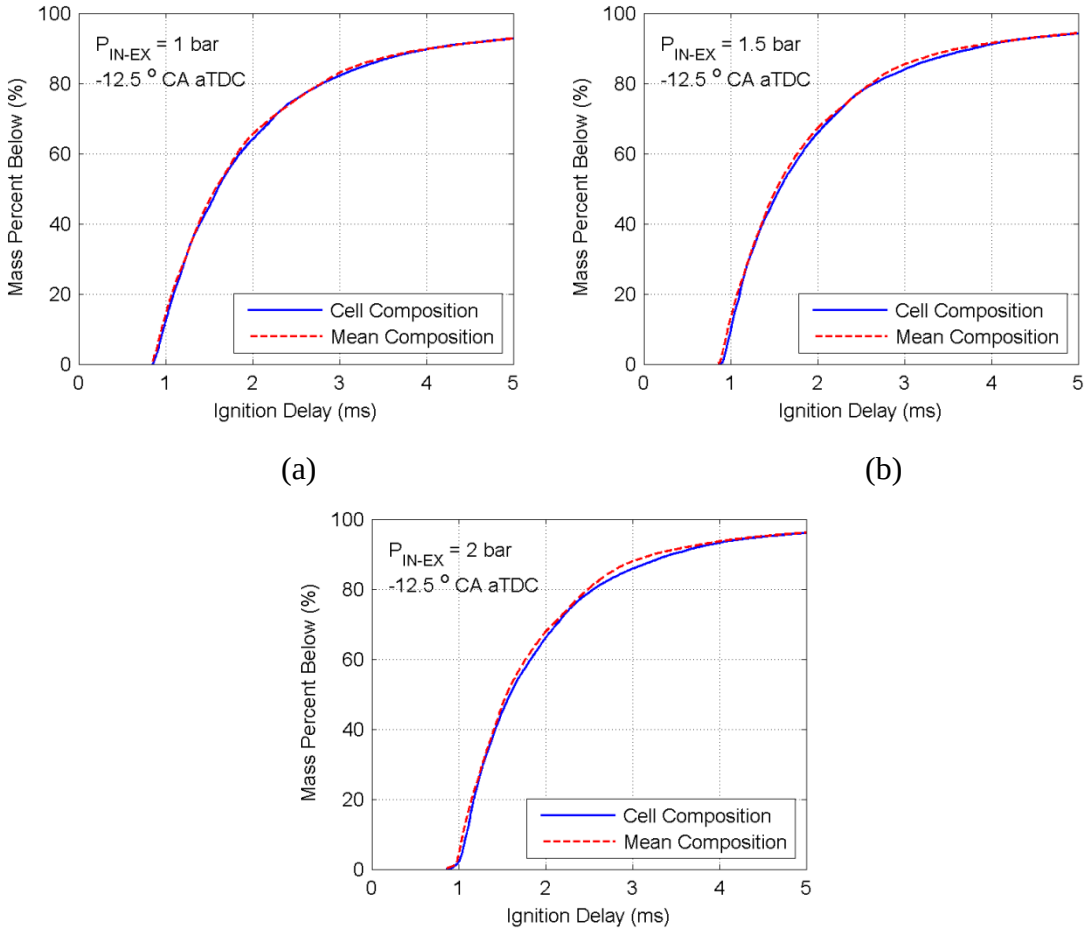

Figure 3.28 – Reaction space (at 12.5° CA bTDC) visualized in terms of the cumulative charge mass below a certain ignition delay computed with the cell level and mean composition for (a) P_{IN-EX}= 1 bar, (b) P_{IN-EX}= 1.5 bar and (c) P_{IN-EX}= 2 bar.

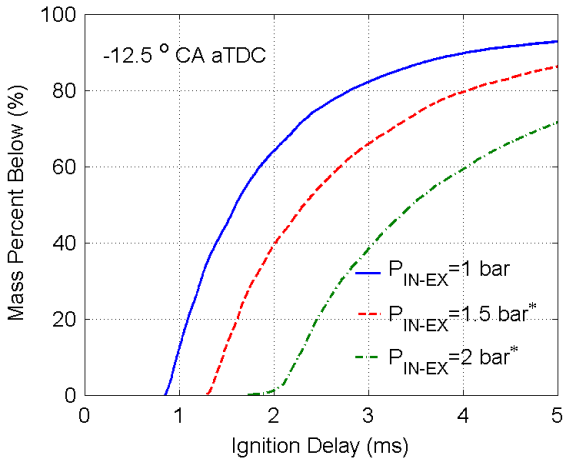

Figure 3.29 – Reaction space at 12.5° CA bTDC visualized in terms of the cumulative charge mass below a certain ignition delay, for the boost pressure sweep computed from non-reacting CFD simulations with cell temperature and composition and baseline pressure. Removing the pressure effect (*) makes the ignition delays for the original higher pressure cases longer.

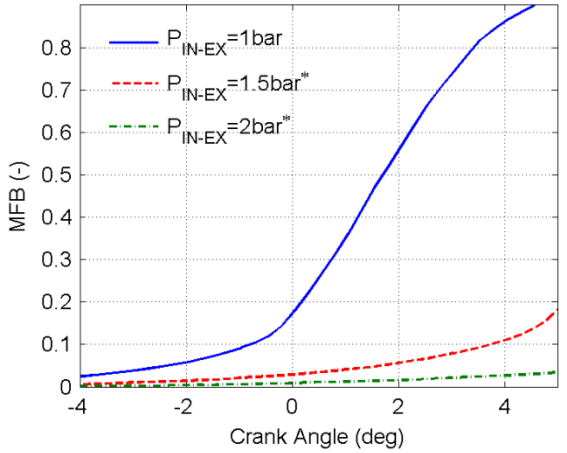

Figure 3.30 – Quasi-D model results for the boost pressure sweep initialized at 12.5° CA bTDC initialize with the baseline pressure to decouple the effect of pressure on combustion characteristics. Removing the pressure effect pushes the phasing later for the original higher pressure (*) cases.

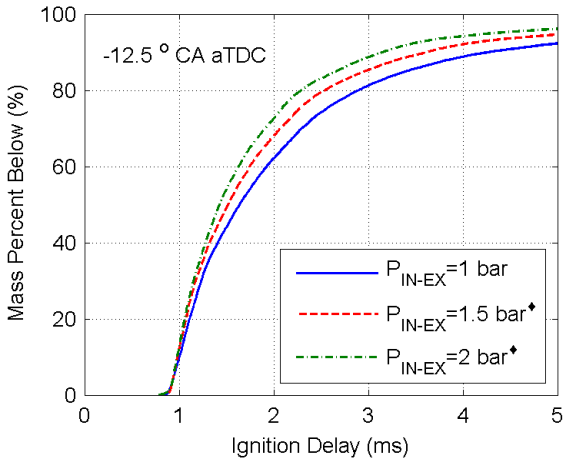

Figure 3.31 – Reaction space (at 12.5° CA bTDC) visualized in terms of the cumulative charge mass below a certain ignition delay, for the boost pressure sweep computed from non-reacting CFD simulations to isolate the effect of stratification. Ignition delays are computed with the baseline pressure, cell composition and leading edge of the temperature distribution matched to the baseline case. The original high pressure (♦) cases have a lower thermal stratification and higher reactivity.

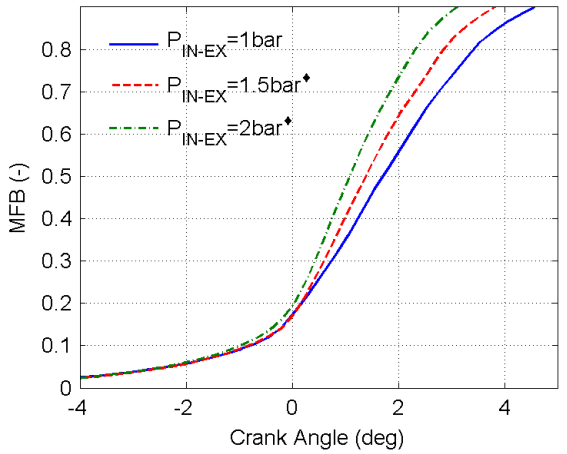

Figure 3.32 – Quasi-D model results for the boost pressure sweep initialized at 12.5° CA bTDC to isolate the effect of stratification on combustion. Cases initialized with baseline pressure and the hottest temperatures are matched to hottest temperature of baseline case. Original high pressure (♦) cases with lower thermal stratification burn faster.

3.6 References

1. Kalghatgi, G. T., Risberg, P., and Angstrom, H. E., "Partially Pre-Mixed Auto-Ignition of Gasoline to Attain Low Smoke and Low NOx at High Load in a Compression Ignition Engine and Comparison with Diesel Fuel," SAE Paper 2007-01-0006, 2006.
2. Dec, J.E., and Yang, Y., "Boosted HCCI for High Power without Engine Knock and Ultra-Low NOx Emissions – using Conventional Gasoline," SAE Int. J. Engines 3(3):750-767, 2010.
3. Johansson, T., Johansson, B., Tunestal, P., and Aulin, H., "HCCI Operating Range in a Turbo-charged Multi Cylinder Engine with VVT and Spray-Guided DI," SAE Paper 2009-01-0494, 2010.
4. Kulzer, A., Lejsek, D., and Nier, T., "A Thermodynamic Study on Turbocharged HCCI: Motivation, Analysis and Potential," SAE Int. J. Engines 3(3):733-749, 2010.
5. Urushihara, T., Hiraya, K., Kakuhou, A., and Itoh, T., "Expansion of HCCI Operating Region by the Combination of Direct Fuel Injection, Negative Valve Overlap and Internal Fuel Reformation," SAE Technical Paper 2003-01-0749, 2003.
6. Ravi, N., Hsien-Hsin L., Jungkunz, A. F., and Gerdes. J. C., "Modeling and control of exhaust recompression HCCI using split injection," American Control Conference (ACC), pp. 3797-3802. IEEE, 2010.
7. Rothamer, D. A., Snyder, J. A., Hanson, R. K., Steeper, R. R., and Fitzgerald, R. P., "Simultaneous imaging of exhaust gas residuals and temperature during HCCI combustion," Proceedings of the Combustion Institute, 32: 2869-2876, 2009.

8. Kodavasal, J., Lavoie, G. A., Assanis, D. N., & Martz, J. B., "The effects of thermal and compositional stratification on the ignition and duration of homogeneous charge compression ignition combustion," Combustion and Flame, 62(2), 451-461, 2015.

9. Kodavasal, J., "Effect of charge preparation strategy on HCCI combustion," PhD Thesis, The University of Michigan, Ann Arbor, MI, 2013.

10. Heywood, J., "Internal combustion engine fundamentals. McGraw-Hill series in mechanical engineering," McGraw-Hill, 1988.

11. Lawler B. J., "A methodology for assessing thermal stratification in an HCCI engine and understanding the impact of engine design and operating conditions," PhD Thesis, The University of Michigan, Ann Arbor, MI, 2013.

12. Kodavasal, J., Lavoie, G. A., Assanis, D. N., & Martz, J. B., "The effect of diluent composition on homogeneous charge compression ignition auto-ignition and combustion duration," Proceedings of the Combustion Institute, 35(3), 3019-3026, 2014.

13. He, X., Donovan, M. T., Zigler, B. T., Palmer, T. R., Walton, S. M., Wooldridge, M. S., and Atreya, A., "An experimental and modeling study of iso-octane ignition delay times under homogeneous charge compression ignition conditions," *Combustion and Flame*, Vol. 142, pp. 266-275, 2005.

CHAPTER 4

EFFECT OF INPUT ACTUATORS ON NVO-DI HCCI COMBUSTION: INJECTION TIMING, NEGATIVE VALVE OVERLAP AND INTAKE TEMPERATURE

HCCI heat release rate is a strong function of ignition timing [1]. The fuel injection timing during recompression (SOI), negative valve overlap (NVO) and intake temperature are common inputs used to control combustion phasing [2-6]. The effect of SOI and NVO on burn duration when ignition (θ_{10}) and total dilution (ϕ') are matched is unclear. In this chapter the effect of varying SOI and NVO on the thermal, compositional and reactivity stratification is analyzed. Additionally, the effect of changing θ_{10} on burn duration is also investigated. Chapter 3 and Chapter 4 provide insight into the changing reactivity stratification and its influence on HCCI combustion rates due to changing inputs and operating conditions. The reactivity stratification for all the sweeps has been presented at 12.5° CA bTDC which is chosen since it is the ignition location of the baseline NVO case described in Chapter 2.

4.1 Effect of Varying Start of Injection (SOI) on NVO-DI HCCI

The start of injection is changed in this study while changing the intake temperature and fueling rate to respectively hold θ_{10} and ϕ' constant at the baseline value. Table 4.1 summarizes the operating conditions for the SOI sweep. The

composition is held constant across the sweep to remove the global effects of these parameters. The second case is the baseline NVO case (Chapter 2) and the other two cases are SOI = 310°CA aTDC (immediately after EVC) and SOI = 430°CA aTDC (just before IVO). SOI is changed asymmetrically about 390°CA aTDC to cover the entire NVO duration. The mean composition is the same and combustion phasing θ_{10} is matched to the baseline by changing the intake manifold temperature, which varies by 8°C during the sweep.

The temperature during NVO is different for the different SOI timings even though NVO reactions are deactivated (for all simulation until Chapter 7). This is attributed to charge cooling and changing γ due to changing composition of mixture due to fuel injection [7]. Figure 4.1 shows the mean charge temperature during NVO for the SOI sweep. Across the three SOI cases, injection is accompanied by significant drop in temperature due to charge cooling. The mixture γ after injection is higher (γ = 1.3) than before injection (γ = 1.29) in all the cases. However different SOI timings affect the amount of compression or expansion with the changed γ which affects the temperature. For the early SOI case (SOI = 310°CA aTDC) the charge is cooled earlier and compression at a higher γ is not able to offset the cooling, resulting in lower temperatures at end of expansion. For injection in expansion, higher γ leads to lower temperatures due to more efficient expansion. However as seen in Figure 4.1 the charge cooling dominates the γ effect here as well. The temperature for the late SOI case (SOI = 430°CA aTDC) falls quickly to match the temperature of the baseline case by end of expansion. Figure 4.2 shows the MFB data from CFD versus crank angle for the SOI sweep. The three curves are nearly matched through combustion with minor differences in burn duration (θ_{10-90} ~ 6.1°CA).

4.1.1 Analysis of reaction space at 12.5°CA bTDC

Figure 4.3 visualizes the mass distribution over temperature and ϕ_{FO} for the SOI cases from non-reacting CFD simulations at -12.5°CA aTDC. The thermal stratification in Figure 4.3(a) is nearly constant throughout the sweep. The compositional stratification depicted in Figure 4.3(b) shows that the early SOI (310°CA aTDC) case has relatively lower stratification compared to the baseline (390°CA aTDC) case and late SOI (430°CA aTDC) cases. This is mainly due to the longer time available for mixing. The cumulative distribution of reactivity visualized at 12.5°CA bTDC is presented in Figure 4.4. Since the curves are nearly matched it is inferred that reactivity is also approximately matched over the entirety of the charge. This results in the nearly identical mass fraction burned curves in Figure 4.2.

Figure 4.5 aims to confirm whether or not thermal stratification dominates the reactivity stratification for the SOI sweep. Here, the ignition delays have again been computed in every CFD cell with the cell temperature and mean composition of the cylinder. It is clear that the distributions do not show a noticeable change using the cell level or mean composition across the sweep, indicating that reactivity stratification is largely driven by the thermal stratification. Hence similar thermal stratification results in the similar burn curves for the SOI sweep.

4.2 Effect of Varying Negative Valve Overlap (NVO) on NVO-DI HCCI

Table 4.2 summarizes the operating conditions for the NVO sweep, where the third case is the baseline NVO case (157° NVO) from Table 4.2. The total dilution (ϕ') and combustion phasing θ_{10} of the other cases are held constant at the baseline NVO value by respectively changing the fueling and intake manifold temperature. Figure 4.6 shows the MFB data versus crank angle from CFD for the NVO sweep. The curves are

aligned until $\theta_{10,}$ with small differences later in combustion. The burn duration (θ_{10-90}) is approximately 6.1°CA for the five cases.

4.2.1 Analysis of reaction space at 12.5°CA bTDC

Figure 4.7 visualizes the mass distribution over temperature from non-reacting CFD simulations at 12.5°CA bTDC for the NVO sweep. There is small variation of thermal stratification and the mean temperature changes by 21 K (from 1031 K to 1052 K) as shown in Figure 4.7(a). The compositional stratification increases with increasing NVO and the mean composition becomes slightly rich (from ϕ_{FO} = 0.4 to ϕ_{FO} = 0.46) as shown in Figure 4.7(b).

The cumulative distribution of reactivity is visualized at 12.5°CA bTDC in Figure 4.8(a). The high NVO cases have higher temperatures, greater ϕ_{FO} and greater charge stratification. $2\sigma T$ ranges from 74 K to 81 K and $2\sigma\phi_{FO}$ from 0.14 to 0.28 respectively. The highest reactivity is matched between all cases, as shown in Figure 4.8(a). The curves seem to deviate initially (1-3 ms) but return back to match each other for $\tau >$ 3.5ms.

The slight variations in the shape of the mass fraction burned curves are due to the changing slope of the cumulative reactivity distribution of charge. This is easier to observe by plotting the mass distribution from the CFD domain at a certain ignition delay shown in Figure 4.8(b). The cases with NVO of 157°CA to 197°CA have more mass at the shortest ignition delays (0.4 ms < τ < 1.2 ms), which results in faster combustion relative to the low NVO cases (NVO's of 117°CA and 137°CA). On the other hand the cases with NVO's 117°CA and 137°CA have more mass at longer ignition delays (1.2 ms < τ <2.25 ms) compared to the higher NVO cases. Hence during the sequential auto-ignition of the charge the low NVO charges burn slowly initially but then faster later in the combustion process, resulting in similar overall combustion durations.

Figure 4.9 analyses the importance of compositional stratification compared to the thermal stratification for each case of the NVO sweep. Here, the ignition delays have again been computed in every CFD cell with the cell temperature and mean cylinder composition in addition to using the individual cell compositions. The similarity of reactivity for either composition demonstrate that the reactivity distributions insensitive to using mean or local composition, which implies that thermal stratification is the dominant factor affecting the combustion rate for the NVO sweep.

4.3 Effect of Varying Intake Temperature on NVO-DI HCCI

Table 4.3 summarizes the operating conditions for the intake manifold temperature sweep. The intake temperature is changed by ±40°C compared to the baseline (Chapter 2), and the injected fuel quantity is varied to hold the total dilution (ϕ') constant at the baseline value. The mean composition remains nearly constant in terms of ϕ_{FO}, $\chi_{O_2}$and RGF. Figure 4.10 plots the reaction progress against crank angle from the CFD simulations. The ignition timing advances as the intake temperature is increased from T_{IN} = 66° C (θ_{10} = 6° CA aTDC) to T_{IN} = 146°C (θ_{10}= −7.4°CA aTDC). Correspondingly the burn duration reduces from θ_{10-90} = 16.5°CA to θ_{10-90} = 4°CA respectively.

4.3.1 Analysis of reaction space at 11.5°CA before θ_{10}

Figure 4.11 visualizes the mass distribution over temperature and ϕ_{FO} for the intake temperature sweep at 11.5°CA before θ_{10} which is selected to remain consistent with the pre-ignition location of the baseline case (since 12.5°CA bTDC is 11.5°CA before θ_{10} = 1°CA bTDC). The thermal and compositional stratification at the fixed crank angle before θ_{10} remains approximately the same between cases as seen in Figure 4.11(a) and Figure 4.11(b) respectively.

The cumulative distribution of reactivity visualized at 11.5°CA bTDC is shown in Figure 4.12. The ignition delays for the T_{IN} = 146°C case are longer than the ignition delays for the baseline case (T_{IN} = 106°C) and T_{IN} = 66°C case has ignition delays shorter than the baseline case. Despite the similar peak temperatures at 11.5°CA bTDC, the pressures used to calculate the reactivity for the three cases differ significantly since they are calculated at different crank angles during compression. Thus later crank angles (low T_{IN}) have greater pressures and higher peak reactivity. Figure 4.13 aims to assess the importance of compositional stratification in determining charge reactivity for the intake temperature sweep. The ignition delays have been computed in every CFD cell with the cell temperature and mean composition of the cylinder to again calculate the cumulative reactivity stratification. This curve has been overlaid with the cumulative reactivity stratification calculated with the cell temperature and composition. The distributions don't show a noticeable change using the cell level or mean composition, indicating that the compositional stratification has little effect on the reactivity for the intake temperature sweep.

4.3.2 Decoupling the combustion timing effect on burn duration

In this section the combustion timing effect on burn duration is removed and the effect of compositional and thermal stratification and differing pressure is maintained. Figure 4.14 shows the reaction progress results from the Quasi-D model initialized at the pre-ignition angle 11.5°CA before θ_{10} for the intake temperature sweep. The trends are similar to reacting CFD simulation results. To remove the combustion timing effect the Quasi-D model is initialized at 12.5°CA bTDC for all cases using the temperature, pressure and composition at 11.5°CA before θ_{10}. Figure 4.15 shows the Quasi-D model results in terms of MFB plotted versus crank angle. The three curves are much closer to each other compared to Figure 4.14 but the lower T_{IN} case is advanced and the higher T_{IN}

case is retarded. This is because although all cases are initialized at the same crank angle with almost the same temperature and composition, the pressure of the lower T_{IN} case is higher and hence the charge is more reactive and the converse is true for the higher T_{IN} case. This MFB trend matches the cumulative reactivity distribution in Figure 4.12.

The Quasi-D model is simulated again starting at 12.5°CA bTDC, with the temperature and composition from each cell at 11.5° CA before θ_{10} and with the pressure of the baseline case at 12.5° CA. As seen in Figure 4.16 the cumulative distribution of the three cases is matched. Similarly, the burn profiles from the Quasi-D model displayed in Figure 4.17 are matched. Hence, the combustion durations are matched when the pressure and combustion timing effect is removed from the results. This indicates that pressure and the combustion timing, not differences in thermal or compositional stratification between the three cases, are the main factor affecting HCCI combustion rates in this sweep.

4.4 Summary and conclusions

In this chapter the effect of changing SOI, NVO and intake temperature on burn profile are explained by means of the reactivity stratification. In case of SOI and NVO sweeps the combustion timing θ_{10} is held constant by varying the intake temperature. For the intake temperature sweep the θ_{10} is allowed to vary. The ϕ' is also held constant in each sweep to keep the total dilution constant.

The thermal stratification does not change with changing SOI. The compositional stratification increases with later injection timings which could be due to the shorter time available for mixing. Compositional stratification has little effect on charge reactivity during the SOI sweeps. The burn duration does not change since the thermal stratification remains the same and the θ_{10} is matched. Although the recompression reactions are deactivated (except in Chapter 7) charge cooling and γ effects due to injection are

competing effects that determine the charge temperature at the end of expansion. The charge cooling effect dominates in this case due to relatively small change in γ of mixture (γ = 1.29 to γ = 1.3) due to injection.

For the NVO sweep, the compositional stratification and mean ϕ_{FO} increases slightly with increasing NVO. The intake temperature is reduced to maintain $\theta_{10}$with increasing NVO. The compositional stratification has little effect on charge reactivity compared to the thermal stratification. The thermal stratification does not change much. There are minor differences in the shape of the burn profile across the sweep but the θ_{10-90} duration remains the same.

Increasing the intake temperature advances the θ_{10} ignition timing which greatly shortens burn duration. The thermal and compositional stratification at 11.5^{o} CA before θ_{10} remains the same between all the cases. Removing the combustion timing effect brings the mass fraction burn curves closer with the lower intake temperature case being more advanced. This is because although the Quasi-D model is initialized at the same crank angle the low T_{IN} case starts at a higher pressure and burns faster while the converse is true for the high T_{IN} case. When the effect of differing pressures is also removed the mass fraction burned curves are matched for the three cases. Hence changing pressure and combustion timing are the main factors affecting combustion for the intake temperature sweep.

Table 4.1 – Operating conditions for SOI sweep

Speed (RPM)	2000	2000	2000
NVO (^{o}CA)	157	157	157
SOI (^{o}CA aTDC)	**310**	**390**	**430**
Intake Temperature (^{o}C)	109	106	116
Fueling Rate (mg/cyc)	9.25	9.25	9.25
$\boldsymbol{\phi_{FO}}$	0.44	0.44	0.44
ϕ	0.58	0.58	0.58
ϕ'(-)	0.32	0.32	0.32
RGF (%)	43	43	43
$\boldsymbol{\chi_{O2}}$ (%)	15.16	15.15	15.18
$P_{IN\text{-}EX}$ (bar)	1	1	1

Table 4.2 – Operating conditions for NVO sweep

Speed (RPM)	2000	2000	2000	2000	2000
NVO (^{o} CA)	**197**	**177**	**157**	**137**	**117**
SOI (^{o}CA aTDC)	390	390	390	390	390
Intake Temperature (^{o}C)	63	90	106	124	143
Fueling Rate (mg/cyc)	8.7	9.1	9.25	9.4	9.8
$\boldsymbol{\phi_{FO}}$	0.47	0.47	0.44	0.41	0.4
ϕ	0.62	0.61	0.58	0.54	0.52
ϕ'	0.32	0.32	0.32	0.32	0.32
RGF (%)	51.0	49.3	43	35.9	30.5
$\boldsymbol{\chi_{O2}}$ (%)	14.3	14.1	15.1	16	16.7
$P_{IN\text{-}EX}$ (bar)	1	1	1	1	1

Table 4.3 – Operating conditions for intake temperature sweep

Speed (RPM)	2000	2000	2000
NVO (^{o}CA)	157	157	157
SOI (^{o}CA aTDC)	390	390	390
Intake Temperature (^{o}C)	**66**	**106**	**146**
Fueling Rate (mg/cyc)	9.6	9.25	8.8
$\boldsymbol{\phi_{FO}}$	0.43	0.44	0.45
ϕ	0.58	0.58	0.59
ϕ'(-)	0.32	0.32	0.32
RGF (%)	42	43	43
$\boldsymbol{\chi_{O2}}$ (%)	15.3	15.1	15.2
$P_{IN\text{-}EX}$ (bar)	1	1	1

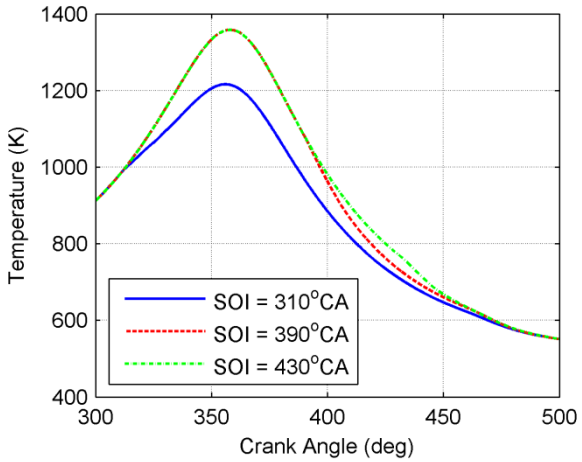

Figure 4.1 – Mean cylinder temperature from CFD during NVO for the SOI sweep in Table 4.1. Temperatures are different for different injection events but match during the intake due to temperature compensation to match θ_{10}.

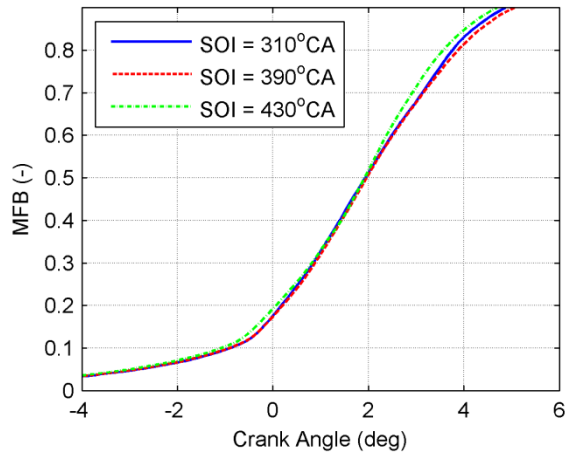

Figure 4.2 – Comparison of MFB curves from CFD for the SOI sweep in Table 4.1. Burn duration remains nearly the same.

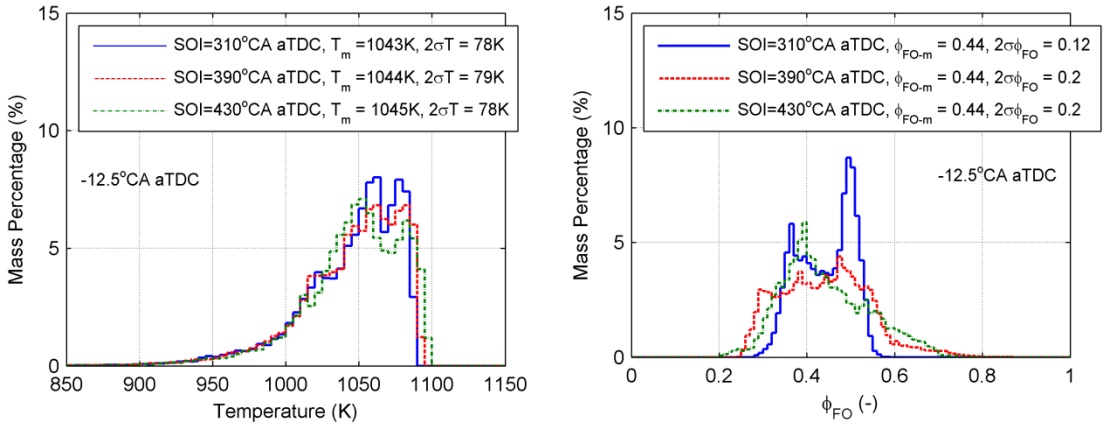

(a) (b)

Figure 4.3 – Mass distribution over (a) temperature and (b)ϕ_{FO} from non-reacting CFD simulations plotted at -12.5°CA aTDC. The thermal stratification remains the same whereas compositional stratification increases with later injection timing.

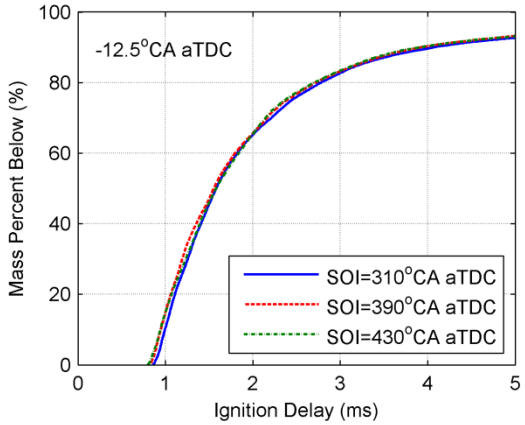

Figure 4.4 – Reaction space (at 12.5°CA bTDC) visualized in terms of cumulative charge mass below a certain ignition delay, for the ϕ' sweep computed from non-reacting CFD simulation

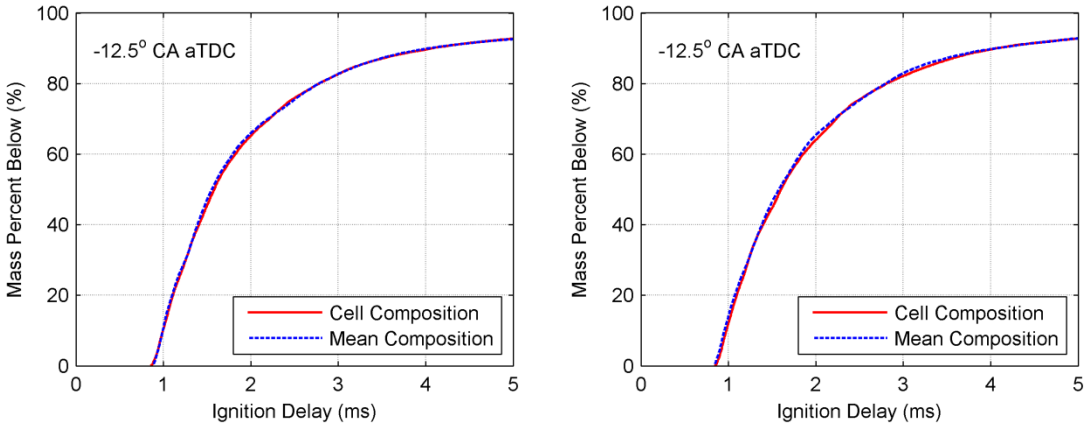

(b)

(b)

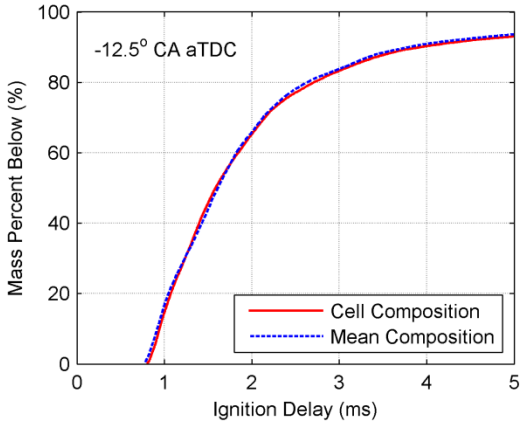

(c)

Figure 4.5– Reaction space (at 12.5°CA bTDC) visualized in terms of cumulative charge mass below a certain ignition delay for the SOI sweep, computed from non-reacting CFD with cell level and mean composition (a) SOI= 310°CA aTDC, (b) SOI= 390°CA aTDC, and (c) SOI= 430°CA aTDC.

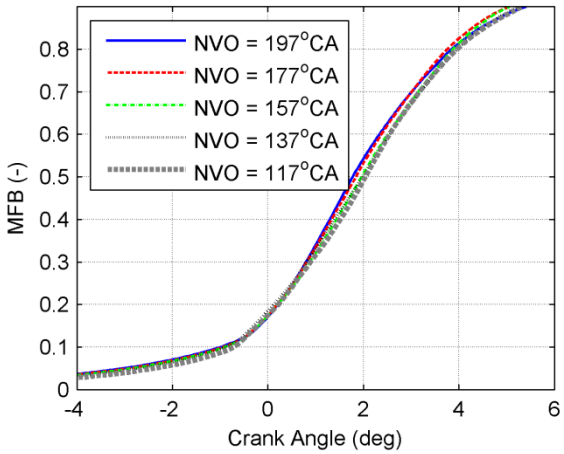

Figure 4.6 – Comparison of MFB curves from CFD NVO sweep in Table 4.2. θ_{10}being matched the burn durations are nearly the same.

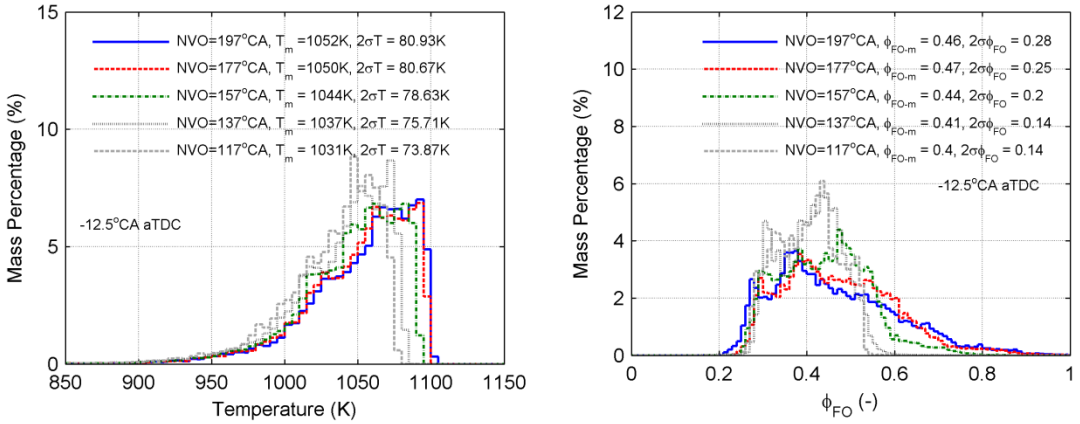

(d) (b)

Figure 4.7 – Mass distribution over (a) temperature and (b)$\phi_{FO}$from non-reacting CFD simulations plotted at -12.5°CA aTDC. The thermal stratification remains the same whereas compositional stratification increases with larger NVOs.

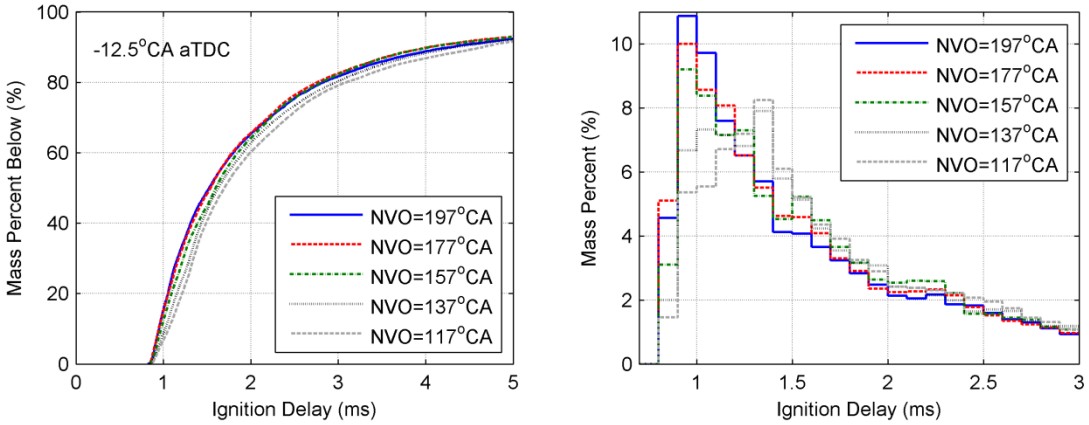

(a) (b)

Figure 4.8 – Reaction space (at 12.5°CA bTDC) visualized in terms of (a) cumulative charge mass below a certain ignition delay and (b) mass at a certain ignition delay, for the NVO sweep computed from non-reacting CFD simulations.

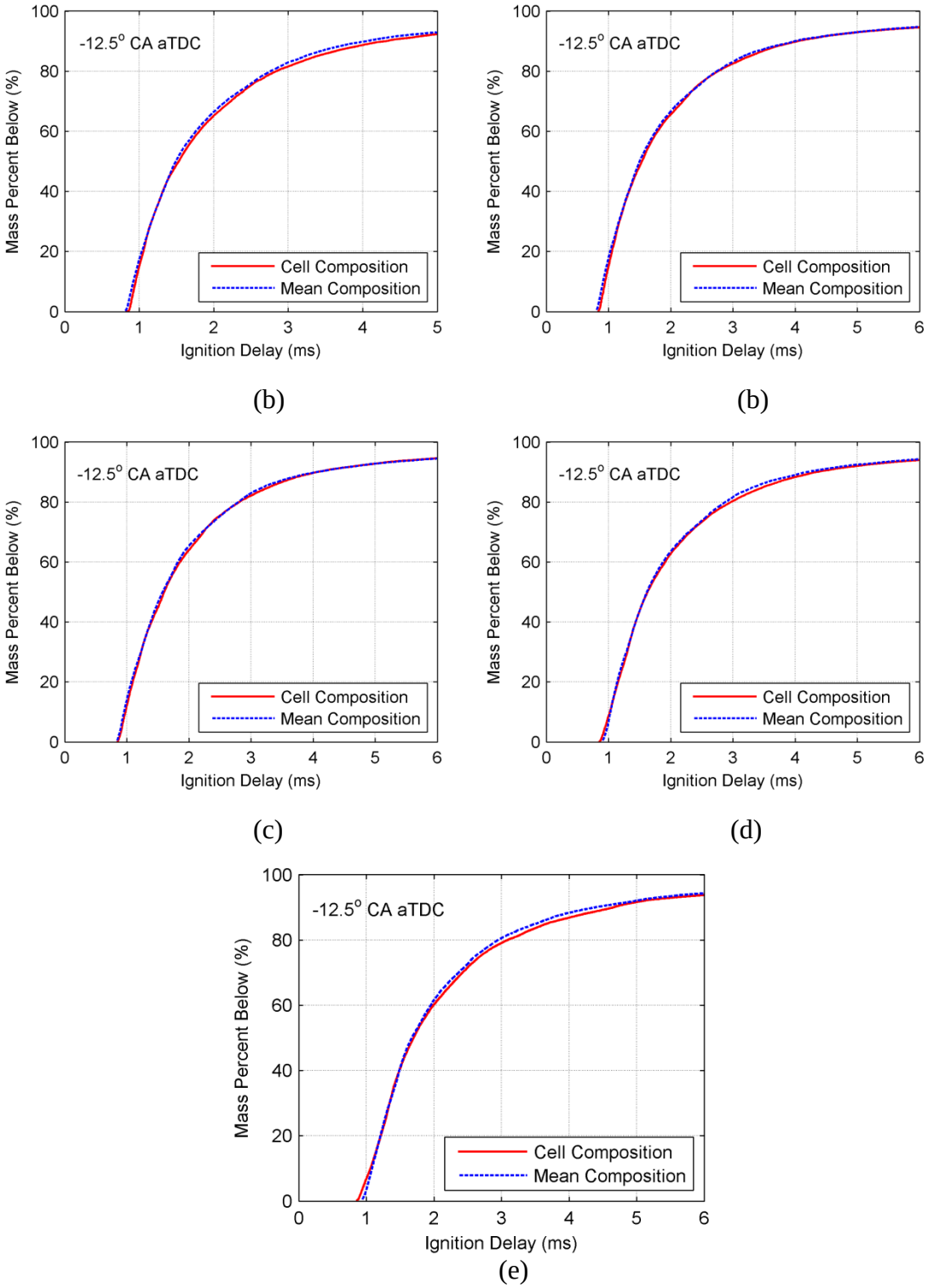

Figure 4.9 – Reaction space (at 12.5°CA bTDC) visualized in terms of cumulative charge mass below a certain ignition delay computed with the cell level and mean composition for (a) NVO = 197°CA, (b) NVO = 177°CA, (c) NVO = 157°CA, (d) NVO = 137°CA and (e) NVO = 117°CA.

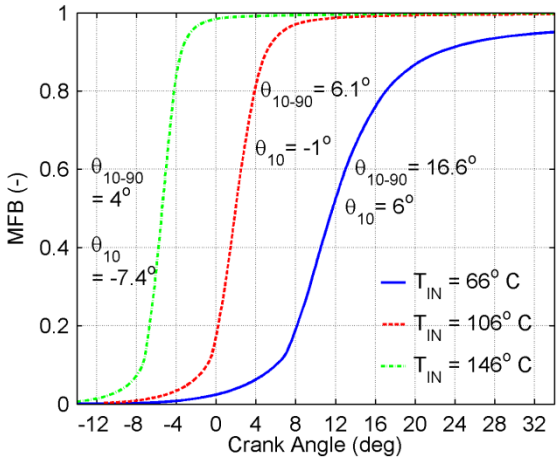

Figure 4.10 – Comparison of MFB curves from CFD for intake temperature sweep in Table 4.3.

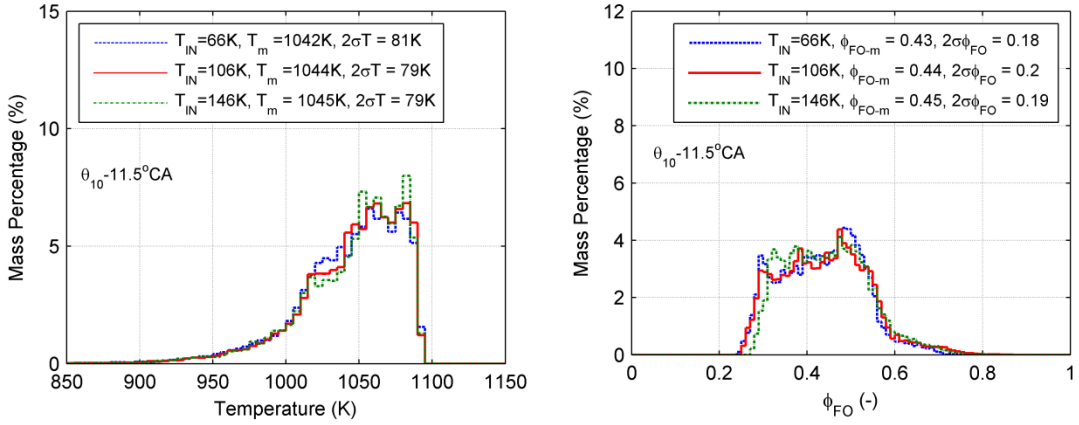

(a) (b)

Figure 4.11 – Mass distribution over (a) temperature and (b)$\phi_{FO}$from non-reacting CFD simulations plotted at 11.5°CA aTDC before θ_{10}. The thermal and ϕ_{FO} stratification remains roughly the same for the intake temperature sweep.

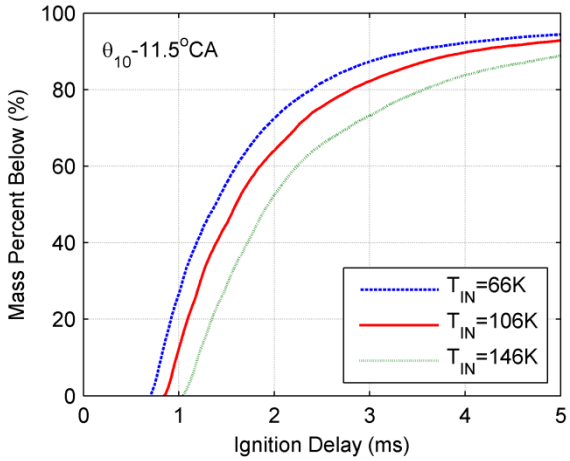

Figure 4.12 – Reaction space (at 11.5°CA before θ_{10}) visualized in terms of cumulative charge mass below a certain ignition delay, for the intake temperature sweep computed from non-reacting CFD simulations with cell temperature and composition.

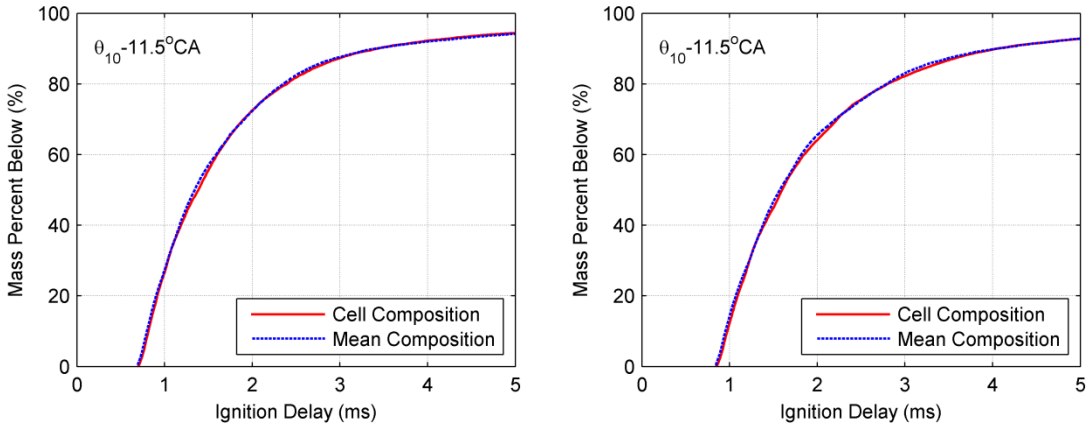

(a)

(b)

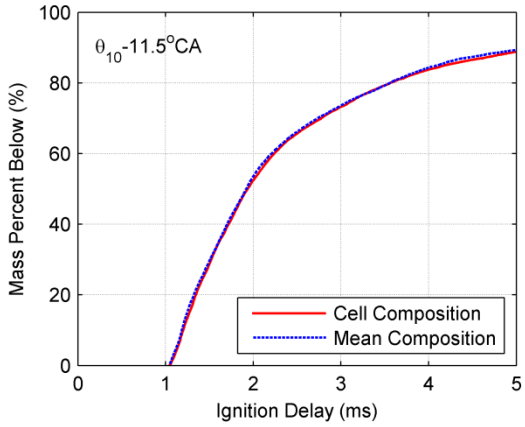

(c)

Figure 4.13 – Reaction space (at 12.5° CA bTDC) visualized in terms of cumulative charge mass below a certain ignition delay computed with the cell level and mean composition for (a) T_{IN}= 66°C, (b) T_{IN}= 106°C and (c) T_{IN}= 146°C

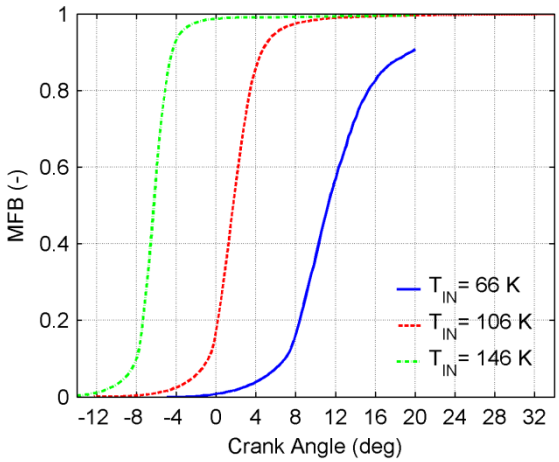

Figure 4.14 – Quasi-D model results for the intake temperature sweep initialized at 11.5°CA before θ_{10} show trends similar to CFD.

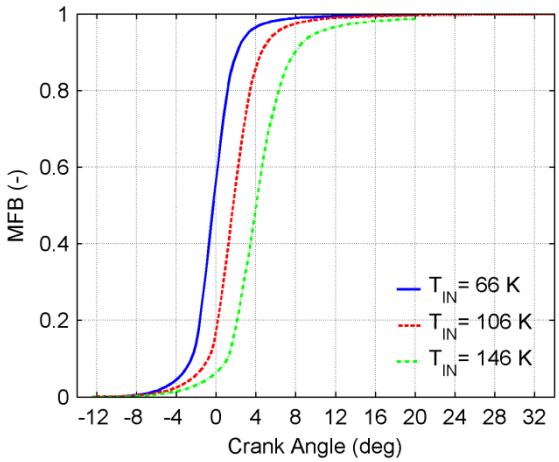

Figure 4.15 – Quasi-D model results for the intake temperature sweep initialized at 12.5°CA bTDC (θ_{ign} of the baseline case). These MFB curves match the cumulative reactivity distribution seen in Figure 4.12.

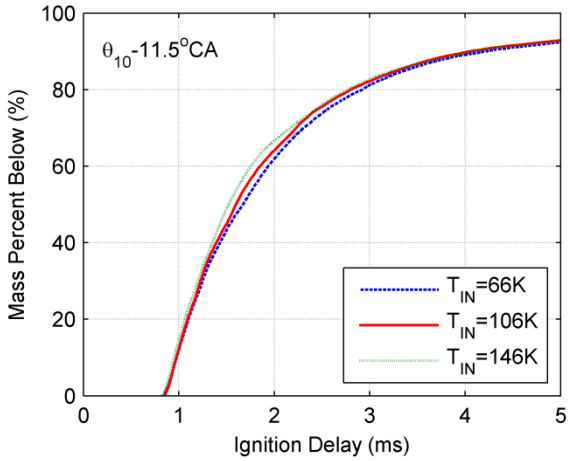

Figure 4.16 –Reaction space (at 11.5°CA before θ_{10}) visualized in terms of cumulative charge mass below a certain ignition delay, for the intake temperature sweep computed from non-reacting CFD simulations with cell temperature and composition while using pressure for baseline case. Removing the θ_{10}timing effect the cumulative reactivity distributions collapse.

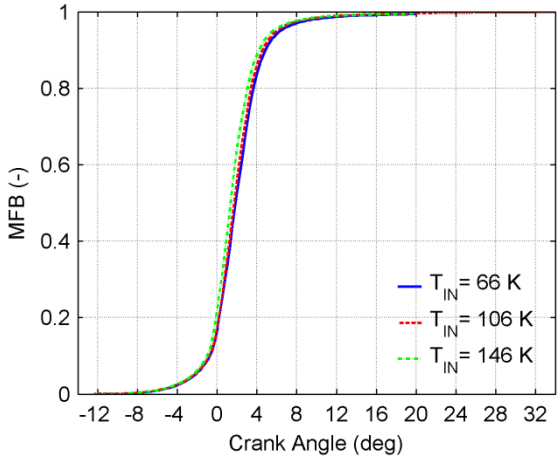

Figure 4.17 – Quasi-D model results for boost pressure sweep initialized at 12.5° CA bTDC to isolate the effect to thermal and compositional stratification on combustion. Cases initialized at the same crank angle have the θ_{10}matched and nearly the same burn profiles.

4.5 References

1. Sjöberg, M., Dec J. E., Babajimopoulos, A., and Assanis, D. N., "Comparing enhanced natural thermal stratification against retarded combustion phasing for smoothing of HCCI heat-release rates," SAE Paper, 2004-01-2994, 2004.

2. Milovanovic N., Chen R., and Turner J., "Influence of the Variable Valve Timing Strategy on the Control of a Homogeneous Charge Compression Ignition Engine", SAE Paper 2004-01-1899, 2004.

3. Ravi N., Liao, H., JungKunz, A., and Gerdes,. C., "Modeling and control of exhaust recompression HCCI using split injection", 972-1-4244-7427-1/10, 2010 American Control Conference, 2010.

4. Hellström, E., Larimore, J., Jade, S., Stefanopoulou, A. G., Jiang, L., "Reducing cyclic variability while regulating combustion phasing in a four-cylinder HCCI engine," IEEE Transactions on Control Syst. Technol., vol. 22, no. 3, pp. 1190–1197, 2014, doi: 10.1109/TCST.2013.2271355.

5. Vaughan, A., "Adaptive Machine Learning for Modeling and Control of Non-Stationary, Near Chaotic Combustion in Real-Time," PhD Thesis, The University of Michigan, Ann Arbor, MI 2015.

6. Shibata, G., and Urushihara, T., "Dual Phase High Temperature Heat Release Combustion," SAE Paper No. 2008-01-0007, 2008.

7. Song, H. H., Padmanabhan, A., Kaahaaina, N. B., and Edwards, C. F., "Experimental study of recompression reaction for low-load operation in direct injection HCCI engines and n-heptane and i-octane fuels," Int. J. Engine Res., 10(4), 215-230, DOI: 10.1243/14680874JER03309, 2009.

CHAPTER 5

ADIABATIC CORE IGNITION MODEL

5.1 Background

CFD simulations with detailed chemical kinetics [1-6] as described in Chapters 3 and 4 can capture the thermal and compositional stratification governing HCCI combustion rates; however they remain too expensive for batch quantity open cycle simulations. On the other hand, single zone 0D simulations with detailed chemistry are relatively fast and can capture ignition characteristics but cannot properly capture the combustion rate, which is affected by thermal and compositional stratification [7, 8]. While quasi-dimensional multi-zone [9-13] models have been developed to address these issues, their zone initialization and subsequent treatment of the domain's thermal and compositional stratification development are uncertain and they remain relatively expensive. Alternatively, highly simplified mean value models appropriate for use in engine ECUs run faster than real time but require extensive calibration and are system specific [14, 15].

Empirical 0D models [16, 17] are perhaps best suited for engine systems level analysis as they capture the physical phenomenon required to describe complex combustion processes while being 100 to 1000 times faster than detailed CFD simulations. Typically these models are divided into ignition and combustion sub-models. The ignition model often consists of an auto-ignition integral (AI) which stems from a SI knock modeling concept originally developed by Livengood and Wu [18]. A modified version of this knock integral model has been utilized for HCCI engine modeling in [17,

19-22]. A key component of these models is an Arrhenius ignition delay expression, which often relies on thermodynamic information for the domain, such as temperature, pressure and composition (e.g. fuel air equivalence ratio, oxygen concentration, etc).

In Chapters 3 and 4, CFD simulations of HCCI were performed under a range of conditions including sweeps of valve timing, fuelling, direct injection timing, engine speed, intake temperature and intake boost. Analyzing the pre-ignition reactivity stratification, it was found that the compositional stratification had little effect on charge reactivity, and the burn profile could be explained largely based on the thermal stratification. It was found that under typical pre-ignition conditions for a NVO-DI case that the charge thermal stratification in terms of $2\sigma T$ = 79 K with a mean temperature of 1044 K, similar to Kodavasal et al. [23]. It was unclear how the temperature of the most reactive charge, which eventually initiates auto-ignition, evolved through compression. Such knowledge is critical for the accurate prediction of ignition. Appropriate treatment of the temperature of the initial auto-igniting charge is one of the most significant challenge faced by phenomenological HCCI ignition models, and is even more critical under the stratified conditions of NVO-DI operation.

Several 0D models use mean cylinder charge temperatures for ignition modeling [16, 19-21], and often must adjust the mean temperature or activation energy in the Arrhenius ignition delay or change its functional form to achieve suitable ignition predictions [17-21]. Others have adopted the use of the adiabatic core temperature for premixed HCCI charges [24] and for the prediction of knock within boosted SI engine operation [25]. Dec et al. [25] have shown that the adiabatic core assumption is applicable to the earliest igniting portions of the HCCI charge under compositionally homogeneous situations. From the previous Chapters, it is clear that compositional stratification has a much lower effect on charge reactivity and that thermal stratification primarily governs combustion rate. It is unclear if modeling the hottest charge

temperature while ignoring compositional stratification is sufficient to accurately predict ignition timing.

This chapter compares the use of the mean and adiabatic core temperature for the modeling of ignition temperature under operating conditions typical of automotive HCCI combustion systems. Based on these results, an ignition model is adopted for the 0D simulation of HCCI ignition.

5.2 Interrogation of HCCI ignition process using CFD

In this section, CFD simulations are used to better understand the ignition behavior of automotive HCCI combustion. Simulations of PVO (low stratification) and NVO (high stratification) HCCI are used for this analysis. The NVO case is the same as introduced in Chapter 2 which is also the baseline cases for simulation in Chapter 3 and 4. The PVO case is matched to the NVO case in all respects of fueling, engine speed and IVC mixture conditions, similar to Kodavasal et al. [27]. External EGR is used to match the total residual of the NVO case and the intake is heated to a temperature greater than the NVO case to match θ_{10}. Table 5.1 summarizes the operating conditions for the simulations. Figure 5.1 shows the mass fraction burned (MFB) profile as a function of crank angle for the PVO and NVO cases. The ignition timing, defined in this work as the crank angle where the mass fraction burned equals 0.1%, is the same for both cases, (θ_{IGN}= -12.5°CA) as indicated in the figure.

The ignition process for the PVO and NVO cases is interrogated with CFD to identify the ignition regimes present in and around the start of ignition, between 15 and 12^o CA bTDC. This is shown in Figure 5.2 by evaluating the local reaction progress ($\bar{c}$) plotted as a function of the local temperature (T) and global equivalence ratio (Φ) where Φ is given by [5]:

$$\Phi = \frac{2C^{\#} + \frac{1}{2}H^{\#}}{O^{\#}} \qquad \text{Equation 5.1}$$

and $\bar{c}$ is given by:

$$\bar{c} = \frac{h^0 + h_R^0}{h_p^0 - h_R^0} \qquad \text{Equation 5.2}$$

Here, h^0 is the enthalpy of formation based on the computational cell composition, h_p^0 is the enthalpy of formation of the major product species obtained from cell stoichiometry, and h_R^0 is the enthalpy of formation of the unburned reactant species corresponding to a given phi and EGR level.

Overall, it is apparent from Figure 5.2 that the NVO case is more compositionally stratified (based upon a wider distribution in Φ) compared to the PVO case. However in both cases, the portions of the charge with $\bar{c}$ greater than zero are localized to the highest temperatures in the distribution. There is no observable low temperature heat release (LTHR) [28], which would be found at temperatures ranging between approximately 650 K and 800 K. Additionally, the temperature of the hottest 1% of the charge ($T_{1\%}$) and mean temperature (T_m) from corresponding non-reacting CFD simulations is plotted in the figure. $T_{1\%}$ corresponds correctly to the portion of charge having the greatest reaction progress during the inspected crank angles leading up to ignition. This indicates that ignition occurs preferentially in the highest temperature (marked by $T_{1\%}$) of the charge distribution, and that there is no LTHR complicating the modeling of the initial ignition process.

5.3 Adiabatic core ignition model performance

$T_{1\%}$ is compared here with two other temperatures readily available within thermodynamic simulations, the mean temperature (T_m), and the adiabatic core temperature (T_{ad}). The adiabatic core temperature is calculated for an isentropic

compression process, from intake valve closing (IVC) to a given crank angle (θ). The pressure, mean temperature and mean composition at IVC are used to compute the initial specific entropy of the charge based on thermodynamic relations:

$$S(IVC) = f_1(P(IVC), T(IVC), X(IVC)) \qquad \text{Equation 5.3}$$

X(IVC) represents the mean composition of the charge in terms of the mole fractions of the gas mixture constituents. By definition, the entropy of the adiabatic core remains constant through compression. Therefore, the adiabatic core temperature can be determined iteratively by another thermodynamic relationship represented here with Equation 5.4, when the cylinder pressure is known for a given crank angle (P(θ)).

$$T_{ad}(\theta) = f_2(P(\theta), S(IVC), X(IVC)) \qquad \text{Equation 5.4}$$

Figure 5.3 compares the evolution of T_{ad} against $T_{1\%}$ and the T_m calculated for all of the CFD cells under motoring conditions for both the PVO and NVO cases. For the PVO case, $T_{1\%}$ is only 1.3% hotter than T_m at IVC. T_{ad} is initialized as $T_m(IVC)$ and approaches $T_{1\%}$ rapidly through compression for the PVO case, and remains within ± 1% of $T_{1\%}$ for θ > -90^o CA aTDC. On the other hand for the NVO case, $T_{1\%}$ is approximately 6.3% hotter than T_m at IVC. T_{ad} approaches $T_{1\%}$ less rapidly compared to the PVO case, reaching values within ± 1% of $T_{1\%}$ for θ> -30^o CA aTDC, until the end of compression. It is acknowledged that the isentropic compression assumption for the adiabatic core temperature is not valid when representing $T_{1\%}$ of the NVO case (due to mixing of the stratified charge). However, T_{ad} predicted by the model is close to $T_{1\%}$ near TDC.

The initial difference in T_{ad} and $T_{1\%}$ is in part due to the assumption of a uniform state of charge at IVC which is not the case for the NVO simulation, which has high initial stratification. Figure 5.4(a) and (b) respectively show the variation of fuel-to-

oxygen equivalence ratio in the hottest 1% of the charge mass ($\phi_{FO-1\%}$) compared to the global mean value (ϕ_{FO-m}) for the PVO and NVO cases respectively. For the PVO case, the $\phi_{FO-1\%}(\theta)$~ 0.44 which is equal to the global ϕ_{FO-m} = 0.44 and nearly constant through the compression process. For the NVO case, $\phi_{FO-1\%}$ starts out rich (~0.76) at IVC and approaches $\phi_{FO_{global}}$ near TDC due to mixing. $\phi_{FO-1\%}$ is within 0.1 of ϕ_{FO-m} beyond 70°CA bTDC however $\phi_{FO-1\%}(\theta_{IGN})$ = 0.4 which is 9.1% smaller than ϕ_{FO-m} on a relative basis. Similarly, Figure 5.5(a) and (b) show the variation of oxygen mole percentage in the hottest 1% of the charge ($\chi_{O_2-1\%}$) compared to the global mean value (χ_{O_2-m}) for both cases. For the PVO case, $\chi_{O_2-1\%}$ is nearly constant ~ 15.1% throughout compression which is the same as the global value χ_{O_2-m}= 15.1%. For the NVO case $\chi_{O_2-1\%}$ starts out at 13% at IVC but approaches χ_{O_2-m} towards end of compression due to mixing. $\chi_{O_2-1\%}$ differs by less than 1% relative to χ_{O_2-m}beyond 50°CA bTDC, however $\chi_{O_2-1\%}$ at θ_{IGN} is 15.1% which is the same as χ_{O_2-m}.

0D thermodynamic models cannot capture in-cylinder compositional stratification. Even though the temperature of hottest charge is correctly predicted up to the time of ignition for both cases, the use of the mean composition for HCCI ignition modeling with NVO valve events may be problematic. To assess the validity of using the mean composition along with the adiabatic core temperature for ignition modeling the cumulative distribution of reactivity is visualized [1]. Ignition delays are calculated in every CFD cell using the Goldsborough correlation [29] at ignition (12.5°CA bTDC), similar to Chapters 3 and 4. To assess the importance of compositional stratification for reactivity, the ignition delays are re-computed at 12.5°CA bTDC using the cell temperature and global mean composition and are overlaid in Figure 5.6 for both the PVO and NVO cases. The reactivity distributions for the PVO case noted in Figure 5.6(a) are closely matched throughout the charge due small compositional stratification. For the NVO case in Figure 5.6(b) the distributions diverge little between the cell level and mean composition, especially at the leading edge of the reactivity distribution, which

is associated with the first igniting portion of the charge. Under these conditions, compositional stratification has a minor effect on the ignition prediction compared to temperature. Therefore, the mean composition can be used within the knock integral for the prediction of ignition for HCCI simulations of PVO or NVO.

The adiabatic core ignition model is now exercised for both the PVO and NVO cases by computing the ignition delays of the charge with three temperatures using the Goldsborough ignition delay expression. Ignition is predicted by evaluating the auto-ignition integral (AI) in Equation 5.5 with the Goldsborough ignition delay correlation, which has been developed and validated over a comprehensive set of conditions. Ignition (t_{IGN}) is defined as the time when the integral reaches the value of 1:

$$\int_0^{t_{IGN}} \frac{1}{\tau} dt = 1 \qquad \text{Equation 5.5}$$

Three ignition delays are calculated using different states. In the first, the ignition delay is calculated using the temperature and composition of the hottest 1% of charge ($T_{1\%} - C_{1\%}$). In the second, the ignition delay is calculated using the mean temperature and composition ($T_{mean} - C_{mean}$) and in the third the ignition delay is calculated using the adiabatic core temperature and mean composition ($T_{ad} - C_{mean}$). Figure 5.7 shows the three ignition delays from -40°CA aTDC to TDC calculated from the non-reacting CFD simulation results for PVO and NVO. With compression the ignition delays all fall exponentially. The $T_{1\%} - C_{1\%}$ lines are significantly lower than the $T_{mean} - C_{mean}$ lines throughout compression. For the PVO case in Figure 5.7(a), the $T_{ad} - C_{mean}$ line matches the $T_{1\%} - C_{1\%}$ line correctly up to TDC. On the other hand for the NVO case in Figure 5.7(b) the $T_{ad} - C_{mean}$ model initially predicts greater ignition delays compared to $T_{1\%} - C_{1\%}$, it approaches the $T_{1\%} - C_{1\%}$ line and remains very close to it for crank

angle between -25°CA aTDC and -10°CA aTDC while predicting shorter ignition delays beyond -5°CA aTDC.

To quantify the error in the different models while making a fair comparison, we compute the auto-ignition integral for the three models. For the PVO case $\theta_{AI-T_{1\%}-C_{1\%}}$= -9.0°CA aTDC which is equal to $\theta_{AI-T_{ad}-C_{mean}}$= -9.0°CA aTDC whereas $\theta_{AI-T_m-C_{mean}}$= -3.4°CA aTDC. Similarly for the NVO case $\theta_{AI-T_{1\%}-C_{1\%}}$= -9.1°CA aTDC which is nearly equal to $\theta_{AI-T_{ad}-C_{mean}}$= -9.2°CA aTDC whereas $\theta_{AI-T_m-C_{mean}}$= -3.1°CA aTDC. The ignition predicted by the adiabatic core ignition model is nearly equal to the ignition predicted for the hottest charge ($T_{1\%}-C_{1\%}$). The mean temperature and composition($T_{mean}-C_{mean}$) predicts a later ignition, by nearly 6°CA for the PVO as well as the NVO case. The adiabatic core ignition model does not track the composition of the initial auto-igniting charge through compression but the charge is relatively well mixed close to ignition. On the other hand the adiabatic core temperature matches the temperature of hottest charge close to TDC. As a result the model correctly predicts ignition delays close to TDC and is therefore appropriate for 0D HCCI ignition modeling under both PVO and NVO-DI operation. The adiabatic core ignition model ($T_{ad}-C_{mean}$) is validated against the CFD sweeps presented in Chapters 3 and 4 and compared with ignition delays predicted by the $T_{mean}-C_{mean}$and $T_{1\%}-C_{1\%}$ methods through compression.

5.4 Validation for RPM sweep

The θ_{10} phasing has been matched for these cases but θ_{IGN} for the 1000 RPM and 3000 RPM cases are -11.5°CA aTDC and -12.8°CA aTDC respectively, different from θ_{IGN} = -12.5°CA aTDC for the baseline 2000 RPM case. For the 1000 RPM case in Figure 5.8(a) at 40°CA bTDC, the $T_{mean}-C_{mean}$ and $T_{ad}-C_{mean}$ models have similar ignition delays although $T_{1\%}-C_{1\%}$ has noticeably shorter ignition delays. Through

compression, the adiabatic core ignition predictions fall progressively closer to the hottest 1% of charge. The ignition delays match slightly before predicted ignition and remain matched up to end of compression. The ignition predictions $\theta_{AI-T1\%-C1\%}$= -8.2°CA and $\theta_{AI-Tad-Cmean}$= -7.5°CA are within 0.7°CA. For the 3000 RPM case in Figure 5.8(c) the trends in ignition delay predictions by the three methods is similar to the 1000 RPM case. The ignition predictions $\theta_{AI-T1\%-C1\%}$= -9.5°CA aTDC and $\theta_{AI-Tad-Cmean}$= -9.5°CA aTDC are the same. The ignition predicted with the mean temperature and composition is nearly 6^{o} CA after the other two ignition models. From these results it is concluded that the adiabatic core ignition model predicts ignition correctly for this range of engine speeds.

5.5 Validation for ϕ' sweep

Figure 5.9 presents the performance of the adiabatic core ignition model for the ϕ'sweep. From Figure 5.9(a) ϕ' = 0.24 and ϕ'= 0.29 (b) the ignition delays computed by the adiabatic core ignition model are well matched with those from the hottest 1% of charge from 40°CA bTDC to the end of compression. Subtle differences are observed at 40°CA bTDC for these ignition predictions at ϕ' = 0.32 and ϕ'= 0.37 in Figure 5.9(c) and (d). However the ignition delays for these two models are well matched from 20°CA bTDC to the end of compression. The ignition predicted by $T_{1\%} - C_{1\%}$ and $T_{ad} - C_{mean}$ is matched to within 0.2°CA throughout the sweep. The ignition predicted by $T_{mean} - C_{mean}$ is about 6°CA later than the ignition predicted by the other two models throughout the sweep.

5.6 Validation for boost sweep

The θ_{10} phasing has been matched the θ_{IGN} timings vary; θ_{IGN} = -12.5°CA aTDC for $P_{IN} = P_{EX} = 1$ bar, θ_{IGN}= -11.6°CA aTDC for $P_{IN} = P_{EX} = 1.5$ bar and θ_{IGN}= -

11.1°CA aTDC for $P_{IN} = P_{EX} = 2$ bar. From Figure 5.10 it is apparent that for the low pressure case (baseline), the adiabatic core ignition model predicts ignition delays closer to the ignition delays predicted by the hottest 1% charge at 40°CA bTDC. For higher boost pressures the predictions by the adiabatic core ignition model are further away compared to the ignition delays predicted by the hottest 1% charge. However the adiabatic core ignition model predictions approach the predictions by the hottest 1% charge as seen in Figure 5.10(a), (b) and (c). The ignition predictions by the two models are within 0.6°CA of each other ($\theta_{AI-Tad-Cmean}$= -9.2°CA aTDC and $\theta_{AI-T1\%-C1\%}$= -9.1°CA aTDC for $P_{IN-EX} = 1$ bar, $\theta_{AI-Tad-Cmean}$= -8.6°CA aTDC and $\theta_{AI-T1\%-C1\%}$= -8.7°CA aTDC for $P_{IN-EX} = 1.5$ bar and $\theta_{AI-Tad-Cmean}$= -8°CA aTDC and $\theta_{AI-T1\%-C1\%}$= -8.6°CA aTDC for $P_{IN-EX} = 2$ bar). The $T_{mean} - C_{mean}$ model has ignition delays much longer than the other two models throughout compression for the entire sweep. Thus the ignition predicted is also much later (~6°CA) compared to the other models.

5.7 Validation for SOI sweep

From Figure 5.11(a), (b) and (c) it is observed that $T_{ad} - C_{mean}$ closely matches the ignition delay trajectory of the hottest 1% of the charge near TDC. The errors in the ignition prediction by the adiabatic core model ($T_{ad} - C_{mean}$) with resepect to those predicted by the hottest 1% of charge ($T_{1\%} - C_{1\%}$) are less than 0.2°CA for the SOI sweep ($\theta_{AI-Tad-Cmean}$= -9.1°CA aTDC and $\theta_{AI-T1\%-C1\%}$= -9°CA aTDC for SOI = 310°CA aTDC, $\theta_{AI-Tad-Cmean}$= -9.2°CA aTDC and $\theta_{AI-T1\%-C1\%}$= -9.1°CA aTDC for SOI = 390°CA aTDC and $\theta_{AI-Tad-Cmean}$= -9.3°CA aTDC and $\theta_{AI-T1\%-C1\%}$= -9.3°CA aTDC for SOI = 430°CA aTDC). The ignition prediction using the mean temperature and composition is nearly 6°CA after the other two models. It is concluded that the adiabatic core ignition model can predict ignition for this range of SOI variation.

5.8 Validation for NVO sweep

Figure 5.12 compares the ignition delay predictions by the three ignition models through compression for the NVO sweep. Similar to other sweeps the adiabatic core ignition model initially (at 40^o CA bTDC) has greater ignition delays than the $T_{1\%} - C_{1\%}$ model. However the ignition delays are well matched close to TDC. The errors in the ignition prediction by the adiabatic core model ($T_{ad} - C_{mean}$) with respect to ignition predicted by the hottest 1% of charge ($T_{1\%} - C_{1\%}$) is less than 1°CA for the entire NVO sweep. The ignition prediction with the mean temperature and composition case is nearly 6^o CA after the other two models. From the results at these operating conditions it is concluded that the adiabatic core ignition model can predict ignition for this range of NVO variation.

5.9 Validation for intake temperature sweep

The ignition timing varies with intake temperature; θ_{IGN} = -9.0°CA aTDC for T_{IN} = 66°C, θ_{IGN} = -12.5°CA aTDC for T_{IN} = 106°C and θ_{IGN} = -17.1°CA aTDC for T_{IN} = 146°C. Figure 5.13 compares the performance of the three ignition models during the compression process for the intake temperature sweep. The three model predictions are trend wise similar to the previous sweeps. The ignition predicted by the adiabatic core ignition model and the hottest 1% of charge are within 0.5°CA for the sweep. ($\theta_{AI-Tad-Cmean}$= -5.5°CA aTDC and $\theta_{AI-T1\%-C1\%}$=-5.1°CA aTDC for T_{IN} = 66°C, $\theta_{AI-Tad-Cmean}$= -9.2°CA aTDC and $\theta_{AI-T1\%-C1\%}$= -9.1°CA aTDC for T_{IN} = 106°C and $\theta_{AI-Tad-Cmean}$= -13.4°CA aTDC and $\theta_{AI-T1\%-C1\%}$ =- 13.5°CA aTDC for T_{IN} = 146°C). The higher the intake temperature, the better the match between ignition delays predicted by the adiabatic core ignition model and the $T_{1\%} - C_{1\%}$ model ignition delays. The $T_{mean} - C_{mean}$ model predicts ignition delays much longer than the other two models throughout the compression process. The ignition predicted is nearly 6°CA after the

ignition predicted by the other methods. Since the adiabatic core ignition model predictions match the ignition location predicted by the hottest 1% charge, it is concluded that the adiabatic core ignition model can predict ignition for a range of intake temperatures.

5.10 Summary

CFD simulations were used to interrogate the ignition regimes present during typical HCCI operation. The results show that there is no observable Low Temperature Heat Release under these conditions, hence ignition delay expressions developed for high temperature ignition regimes can be used to accurately predict ignition, greatly simplifying HCCI ignition modeling. The initial reaction progress at ignition is localized to the hottest portion of the charge.

Two simplified thermodynamic ignition models are compared, one utilizing the adiabatic core temperature ($T_{ad} - C_{mean}$) and one using the mean gas temperature ($T_m - C_m$). Both models use the mean charge composition, as compositional stratification did not significantly affect ignition delay near TDC. The ignition delay trajectories were compared through compression with those calculated from the hottest 1% of the charge ($T_{1\%} - C_{1\%}$) and its associated composition, where ignition is first observed in the CFD simulations. Ignition delays and location predicted from the adiabatic core temperature and the hottest 1% of the charge is closely matched for the PVO case due to the prediction of similar temperature time histories with low compositional stratification. However, even for the more stratified NVO cases, the ignition delays predicted by the adiabatic core model match those from the hottest 1% of the charge near TDC, leading to good ignition predictions. The adiabatic core ignition model also performs satisfactorily compared to CFD parameter sweeps from Chapter 3

and 4, namely sweeps of engine speed, ϕ', boost, SOI, NVO and intake manifold temperature.

Table 5.1 – CFD simulation conditions for the PVO, NVO study

Parameter	PVO	NVO
Fueling	DI	DI
Fueling Rate (mg/cyc)	9.25	9.25
NVO (^{o}CA)	0	157
SOI	390	390
ϕ	0.58	0.58
$\boldsymbol{\phi_{FO}}$ (mean)	0.44	0.44
ϕ'	0.32	0.32
$\boldsymbol{\chi_{O2}}$ (mean)	15%	15%
Intake Temperature (^{o}C)	251°C	106°C
Internal Residual	7%	43%
External Residual	36%	0%
Total RGF	43%	43%

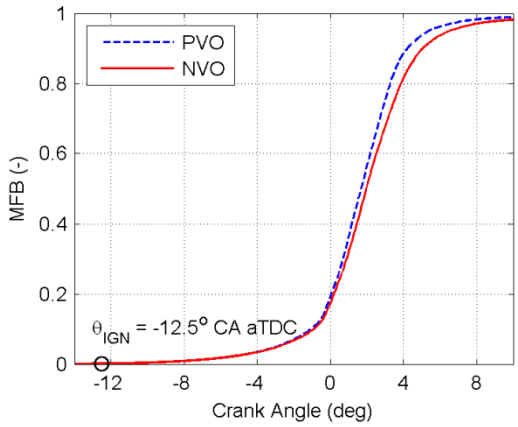

Figure 5.1 – Variation of overall reaction progress denoted by mass fraction burned (MFB) with crank angle for the PVO and NVO case respectively from Table 5.1

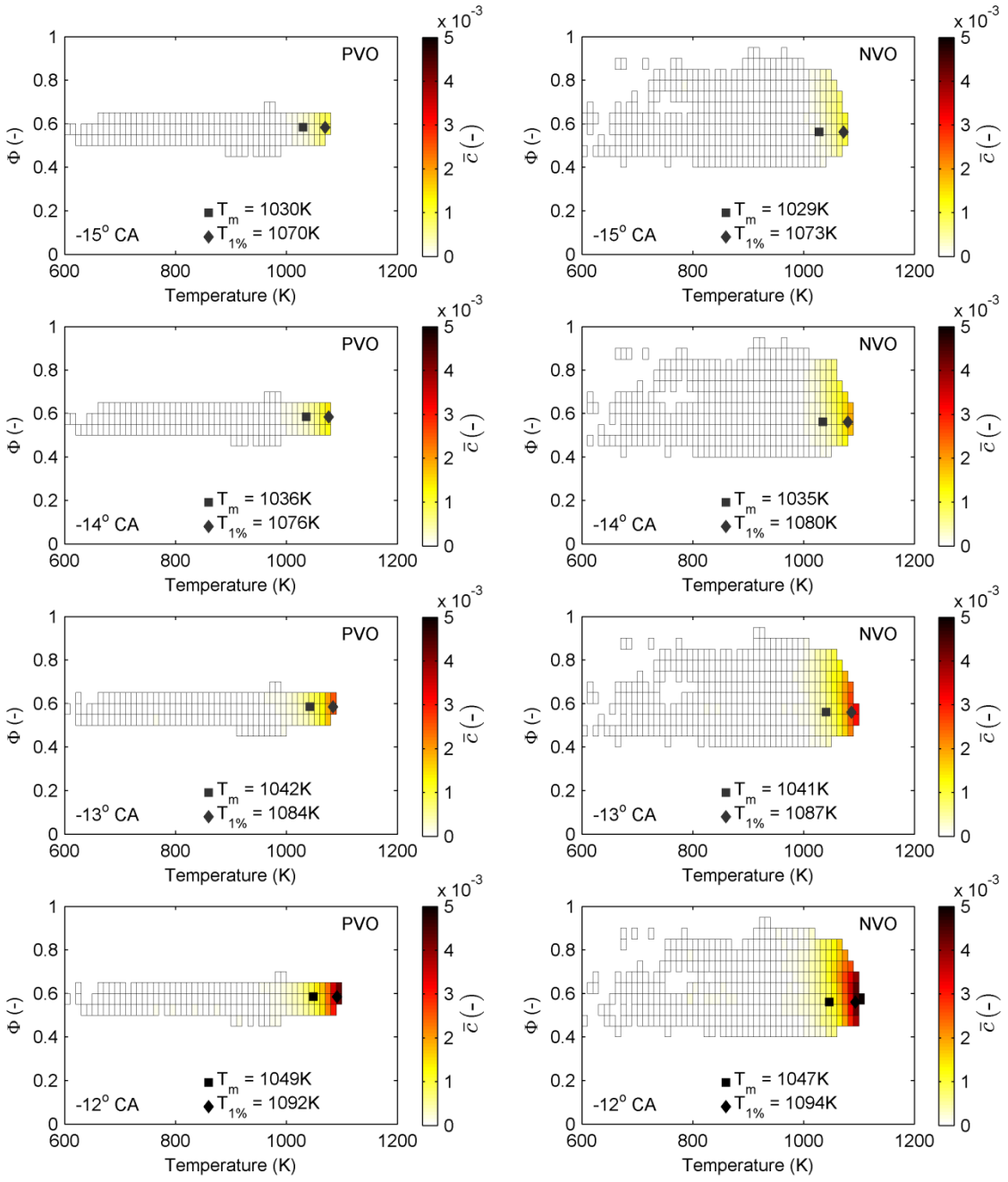

Figure 5.2 – Reaction space from CFD simulation visualized in terms of Φ, Temperature and Reaction Progress ($\bar{c}$) for PVO and NVO.

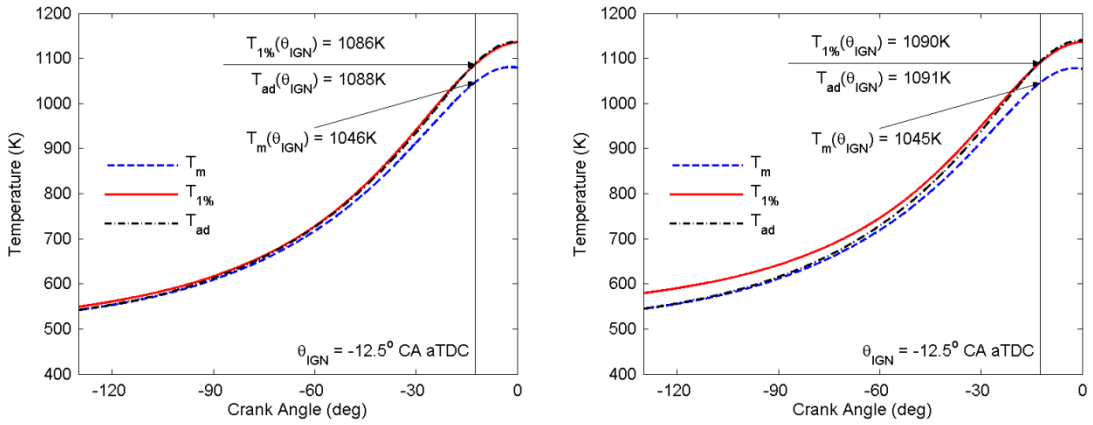

Figure 5.3 – Comparison of mean temperature (T_m), temperature of the hottest 1% of the charge mass ($T_{1\%}$) and the adiabatic core temperature (T_{ad}) for two operating conditions (a) PVO and (b) NVO from IVC to TDC of a motoring CFD simulation

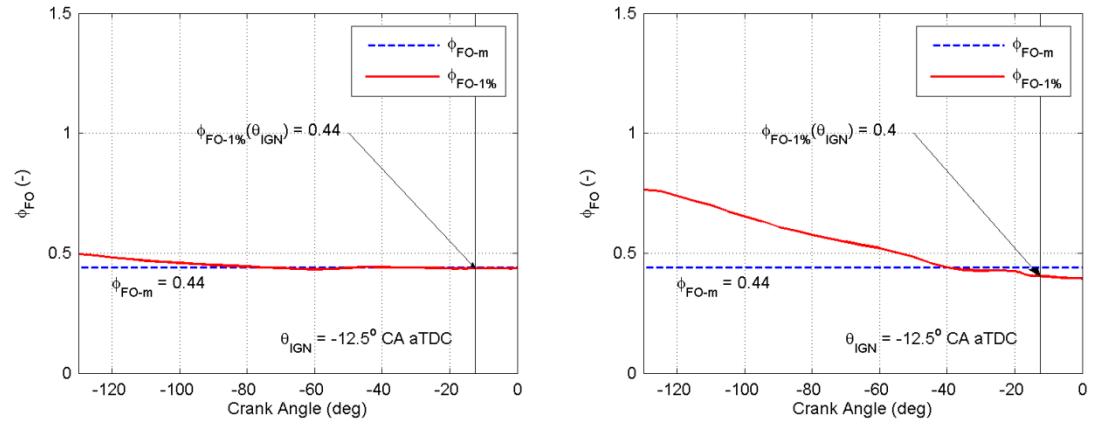

Figure 5.4 – Comparison of fuel-to-oxygen equivalence ratio in the global vs. the hottest 1% of the charge through the compression stroke, for (a) PVO and (b) NVO

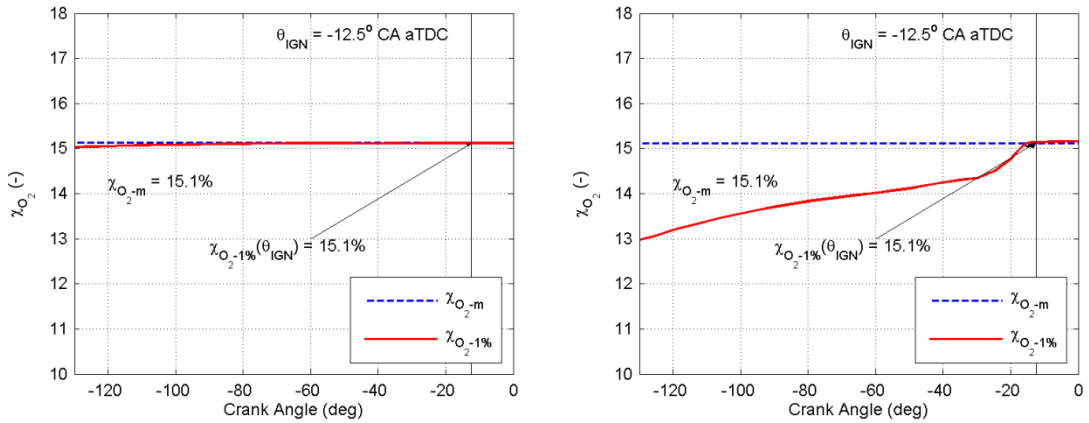

Figure 5.5 – Comparison of molar percentage of oxygen in the global vs. the hottest 1% of charge through the compression stroke, for (a) PVO and (b) NVO

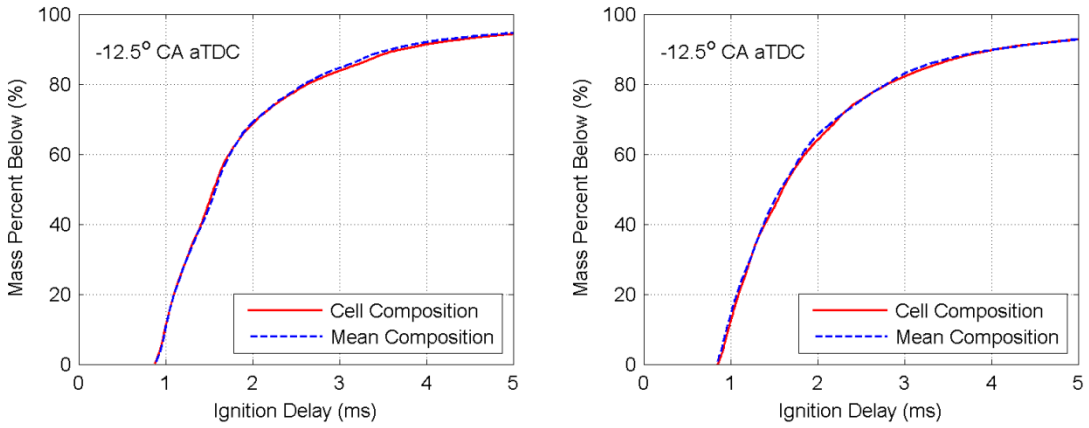

Figure 5.6 –Reaction space (at 12.5° CA bTDC) visualized in terms of the cumulative charge mass below a certain ignition delay, for (a) PVO (~0° NVO) and (b) NVO (157° NVO) computed from non-reacting CFD simulations

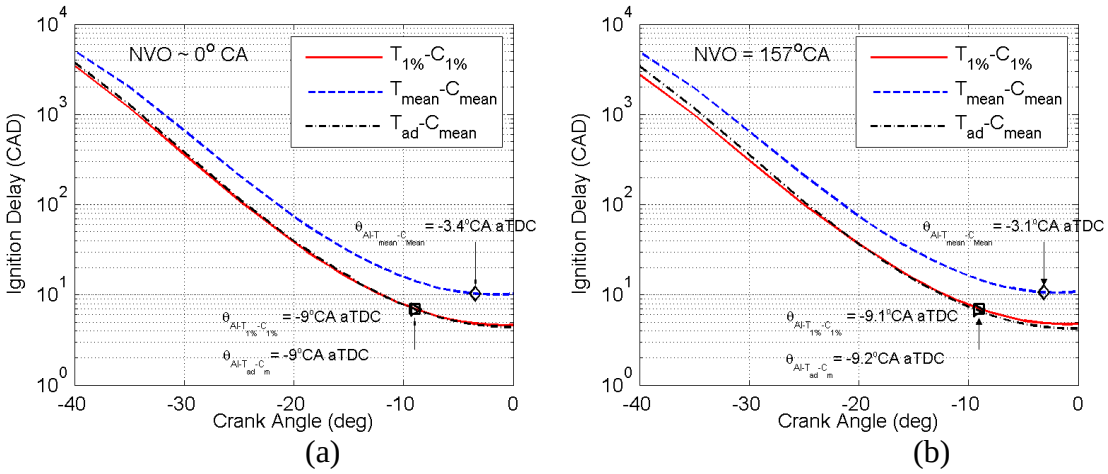

Figure 5.7 – Ignition delay vs. crank angle for the temperature and composition of hottest 1% of the charge ($T_{1\%} - C_{1\%}$ denoted by the dark solid line), the global mean charge temperature and composition ($T_{mean} - C_{mean}$ denoted by the light solid line) and the adiabatic core temperature and composition ($T_{ad} - C_{mean}$ denoted by the dashed line) for the (a) PVO and (b) NVO cases.

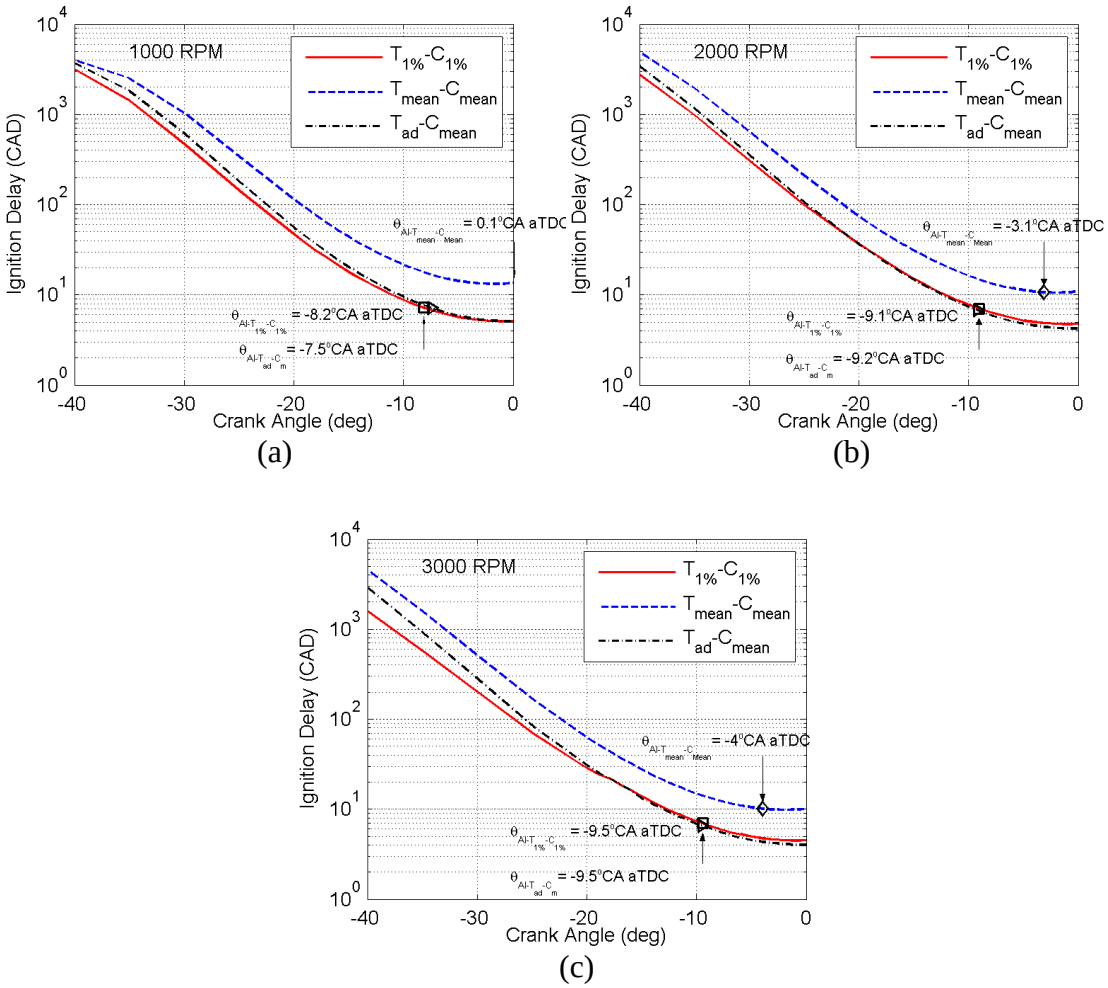

Figure 5.8 – Ignition delay vs. crank angle for the temperature and composition of hottest 1% of the charge ($T_{1\%} - C_{1\%}$ denoted by the dark solid line), the global mean charge temperature and composition ($T_{mean} - C_{mean}$ and denoted by the light solid line) and the adiabatic core temperature and composition ($T_{ad} - C_{mean}$ and denoted by the dashed line) for the (a) 1000 RPM, (b) 2000 RPM and (c) 3000 RPM cases.

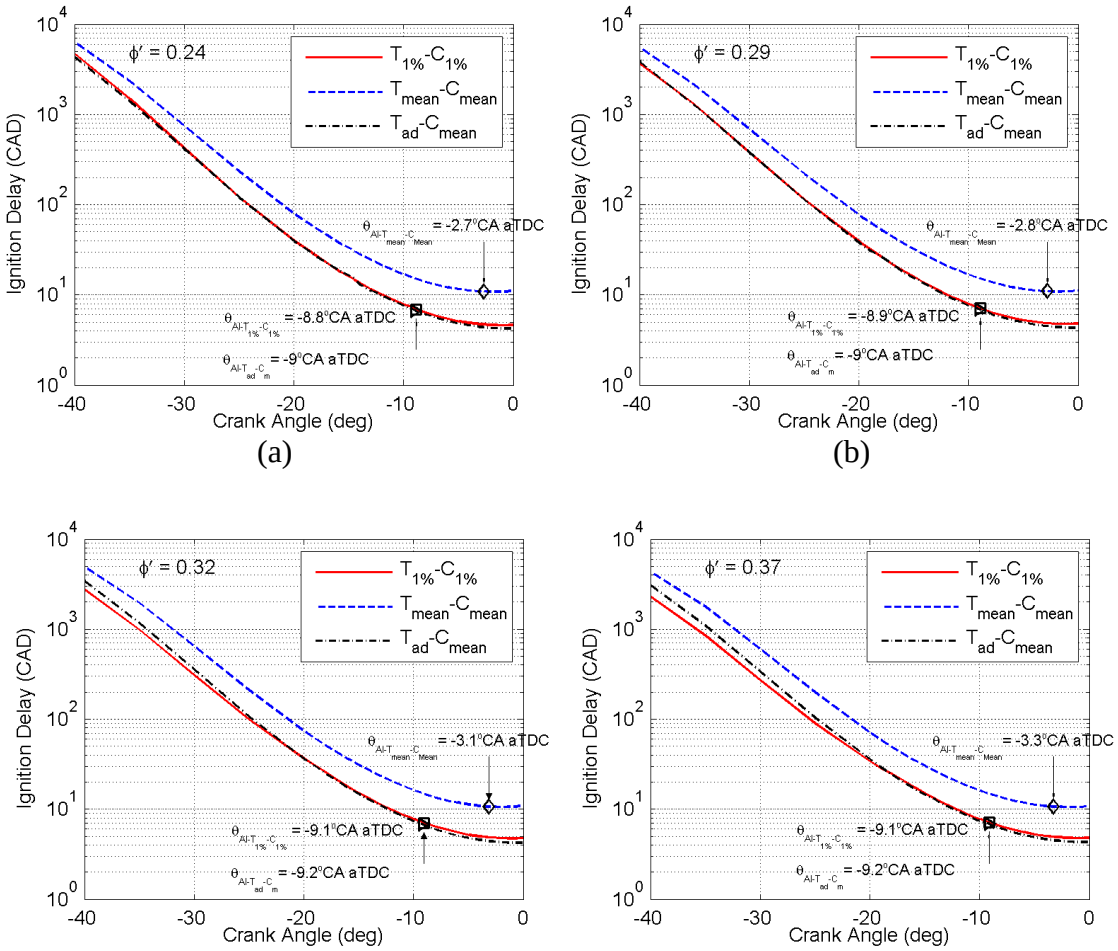

Figure 5.9 – Ignition delay vs. crank angle for the temperature and composition of hottest 1% of the charge ($T_{1\%} - C_{1\%}$ denoted by the dark solid line), the global mean charge temperature and composition ($T_{mean} - C_{mean}$ and denoted by the light solid line) and the adiabatic core temperature and composition ($T_{ad} - C_{mean}$ and denoted by the dashed line) for the ϕ' sweep (a) ϕ' = 0.24, (b) ϕ' = 0.29, (c) ϕ' = 0.32 and (d) ϕ' = 0.37.

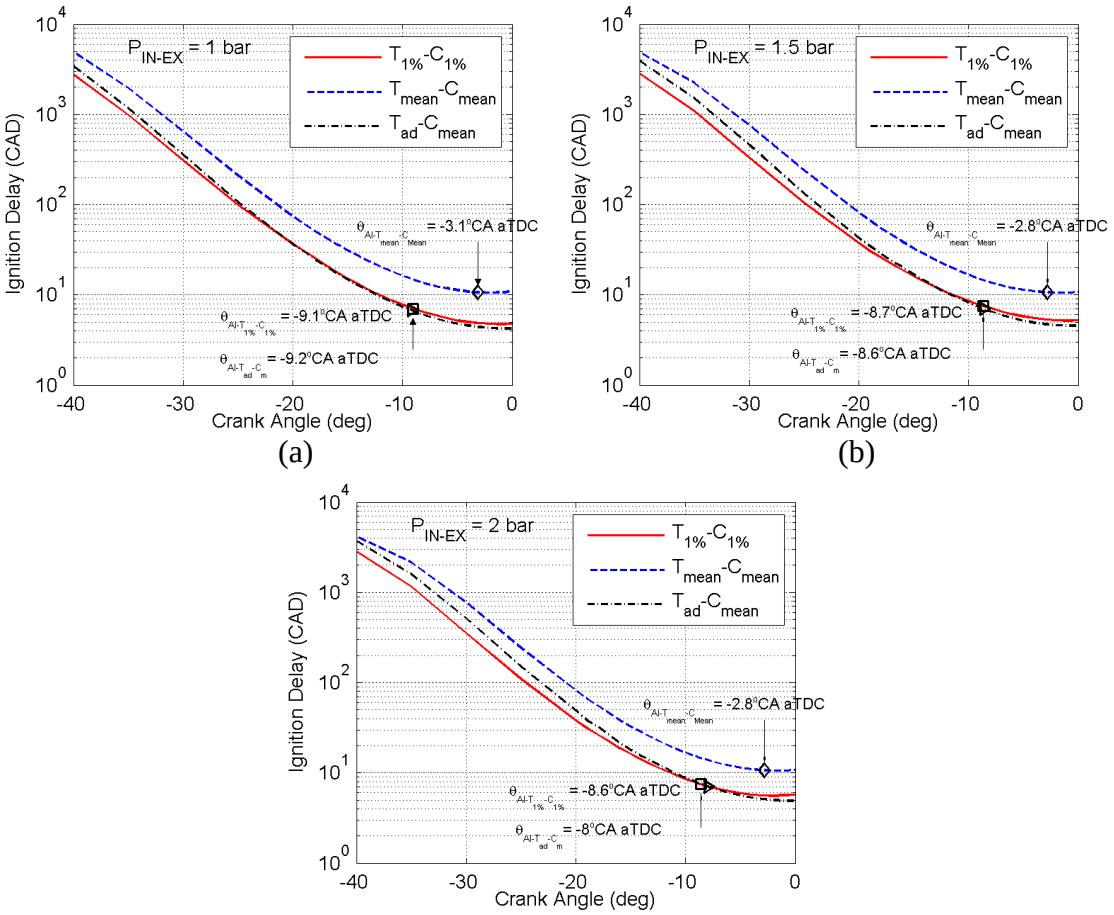

Figure 5.10 – Ignition delay vs. crank angle for the temperature and composition of hottest 1% of the charge ($T_{1\%} - C_{1\%}$ denoted by the dark solid line), the global mean charge temperature and composition ($T_{mean} - C_{mean}$ and denoted by the light solid line) and the adiabatic core temperature and composition ($T_{ad} - C_{mean}$ and denoted by the dashed line) for the boost sweep (a) P_{IN-EX} = 1 bar, (b) P_{IN-EX} = 1.5 bar and (c) P_{IN-EX} = 2 bar

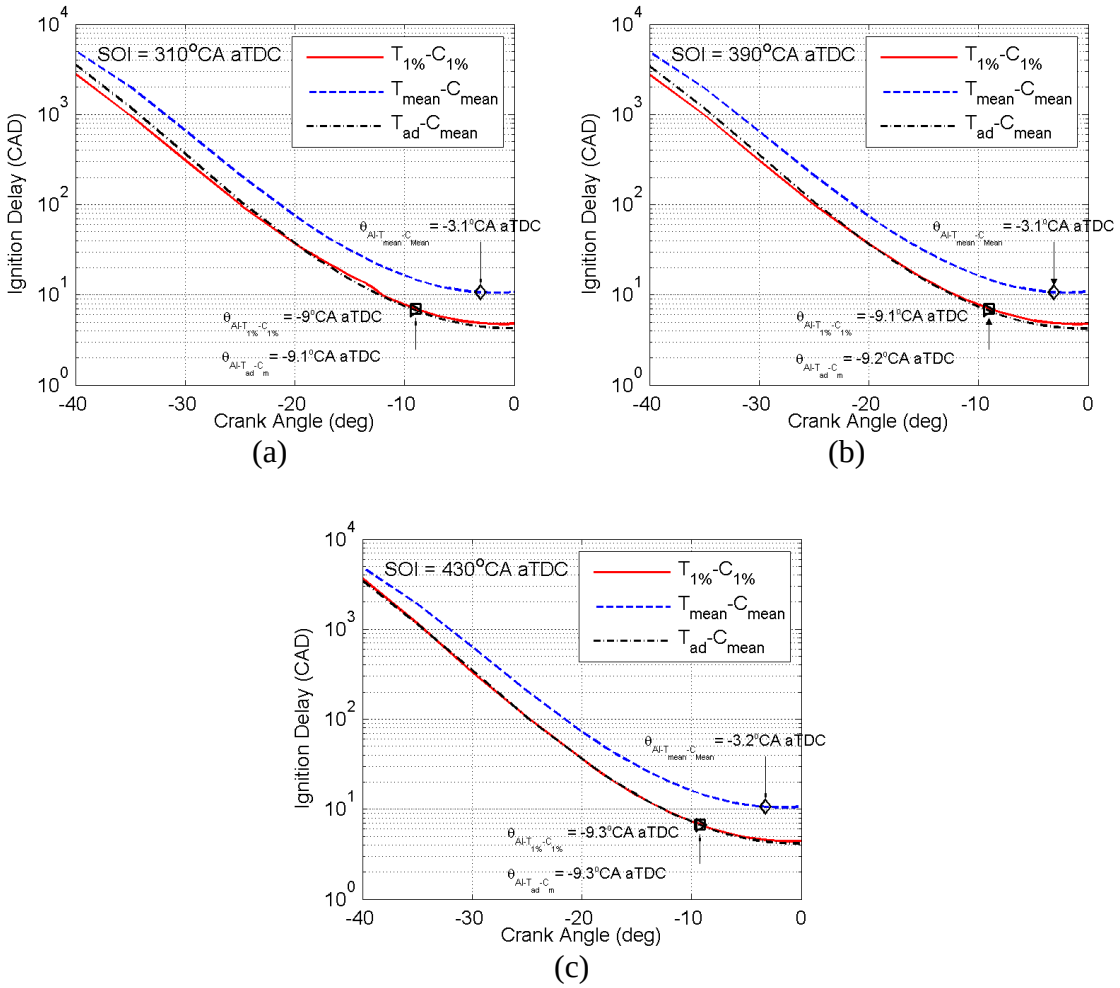

Figure 5.11 – Ignition delay vs. crank angle for the temperature and composition of hottest 1% of the charge ($T_{1\%} - C_{1\%}$ denoted by the dark solid line), the global mean charge temperature and composition ($T_{mean} - C_{mean}$and denoted by the light solid line) and the adiabatic core temperature and composition ($T_{ad} - C_{mean}$and denoted by the dashed line) for the SOI sweep (a) SOI = 310^{o} CA aTDC (b) SOI = 390^{o} CA aTDC and (c) SOI = 430^{o} CA aTDC cases

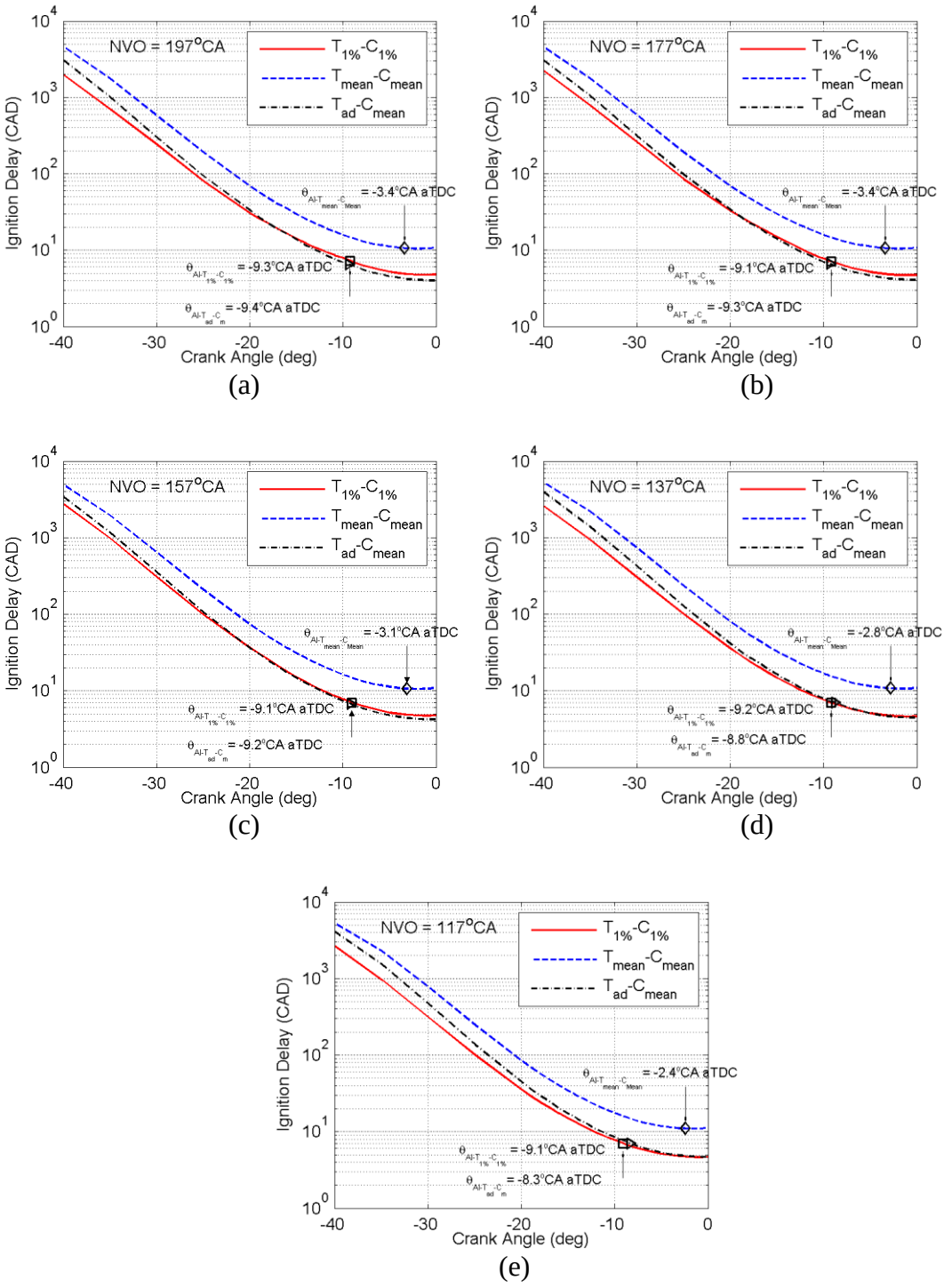

Figure 5.12 – Ignition delay vs. crank angle for the temperature and composition of hottest 1% of the charge ($T_{1\%} - C_{1\%}$ denoted by the dark solid line), the global mean charge temperature and composition ($T_{mean} - C_{mean}$ and denoted by the light solid line) and the adiabatic core temperature and composition ($T_{ad} - C_{mean}$ and denoted by the dashed line) for the NVO sweep (a) NVO = 197° CA, (b) NVO = 177° CA, (c) NVO = 157° CA, (d) NVO = 137° CA and (e) NVO = 117° CA cases

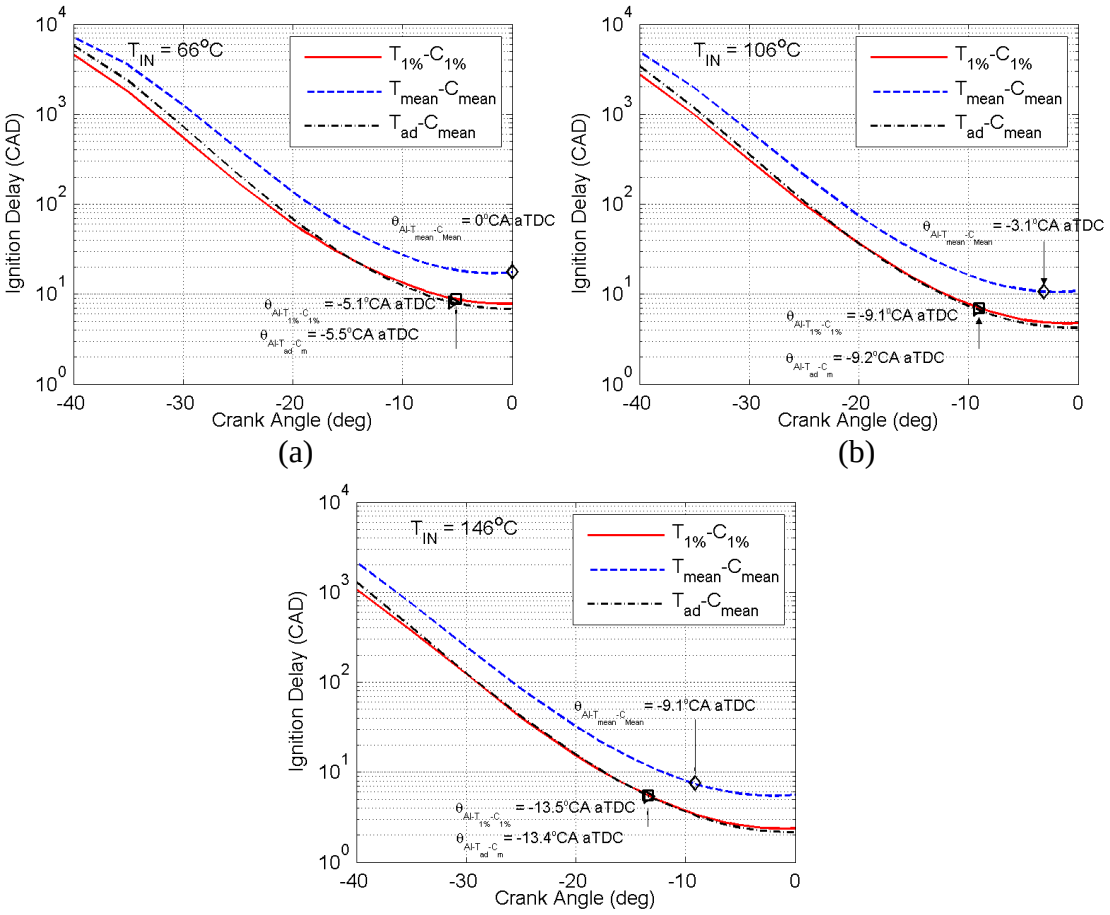

Figure 5.13 – Ignition delay vs. crank angle for the temperature and composition of hottest 1% of the charge ($T_{1\%} - C_{1\%}$ denoted by the dark solid line), the global mean charge temperature and composition ($T_{mean} - C_{mean}$ and denoted by the light solid line) and the adiabatic core temperature and composition ($T_{ad} - C_{mean}$ and denoted by the dashed line) for the intake temperature sweep (a) T_{IN}=66° C, (b) T_{IN}=106° C and (c) T_{IN}=146° C

5.11 References

1. Agarwal, A., and Assanis, D.N., "Multi-dimensional modeling of natural gas ignition under compression ignition conditions using detailed chemistry," SAE Paper 980136, 1998.
2. Kong, S.-C., Marriot, C.D., Reitz, R.D., and Christensen, M., "Modelling and experiments of HCCI engine combustion using detailed chemical kinetics with multidimensional CFD," SAE Paper 2001-01-1026, 2001.
3. Aceves, S.M., Flowers, D.L., Westbrook, C.K., Smith, J.R., Dibble, R.W., Christensen, M., Pitz, W.J., and Johansson, B., "A multi-zone model for prediction of HCCI combustion and emissions," SAE Paper 2000-01-0327, 2000.
4. Babajimopoulos, A., Lavoie, G.A., and Assanis, D.N., "Modeling HCCI combustion with high levels of residual gas fraction – a comparison of two VVA strategies," SAE Paper 2003-01-3220, 2003.
5. Babajimopoulos, A., Assanis, D.N., Flowers, D.L., Aceves, S.M., and Hessel, R.P., "A fully coupled computational fluid dynamics and multi-zone model with detailed chemical kinetics for the simulation of premixed charge compression ignition engines," Int. J. Engine Res. 6, pp. 497–512, 2005.
6. Kodavasal, J., Keum, S., and Babajimopoulos, A., "An extended multi-zone combustion model for PCI simulation. Combust Theory and Modeling," 15(6): 893–910, 2011.
7. Fiveland, S. B., and Assanis, D. N., "A Four-Stroke Homogeneous Charge Compression Ignition Engine Simulation for Combustion and Performance Studies," SAE paper 2000-01-0332, 2000.

8. Knierim, K. L., Park, S., Ahmed, J., Kojic, A., Orlandini, I., and Kulzer, A., "Simulation of Misfire and Strategies for Misfire Recovery of Gasoline HCCI," Proceedings of the American Control Conference, pp. 831-836, 2008.

9. Aceves, S.M., Flowers, D.L, Westbrook, C.K, Smith, R. J., Pitz, W., Dibble, R., Christensen, M., and Johansson, B., "A multizone model for prediction of HCCI combustion and emissions." SAE paper 2000-01-0327, 2000.

10. Babajimopoulos, A., Fiveland, S. B., and Assanis, D. N., "An Approach for Modeling the Effects of Gas Exchange Processes on HCCI Combustion and its Application in Evaluating Valve Timing Control Strategies," SAE paper 2002-01-2829, 2002.

11. Ogink., R., and Golovitchev., V., "Gasoline HCCI modeling: an engine cycle simulation code with a multi-zone combustion model," SAE paper 2002-01-1745, 2002.

12. Orlandini I, Kulzer A, Weberbauer F, et al., "Simulation of self ignition in HCCI and partial HCCI engines using a reduced order model," SAE paper 2005-01-0159, 2005.

13. Kodavasal, J., McNenly, M. J., Babajimopoulos, A., Aceves, S. M., Assanis, D., Havstad, M. A., Flowers, D. L., "An accelerated multi-zone model for engine cycle simulation of homogeneous charge compression ignition combustion," International Journal of Engine Research, 14(5) 416–433, 2013.

14. Gambarotta, A., Lucchetti, G., & Vaja, I., "Real-time modeling of transient operation of turbocharged diesel engines," Proceedings of the Institution of

Mechanical Engineers, Part D: Journal of Automobile Engineering, 225(9), 1186-1203.

15. Guzzella, L., and Amstutz, A., (1998). "Control of diesel engines," IEEE Contr. Syst. Mag., 18(2), 53-71, 1998.

16. Chang, K., Babajimopoulos, A., Lavoie, G. A., Filipi, Z. S., and Assanis, D. N., "Analysis of Load and Speed Transitions in an HCCI Engine Using 1-D Cycle Simulation and Thermal Networks," SAE Paper 2006-01-1087, 2006.

17. Babajimopoulos, A., Challa, P.C.V.S.S., Lavoie, G., and Assanis, D. N., "Model-Based Assessment of Two Variable Cam Timing Strategies for HCCI Engines: Recompression Vs. Rebreathing," Proceedings of the ASME International Combustion Engine Division Spring Technical Conference, ICES2009-76103, 2009.

18. Livengood, J. C. and Wu, P. C., "Correlation of autoignition phenomenon in internal combustion engines and rapid compression machines," In Proceedings of the Fifth International Symposium on Combustion, Pittsburgh, Pennsylvania, USA, pp. 347-356, 30 August-3 September 1954.

19. Potrzebowski, A., Misztal, J., Xu, H-M., Wyszynski, M. L., and Qiao, J., "An autoignition combustion model for homogeneous charge compression ignition engine cycle simulations," Proceedings of the Institution of Mechanical Engineers, Part D: Journal of Automotive Engineering, vol. 223, no.9, pp. 1027-1221, 2009.

20. Swan, K., Shahbakhti, M., and Koch, C. R., "Predicting start of combustion using a modified knock integral method for an HCCI engine," SAE Paper 2006-01-1086, 2006.

21. Shahbakhti, M., Lupul, R., and Koch, C. R., "Predicting HCCI auto-ignition timing by extending a modified knock-integral method," SAE Paper 2007-01-0222, 2007.

22. Hellstrom, E., and Stefanopoulou A. G., "Modeling cyclic dispersion in autoignition combustion," Proceedings of the 50th IEE Conference on Decision and Control, pp. 6834-6839, 2011.

23. Kodavasal, J., Lavoie, G. A., Assanis, D. N., and Martz, J. B., "The effects of thermal and compositional stratification on the ignition and duration of homogeneous charge compression ignition combustion," Combustion and Flame, 162(2), 451-461, 2015.

24. Fiveland, S. B., and Assanis, D. N., "Development of a two-zone HCCI combustion model accounting for boundary layer effects," SAE Technical paper 2001-01-1028, 2001.

25. Hoepke, B., Jannsen, S., Kasseris, E. and Cheng, W., "EGR Effects on Boosted SI Engine Operation and Knock Integral Correlation," SAE Int. J. Engines5(2): doi:10.4271/2012-01-0707, 2012.

26. Dec, J.E., Hwang, W., and Sjöberg, M., "An Investigation of Thermal Stratification in HCCI Engines Using Chemiluminescence Imaging," SAE Paper 2006-01-1518, 2006.

27. Kodavasal, J., “Effect of charge preparation strategy on HCCI combustion”, PhD Thesis, The University of Michigan, Ann Arbor, MI, 2013.

28. Vourliotakis, G., Kolaitis, D. I., and Founti, M. A., “Development and Parametric Evaluation of a Tabulated Chemistry Tool for the Simulation of n-Heptane Low-Temperature Oxidation and Autoignition Phenomena,” Journal of Combustion, vol. 2014, Article ID 237049, 13 pages, doi:10.1155/2014/237049, 2014.

29. Goldsborough, S. S., “A chemical kinetically based ignition delay correlation for iso-octane covering a wide range of conditions including the NTC region,” Combustion and Flame, 156(6), 1248-1262, 2009.

CHAPTER 6

EMPIRICAL BURN PROFILE AND VALIDATION OF COMBUSTION MODEL

6.1 Background

In 0D engine models the post ignition combustion is typically described by an empirically derived algebraic correlation. Auto-ignition is conceptually modeled as an auto-ignition cascade which depends on the location of ignition and operating conditions (engine speed, total dilution, etc.) [1-4]. Thus, typically the burn correlation consists of an algebraic expression which is used to determine the location of key mass fraction burned locations during combustion ($\theta_{50}$and θ_{90}). The burn profile is then modeled as a Wiebe curve [5] which has been shown to roughly approximate the burn profiles in SI and HCCI engines. Wiebe curves have been extensively used for 0D modeling in systems level studies since its initial publication. Ghojel [6] provides an exhaustive review of Wiebe function development and its evolution to recent times.

Prior empirical models are mostly based on closed cycle CFD [1] results or limited engine experiments [2-3]. Closed cycle CFD results typically tend to predict faster burn rates compared to engine experiments [4]. Chang et al. [2] for their burn correlation used a very small experimental data set of 28 points collected on a single cylinder 0.5 L engine representative of most passenger automotive engines with a higher geometric compression ratio of 12.5:1. They used a rebreathing type valve strategy with a small secondary exhaust event during intake in order to re-induct hot residual; however this strategy has fallen out of favor for potential commercial applications in recent years. Ortiz-Soto [3] used engine data from a single cylinder of similar dimensions and

geometric compression ratio in addition to closed cycle CFD simulations for the development of his burn rate model. Although 535 experimental data points were used for the fit there was no variation in terms of engine speed (constant at 2000 RPM) and very limited variation in terms of intake boost (1 bar – 1.2 bar). He also modified the algebraic expression without clean experiments or CFD studies justifying the sensitivities of individual parameters to combustion. Hellstrom et al. [21] and other control oriented studies typically adopt an even simpler function to model the post combustion burn in the interest of simplicity and saving computation time.

Potrzebowski et al. [19] and Qin et al. [9] have demonstrated through their HCCI gasoline heat release data that the burn profile can be divided into an initial slow burn followed by a fast burn portion. Both have presented burn profile models independent of Wiebe functions and based on a more complicated diesel correlation obtained by Watson et al. [11]. Qin et al. tuned their model with only six experimental points from 1500 rpm to 2000 rpm, only at ϕ=1 and naturally aspirated conditions. On the other hand Potrzebowski et al. had a larger data set of 45 points for model tuning over 1000 rpm to 2900 rpm, $0.77 < \phi < 1$ and naturally aspirated conditions.

This chapter focuses on two topics; (i) development of the new burn correlation, and (ii) performance evaluation of the full 0D combustion model including the adiabatic core ignition model. The new burn correlation models post ignition burn as a three step process; initial slow burn, fast burn and slow late burn. The burn model is still essentially an algebraic correlation that is a function of the following parameters: ignition location, engine speed, total dilution and a measure of intake boost. To avoid over fitting only the parameters that showed sensitivity to combustion were selected based on the KIVA simulations from Chapters 3 and 4. The engine and experiments used to fit the new correlation cover a much wider range of operating conditions compared to prior work as discussed in Chapter 2. The burn correlation along with the adiabatic core ignition model

are implemented in GT-Power© with the user subroutines. This model performance is then evaluated against experimental transient studies.

6.2 Burn profile model

Chapter 2 describes the three pressure analysis (TPA) in GT-Power used to obtain the heat release data from engine experiments. Figure 6.1(a) presents a mass fraction burned (MFB) profile (normalized by combustion efficiency) predicted by TPA for one of the measured cases (1500 rpm, 17.5 mg fuel/cycle/cylinder, 95^{o}CA NVO and 1.4 bar boost). HCCI combustion can be interpreted as a three-step process. First, intermediate temperature heat release [10], starting from -10^{o} CA there is a slow burning process up to around 2^{o}CA. Beyond 2^{o}CA the combustion proceeds rapidly which is the high temperature heat release, until 20^{o}CA aTDC. Beyond 20^{o}CA, there is slow burning until after 80^{o}CA aTDC which could be due to reactions in the cooler thermal boundary regions adjacent to the walls as shown by chemiluminescence imaging by Dec et al. [25] and predicted by Fiveland [18] and Yasar et al. [19].

Initial attempts to fit the experimental data with single and double Wiebe functions were not successful in capturing the experimental MFB profile shown in Figure 6.1(a). Instead, the three-step combustion process is modeled as three functions described schematically in Figure 6.1(b). The majority of the heat release, denoted by MFB_2, the blue curve in Figure 6.1(b), continues to be modeled as a Wiebe function [5, 6] which is defined based on θ_{IGN}, θ_{25}, θ_{50} and θ_{75}. The adiabatic core ignition model (Chapter 5) provides θ_{IGN} whereas θ_{25}, θ_{50} and θ_{75} are correlated as a function of θ_{IGN}, engine speed and other thermodynamic parameters. We know from Chapter 3 and Chapter 4 that the variables that have the most effect on HCCI burn profile are: Ignition timing (θ_{IGN}), total mixture dilution (ϕ'), engine speed (RPM) and boost pressure. Thus, Equation 6.1 through Equation 6.3 describe the forms of fit for θ_{25}, θ_{50} and θ_{75}.

$$\theta_{IGN-25} = (a_1^2\theta_{IGN}^2 + a_2\theta_{IGN} + a_3)\left(\frac{\phi'}{0.35}\right)^{x_1}\left(\frac{RPM}{2000}\right)^{x_2}\left(\frac{P_{TDC}}{25}\right)^{x_3} \quad \text{Equation 6.1}$$

$$\theta_{25-50} = (a_4^2\theta_{25}^2 + a_5\theta_{25} + a_6)\left(\frac{\phi'}{0.35}\right)^{x_4}\left(\frac{RPM}{2000}\right)^{x_5}\left(\frac{P_{TDC}}{25}\right)^{x_6} \quad \text{Equation 6.2}$$

$$\theta_{50-75} = (a_7^2\theta_{50}^2 + a_8\theta_{50} + a_9)\left(\frac{\phi'}{0.35}\right)^{x_7}\left(\frac{RPM}{2000}\right)^{x_8}\left(\frac{P_{TDC}}{25}\right)^{x_9} \quad \text{Equation 6.3}$$

where, θ_{IGN-25} = burn duration from ignition to 25% MFB,

θ_{25-50} = burn duration from 25% to 50% MFB,

θ_{25-50} = burn duration from 50% to 75% MFB,

RPM = engine speed (rpm),

ϕ' = fuel-to-charge equivalence ratio = $(m_{fuel}/(m_{total} - m_{fuel}))/(m_{fuel}/m_{air})_{st}$,

P_{TDC} = pressure at TDC calculated based on IVC conditions (bar) = $P_{IVC} \cdot (V_{IVC}/V_{TDC})^{\gamma_{IVC}}$ (measure of intake boost)

Figure 6.2 shows the comparison of the burn model predictions to the experimental values of θ_{25}, θ_{50} and θ_{75}. The good quality of fit suggests that if ignition is predicted correctly the main portion of the burn curve can be predicted with high accuracy.

The first (MFB_1), represented by the green line, and third (MFB_3) stage of combustion, represented by the red line in Figure 6.1(b) are described by the exponential and linear functional forms presented in Equation 6.4 and Equation 6.7 respectively. The range of crank angle (θ_{fit1}) selected for fitting MFB_1 is from the crank angle where MFB = 0.1% (θ_{IGN}) to the crank angle where $dRoHR/d\theta$ is at its maximum value; θ_{fit3} is selected for MFB_3 is from the crank angle where MFB = 95% to the crank angle where MFB = 100%. These fit ranges have been chosen in order to capture the shape of the curve correctly over the range of available data. Coefficients *A*, *B*, *M* and *C* are calculated for each of the measured experimental cases from the DOE such that the difference between the modeled and actual MFB is minimized over θ_{fit1} and θ_{fit2} respectively.

These coefficients are correlated to θ_{IGN} or θ_{50}, ϕ', RPM and P_{TDC} according to functional forms described in Equation 6.4 to Equation 6.9.

$$MFB_1(\theta) = A\exp(B\theta) \quad \text{Equation 6.4}$$

$$A = d_1 \exp(-d_2\theta_{IGN})\left(\frac{\phi'}{0.35}\right)^{c_1}\left(\frac{RPM}{2000}\right)^{c_2}\left(\frac{P_{TDC}}{25}\right)^{c_3} \quad \text{Equation 6.5}$$

$$B = (d_3\theta_{IGN}^2 + d_4\theta_{IGN} + d_5)\left(\frac{\phi'}{0.35}\right)^{c_4} \quad \text{Equation 6.6}$$

$$MFB_3(\theta) = M\theta + C \quad \text{Equation 6.7}$$

$$M = f_1 \exp(-f_2\theta_{50})\left(\frac{\phi'}{0.35}\right)^{e_1}\left(\frac{RPM}{2000}\right)^{e_2}\left(\frac{P_{TDC}}{25}\right)^{e_3} \quad \text{Equation 6.8}$$

$$C = (f_3 \exp(-f_4\theta_{50}) + 1)\left(\frac{\phi'}{0.35}\right)^{e_4}\left(\frac{RPM}{2000}\right)^{e_5} \quad \text{Equation 6.9}$$

The coefficients $a_1 - a_9$, $x_1 - x_9$, $c_1 - c_4$, $d_1 - d_5$, $e_1 - e_5$ and $f_1 - f_4$ are determined by fitting expressions to the DOE data by the method of linear least squares using the MATLAB optimization toolbox. Quadratic Bezier curves expressed by Equation 6.10 are employed for smooth transitions from $MFB_1$to MFB_2 and MFB_2 to MFB_3.

$$B(t) = (1-t^2)P_k + 2(1-t)tP_{k+1} + t^2P_{k+2} \quad \text{Equation 6.10}$$

where P_i are three control points and *t* is the unit distance traversed in the blending space. Referring back to Figure 6.1(b), the intersection between MFB_1 and MFB_2:P_1 and MFB_2 and MFB_3:P_4 are selected as the middle control point (P_{k+1} in Equation 6.10) for the transitions. Selecting the first and third points for the transition is a matter of calibration. Control point P0 is set as the crank angle at 1.5^o CA before P1 and the corresponding MFB while P2 is set as the crank angle at 1.5^{o}CA after P1 and the corresponding MFB. Similarly control point P3 is set as the crank angle at 1.5^o CA before P4 and the corresponding MFB and P5 is set as the crank angle at 8^{o}CA after P4 and the corresponding MFB. These values produce agreeable MFB and ROHR curve predictions

for the entire data set in terms of smooth transitions and matching the experimental curves.

The normalized cumulative mass fraction burned (norm. MFB) is a combination of the three distinct functions as explained earlier. However the true MFB curve has to account for the combustion efficiency as shown in Equation 6.11.

$$MFB(\theta) = C_{eff} \cdot [norm.MFB(\theta)] \quad \text{Equation 6.11}$$

The combustion efficiency is estimated by GT-Power TPA [5] based on HC and CO emissions data. These combustion efficiency values agree well with those estimated by Ortiz-Soto et al. [22]. The authors of [1] have shown that combustion efficiency is a strong function of maximum cylinder temperature and suggested using a hyperbolic fit to describe this dependency. Figure 6.3 shows the strong dependence of combustion efficiency on maximum cylinder temperature. The method used in this work to model the combustion efficiency is based on Ortiz-Soto [3]. The two conceptual intersecting lines in Figure 6.3 are used to fit a hyperbola which is a function of peak temperature and other global thermodynamic parameters, similar to the rest of the burn profile model. Equation 6.12 shows the form of fit for combustion efficiency.

$$C_{eff} = Fn_1(T_{peak})\left(\frac{\phi'}{0.35}\right)^{b_3}\left(\frac{rpm}{2000}\right)^{b_4}\left(\frac{P_{TDC}}{25}\right)^{b_5} \quad \text{Equation 6.12}$$

The hyperbolic function $Fn_1(T_{peak})$ is described in Equation 6.13-Equation 6.15.

$$Fn_1(T_{peak}) = \frac{-Fn_2(T_{peak}) - \sqrt{Fn_2(T_{peak})^2 - 4 \cdot Fn_3(T_{peak})}}{2} \quad \text{Equation 6.13}$$

$$Fn_2(T_{peak}) = -b_0(T_{peak} - b_1) - 2\eta_0 \quad \text{Equation 6.14}$$

$$Fn_3(T_{peak}) = \eta_0[\eta_0 + b_0(T_{peak} - b_1)] - b_2 \quad \text{Equation 6.15}$$

The parameter η_0 corresponds to the value of the horizontal line in Figure 6.3, is set as the maximum combustion efficiency of the engine from the data. Parameters b_i are also fit using the DOE data (Chapter 2) by the method of least squares using the MATLAB optimization toolbox. A R^2 value of 0.6 as seen in Figure 6.4 is attained after fitting. It is important to note that implementing the combustion efficiency model is non-trivial since combustion efficiency depends on peak temperature, and peak temperature is in turn based on combustion efficiency, therefore it is necessary to iterate the solution post ignition to achieve a converged value of peak temperature, starting from an initial guess.

6.3 Model validation

The adiabatic core ignition model, the three step burn profile model and combustion efficiency model have been implemented in GT-Power using the user subroutines. Figure 6.5 shows the predicted cylinder pressure, mass fraction burned (MFB) and rate of heat release (ROHR) for an example case (1500 rpm, 17.5 mg fuel/cycle/cylinder, 95^{o}CA NVO and 1.4 bar boost) from the simulation when the combustion phasing (θ_{50}) is matched to the experiment. The grey lines show all the cycles (300) recorded at steady state, the black line shows the cycle with the peak pressure closest to the mean peak pressure of all cycles at that operating condition and the dashed black line shows the simulation result. Overall the model shows good agreement with the experiment. The predicted peak pressure is higher by ~1 bar, which may result from the higher predicted pressure at TDC. The peak RoHR matches well with the experiment and even the shape is very similar to the experiment. The three step combustion process is visible from the MFB curve with the initial curve, Wiebe function and the slow late burn in the end. The end value of the MFB curve also lies within the experimental spread indicating that the combustion efficiency model performs well.

6.3.1 Ignition model calibration

The ignition model requires additional calibration to better match the experiments over the wide range of conditions within the dataset (Chapter 2), which includes large variations in the valve events, injection timing, manifold pressures, dilution levels and engine speed. This is achieved by applying a calibration factor (δE_{AC}) to the activation energy of the Goldsborough correlation such that $E_{AC-tuned} = E_{AC}/\delta E_{AC}$. As a result the predicted θ_{50} better matches the experimental θ_{50}. The calibration factor is then correlated to input parameters as shown in Equation 6.16.

$$\delta E_{AC} = \left(n_0 + n_1 \left(\frac{RGF}{45}\right) + n_2 \left(\frac{RPM}{2000}\right) + n_3 \left(\frac{RGF}{45}\right)^2 + n_4 \left(\frac{RGF}{45}\right)\left(\frac{RPM}{2000}\right) + n_5 \left(\frac{RPM}{2000}\right)^2 \right) \left(\frac{P_{TDC}}{25}\right)^{n_6} \quad \text{Equation 6.16}$$

Figure 6.6 shows the model predictions of θ_{50} against experiment with the activation energy of the Goldsborough ignition delay modified in three different ways. Figure 6.6(a) shows that the model results with un-tuned activation energy which predicts a late θ_{50} compared to experiments. This can be justified since the Goldsborough correlation is for isooctane whereas the experiments are performed with gasoline which has shorter ignition delay times compared to isooctane. Figure 6.6(b) shows the model prediction when the activation energy for the Goldsborough correlation has been reduced by a factor of 1.04 which is the mean of the activation energy reduction over the entire data set. Here the model performance is much better compared to the un-tuned correlation achieving an R^2 of 0.26 with an RMS error of 2.35^{o}CA. Figure 6.6(c) compares the prediction of the model with the Goldsborough correlation activation energy tuned as per Equation 6.16. The model achieves an even better prediction with an R^2 value of 0.63 and an RMS error of 1.7^{o}CA.

6.3.2 Transient response to changing engine speed

The performance of the improved HCCI model evaluated for a speed transient compared to experiments. The transient boundary conditions are prescribed per cycle, including the fuelling rate, engine speed, valve timings, injection timing, and instantaneous intake and exhaust pressures and intake and exhaust runner temperatures. The details are summarized in Table 6.1. Figure 6.7(a) shows the engine speed input to the experiment and model. It consists of a steady start at 2500 RPM followed by a ramp down from 2500 RPM to 1500 RPM in 2 seconds, a dwell at 1500 RPM for 5 seconds followed by a ramp up from 1500 RPM to 2500 RPM in 2 seconds and another steady state at 2500 RPM. Figure 6.7(b) shows the fuel-air equivalence ratio (ϕ) measured by the exhaust lambda sensor and in-cylinder ϕ predicted by the model. The model captures the experimental trend although being slightly lean in comparison ($\delta\phi$ = 0.02). The small difference could be due to the experimental value being measured in the exhaust after the catalyst for the total engine while the simulated value is the in-cylinder value for cylinder 1. Figure 6.7(c), (d) and (e) show the variation of ϕ', $\theta_{IGN}$and P_{TDC}, respectively; which are the variable that have an on the burn profile based on the model (Equation 6.1-Equation 6.3). ϕ' follows the curves of measured and predicted ϕ. The shape of θ_{IGN} response is the opposite of ϕ'; with greater ϕ' values at the initial and final steady state point correspond to an earlier θ_{IGN} while the lower ϕ' values in the middle correspond to a later θ_{IGN}. P_{TDC} does not change much through the transient since the intake manifold pressure remains roughly the same. Figure 6.7(f) shows the measured and predicted $\theta_{50}$for the speed sweep. The experimental θ_{50} is initially at a steady value of ~2.5°CA aTDC, which retards quickly with the speed ramp down (to ~ 9°CA aTDC), and continues to be pushed later (~ 10.5°CA aTDC) during the dwell period at 1500 rpm. As the engine speed is increased from 1500 rpm to 2500 rpm the phasing returns to ~ 2.75° CA aTDC. The model predicts a similar trend, with an initially advanced θ_{50} (1.6° CA

aTDC) at 2500 rpm, retarding to ~ 10°CA aTDC during the dwell. As the speed increases back to 2500 rpm the predicted θ_{50}advances to 1.75°CA aTDC. Figure 6.7(g) compares the measured and predicted 10-90 burn duration (θ_{10-90}). The trends in θ_{10-90}follow the trends in θ_{50}; initially the burn duration is short at ~5.5°CA which increases with decreasing speed to ~8.5°CA at 1500 rpm. As the speed increases back to 2500 RPM the θ_{10-90} reduces back to ~5.5°CA. In Figure 6.7(h) and (i) the peak pressure rise rate (PPRR) and peak pressure (P_{MAX}) trends follow from the trends of combustion phasing and burn duration. An early phasing and short duration produces higher PPRR's and P_{MAX} and vice versa. The model predictions match the experiment with good agreement for the PPRR. The peak pressure predictions match the experimental trend at the initial and final steady state but tend to over predict by about 1bar in the middle dwell period at 1500 rpm. Figure 6.7(j) shows the variation of the experimental and predicted gross (IMEPg) and net IMEPs (IMEPn) through the engine speed transient. The model matches experimental trend while but over predicts IMEPg by up to 15 kPa and IMEPn by up to 7 kPa. This is in part due to the model tending to over predict the peak pressure, increasing the area under the p-V curve during expansion.

Figure 6.8 presents analysis to isolate the relative importance of the components of the burn profile model. Figure 6.8(a) and (b) show the $\theta_{50}$and θ_{10-90}variation for the speed transient if θ_{IGN}, engine speed, $\phi'$and P_{TDC}trajectories are imposed independently while holding the other variables constant at the initial values. The solid black line denotes results when all the changing variables are imposed on the burn correlation producing the 'Default' result. The contributions of $\phi'$and $P_{TDC}$to the burn profile are minimal and in the opposite direction essentially cancelling each other out. However θ_{IGN} and engine speed have a dominant effect on the burn profile. If the θ_{IGN} alone is changed the $\theta_{50}$is more retarded and $\theta_{10-90}$is longer than the 'Default' case. On the other hand the engine speed has an opposite effect on the burn profile compared to θ_{IGN}. As a result

even though reducing engine speed should advance combustion; it pulls the phasing back a little reducing the effect of late ignition timing.

6.3.3 Transient response to changing EVC timing

The performance of the improved HCCI model is evaluated for an EVC input transient compared to experiments in a manner similar to the speed transient. The details of the operating conditions for experiment are summarized in Table 6.2. Figure 6.9(a) shows the EVC input to the experiment and model. Starts off at a steady input of EVC = 303°CA aTDC followed by a step change to 293°CA aTDC, then a dwell of 8 seconds followed by a step change back to 303°CA aTDC. Figure 6.9(b) shows the simulated ϕ following the experimental value with a slight difference at the beginning and end of the initial and final steady state. The ϕ' follows the curves of measured and predicted ϕ. θ_{IGN} trace is trend wise opposite to the ϕ' trace as seen in the previous section. P_{TDC} changes minimally through the transient again since the intake manifold pressure does not change much. In Figure 6.9(f), the experimental θ_{50} is initially at a steady value ~4.5°CA aTDC, advances quickly to ~2.5°CA aTDC with the EVC change and stays there during the dwell period. θ_{50} returns to ~ 4.25°CA aTDC as EVC changes back to 303°CA. The model behavior is similar to the experiment but predicts late θ_{50} (by ~2.5°CA) for the initial and final steady point. The θ_{10-90} trend shown in Figure 6.9(g) follows the θ_{50} trend and the model predictions match the experiment with slight variations. Similarly the PPRR and P_{MAX} predictions match the experimental trends in Figure 6.9(h) and (i). The model over predicts the IMEPg IMEPn by up to 10 kPa as seen in Figure 6.9(j).

The effect of changing θ_{IGN}, RPM, $\phi'$and P_{TDC}independently on the burn profile through the transient is presented in Figure 6.10 (a) and (b). Similar to the speed transient the solid black line presents the 'Default' result when all the varying inputs are imposed on the correlation. The effect of $\phi'$and P_{TDC} on θ_{50} is minimal and in the opposite

direction to each other, cancelling each other out as seen in Figure 6.10(a). The engine speed has no effect at all since it is held constant during this transient. $\phi'$and P_{TDC} are relatively more important for θ_{10-90} compared to θ_{50} as seen in Figure 6.10(b). θ_{IGN} and ϕ' shorten θ_{10-90} drastically whereas P_{TDC} makes it a little long.

6.3.4 Transient response to change in SOI

The details of SOI transient are summarized in

Table 6.3. Figure 6.11(a) shows the SOI input to the experiment and model; step change from 420°CA aTDC to 360°CA aTDC followed by a dwell for 8 seconds followed by a step change back from 360°CA aTDC to 420°CA aTDC. Figure 6.11(b) shows the measured and predicted value of fuel-air equivalence ratio (ϕ). The model captures the experimental trend although being slightly leaner at the initial and final steady state. ϕ' trend in Figure 6.11(c) matches the trend in ϕ and θ_{IGN} trend is opposite to the ϕ' trend as seen in Figure 6.11 (d). Similar to the previous two transients, P_{TDC} hardly changes by 1 bar through the transient as seen in Figure 6.11 (e). θ_{50} advances from ~8.3°CA aTDC to ~3°CA aTDC with advancing SOI and vice versa as seen in Figure 6.11(f). The model predictions match the experimental θ_{50} very well. Similar to the previous transients θ_{10-90}, PPRR and P_{MAX} follow the combustion phasing trends as seen in Figure 6.11(g), (h) and (i). Model predictions for burn duration are consistently shorter than the experiment by less than 1^{o}CA. The PPRR model predictions nearly match the experiment but the peak pressure is over predicted by up to 1.5 bar through the transient. The model over predicts IMEPg by up to 12 kPa and over predicts the IMEPn by up to 6 kPa as seen in Figure 6.11(j).

In Figure 6.12 the result isolates the effects of independently varying θ_{IGN}, engine speed, $\phi'$and P_{TDC} on the burn profile for the SOI transient. In Figure 6.12 (a) and (b) for θ_{50} and θ_{10-90}resepectively, the solid black line shows the 'Default' result when all the inputs to the burn correlation are varied. From Figure 6.12(a), similar to the EVC

transient, the contributions of $\phi'$and P_{TDC} to θ_{50} are minimal and in the opposite direction cancelling each other. From Figure 6.12(b) for θ_{10-90}, the effect of $\phi'$and P_{TDC} are relatively important compared to θ_{IGN} but they still have an opposite effect and cancel each other out. The timing θ_{IGN} has the most effect on the burn profile for SOI transient.

6.3.5 Transient response to change in fueling

This section analyzes the fuel step change in a manner similar to the previous sections. Figure 6.13 presents the model predictions compared to experiments. The model trends match the experiment overall with slight variations in the absolute values.

The effect of independently varying θ_{IGN}, engine speed, $\phi'$and P_{TDC} on the burn profile is presented in Figure 6.14. $\phi'$and P_{TDC} have a negligible and opposite effect on θ_{50}, cancelling each other as seen in Figure 6.14(a). θ_{IGN} has a dominant effect on θ_{50} for the fuel step change. ϕ' has a relatively greater effect on θ_{10-90}, while P_{TDC} still has a negligible effect. θ_{IGN} and ϕ' shorten the of burn duration in equal parts as seen in Figure 6.14(b).

6.4 Summary

In this chapter a new burn profile correlation is formulated and tuned based on experimental heat release data. The new burn correlation captures the slope of the main burn, models the initial intermediate temperature heat release as well as the late slow burn observed in the experiment. The burn correlation produces a mass fraction burned profile that is well matched to the experiment provided the ignition is matched. The ignition model needs some calibration for it to predict experimental behavior nicely over the entire engine operating range. This is achieved by modifying the activation energy in the ignition delay correlation based on engine speed, RGF and intake boost. This is perhaps due to the fact that the adiabatic core ignition model operates under the

assumption of a uniform charge at IVC which is not valid for NVO-DI HCCI. The error may also be compounded by the fact that the ignition delay correlation for iso-octane is used in the ignition model while HCCI experiments used gasoline fuel. The calibrated model reproduces transient experiment trends for changing engine speed, EVC, SOI and mass of fuel injected. There are slight variations in the absolute values predicted by the model compared to the experiment. Some amount of cyclic coupling is captured by the model but it is unable to capture the large cycle-to-cycle variations. This could in part be because of NVO heat release which is not being modeled.

Additionally, the burn correlation is exercised as a tool to isolate the effects of engine speed, ϕ', intake boost and ignition timing on the burn profile. For the engine speed transient, the resulting changes in θ_{IGN} and engine speed had a dominant and opposite effect on burn duration. Retarding or advancing θ_{IGN} made the burn duration longer or shorter, respectively, while reducing or increasing speed makes the burn duration shorter or longer respectively. For the EVC and SOI transients, θ_{IGN} had the most effect on the burn duration. For the fuel transient, θ_{IGN} and ϕ' equally affected the burn duration. Advancing θ_{IGN} or increasing ϕ' shortened the burn duration while retarding θ_{IGN} or decreasing ϕ' lengthened the burn duration.

Table 6.1 – Experimental operating conditions for speed transient

Actuator	**Value**
Fuel injected	9.72 mg/cycle
Engine Speed	2500 → 1500 → 2500 RPM
EVC	298°CA aTDC
IVO	417.3°CA aTDC
Start of Injection	360°CA aTDC

Table 6.2 – Experimental operating conditions for exhaust valve timing transient

Actuator	**Value**
Fuel injected	11.12 mg/cycle
Engine Speed	1500 RPM
EVC	306 → 296 → 306°CA aTDC
IVO	417.3°CA aTDC
Start of Injection	360°CA aTDC

Table 6.3 – Experimental operating conditions for injection timing transient

Actuator	**Value**
Fuel injected	11.12 mg/cycle
Engine Speed	1500 RPM
EVC	292°CA aTDC
IVO	417.3°CA aTDC
Start of Injection	420→ 360 → 420°CA aTDC

Table 6.4 – Experimental operating conditions for mass of fuelling transient

Actuator	**Value**
Fuel injected	10.4 →12.6 mg/cycle
Engine Speed	1800 RPM
EVC	285°CA aTDC
IVO	431°CA aTDC
Start of Injection	440°CA aTDC

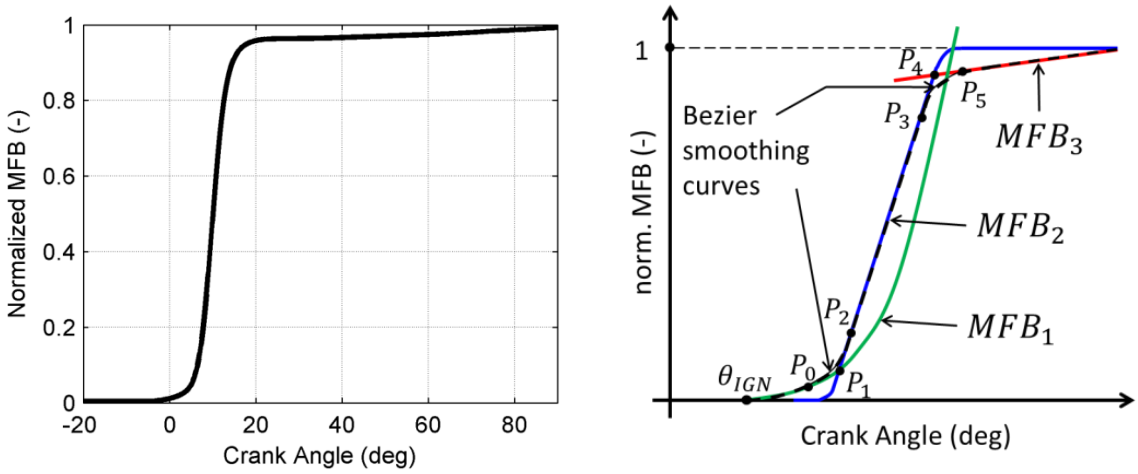

(a) (b)

Figure 6.1 – (a) Example MFB curve for measured HCCI case, (b) Schematic description of the three-step HCCI combustion process.

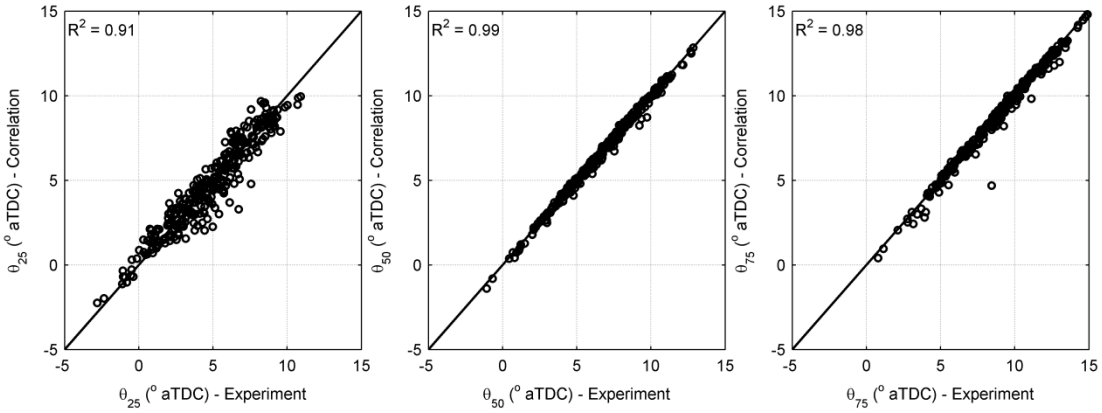

(a) (b) (c)

Figure 6.2 – Comparison of correlation predictions to the experimental values of (a) location of 25% fuel burned (θ_{25}), (b) location of 50% fuel burned (θ_{50}) and (c) location of 75% fuel burned (θ_{75})

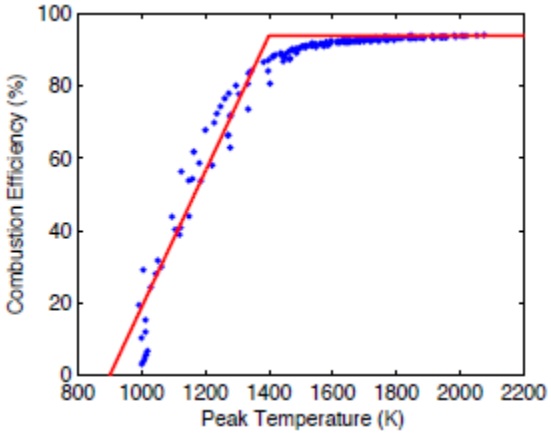

Figure 6.3 – Combustion efficiency variation with peak temperature from closed cycle reacting CFD simulations [3]. The two intersecting lines provide a basis for the hyperbolic fit used in the model.

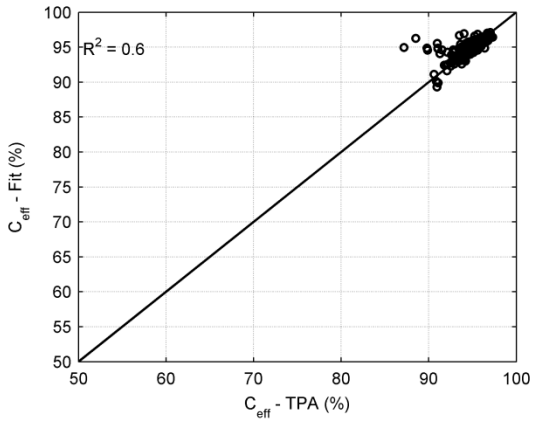

Figure 6.4 - Comparison of correlation predictions to the experimental values of combustion efficiency

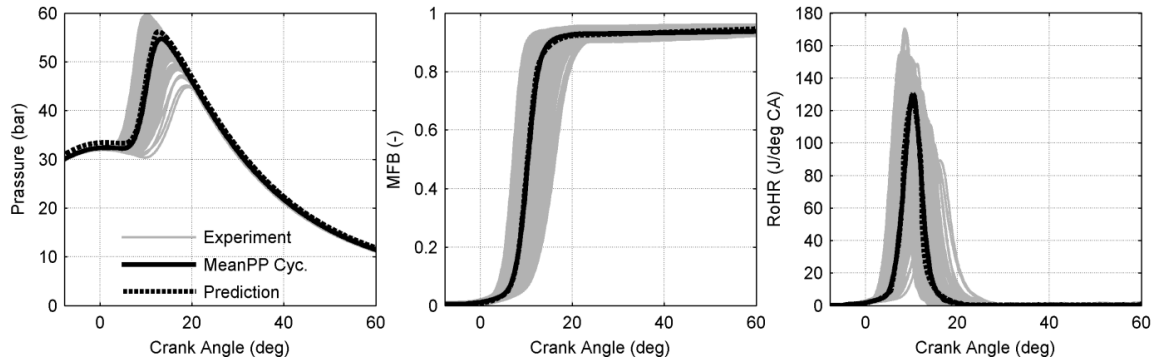

(a) (b) (c)

Figure 6.5 – Comparison between experiment and simulation (a) pressure trace, (b) mass fraction burned and (c) rate of heat release at 1500 RPM, 17.5 mg fuel, 95 deg NVO and 1.4 bar boost. The grey lines represent all cycles, the black line represents the cycle with the peak pressure closest to the mean PP and the dashed black line represents the simulation result.

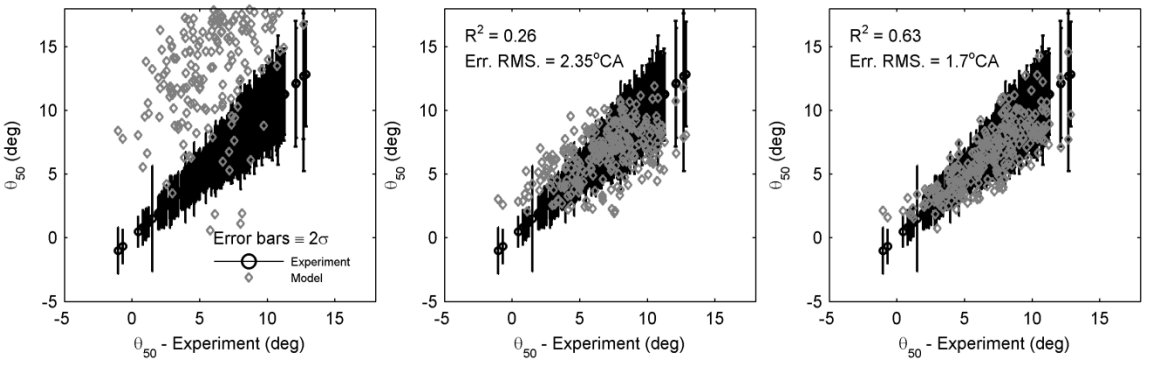

(a) (b) (c)

Figure 6.6 – Location of 50% MFB (θ_{50}) for the mean PP cycle as a function of the mean experimental location of θ_{50} with the Goldsborough correlation activation energy (a) un-tuned, (b) divided by a constant $\overline{\delta E_{AC}}$=1.04 and (c) divided by the calibration factor δE_{ac}

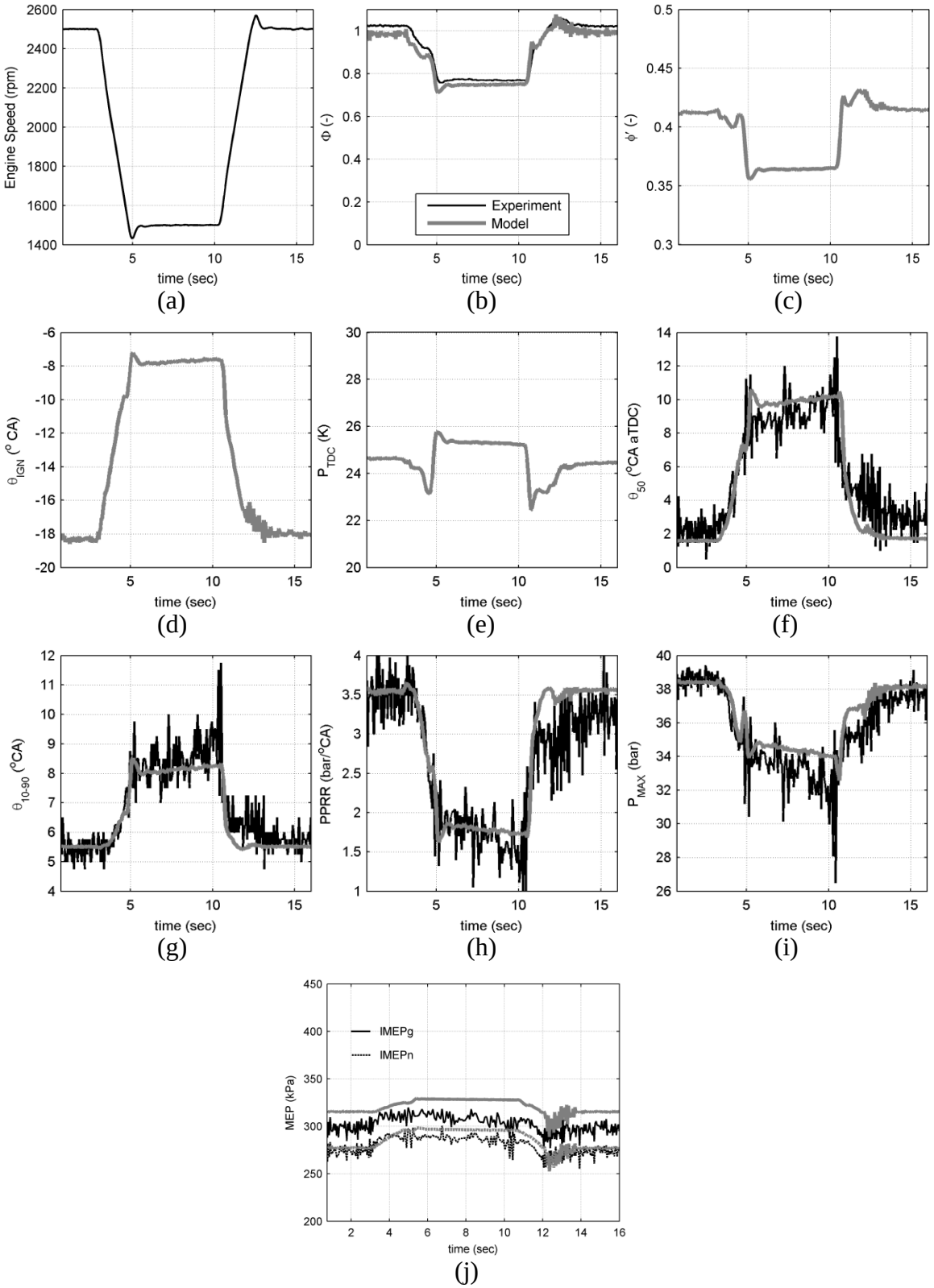

Figure 6.7 – Model predictions and experimental measurements for a transient speed change: (a) speed input (b) ϕ, (c) ϕ', (d) θ_{IGN}, (e) P_{TDC}, (f) θ_{50}, (g) θ_{10-90}, (h) PPRR, (i) P_{MAX} and (j) MEP's.

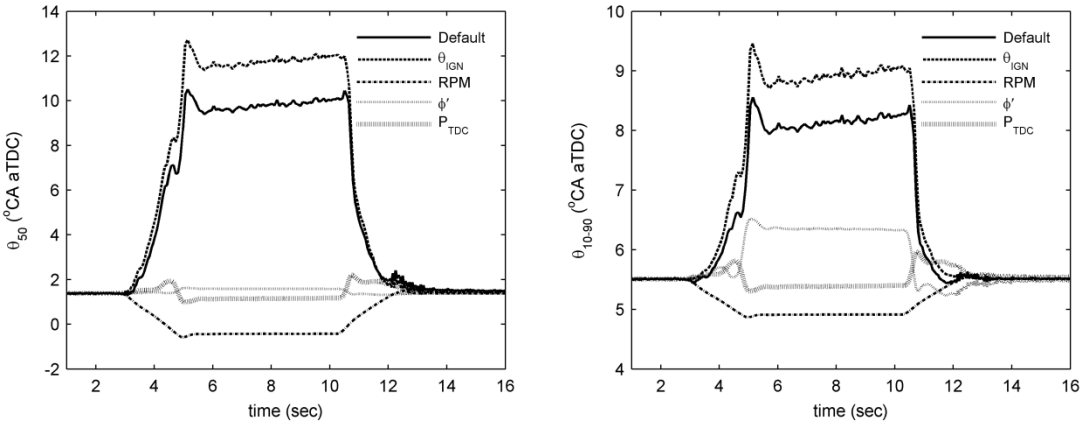

(a) (b)

Figure 6.8 – Effect of individual variables on the burn profile for speed transient; (a) θ_{50}, (b) θ_{10-90}

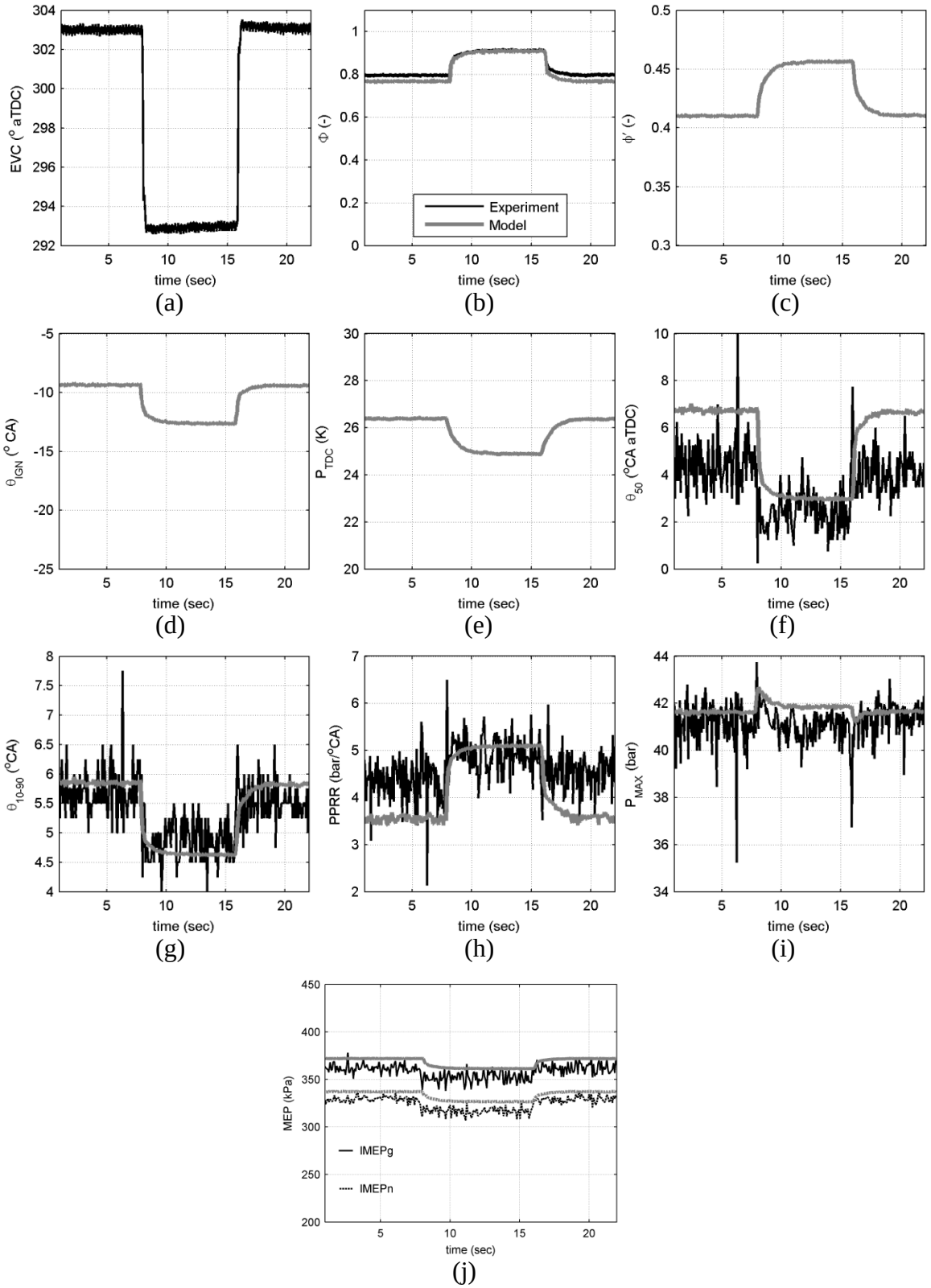

Figure 6.9 – Model predictions compared to experiment for a transient exhaust valve timing change: (a) EVC input, (b) ϕ, (c) ϕ', (d) θ_{IGN}, (e) P_{TDC}, (f) θ_{50}, (g) θ_{10-90}, (h) PPRR, (i) P_{MAX} and (j) MEP's.

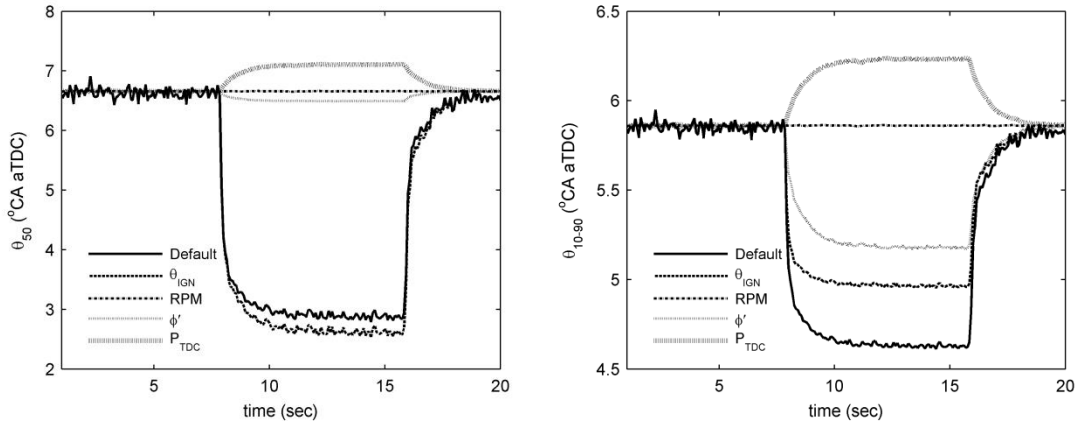

(a) (b)

Figure 6.10 – Effect of individual variables on the burn profile for EVC transient; (a) θ_{50}, (b) θ_{10-90}

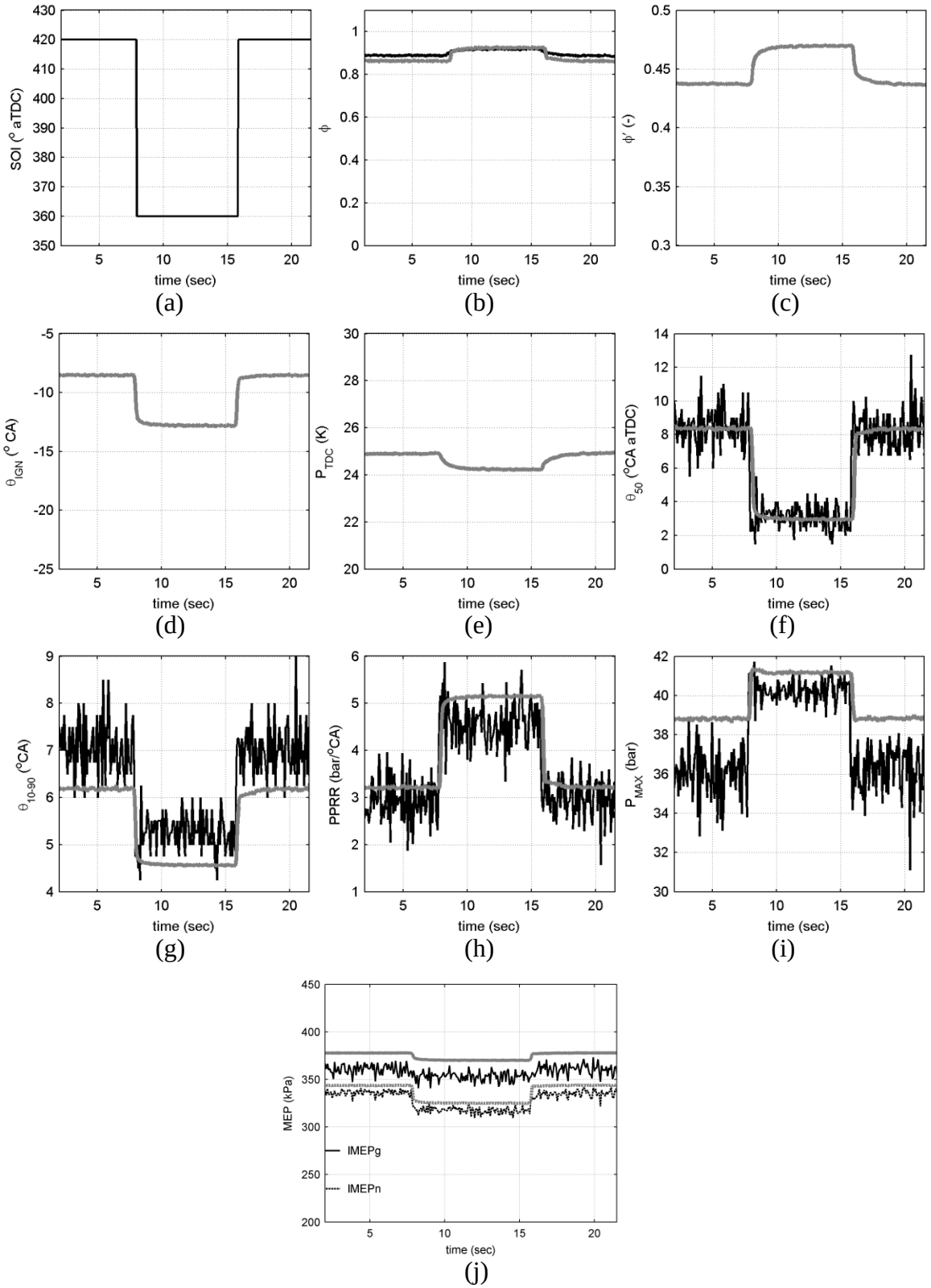

Figure 6.11 – Model predictions compared to experiment for a transient start of injection timing change: (a) injection timing, (b) ϕ, (c) ϕ', (d) θ_{IGN}, (e) P_{TDC}, (f) θ_{50}, (g) θ_{10-90}, (h) PPRR, (i) P_{MAX} and (j) MEP's.

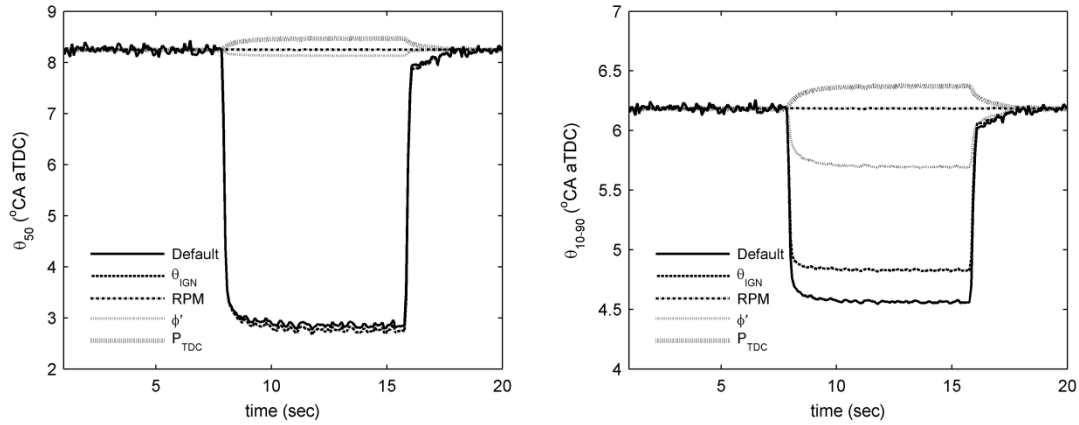

(b) (b)

Figure 6.12 – Effect of individual variables on the burn profile for SOI transient; (a) θ_{50}, (b) θ_{10-90}

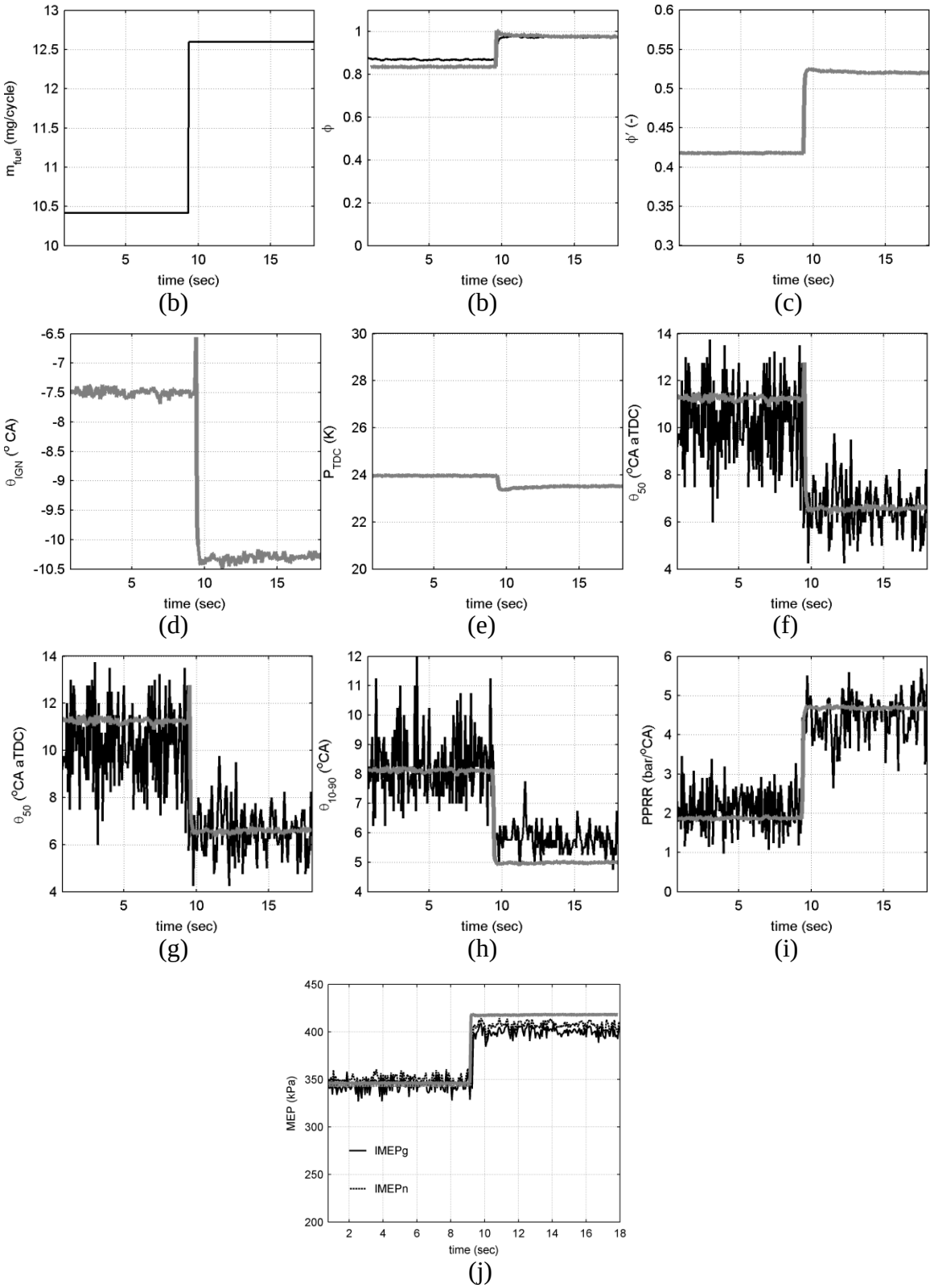

Figure 6.13 – Model predictions compared to experiment for a transient in fuel mass injected: (a) m_{fuel} per cycle per cylinder, (b) ϕ, (c) ϕ', (d) θ_{IGN}, (e) P_{TDC}, (f) θ_{50}, (g) θ_{10-90}, (h) PPRR, (i) P_{MAX} and (j) MEP's.

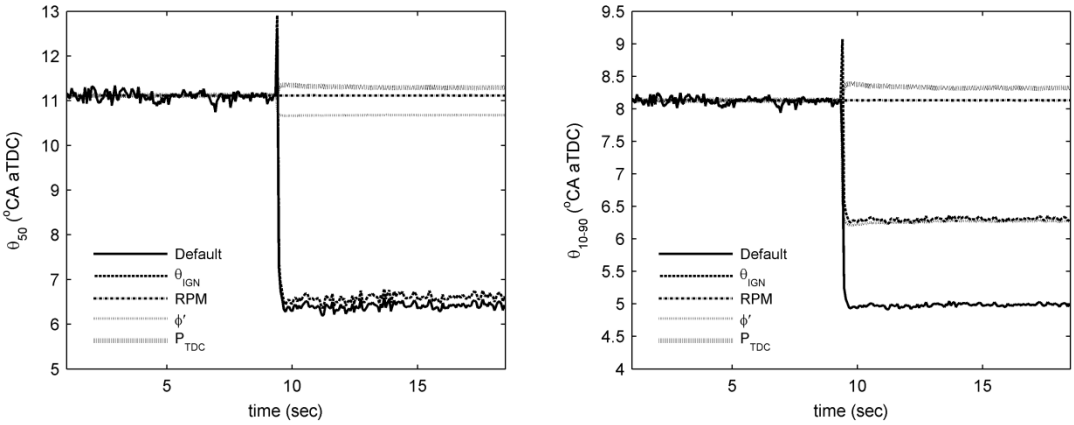

(c) (b)

Figure 6.14 – Effect of individual variables on the burn profile for fuel mass transient; (a) θ_{50}, (b) θ_{10-90}

6.5 References

1. Babajimopoulos, A., Challa, P.C.V.S.S., Lavoie, G., and Assanis, D. N., "Model-Based Assessment of Two Variable Cam Timing Strategies for HCCI Engines: Recompression Vs. Rebreathing. Proceedings of the ASME International Combustion Engine Division 2009 Spring Technical Conference," ICES2009-76103, 2009.
2. Chang, K., Babajimopoulos, A., Lavoie, G. A., Filipi, Z. S., & Assanis, D. N., "Analysis of load and speed transitions in an HCCI engine using 1-D cycle simulation and thermal networks," SAE Technical Paper 2006-01-1087, 2006.
3. Ortiz-Soto, E., "Combustion modeling of spark assisted compression ignition engines for experimental analysis and engine system simulations," PhD Thesis, The University of Michigan, Ann Arbor, MI, 2013.
4. Shingne, P., Assanis, D., Babajimopoulos, A., Mond, A., & Yilmaz, H., "Application of a Supercharger in a Two-Stage Boosting System for a Gasoline HCCI Engine: A Simulation Study," Proceedings of ASME Internal Combustion Engine Division Fall Technical Conference, pp. 547-556, 2011.
5. GT-Suite Engine Performance Application Manual., Version 7.23.
6. Ghojel, J. I., "Review of the development and applications of the Wiebe function: a tribute to the contribution of Ivan Wiebe to engine research," International Journal of Engine Research, 11(4), 297-312, 2010.
7. Hellstrom, E., and Stefanopoulou A. G., "Modeling cyclic dispersion in autoignition combustion," Proceedings of the 50th IEE Conference on Decision and Control, pages 6834-6839, 2011.

8. Potrzebowski, A., Misztal, J., Xu, H-M., Wyszynski, M. L., and Qiao, J., "An autoignition combustion model for homogeneous charge compression ignition engine cycle simulations," Proceedings of the Institution of Mechanical Engineers, Part D: Journal of Automotive Engineering, 223: 1207, 2009.

9. Qin, J., Xie, H., Zhang, Y., & Zhao, H. "A combustion heat release correlation for CAI combustion simulation in 4-stroke gasoline engines," SAE Technical Paper 2005-01-0183, 2005.

10. Dec, J. E., Yang, Y. and Dronniou, N., "Boosted HCCI - Controlling Pressure-Rise Rates for Performance Improvements using Partial Fuel Stratification with Conventional Gasoline," *SAE Int. J. Engines* **4**(1):1183-1203, 2011.

11. Watson, N., Piley, A. D., and Marzouk, M., "A combustion correlation for diesel engine simulation," SAE Paper 800029, 1980.

12. Polovina, D., McKenna, D., Wheeler, J., Sterniak, J., Miersch-Wiemers, O., Mond, A., & Yilmaz, H., "Steady-state combustion development of a downsized multi-cylinder engine with range extended HCCI/SACI capability," SAE Int. J. Engines 6(1), doi: 10.4271/2013-01-1655, 2013.

13. Stivender, D. L., "Development of a Fuel-based mass emission measurement procedure," SAE Paper 710604.

14. Shingne, P., Assanis, D., Babajimopoulos, A., Keller, P., Roth, D., and Becker, M., "Turbocharger Matching for a 4-Cylinder Gasoline HCCI Engine Using a 1D Engine Simulation," SAE Paper 2010-01-2143, 2010.

15. Shingne, P. S., Gerow, M. S., Triantopoulos, V., Bohac, S. V., & Martz, J. B., "A Comparison of Valving Strategies Appropriate For Multimode Combustion

Within a Downsized Boosted Automotive Engine—Part I: High Load Operation Within the Spark Ignition Combustion Regime," Journal of Engineering for Gas Turbines and Power, 136(10), 101507, 2014.

16. Woschni, G., "A Universally Applicable Equation for the Instantaneous Heat Transfer Coefficient in the Internal Combustion Engine," SAE Technical Paper 670931, doi:10.4271/670931, 1967.

17. Dec, J.E., Hwang, W., and Sjöberg, M., "An Investigation of Thermal Stratification in HCCI Engines Using Chemiluminescence Imaging," SAE Paper 2006-01-1518, 2006.

18. Fiveland, S. B., "Modeling and experimental studies of a large-bore natural gas engine operating on homogeneous charge compression ignition," PhD Thesis, The University of Michigan, Ann Arbor, MI, 2002.

19. Yasar, H., Soyhan, H. S., Walmsley, H., Head, B., and Sorusbay, C., "Double-Wiebe function: an approach for single-zone HCCI engine modeling," Applied Thermal Engineering 28: 1284-1290, 2008.

20. Stivender, D. L., "Development of a Fuel-based mass emission measurement procedure," SAE 710604, 1971.

21. K. Chang, "Modelling and analysis of an HCCI engine during thermal transients using a thermodynamic cycle simulation with a coupled wall thermal network," Ph. D. Thesis, University of Michigan, Ann Arbor, MI, 2010.

22. Ortiz-Soto, E. A., Lavoie, G. A., Martz, J. B., Wooldridge, M. S., & Assanis, D. N., "Enhanced heat release analysis for advanced multi-mode combustion engine experiments," Applied Energy, 136, 465-479, 2014.

CHAPTER 7

HCCI RECOMPRESSION HEAT RELEASE AND CYCLIC COUPLING

At certain operating conditions HCCI has high cyclic variability even though all the inputs are held constant [1, 2]. HCCI cyclic variability has been historically attributed to both stochastic effects and deterministic coupling between cycles. Much work has been done since the 70's and 80's to understand cyclic variability in engines. Finney et al. provide an exhaustive review of developing understanding of cyclic variability in internal combustion engines [3]. Hellstrom et al. [4] have attributed the coupling between cycles to unburned fuel being carried over from the previous cycle to re-compression where it reacts and releases heat. Figure 7.1 shows the phasing variability for consecutive cycles for high variability HCCI operation. Note the high recompression peak pressure due to heat release for Cycle [451+2] following a near misfire for the main compression of Cycle [451+1]. Figure 7.2 shows optical images of chemiluminescence of OH from 20°bTDC to TDC of main and recompression. The image depicts high OH at TDC of main compression and noticeable OH is also seen around TDC NVO indicating heat release.

Several experimental studies have investigated recompression (or NVO) heat release by varying the amount and timing of fuel injected during NVO. Song and Edwards [6] speculate that recompression processes encompass fuel pyrolysis, reformation, exothermic reactions and charge cooling. They observed increased exothermic reactions with progressive leaning of the mixture. Fitzgerald and Steeper [7] have reported lowering NVO combustion efficiency with increasing fuel delivery into NVO. Comparing main cycle combustion phasing with and without NVO injection, while

matching main compression temperatures, they concluded that the effect of recompression heat release on the main cycle was primarily thermal. Hunicz et al. [8] inferred a temperature rise at the end of NVO expansion for early injection (40°bTDC NVO) into a lean charge (ϕ=0.83) with varying amount of fuel delivery in their split injection study. In the same study for a stoichiometric charge, early injection with varying fuel mass delivery produced only charge cooling and lower end of NVO temperatures. Another study by Hunicz et al. [9] reports a retard in main combustion phasing with retarding injection timing from TDC to 60°CA aTDC NVO.

Researchers have modeled NVO heat release with a range of fidelity. Controls oriented models like the one by Hellström et al. [10] reproduce the dynamic evolution of cyclic variability. Others have modeled the process as a 0D variable volume reactor with chemical kinetics [7, 11 12]. While these studies are instructive, they neglect the effects of compositional and thermal stratification associated with fuel injection, residuals and heat loss which are important for HCCI combustion. A limited number of CFD studies have also modeled NVO heat release. Aroonsrisopon et al. [13] modeled fuel injection during NVO in an iso-octane fueled HCCI engine with 2D KIVA-3V. The simulations were initialized using a uniform composition of combustion products and intermediates measured in the exhaust. This model captured the thermal stratification and compositional stratification associated with the fuel injection. There was uncertainty in the initialization of the model state at exhaust valve closing. Hessel et al. [14] modeled NVO HCCI experiments with a multi-zone combustion model implemented in KIVA-3V for a full cycle with a 3D mesh. The study used a 33 species skeletal PRF mechanism [15]. NVO heat release similar in magnitude to the experiment was observed and no LTHR was observed. The simulations also suggested that thermal effects are more important than the chemical effects of carried over charge, for the main heat release.

It is unclear if the recompression heat release mechanism is primarily auto-ignition of unburned gas or if this heat release results from the oxidation of the directly

injected fuel Additionally the extent of thermal and compositional stratification, especially with changing fuel injection timing, during recompression and its effect on heat release is unknown. It is also unclear if the thermal or chemical (intermediate species) effect of recompression on the subsequent cycle is dominant. CFD simulations performed to draw insight into the underlying NVO processes are described in this chapter. These simulations are performed for a second cycle with chemistry active through NVO in KIVA-3V using the threshold and chemical mechanism swap method (described in Chapter 2) proposed by Middleton and Martz [16]. It is demonstrated that CFD can capture the deterministic coupling between cycles. Mechanisms of NVO heat release are described, and the state of reacting charge is presented in terms of temperature and composition. A simple 0D model is then proposed based on the findings.

7.1 Multi-cycle simulation of HCCI with late combustion phasing

KIVA simulation was conducted based on the NVO case in Chapter 2. The intake temperature was reduced by 40°C to retard combustion phasing to θ_{50}=12°CA aTDC. A second consecutive cycle was also simulated following the late phasing first cycle using the thresholding method previously described in Chapter 2 [16]. An additional cycle was simulated with heat release during NVO disabled. Details of the operating conditions are found in Table 7.1. Figure 7.3 displays the (a) pressure traces and (b) mass fraction burned from experiment and CFD. The CFD prediction lies within the experimental spread of 200 consecutive cycles recorded at steady state. Figure 7.4 presents the pressure traces during (a) NVO and (b) main compression for cycle 1 and cycle 2. An increase in the NVO peak pressure of 0.3 bar from cycle 1 to cycle 2 is accompanied by an advance of 5°CA in the θ_{50} phasing. It is speculated that the increase in the experimental NVO pressure is due to heat release. Figure 7.5 shows the predicted (a) cumulative heat release during NVO/main compression and (b) mean temperature during NVO with and without

heat release active in the model. The cumulative heat release during main compression is 400 J whereas during NVO only 5 J of heat is released. It is noted that the main burn starts relatively late (-10°CA aTDC) and is completed in a relatively short duration by 30°CA aTDC. On the other hand the heat release during NVO starts relatively early, at -40°CA aTDC-NVO and is completed by 20°CA aTDC-NVO, before injection starts at 30°CA aTDC-NVO. The 5 J of heat released leads to a ~20 K increase in the peak mean temperature of the charge. The hotter residuals increase the charge temperature at IVC for the second cycle by 5 K advancing the combustion phasing. The thermal and chemical effects of NVO heat release on combustion of cycle 2 are isolated in subsequent sections.

Figure 7.6 shows the evolution of species mass fractions through NVO (a) fuel, (b) intermediates and (c) oxygen and products of complete combustion. Note the initial fuel species mass fractions are very small (of the order of 10^{-4}) and reduce further until TDC of NVO. The mass fractions of CO, H_2, CH_2O and H_2O_2 fall until TDC of NVO, whereas the mass fraction of OH increases, peaking at TDC of NVO and falling to nearly zero by the start of injection. The CO mass fraction is several orders of magnitude greater than other species. CO_2 and O_2 mass fractions change slightly whereas H_2O mass fraction remains roughly the same. These results imply that the 5 J of heat release during NVO is due to oxidation of CO, CH_2O and other intermediates.

7.1.1 Validity of reduced gasoline reaction mechanism for lean NVO conditions

The reaction scheme described in Chapter 2 has been used for the reacting simulations during NVO. The reduced gasoline mechanism [17] used here is based on the detailed mechanism [18] which captures a wide range of engine operating conditions in terms of pressure, temperature, fuel reformation, and pyrolysis. Ignition delays computed by the two mechanisms are compared at a crank angle location during the baseline case simulation to confirm the validity of the reduced mechanism. Non-reacting CFD

simulations for the baseline condition are performed for NVO up to 380°CA bTDC (20°CA bTDC of NVO). Ignition delays using constant volume homogeneous adiabatic reactor are computed for the local thermodynamic states at this location. Figure 7.7 shows the ignition delays computed by detailed and reduced mechanisms for selected and all CFD cells respectively. The red dots are the ignition delays for all CFD cells computed by the reduced mechanism. For comparison, cells are selected across the range of temperatures to compute the ignition delays using the detailed mechanism denoted by the blue circles and the corresponding ignition delays using the reduced mechanism are denoted by the black squares. Although the ignition delays vary up to two orders of magnitude (0.01 ms to 1 ms) within the CFD domain, the reduced mechanism predicts only slightly longer ignition delays compared to the detailed mechanism and the results are directionally matched. For the shortest ignition delays, the error is 0.02 ms which is equivalent to 0.24°CA at 2000 RPM while for the longest ignition delays, the error is 0.1 ms which is equivalent to 1.2°CA. The difference in ignition delays predicted by the reduced mechanism compared to the detailed mechanism is relatively small, providing confidence in the reduced mechanism under lean NVO conditions.

7.2 Impact of NVO heat release on cylinder temperature and subsequent cycle

At the IVC of cycle 2 the mean cylinder temperature is 531 K, 6 K hotter than the mean temperature at IVC for cycle 1. Another CFD simulation is performed from the IVC of the second cycle to isolate the effect of temperature on the combustion phasing. This is done by the thresholding method with higher threshold values to force only the primary species to remain, while maintaining the temperature. Table 7.2 summarizes the mass fractions of species at IVC of second cycle with the actual and the simple composition. Figure 7.8 shows the second cycle with the default composition and with the simple composition with the experimental data. The two simulation curves lie nearly

on top of each other. This shows that the effect of NVO heat release on the next cycle is primarily thermal.

7.3 Effect of residual fuel on the next cycle without NVO heat release

To isolate the chemical effect of carried over species from the previous cycle on combustion of the second cycle another simulation is performed. In this case the species from the previous cycle are carried over to the next cycle with combustion during NVO disabled. The IVC temperature of cycle two without NVO heat release is the same as IVC temperature of cycle 1 (525 K). The IVC composition includes several intermediate species summarized in Table 7.3. Figure 7.9 shows cycle 2 with and without NVO heat release. Carrying over unburned fuel and species from the previous cycle without NVO heat release advances combustion phasing by about 2.5°CA. This is half the effect compared to having higher IVC temperatures due to NVO heat release (5°CA advance).

7.4 Effect of combustion efficiency on the subsequent cycle

An intake temperature sweep is performed based on the baseline late phasing case (Table 7.1). Table 7.4 summarizes the operating conditions for the intake temperature sweep including the combustion efficiency for cycle 1, $\theta_{50-cycle1}$and $\Delta\theta_{50}$ from cycle 1 to 2. Note that the cylinder composition is the same between cases. Combustion phasing is retarded and combustion efficiency is lower for cases with lower intake temperature. Figure 7.10 shows the (a) pressure traces and (b) mass fraction burned for cycle 1 of the intake temperature sweep. Figure 7.11 shows the pressure traces of cycle 1 and cycle 2 for the intake temperature sweep, (a) T_{IN} = 81°C, (b) T_{IN} = 66°C and (c) T_{IN} = 51°C. Low intake temperature cases with the later phasing in cycle 1 have a greater advance in phasing for cycle 2. This is due to more unburned fuel being available for heat release during NVO. Figure 7.12 shows the (a) cumulative heat release during NVO and (b) the

corresponding mean temperature during NVO. Low intake temperature cases have higher heat released during NVO, which leads to a larger temperature rise during NVO heat release and correspondingly higher T_{IVC} of cycle 2. This results in a proportional advance in the combustion phasing of cycle 2. Although the amount of heat released during NVO is different, the three curves are self-similar and heat release is complete before start of injection at -330°CA.

7.5 Effect of injection timing on NVO heat release

An injection timing sweep is performed during recompression of the second cycle where start of injection (SOI) is swept from 330°CA bTDC to 390°CA bTDC. Table 7.5 summarizes the operating conditions for the injection timing sweep including the θ_{50} for cycle 1 and cycle 2. Combustion timing advances with advancing injection timing. Figure 7.13 shows the (a) pressure traces and (b) mass fraction burned for cycle 2 for which the injection timing has been varied. The combustion timing advance is relatively small until θ_{inj}= -360°CA aTDC. Advance in θ_{50} is greater than 14^{o}CA for injection timing before TDC of NVO. Engines would typically not operate at these timings to avoid knock and loss of efficiency. Figure 7.14 shows (a) the cumulative NVO heat release and (b) the cumulative heat release for the main compression. The total heat release during NVO for injection timings up to -345°CA aTDC is the same. A slight rise is observed for the -360°CA aTDC case. The early injection cases have significant heat release during NVO, up to 100 J for the case with θ_{inj}= -390°CA aTDC. The total heat release between NVO and main compression for all cases remains roughly constant at 420 J. Figure 7.15 shows the mean temperature during NVO as the injection timing is varied. The slopes of the curves during expansion for the early injection cases are significantly different from the later timing cases. This behavior suggests that the combustion for these cases is mixing

controlled. More analysis is presented for these cases by inspecting the state of the reacting charge and mixing rates in the next sections.

7.5.1 Validity of reduced reaction mechanism for rich NVO conditions

Similar to Section 7.1.1 non-reacting CFD simulations are performed for the earliest SOI case (390°CA bTDC) until the end of injection (375°CA bTDC). Figure 7.16 shows the global Φ and temperature within each CFD cell at 375°CA bTDC. The cells marked with the red crosses are selected for comparison of the detailed and reduced gasoline surrogate mechanism ignition delays. Ignition delay is computed with both mechanisms for each of the selected cells and deliberately sweeping the temperature between 700K and 1400 K. Figure 7.17 (a) and (b) show the comparison of the ignition delays. Note that the ignition delays under all the inspected rich conditions are greater than 1 ms except for temperatures greater than 1250 K. According to Babajimopoulos et al. [19] ignition delays shorter than 1 ms (corresponding to 12°CA at 2000 RPM) noticeably contribute to combustion for HCCI and those greater than 1 ms are insignificant for combustion. The reduced mechanism follows the trend of the detailed mechanism across the entire temperature range. Moreover the maximum error between the mechanisms for ignition delays shorter than 1 ms are 0.2 ms which is equivalent to 2.4°CA at 2000 RPM. Thus even for highly rich conditions the reduced mechanism closely mimics the behavior of the detailed mechanism and justifies its usage.

7.6 State of reacting charge during NVO

The state of the reacting charge is analyzed to inspect the in-cylinder stratification and to guide the development of a simplified NVO HR model.

7.6.1 Late injection

Figure 7.18 shows the reaction space for the T_{IN}= 51°C case in Table 7.4. The CFD domain is represented in terms of temperature, global equivalence ratio (Φ) and reaction progress ($\bar{c}$), consistent with the analysis in Chapter 5. At the earliest crank angle (-381°CA aTDC), the charge is already reacted to between 0.6 < $\bar{c}$ < 1 since it is the residual carried over after main compression and exhaust. There is a narrow distribution in composition about the mean ϕ=0.58 with a wide distribution in temperature from 600K to 1400K. As the charge is compressed the remaining reactants in the charge are converted to products of complete combustion. This is reflected in Figure 7.18 by the lighter colored bins becoming darker as time advances and the charge is compressed while reacting and releasing heat. In this configuration NVO heat release can be modeled as the sequential auto-ignition of the hottest portion of.

7.6.2 Early injection

Figure 7.19 shows the reaction progress evolution during NVO from -391°CA aTDC to -275°CA aTDC for the θ_{inj} = -390°CA aTDC case. At the earliest crank angle, before the start of injection the charge has a narrow distribution in composition about the mean ϕ=0.58 and a wide distribution in temperature from 600K to 1000K. The charge is almost completely reacted since this case has a high combustion efficiency (η_{comb} = 0.95) for the main combustion event. After the start of injection more fuel is introduced in the chamber shown by the bins with low reaction progress and high ϕ, up to or greater than $\phi > 4$. Further during compression the charge undergoes mixing, producing bins in the reaction space that are spread over a wide range from 0.5 < ϕ < 4.0. Additionally, the charge is heated due to compression, which increases the reactivity of the charge and leads to greater reaction progress, as visible in Figure 7.19, -360°CA aTDC onward. The

highest reaction progress and local temperatures correspond to the charge with ϕ=1.1 since that is where the adiabatic flame temperature is highest.

7.7 Effect of varying mass diffusion on NVO heat release for early injection

The importance of turbulent mass diffusion on heat release can be assessed by varying the Schmidt number (Sc), defined as the ratio of momentum diffusivity to mass diffusivity. At a high Schmidt number the influence of mass diffusion is minimized, while at low Schmidt number mass diffusion dominates. Two additional simulations are performed corresponding to the early injection cases of θ_{inj}=-390°CA aTDC. For the first case the Sc $\rightarrow \infty$ and for the third case Sc = 0.2 while Sc=0.85 is the baseline value. Figure 7.20 shows the (a) cumulative NVO heat release and (b) mean temperature for the early SOI case while the Schmidt number is varied. The total heat released during NVO is sensitive to changes in the Schmidt number, suggesting that that under early injection timing conditions fuel mixing has a significant effect on NVO heat release behavior.

7.8 0D model for NVO heat release

The CFD results suggest that for late injection, recompression heat release during NVO can be modeled within a 0D framework (GT-Power) in a manner similar to the main combustion event. A simple recompression heat release model is developed and presented here based on the previously discussed CFD results. Further extension of the model to additional operating conditions would require additional parametric studies. Ignition is determined by an auto-ignition integral (Chapter 5) and the burn profile is modeled by an empirical correlation (Chapter 6). As seen in Figure 7.5(a) heat release during NVO starts earlier compared to the main heat release (relative to the respective TDC). This is due to hotter charge temperatures compared to main compression and lighter fuel species with other intermediates as seen in Figure 7.5(b) and Figure 7.6

respectively. Figure 7.21 shows ignition delay calculations from a constant volume homogeneous reactor for all cells in the CFD domain at 20°CA bTDC of NVO for the baseline case (Table 7.1) denoted by red dots. Ignition delays for a fresh charge with ϕ=0.32 due to air dilution (blue circles) and EGR dilution (ϕ=0.58, RGF=45%, black squares) are also plotted. The ignition delays for cells from NVO are an order of magnitude shorter than the ignition delays for the fresh charge. This difference can be modeled by reducing the activation energy of an ignition delay correlation by 20%. This is physically valid since the lighter fuels and intermediates present during recompression are more reactive than a fresh fuel air mixture.

The ignition is modeled is a manner similar to Chapter 5, with an auto-ignition integral using the adiabatic core temperature and uniform composition. The Goldsborough correlation [20] is used to compute the ignition delays while reducing the activation energy by 20% according to the previous explanation. The recompression heat release profile is modeled in a manner similar to the main burn correlation described in Chapter 6, and the profile here is selected as specified a single Wiebe function [21]. Equation 7.1 to Equation 7.3 describe the form of the fit for the parameters θ'_{25}, θ'_{50} and θ'_{75}.

$$\theta'_{IGN-25} = (a_1\theta'_{IGN} + a_2)\left(\frac{\phi}{0.35}\right)^{x_1}\left(\frac{RPM}{2000}\right)^{x_2}\left(\frac{P'_{TDC}}{25}\right)^{x_3} \quad \text{Equation 7.1}$$

$$\theta'_{25-50} = (a_3\theta'_{25} + a_4)\left(\frac{\phi}{0.35}\right)^{x_4}\left(\frac{RPM}{2000}\right)^{x_5}\left(\frac{P'_{TDC}}{25}\right)^{x_6} \quad \text{Equation 7.2}$$

$$\theta'_{50-75} = (a_5\theta'_{50} + a_6)\left(\frac{\phi}{0.35}\right)^{x_7}\left(\frac{RPM}{2000}\right)^{x_8}\left(\frac{P'_{TDC}}{25}\right)^{x_9} \quad \text{Equation 7.3}$$

where, θ_{IGN-25} = burn duration from ignition to 25% MFB,

θ_{25-50} = burn duration from 25% to 50% MFB,

θ_{25-50} = burn duration from 50% to 75% MFB,

RPM = engine speed (rpm),

ϕ' = fuel-to-air equivalence ratio,

P'_{TDC} = pressure at NVO TDC calculated based on EVC conditions (bar) = $P_{EVC} \cdot (V_{EVC}/V'_{TDC})^{\gamma_{EVC}}$

The coefficients $x_1 - x_9$ are intentionally kept the same as in Chapter 6 while coefficients $a_1 - a_6$ are tuned based on the CFD mass fraction burned result for the baseline case. The combustion efficiency model is the same as described in Chapter 6. The NVO heat release model is implemented as a user function in GT-Power sub routines.

A late phasing HCCI case is simulated to observe the effect of NVO heat release on the cycle simulation. Table 7.6 summarizes the operating conditions for the simulation. Figure 7.22 displays three consecutive cycles at the operating conditions with NVO heat release (dark lines) and without NVO heat release (light lines). Cycle [i] with NVO heat release active has a very late phasing, θ_{50}=25°CA aTDC. This is followed by significant NVO heat release seen in the pressure trace for Cycle [i+1] and an early phasing θ_{50}=14°CA aTDC. Cycle [i+2] has negligible NVO heat release and followed by late phasing θ_{50}= 25°CA aTDC. The three consecutive cycles simulated with NVO heat release deactivated lie on top of each at a combustion phasing of θ_{50}= 22°CA aTDC. This behavior for the deactivated case is unphysical and such a late phasing would typically cause unstable operation. Thus including NVO heat release makes the model behavior closer to reality.

7.9 Summary

Multi-cycle CFD simulations of HCCI are performed to analyze recompression heat release and its effect on the next cycle. It is shown that NVO heat release is due to auto-ignition of unburned charge for late fuel injection. For the lean conditions studied, NVO heat release is inversely proportional to the combustion efficiency of the main

combustion event. The effect of NVO heat release on the subsequent cycle is primarily thermal. Retaining fuel and intermediate species from the previous cycle with chemistry deactivated during NVO advances combustion (θ_{50}) by half the amount when the chemistry is active during NVO. NVO heat release is mixing controlled when fuel is injected before TDC of NVO. For late injection NVO heat release can be modeled simply as a sequential auto-igniting charge similar to the main combustion. A cycle simulation is performed for a late phasing case with and without NVO heat release. The simple model demonstrates the cyclic variability when the NVO model is active. More work is needed to match the model to experiments and to parameterize the NVO burn correlation under different operating conditions.

Table 7.1 – CFD simulation conditions for late phasing NVO-DI case.

Parameter	NVO-DI
Fueling rate (mg/cyc)	9.3
NVO (^{o}CA)	157
SOI (^{o}CA bTDC)	330
Speed (RPM)	2000
$\boldsymbol{\phi_{FO}}$ (mean)	0.44
$\boldsymbol{\chi_{O2}}$ (mean)	15%
T_{in}	66°C
Internal Residual (%)	43%

Table 7.2 – Mass percent of species at IVC of cycle 2 after recompression heat release.

Species	Cycle 2 – actual composition (%)	Cycle 2 – simple composition (%)
C8H18	0.85309	0.86039
C7H16	0.23453	0.23640
C6H5CH3	0.43166	0.43584
C5H10	0.05688	0.05737
O2	17.89621	17.91706
N2	74.42115	74.42115
CO2	4.33795	4.35558
H2O	1.73064	1.71620
H2	0.00003	0
H2O2	0.00014	0
CO	0.03558	0
CH2O	0.00032	0
CH4	0.00023	0
C2H4	0.00036	0
CH2CO	0.00015	0
C2H3CHO	0.00039	0
C3H6	0.00012	0
C4H8	0.00022	0
HOC6H4CH3	0.00036	0

Table 7.3 – Mass percent of species at IVC of cycle 2 without recompression heat release.

Species	Cycle 2 – composition (%)	Cycle 2 – composition w/o NVO-HR (%)
C8H18	0.85309	0.84782
C7H16	0.23453	0.23291
C6H5CH3	0.43166	0.42977
C5H10	0.05688	0.05654
O2	17.89621	17.99753
N2	74.42115	74.44161
CO2	4.33795	4.21412
H2O	1.73064	1.70140
H2	0.00003	0.00012
H2O2	0.00014	0.00066
CO	0.03558	0.06885
CH2O	0.00032	0.00193
CH4	0.00023	0.00092
C2H4	0.00036	0.00166
CH2CO	0.00015	0.00096
C2H3CHO	0.00039	0.00147
C3H6	0.00012	0.00072
C4H8	0.00022	0.00102
HOC6H4CH3	0.00036	0

Table 7.4 – CFD simulation conditions for intake temperature sweep. Other parameters such as fueling rate = 9.3 mg/cyc, NVO = 157°CA, Speed = 2000 RPM, ϕ_{FO}=0.44, χ_{O_2}=15%, SOI = 330°CA bTDC and RGF = 43% are held constant.

Parameter	T_{IN}=81°C	T_{IN}=66°C	T_{IN}=51°C
$\theta_{50-cycle1}$(°CA aTDC)	7.5	12	21
$\eta_{comb-cycle1}$(%)	99	95	78
$\Delta\theta_{50}$(°CA)	1	5	21
$\theta_{50-cycle2}$(°CA aTDC)	6.5	7	0

Table 7.5 – CFD simulation conditions for injection timing sweep. Other parameters such as fueling rate = 9.3 mg/cyc, NVO = 157°CA, Speed = 2000 RPM, ϕ_{FO}=0.44, χ_{O_2}=15%, T_{IN}= 66°C and RGF = 43% are held constant.

Parameter	SOI=330° bTDC	SOI=345° bTDC	SOI=360° bTDC	SOI=375° bTDC	SOI=390° bTDC
$\theta_{50-cycle1}$ (°CA aTDC)	7.5	7.5	7.5	7.5	7.5
$\theta_{50-cycle2}$ (°CA aTDC)	7.0	6.0	3.0	-7.0	-22.0

Table 7.6 – Simulation conditions for NVO heat release demonstration in GT-Power.

Parameter	T_{IN}= 30°C
Fueling rate (mg/cyc)	9.5
NVO (^{o}CA)	157
SOI (^{o}CA bTDC)	330
Speed (RPM)	1750
$\boldsymbol{\phi_{FO}}$ (mean)	0.55
$\boldsymbol{\chi_{O2}}$ (mean)	13%
Internal Residual (%)	39%

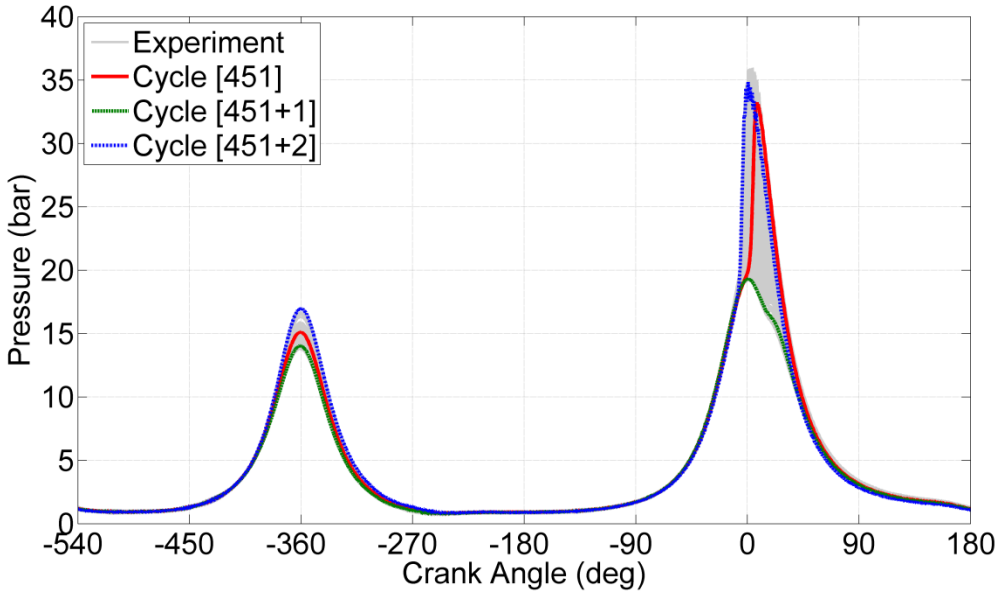

Figure 7.1 – Pressure traces for high variability cycles showing consecutive early and late phasing cycles.

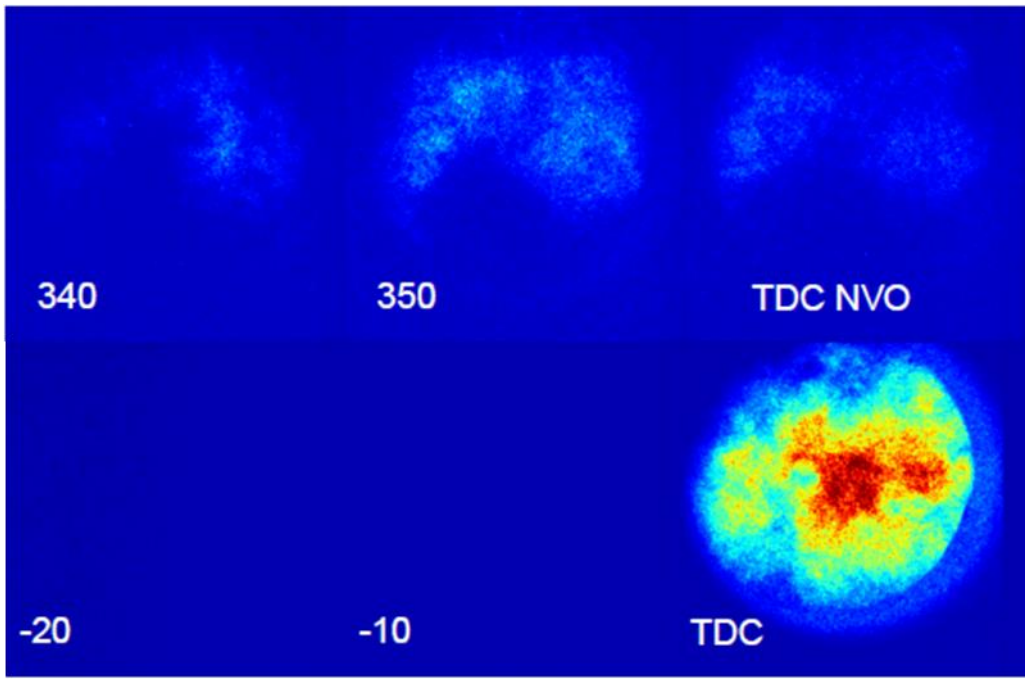

Figure 7.2 – Average images of chemiluminescence from 10 separate HCCI cycles at respective crank angles. OH radicals are seen during NVO in addition to near TDC main.

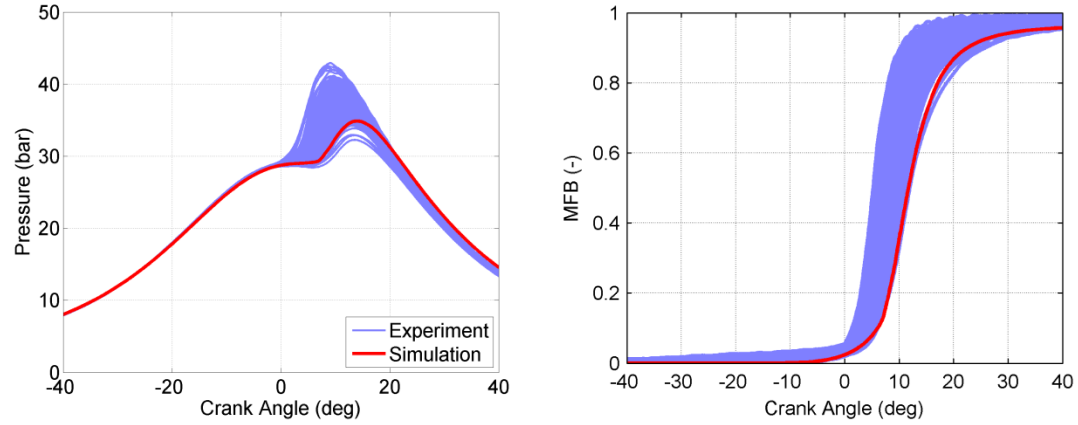

(a) (b)

Figure 7.3 – (a) Pressure traces and (b) mass fraction burned for experiments versus CFD: 9.4 mg/cycle injected, NVO =157°CA, T_{in} = 66°C, RGF (experiment) = 48%, RGF (CFD) = 43%, Φ (experiment) = 0.6, Φ (CFD) = 0.58.

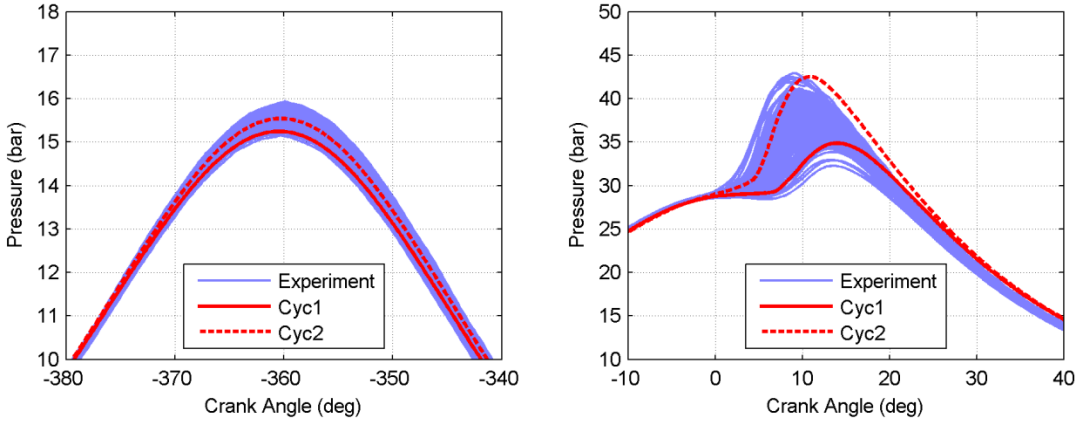

(a) (b)

Figure 7.4 – Pressure traces from the experiment, Cycle 1 and Cycle 2 (from CFD) (a) during NVO and (b) during main compression.

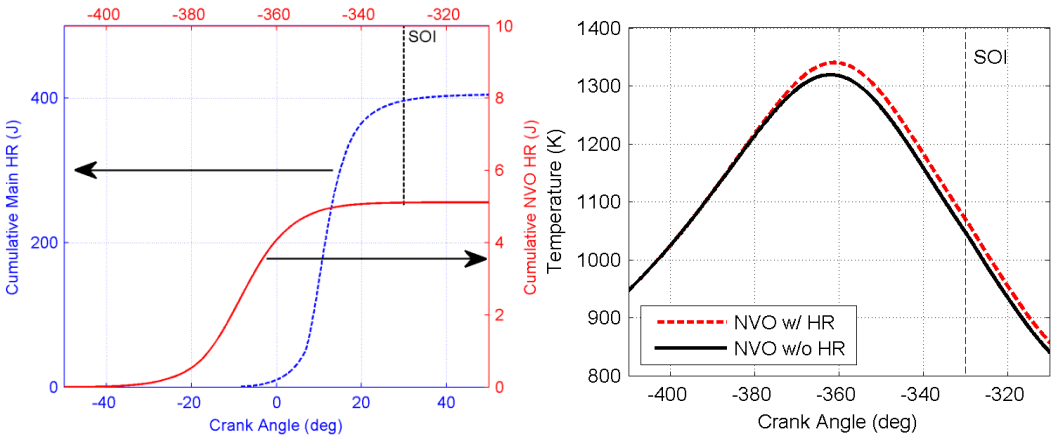

(a) (b)

Figure 7.5 – (a) Cumulative heat release for NVO and main compression and (b) Mean temperature during NVO with and without heat release.

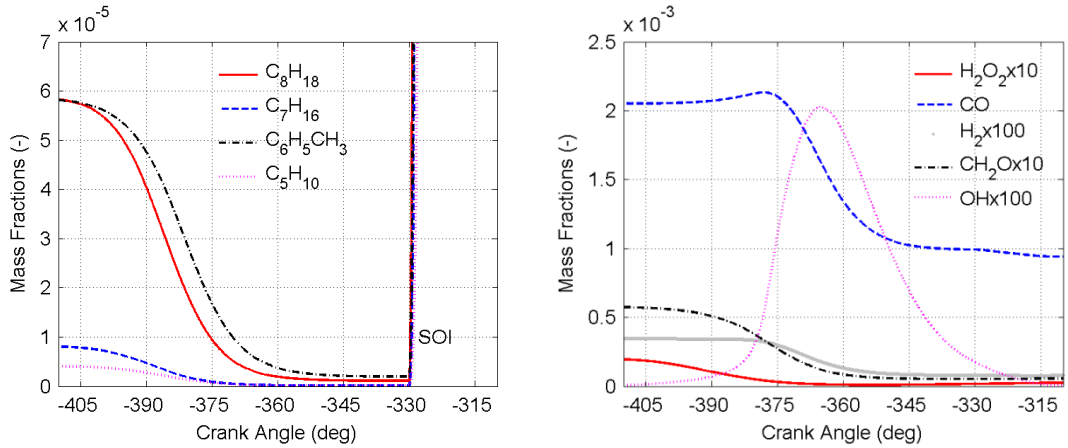

(a) (b)

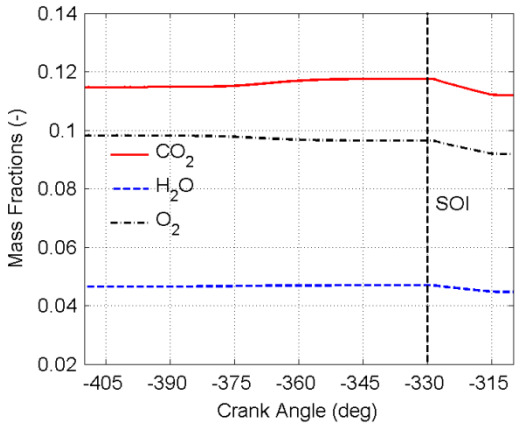

(c)

Figure 7.6 – Evolution of species mass fractions through NVO (a) fuel, (b) intermediates and (c) oxygen and products of complete combustion.

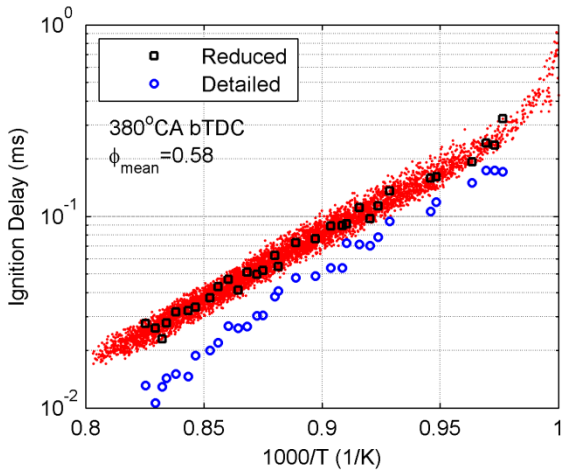

Figure 7.7 – Comparison of ignition delays computed by the reduced [17] and detailed [18] gasoline surrogate mechanisms for selected KIVA cells at 380°CA bTDC for the baseline case.

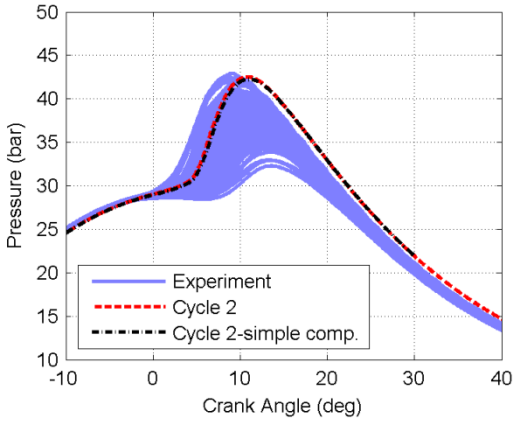

Figure 7.8 – CFD result for second cycle simulation with carried over species and simple composition with the same T_{IVC}.

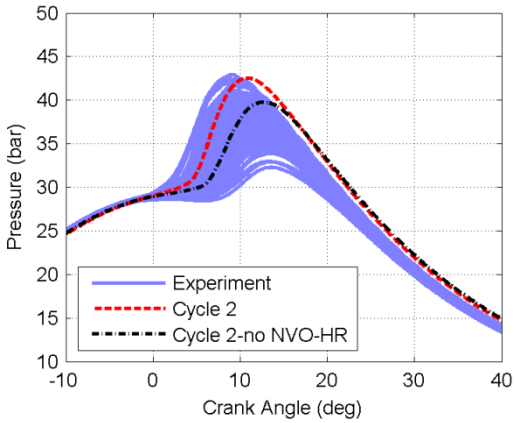

Figure 7.9 – CFD result for second cycle simulation with and without NVO heat release while carrying over species from previous cycle.

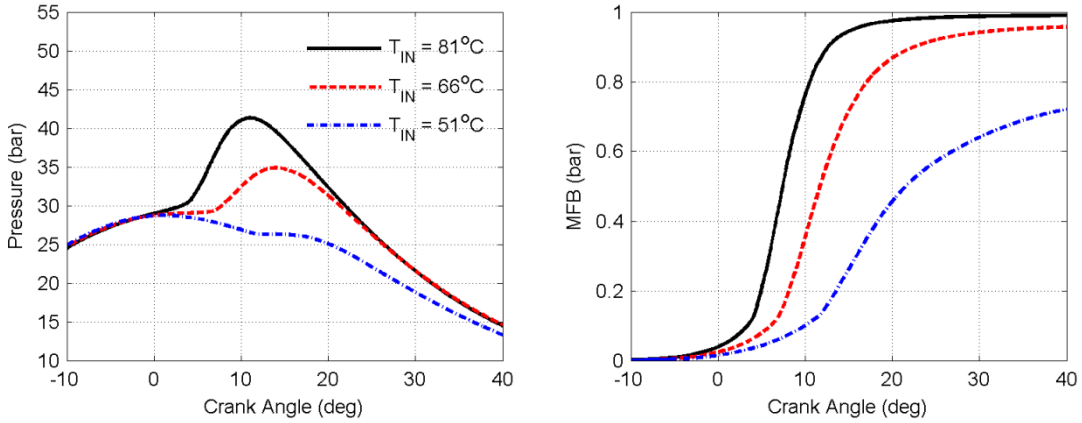

(a) (b)

Figure 7.10 – (a) Pressure traces and (b) MFB from CFD intake temperature sweep for Cycle 1.

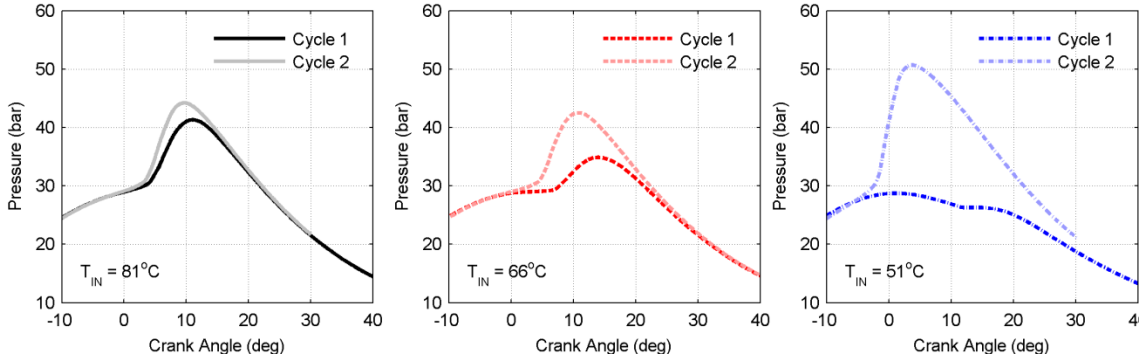

(a) (b) (c)

Figure 7.11 – Pressure traces of Cycle 1 and Cycle 2 for the intake temperature sweep. (a) T_{IN} = 81°C, (b) T_{IN} = 66°C and (c) T_{IN} = 51°C.

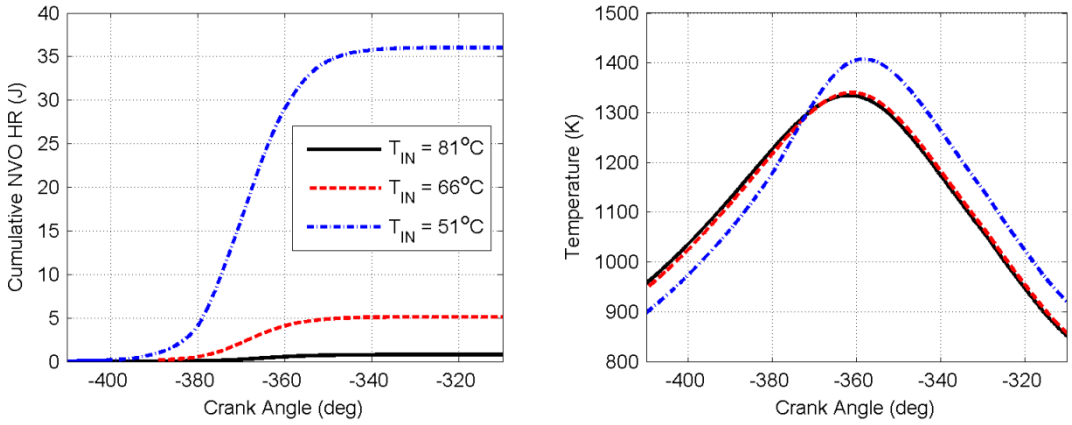

(a) (b)

Figure 7.12 – (a) Cumulative heat release and (b) mean cylinder temperature during NVO for the intake temperature sweep.

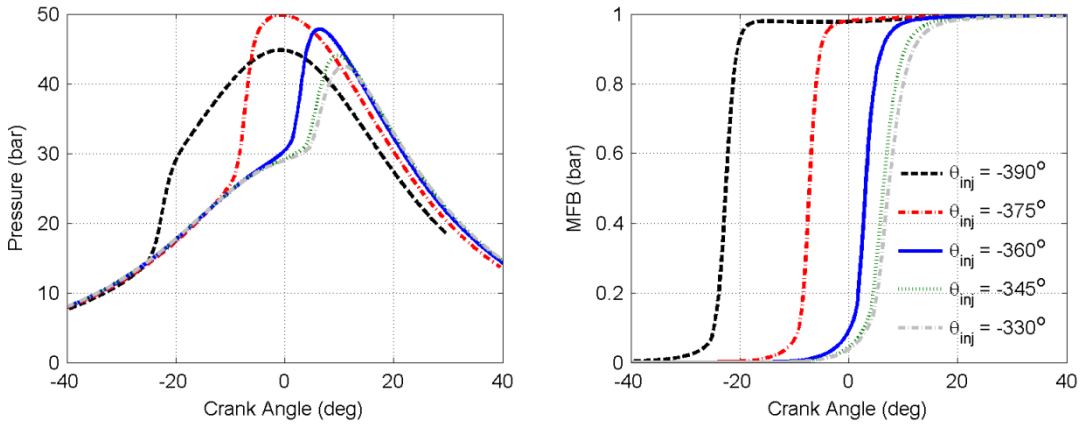

(a) (b)

Figure 7.13 – (a) Pressure traces and (b) MFB from CFD for Cycle 2 of the SOI sweep. Combustion advances with advancing SOI as there is more heat release during NVO.

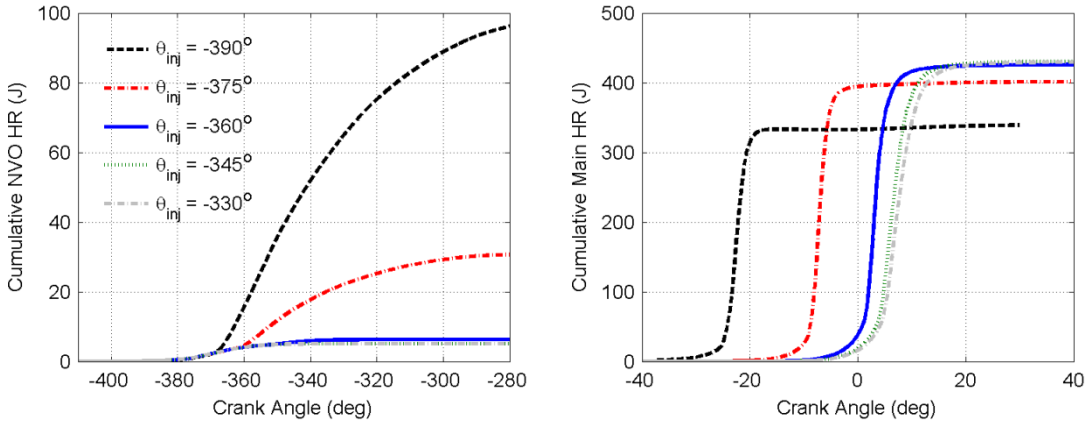

(a) (b)

Figure 7.14 – Cumulative (a) NVO HR and (b) Main HR from CFD for Cycle 2 of the SOI sweep.

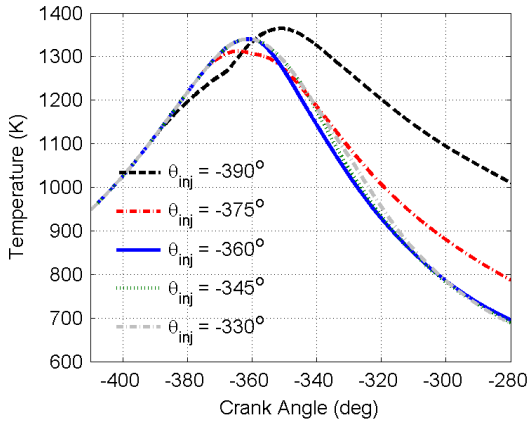

Figure 7.15 – Mean temperature through NVO from CFD for the SOI sweep.

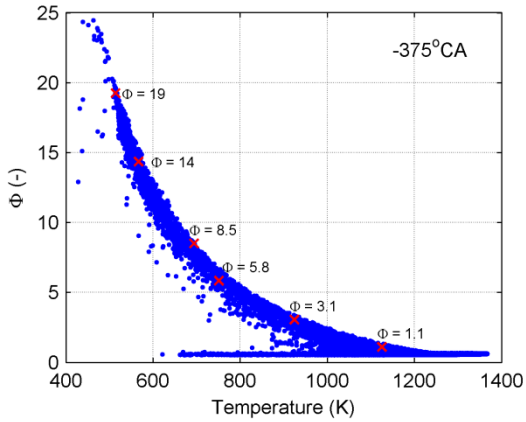

Figure 7.16 –Global Φ and temperature of each cell at end of injection (-375°CA).

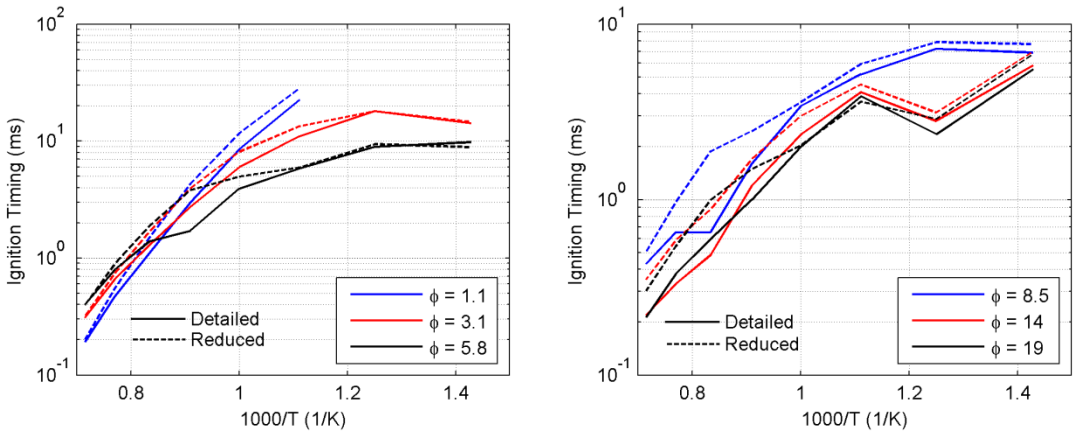

Figure 7.17 – Comparison of the detailed and reduced gasoline surrogate mechanism ignition delays over a range of temperatures for selected cells with (a) $1 < \Phi <$ and (b) $8.5 < \Phi < 20$. The solid lines denote the detailed mechanism and the dashed line denote the reduced mechanism.

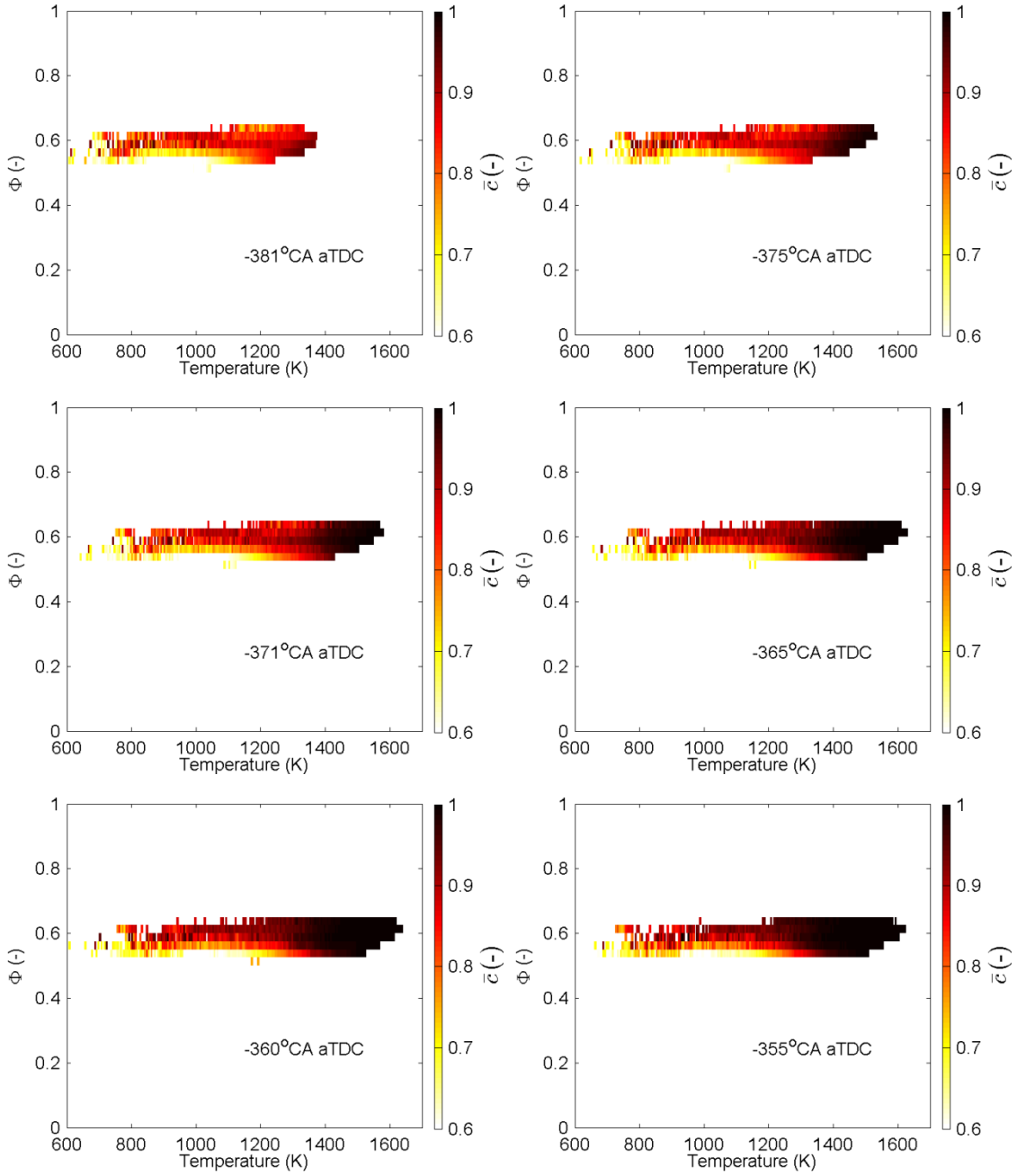

Figure 7.18 – Reaction progress plotted against local temperature and global equivalence ratio from -381°CA aTDC to -355°CA aTDC for T_{IN}=51°C case.

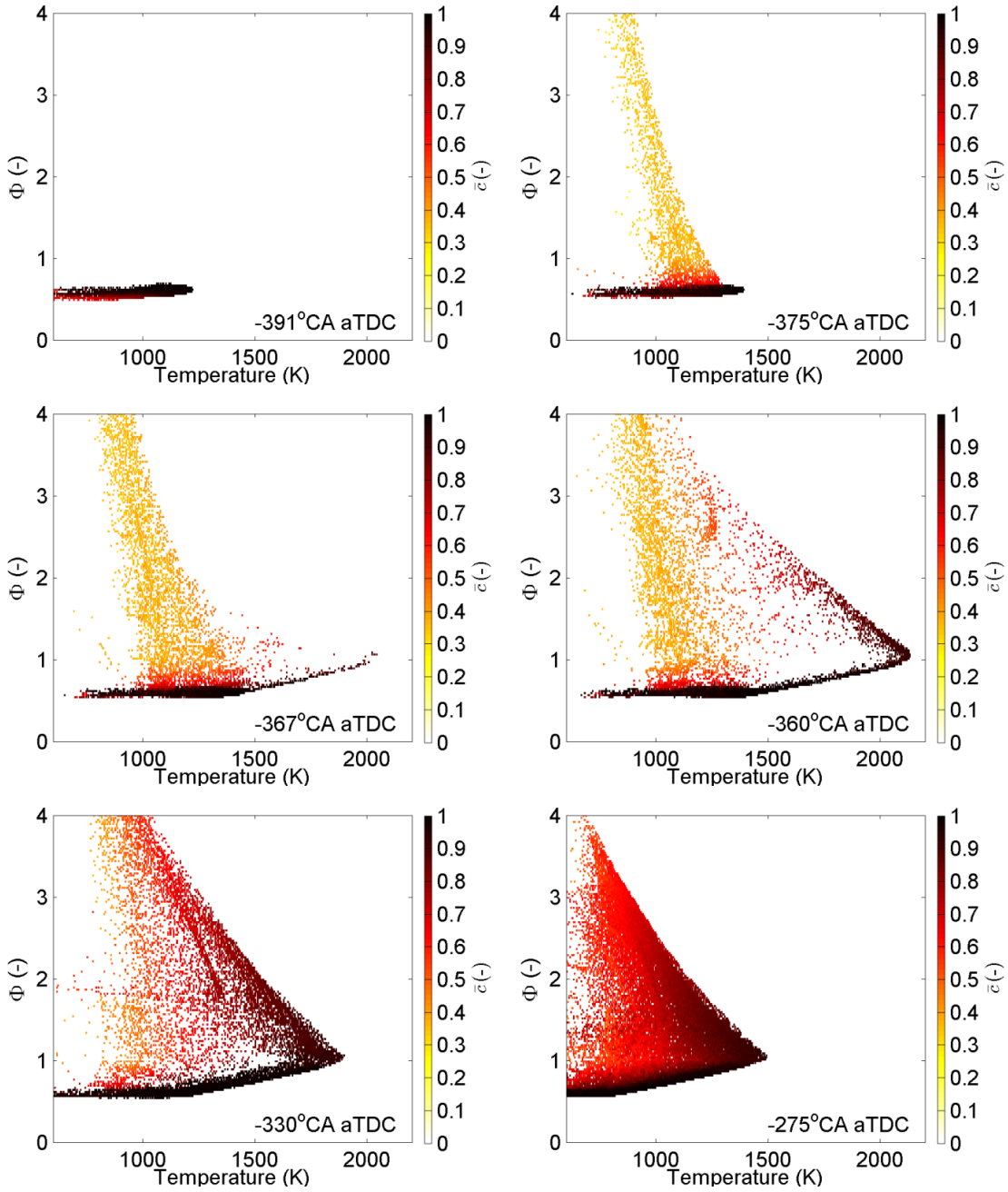

Figure 7.19 – Reaction progress plotted against local temperature and global equivalence ratio from -391°CA aTDC to -275°CA aTDC for SOI=390°CA bTDC case.

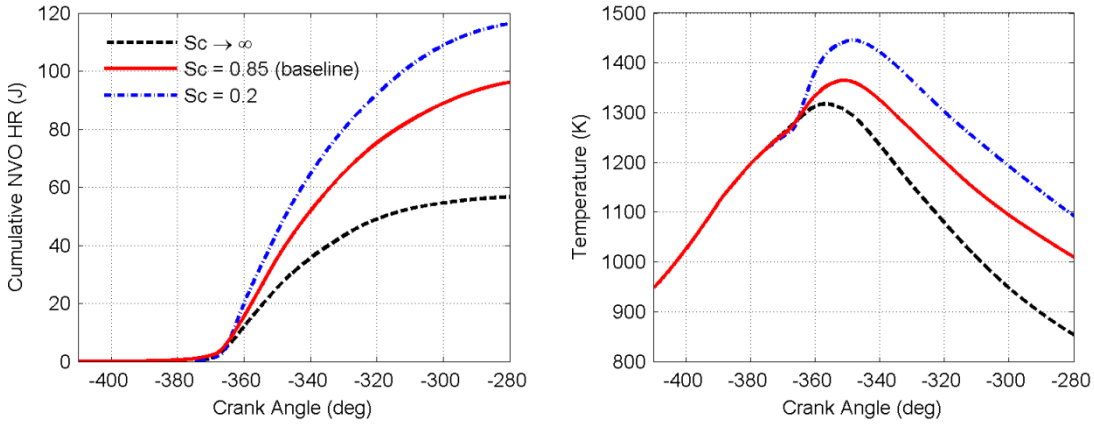

(a) (b)

Figure 7.20 – Cumulative (a) NVO HR and (b) NVO mean temperature from CFD for a Schmidt Number sweep.

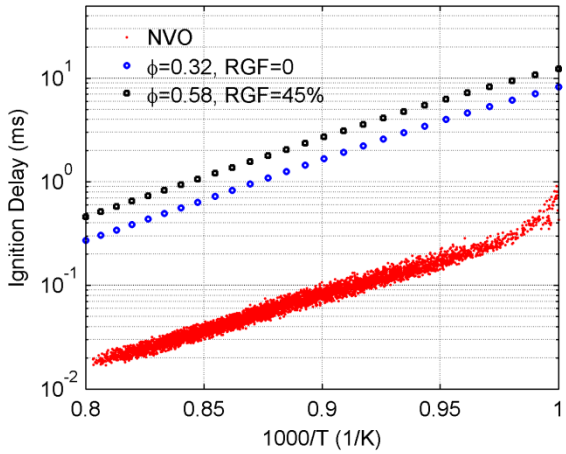

Figure 7.21 – Homogeneous constant volume ignition delays calculated for all KIVA cells at 20°bTDC NVO for the baseline case (red dots) compared to air dilute (blue circles) and EGR dilute (black squares) charge at the global ϕ'=0.32 and the same temperature as the CFD domain.

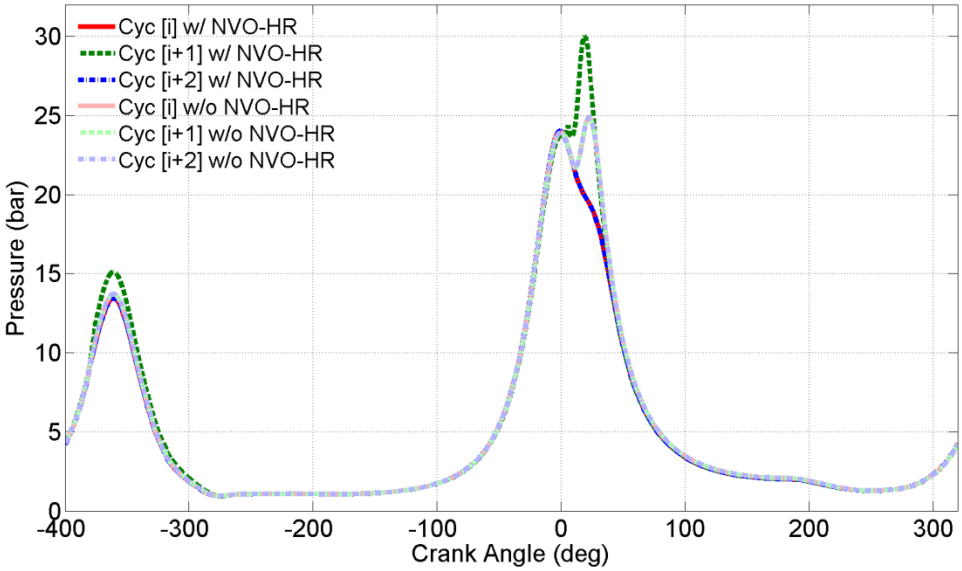

Figure 7.22 – Three consecutive cycles simulated in GT-Power cycle simulation with NVO-HR (dark likes) and without NVO-HR (light lines).

7.10 References

1. Thring, R., "Homogeneous-Charge Compression-Ignition (HCCI) Engines," SAE Technical Paper 892068, 1989.
2. Koopmans, L. and Denbratt, I., "A Four Stroke Camless Engine, Operated in Homogeneous Charge Compression Ignition Mode with Commercial Gasoline," SAE Technical Paper 2001-01-3610, 2001.
3. Finney, C. E., Kaul, B. C., Daw, C. S., Wagner, R. M., Edwards, K. D., and Green, J. B., "Invited Review: A review of deterministic effects in cyclic variability of internal combustion engines," International Journal of Engine Research, 16(3), 366-378, 2015.
4. E. Hellström, A. Stefanopoulou, J. Vavra, A. Babajimopoulos, et al. "Understanding the dynamic evolution of cyclic variability at the operating limits of HCCI engines with negative valve overlap," SAE International Journal of Engines, 5 (3), pp. 995–1008, 2012.
5. Vaughan, A., "Adaptive machine learning for modeling and control of non-stationary, near chaotic combustion in real-time," PhD Thesis, The University of Michigan, Ann Arbor, MI, 2015.
6. Song, H. H., Padmanabhan, A., Kaahaaina, N. B., and Edwards, C. F., "Experimental study of recompression reaction for low-load operation in direct injection HCCI engines and n-heptane and i-octane fuels," Int. J. Engine Res., 10(4), 215-230, DOI: 10.1243/14680874JER03309, 2009.
7. Fitzgerald R. P., and Steeper R. R., "Thermal and chemical effects of NVO fuel injection on HCCI combustion," SAE Int J Engines,3:46–64, 2010.
8. Hunicz, J., Kordos, P., and Ignaciuk, P., "Experimental Investigation into Thermal and Chemical Effects of Negative Valve Overlap Injection in a Gasoline HCCI Engine," SAE Technical Paper 2014-01-2660, 2014.

9. Hunicz, J., “An Experimental Study of Negative Valve Overlap Injection Effects and their Impact on Combustion in a Gasoline HCCI Engine,” Fuel 117:236-250, 2014.
10. E. Hellstrom and A. Stefanopoulou, “Cyclic variability and dynamical ¨ instabilities in autoignition engines with high residuals,” IEEE Trans. Contr. Syst. Technol., vol. 21, no. 5, pp. 1527–1536, 2013.
11. H. H. Song and C. F. Edwards, “Understanding chemical effects in low-load-limit extension of homogeneous charge compression ignition engines via recompression reaction,” Int. J. Engine Res., 10(4):231–250, 2009.
12. Kalaskar, V. B., Szybist J. P, Splitter, D. A., Pihl, J. A., Gao, Z., and Daw. C. S., "In-Cylinder Reaction Chemistry and Kinetics During Negative Valve Overlap Fuel Injection Under Low-Oxygen Conditions." In ASME 2013 Internal Combustion Engine Division Fall Technical Conference, pp. V002T02A017-V002T02A017. American Society of Mechanical Engineers, 2013.
13. Aroonsrisopon, T., Nitz, D. G., Waldman, J. O., Foster, D. E., and Lida, M., “A computational analysis of direct fuel injection during the negative valve overlap period in an iso-octane fueled HCCI engine, SAE 2007-01-0227, 2007.
14. Hessel, R. P., Steeper, R., Fitzgerald, R., Aceves, S., and Flowers, D., “Full Cycle CFD Simulations to Study Thermal and Chemical Effects of Fuel Injection during Negative Valve Overlap in an Automotive Research Engine,” SAE 2010-01-2236, 2010.
15. Tsurushima, T., “A New Skeletal PRF Kinetic Model for HCCI Combustion,” Proceedings of the Combustion Institute 32(2):2835-2841, 2009, doi:10.1016/j.proci.2008.06.018
16. Middleton, R. J., and Martz, J. B., “An efficient model of gas exchange for multi-cycle CFD simulations with detailed chemistry,” Publication in preparation.
17. Mehl, M., Chen, J.Y., Pitz, W.J., Sarathy, S.M., and Westbrook, C. K., “An Approach for Formulating Surrogates for Gasoline with Application toward a Reduced

Surrogate Mechanism for CFD Engine Modeling," Energy & Fuels, Vol. 25, Issue 11, pp. 5215-5223, 2011.

18. Mehl, M., Pitz, W.J., Westbrook, C.K., and Curran, H.J., "Kinetic Modeling of Gasoline Surrogate Components and Mixture Under Engine Like Conditions", Proceedings of the Combustion Institute, 33:193-200, 2011.
19. Babajimopoulos, A., Lavoie, G. A., and Assanis, D. N., "On The Role Of Top Dead Center Conditions In The Combustion Phasing Of Homogeneous Charge Compression Ignition Engines", Combustion Science and Technology, 179: 9, 2039 — 2063.
20. Goldsborough, S. S., "A chemical kinetically based ignition delay correlation for iso-octane covering a wide range of conditions including the NTC region," Combustion and Flame, 156(6), 1248-1262, 2009.
21. Ghojel, J. I., "Review of the development and applications of the Wiebe function: a tribute to the contribution of Ivan Wiebe to engine research," International Journal of Engine Research, 11(4), 297-312, 2010.

CHAPTER 8

SUMMARY, CONCLUSIONS AND RECOMMENDATIONS

The work presented in this thesis focused on understanding the effect of varying operating conditions on NVO-DI HCCI combustion and recompression heat release. CFD was used to understand the effect of these varying conditions on reactivity stratification and HCCI combustion. This understanding was used to propose an improved ignition and empirical burn profile model which was then implemented in a 0D thermodynamic engine simulation. The improved model could correctly capture the trend-wise behavior of HCCI transients, with limited agreement for cycle to cycle behavior. It was hypothesized that the cyclic coupling was in part due to recompression heat release. CFD was exercised again to draw new insight into the recompression heat release process. Based on this knowledge a simple NVO heat release model was briefly demonstrated. The major conclusions and recommendations for future work are summarized below.

8.1 Summary and conclusions

8.1.1 Effect of operating conditions on reactivity stratification and HCCI combustion

CFD was used in Chapter 3 and Chapter 4 to analyze the effect of speed, load (total dilution ϕ'), boost, injection timing, NVO and intake manifold temperature on HCCI combustion. Simulations were performed where the input variable was swept while changing the intake manifold temperature to hold the location of 10% mass fraction burned (θ_{10}) constant (except for intake temperature sweep). Injected fuel mass was changed to hold the total mixture dilution constant (except for the load sweep). The effect

of each input on the pre-ignition reactivity distributions and HCCI combustion rates was isolated.

While some variation in ϕ_{FO} stratification was noted for the engine speed, SOI and NVO studies, the cumulative reactivity distributions computed near TDC from the cell level and mean compositions of these cases showed little difference.

- Therefore, under the conditions studied, the observed compositional stratification has negligible effect on HCCI charge reactivity and combustion rates compared to thermal stratification. Based on these results, it can be concluded that compositional stratification is not important to combustion rates under the conditions studied.

As engine speed was swept, mean charge temperatures increased with speed to hold the θ_{10}, the crank angle of 10% mass fraction burned constant, given the reduced residence time of these charges. Despite these shifts, thermal stratification did not vary significantly with speed.

- Therefore, the combustion rate increases observed with speed result from the reactivity shift of the entire charge which is necessary to match θ_{10}.

With increasing load [total dilution (ϕ')] the mean temperatures were slightly lowered to match θ_{10}.

- The thermal stratification remained the same between cases, therefore the observed reactivity increases and shorter burn durations for the high load cases result from lower levels of charge dilution.

During the boost sweep, increasing manifold pressures had to be accompanied with significantly lower intake temperatures to hold θ_{10} constant at the baseline value. The thermal stratification decreased with increasing boost.

- Decreases in boost were compensated for with higher mean temperatures, which produced greater wall heat losses and additional thermal stratification.
- The combustion durations reduced with increasing boost primarily due to lower thermal stratification when the combustion timing was the same between all cases.

For the SOI sweep, the thermal stratification remained the same and the mean temperatures were also matched. The charge temperature at the end of NVO expansion depended on the amount of charge cooling and changing γ due to fuel injection timing. The intake manifold temperature had to be increased as the injection timing was retarded or advanced from the baseline (-330°CA aTDC) to maintain θ_{10}.

- However since the thermal stratification remained constant the burn durations did not change.

To hold θ_{10}constant during the NVO sweep, the intake temperature was reduced to compensate for the increased quantity of hot residuals.

- Changing NVO did not affect thermal stratification and the burn durations did not change.

For the intake temperature sweep, the thermal stratification and mean temperature at 11.5^{o} CA before θ_{10} remained the same between all the cases yet the combustion

process was significantly different from case to case. As the intake temperature was increased, the θ_{10} timing advanced and the burn durations became shorter.

- The changing burn rates for the intake temperature sweep were due to changing combustion timing (θ_{10}) and the different pressures at θ_{10} between the cases.

The main finding from the above mentioned investigations was that if an input parameter is changed while holding the combustion timing and total dilution constant the combustion is determined by the pre-ignition peak temperature and the thermal stratification.

8.1.2 Adiabatic core ignition model

CFD was used in Chapter 5 to interrogate the HCCI ignition process for a low stratification PVO case and high stratification NVO case. Auto-ignition began in the hottest portion of the charge at high temperatures, without low temperature heat release for these typical HCCI operating conditions. Current ignition modeling approaches employing high temperature Arrhenius ignition delay expressions are therefore appropriate for such conditions.

Two ignition models (Adiabatic core and mean temperature) were validated for PVO and NVO valve events predicted from CFD, along with the CFD data from Chapters 3 and 4. The model using mean temperature and composition, consistently predicts late ignition.

- For the new ignition model using the adiabatic core temperature and mean composition, the assumption of uniform state (temperature and composition) at IVC

for computing the initial entropy is not valid since the charge is fairly stratified at IVC.

- However, the adiabatic core temperature matches the temperature of the hottest 1% charge near TDC, resulting in improved ignition predictions for all examined simulations.

8.1.3 New burn correlation and improved 0D model performance

In Chapter 6, a new phenomenological combustion rate model was developed from HCCI experimental heat release data, modeling HCCI combustion as a three step process; the initial slow burn, a fast burn where the majority of the chemical energy is released and a late slow burn. The burn model is in an algebraic form that is a function of ignition location, engine speed, total dilution and intake boost, similar to previous work. To avoid over fitting, only the parameters that combustion showed sensitivity to, were selected for regression, based on the KIVA simulations from Chapters 3 and 4. The burn correlation along with the adiabatic core ignition model was implemented in GT-Power with user subroutines. The new burn correlation was evaluated with the adiabatic core ignition model against transient HCCI experimental data.

The new burn correlation that modeled the main burn as well as the initial intermediate temperature heat release and late slow burn matched the experimental mass fraction burned profile better than simply using a single Wiebe function. The full model trend wise matched transient experiments for changing engine speed, EVC, SOI and mass of fuel injected. The model also captured some amount of cycle-to-cycle coupling.

- The large cycle to cycle variations in combustion phasing were not captured in part due to NVO heat release not being modeled.

The burn correlation was exercised as a tool to isolate the effects of engine speed, ϕ', intake boost and ignition timing on the combustion profile. The manifold pressures did not change greatly for the examined transients resulting in minimal effect on post ignition burn profiles.

- For the engine speed transient, the resulting changes in θ_{IGN} and engine speed had a dominant and opposite effect on burn duration. Retarding or advancing θ_{IGN} made the burn duration longer or shorter, respectively, while reducing or increasing speed makes the burn duration shorter or longer respectively.
- For the EVC and SOI transients, θ_{IGN} had the most effect on the burn duration.
- For the fuel transient, θ_{IGN} and ϕ' equally affected the burn duration. Advancing θ_{IGN} or increasing ϕ' shortened the burn duration while retarding θ_{IGN} or decreasing ϕ' lengthened the burn duration.

8.1.4 Recompression heat release

In Chapter 7, multi-cycle CFD simulations of HCCI were performed to analyze recompression heat release and its effect on the next cycle. CFD simulations were performed for a second cycle with chemistry active through NVO in KIVA-3V.

- NVO heat release was due to auto-ignition of unburned charge within the residual from the previous cycle when fuel injection was late (after NVO TDC).
- The amount of NVO heat release was inversely proportional to the combustion efficiency of the previous main combustion event, provided the charge is overall lean (ϕ<1).

- The effect of NVO heat release on the subsequent cycle was primarily thermal in nature, resulting from the increased residual temperature associated with the NVO heat release.
- While unburned fuel and intermediate species from the previous cycle without NVO heat release advanced combustion phasing, the effect was approximately one half of that observed when NVO heat release was active and the charge temperature increased due to chemical reactions. For early injection (before NVO TDC), the charge was highly stratified in terms of global Φ at the end of injection ($0.4< \Phi<20$). There was significant heat release during NVO, which was sensitive to mixing rates (late NVO heat release was not).

For the purposes of thermodynamic modeling, NVO heat release for late injection can be treated as a sequential auto-ignition process similar to that used for the modeling of the main combustion event. A cycle simulation was performed for a late phasing case with and without NVO heat release. The simple model demonstrates the prediction of cyclic variability when the NVO heat release model is activated.

8.2 Scientific Contributions

There are three main contributions of this dissertation. First, explanation of the physical effects of changing operating conditions on HCCI combustion. Prior work [1] has explained the effect of different charge preparation strategies on HCCI combustion. This work has described the effect of operating conditions on HCCI stratification and combustion for a fixed method of charge preparation namely NVO-DI. The following findings were noteworthy and shown for the first time. Compositional stratification changes with operating conditions (NVO, SOI and engine speed) but has negligible effect

on charge reactivity and combustion. For the boost sweep with constant location of combustion onset the shorter burn durations at higher boost were shown to be primarily due to smaller thermal stratification which was a surprising finding. Another surprising finding was that the changing SOI and NVO did not affect the burn rates when the onset of combustion and total dilution were held constant.

Second, the effectiveness of the adiabatic core concept to model ignition under stratified conditions over a wide operating range was examined. The adiabatic core concept was shown to be applicable to the earliest igniting portions of HCCI for compositionally homogeneous charge by Dec et al. [2]. The adiabatic core temperature was used for the prediction of knock within SI engines by Hopke et al. [3] and for premixed HCCI charges by Fiveland et al. [4]. This thesis for the first time showed the validity of using the adiabatic core concept to model the hottest portion of HCCI charge temperature under compositionally stratified conditions. The adiabatic core ignition model was shown to be valid under a wide range of inputs and operating conditions. The new 0D model utilizing the adiabatic core ignition model was able to reproduce trends of large experimental transients without modifying the Arrhenius threshold of the auto-ignition integral.

Third, new insight provided into the NVO heat release process and its effect on the subsequent cycle. Multi-cycle 3D CFD simulation of HCCI using a gasoline surrogate mechanism with chemistry active during NVO were performed for the first time as part of this thesis. For late injection timing the hypothesis that NVO heat release is due to auto-ignition of residual from previous cycle [5] was confirmed by this work. It was shown for the first time that early injection heat release is in part mixing controlled. The hypothesis that the effect of NVO heat release on the next cycle is primarily thermal [6] was confirmed by this work. It was shown that carrying over fuel/intermediates from previous cycle with NVO chemistry deactivated only partially captured the coupling between cycles.

8.3 Recommendations for future work

Based on the understanding developed in this thesis the following recommendations are made for future work. This work has shown that thermal and compositional stratification change significantly with operating conditions (speed, boost, etc.). Kodavasal [1] and Middleton [5] have validated the spray and mixing models used here. However higher fidelity spray models and improved mixing models along with finer grid and techniques such as LES might provide further insight into the pre-ignition stratification development.

It has been shown that for early fuel injection into a lean mixture during recompression, the combustion during NVO is mixing controlled. More work needs to be done to investigate the possibility of diffusion flames generated by fuel injection during NVO.

The multi-cycle RANS CFD simulations have shown the ability to capture part of the coupling between cycles observed in experiments. LES, which can capture smaller scale fluctuations, can be exercised with HCCI combustion to capture the stochastic cyclic variability speculated to be driven by turbulence mixing.

Combustion phasing and injection timing have been shown to have a significant effect on recompression heat release and the subsequent cycle. A comprehensive parametric sweep can be performed to observe the effect of changing engine operating parameters on NVO heat release. This would include changing speed, ϕ and boost.

A simple 0D model for NVO heat release has been demonstrated. Based on an improved understanding of the physical processes involved in recompression heat release for early injection and a comprehensive parametric sweep an improved model can be implemented into a 0D framework.

8.4 References

1. Kodavasal, J., “Effect of charge preparation strategy on HCCI combustion,” PhD Thesis, The University of Michigan, Ann Arbor, MI, 2013.
2. Dec, J.E., Hwang, W., and Sjöberg, M., “An Investigation of Thermal Stratification in HCCI Engines Using Chemiluminescence Imaging,” SAE Paper 2006-01-1518, 2006.
3. Hoepke, B., Jannsen, S., Kasseris, E. and Cheng, W., “EGR Effects on Boosted SI Engine Operation and Knock Integral Correlation,” SAE Int. J. Engines5(2): doi:10.4271/2012-01-0707, 2012.
4. Fiveland, S. B., and Assanis, D. N., “Development of a two-zone HCCI combustion model accounting for boundary layer effects,” SAE Technical paper 2001-01-1028, 2001.
5. E. Hellström, A. Stefanopoulou, J. Vavra, A. Babajimopoulos, et al. “Understanding the dynamic evolution of cyclic variability at the operating limits of HCCI engines with negative valve overlap,” SAE International Journal of Engines, 5 (3), pp. 995–1008, 2012.
6. Fitzgerald R. P., and Steeper R. R., “Thermal and chemical effects of NVO fuel injection on HCCI combustion,” SAE Int J Engines,3:46–64, 2010.
7. Middleton, R. J., “Simulation of spark assisted compression ignition combustion under EGR dilute engine operating conditions,” PhD Thesis, The University of Michigan, Ann Arbor, MI, 2014.